# Polarimeter Development for Electric Dipole Moment Measurements in Storage Rings

Von der Fakultät für Mathematik, Informatik und Naturwissenschaften der RWTH Aachen University zur Erlangung des akademischen Grades eines Doktors der Naturwissenschaften genehmigte Dissertation

vorgelegt von

Master of Science Physics

Fabian Müller

aus Heiden in der Schweiz

Berichter: Univ.-Prof. Dr. rer. nat. Jörg Pretz
Univ.-Prof. Dr. rer. nat. Lutz Feld

Tag der mündlichen Prüfung: 27. November 2019

**Abstract**

The ***J****ülich* ***E****lectric* ***D****ipole* ***I****nvestigation* (JEDI) collaboration aims at the measurement of a charged particle ***E****lectric* ***D****ipole* ***M****oments* (EDM) for protons and deuterons with a statistical sensitivity of $\sim 10^{-29}\,e\,\mathrm{cm}$ in a storage ring based experiment. This should be achieved by an interaction of the EDM with a radial electric field that causes a vertical polarization build-up in a previously vertically polarized, coherent beam. To measure this minuscule polarization build-up, a designated polarimeter based on heavy LYSO crystals was developed. The polarimetry reaction employed to measure the polarization is the elastic scattering of polarized particles off an unpolarized carbon target. The measured scattering asymmetry can be related to the beam polarization if the *analyzing power* of the reaction is known. This work consists of two major parts. In the first part, the analysis of the *database experiment*, which aimed at the measurement of the vector analyzing power for the deuteron carbon elastic scattering reaction using seven different beam energies, will be presented. This experiment was performed at the ***Co****oler* ***Sy****nchrotron* (COSY) accelerator facility at the *Forschungszentrum Jülich* in Germany. Different methods for the extraction of the scattering asymmetry will be presented and the result for the extracted deuteron carbon vector analyzing power and the unpolarized differential cross section for this reaction will be given. In the second part, the iterative development process of the designated polarimeter will be described in detail. For this device, a modular approach was chosen based on individual detector modules. These modules consist of an inorganic LYSO scintillator crystal that is optically coupled to a SiPM array that converts the scintillation light into an electric signal that can be processed by fast flash-ADC. Multiple properties of these modules such as resolution or linearity were tested and proved the concept to be well suited for the final designated polarimeter.

# Contents

# Chapter 1

# Motivation

Our whole world is made from ordinary (baryonic) matter. As far as we can tell this is the case for our whole solar system, our galaxy and probably for the entire universe. The ratio between matter and anti-matter in the universe can be estimated using the baryon asymmetry parameter $\eta$ defined as follows:

$$\eta = \frac{N_B - N_{\bar{B}}}{N_\gamma} \approx \frac{N_B - N_{\bar{B}}}{N_B + N_{\bar{B}}}, \tag{1.1}$$

with $N_B$ being the number of baryons, $N_{\bar{B}}$ the number of anti-baryons and $N_\gamma$ the number of photons. For a certain period after the big bang, the temperature was high enough for the pair creation and annihilation to be in thermal equilibrium. When the temperature dropped below the threshold of pair creation, the vast majority of the matter annihilated with the anti-matter into photons and hence $N_B + N_{\bar{B}} \approx N_\gamma$. It is possible to estimate $\eta$ from the ***C**osmic **M**icrowave **B**ackground* (CMB) spectrum and the analysis of the distribution of chemical elements in the ***I**nter**g**alactic **M**edium* (IGM). The results of both methods are compatible and suggest a value of $\eta \approx 6 \cdot 10^{-10}$ [1]. However, this result is not in agreement with the ***S**tandard **M**odel of Particle Physics* (SM) combined with the *standard model of cosmology* (SCM) which predicts a value of $\eta \approx 10^{-18}$ [2].

To explain the asymmetry between matter and anti-matter, *Andrei Sakharov* in 1967 defined three conditions that have to be fulfilled [3]:

1. Baryon number violation. Without this violation, it would not be possible for a system to evolve from a state with no baryons into a state with baryons, as the system initially was in a state with a baryon number $B = 0$.

2. $\mathcal{C}$ and $\mathcal{CP}$ violation: If $\mathcal{C}$ and $\mathcal{CP}$ invariance were fully conserved, for each process that created a particle another process that created an antiparticle with the exact same probability would exist, and therefore also no baryon asymmetry could have developed.

3. Deviation from thermal equilibrium. In thermal equilibrium, the expected value of all physical quantities, are stable and it would be impossible for the system to transit from a $B = 0$ into a $B \neq 0$ state.

The SM does fulfill these requirements up to a certain extent, but the amount of $\mathcal{CP}$ violation is too small to account for the observed baryon asymmetry. This means that other sources of $\mathcal{CP}$ invariance have to be found. This is where the ***E**lectric **D**ipole **M**oment* (EDM) of particles such as neutrons and protons enter the stage.

The EDM is classically defined as two charges $q$ and $-q$ separated at a distance $\vec{r}$ and therefore represents a vectorial quantity. In the framework of quantum mechanics, the EDM of a fundamental particle is defined as follows:

$$\vec{d} = d \cdot \vec{s} \quad \text{with} \quad d = \eta \frac{q\hbar}{2mc}, \tag{1.2}$$

where the particle's charge is given by $q$ and its mass by $m$. The electric dipole is denoted by the dimensionless quantity $\eta$. To retain the vector nature of the EDM, it has to be aligned with the spin $\vec{s}$ as this represents the only quantization axis available. The EDM is defined in analogy to the ***M**agnetic **D**ipole **M**oment* (MDM) of a particle that is given by:

$$\vec{\mu} = \mu \cdot \vec{s} \quad \text{with} \quad \mu = g \frac{q\hbar}{2m}, \tag{1.3}$$

and is aligned with the spin as well. The factor $g$ is the dimensionless magnetic dipole (also called "g-factor"). The existence of EDMs would break the $\mathcal{P}$ and the $\mathcal{T}$ invariance and as a consequence of the latter the $\mathcal{CP}$ invariance as well (see Section 2.1.2). This can be seen by applying the $\mathcal{P}$ and the $\mathcal{T}$ transformation (see Section 2.1.1 for more details about these symmetries) on the Hamiltonian that describes the EDM and the MDM in external electric $\vec{E}$ and magnetic $\vec{B}$ fields for a particle at rest:

$$\hat{\mathcal{H}} = -d \cdot \vec{s} \cdot \vec{E} - \mu \cdot \vec{s} \cdot \vec{B} \tag{1.4}$$

$$\mathcal{P} : \hat{\mathcal{H}} = +d \cdot \vec{s} \cdot \vec{E} - \mu \cdot \vec{s} \cdot \vec{B} \tag{1.5}$$

$$\mathcal{T} : \hat{\mathcal{H}} = +d \cdot \vec{s} \cdot \vec{E} - \mu \cdot \vec{s} \cdot \vec{B} \tag{1.6}$$

The parity transformation in Equation (1.5) inverts the direction of the electric field $\vec{E}$ but leaves the magnetic field $\vec{B}$ and the spin $\vec{s}$ unchanged. The sign of the EDM term changes but the MDM term remains the same. Therefore, one can state that the EDM violates the $\mathcal{P}$ invariance while the MDM preserves the parity. The same is true for the time reversal transformation of Equation (1.6) where the spin and the magnetic field are inverted while the electric field remains the same.

The $\mathcal{CP}$ symmetry breaking property of the EDM makes it an interesting candidate for an additional source of $\mathcal{CP}$ violation that is needed according to Sakharov's $2^{\text{nd}}$ condition. However, the SM predicts the EDM to be very small or even zero. Recent measurements on the neutron EDM have found an upper limit of $3 \times 10^{-26}\, e\,\text{cm}$. For charged particles such as protons and deuterons, no direct measurements have been performed yet. The ***J**ülich **E**lectric **D**ipole **I**nvestigation* (JEDI) collaboration aims at the measurement of such a charged particle EDM for protons and deuterons. A lot of effort has been put into the research and development of the tools needed to perform this measurement using a designated all-electric storage ring. A precursor experiment is planed to be conducted at the ***Co**oler **Sy**nchrotron* (COSY) accelerator facility located at the *Forschungzentrum Jülich* in Germany. A detailed review of the activity of the JEDI collaboration can be found in [4].

To measure the EDM of charged particles in a storage ring, one starts with coherently horizontally polarized particles that are kept in the ring. It will in this sense act similar to the magnetic traps used in the neutron EDM measurements, but for charged particles and with the advantage of the large number of particles that can be stored like this. The particles will interact with a radial electric field that couples to the EDM and cause a small vertical polarization build-up which is proportional to the magnitude of the EDM. Special effort is needed to assure that there are no radial magnetic fields present as they will couple to the MDM and create a vertical polarization build-up that can be mistaken for an EDM signal. To measure the polarization build-up, a precise and very stable polarimeter is needed. The main objective of this thesis is the development of such a device. Chapter 5 describes the requirements imposed on such a polarimeter together with the development and test process. The polarimetry reaction needed to measure the beam polarization is provided by elastic scattering off a carbon target. This scattering reaction produces a left/right asymmetry in the number of recorded events in the polarimeter. This asymmetry is proportional to the product of beam polarization and a quantity called *analyzing power*, which is a property of the target material, beam energy, and scattering angle. Chapter 2 will provide a theoretical introduction to the analyzing power and Chapter 4 is fully designated to measure the deuteron carbon analyzing power for different beam energies.

The development of a designated polarimeter and the measurement of the deuteron carbon analyzing power needed to extract the beam polarization will add a small piece to the huge endeavor that is undertaken by the JEDI collaboration to measure an EDM of charged particles and approach a statistical sensitivity of $\sim 10^{-29}\,e\,\mathrm{cm}$. They, in turn, take all of this effort with the objective to add a small share to the answers of the most fundamental questions of nature and our very existence.

# Chapter 2

# Theoretical Introduction

## 2.1 Symmetries and Symmetry Violation

Symmetries play a crucial role in physics as they are connected with the fundamental conservation laws that have been found in nature. The conservation of quantities such as energy, momentum, or charge build the base of our understanding of the universe and are therefore interwoven in all physics models. For a long time, these symmetries were assumed to hold in every case but in the last 60 years, it was experimentally found that there exist situations where symmetry can be violated. In this section, a brief overview of these symmetries and the symmetry violations will be given.

### 2.1.1 Symmetries and Conservation Laws

The conservation of energy, momentum and angular momentum was known to be valid for a long time and was an integral part of the formal description of the classical mechanics formulated by *Joseph-Louis Lagrange* or *William Rowan Hamilton*. In 1918, the mathematician *Emmy Noether* found a formal connection between the conservation of a physical quantity and the invariance of the according system under a transformation which defines a symmetry. She found that the energy conservation was a result to the invariance of a system to a time transformation, the momentum conservation is connected to the translation invariance and the rotation invariance defines the conservation of angular momentum. These invariances under a given transformation are called *continuous symmetries*.

With the development of quantum mechanics at the beginning of the $20^{\text{th}}$ century, the Noether-theorem was adapted to this theory, and it proved to be consistent with this new formalism. With the rise of particle physics, new *discrete symmetries* were found, which are described by a corresponding transformation operator that can be applied to the quantum system: The *Parity* transformation describes the inversion of all spatial coordinates. Polar vectors such as the momentum or the position will be inverted by this transformation but axial vectors such as spin and angular momentum are not affected. For the eigenstates of the parity operator $\mathcal{P}$, one needs to distinguish between *intrinsic* and *non-intrinsic* parity. The parity eigenvalue $\pi$ for a system of particles that is described by a wave function which is given in terms of spherical harmonics (e.g. the H-atom), one finds $\pi = (-1)^l$ with $l$ being the quantum number for the orbital angular momentum. This is an example of a non-intrinsic parity eigenvalue. For single particles, the intrinsic parity was assigned by convention: Fermions were set to $\pi = +1$, and the photon was assigned to $\pi = -1$. The parity of all the other particles was determined experimentally by the analysis of their decay products.

Another new symmetry of the quantum world is the *Charge Conjugation* $\mathcal{C}$. Applying the $\mathcal{C}$-transformation replaces a particle with its antiparticle. Therefore, only particles which are their own antiparticle (i.e. the $\pi^0$-meson) have a well defined $\mathcal{C}$-eigenvalue $\eta$. Charge conjugation inverts additive quantum numbers such as charge, baryon and lepton number or strangeness but does not affect spin, momentum, mass or lifetime of a particle. As the charge gets inverted, the magnetic and electric fields will change their sign under a $\mathcal{C}$-transformation. The conservation of the charge conjugation can explain why certain decay modes are not observed, even if they would be allowed according to other conservation laws: The $\pi^0$ ($\eta_{\pi^0} = +1$) decays into two $\gamma$ particles ($\eta_\gamma = -1$). This reaction conserves the charge conjugation: $\eta_{\pi^0} = +1 = \eta_\gamma \cdot \eta_\gamma$. However, the decay $\pi^0 \to 3\gamma$ has not been observed even if momentum conservation would allow it. The charge conjugation for this reaction is not conserved and would, therefore, violate the $\mathcal{C}$-symmetry.

The third symmetry in quantum mechanics is the so-called *Time Reversal*-symmetry $\mathcal{T}$. As the name implies, a $\mathcal{T}$-transformation mirrors a system on the time axis, i.e. $t \to -t$. The macroscopic world is obviously not invariant under such a transformation, as the direction of time is connected to the increase of entropy. A $\mathcal{T}$-invariance would violate the 2$^{\text{nd}}$ law of thermodynamics. However, on a microscopic level, the time invariance was found to be true. The $\mathcal{T}$ operator inverts the spin and the momentum but has no effect on the position vector. As there are no observable eigenstates of the $\mathcal{T}$ operator, no statements about $\mathcal{T}$-allowed or $\mathcal{T}$-forbidden transitions can be made.

### 2.1.2 Symmetry Breaking

Up until the mid-1950s, it was assumed that these symmetries are universal and will hold in all cases. This certainty started to crumble in 1956, when *Tsung-Dao Lee* and *Chen-Ning Yang* studied the decay of two newly discovered particles $\Theta^+$ and $\tau^+$ ($\Theta$-$\tau$-puzzle). These particles were found to be identical from the experimental point of view, i.e., they had the same mass, spin, charge, and lifetime, but according to their decay products had a different parity. They suggested that these two particles were identical, but their decay would violate the parity conservation. It turned out that they were right and the allegedly two particles were indeed both $K^+$ mesons. Their findings motivated *Chien-Shiung Wu* to perform her famous experiment on $^{60}$Co which produced the experimental proof of the parity violation in the weak interaction. Another significant result of this experiment considers the neutrinos. It was found that neutrinos have a negative helicity (i.e., projection of the spin axis on the momentum vector) while anti-neutrinos have a positive helicity. In this context, it is common to refer to neutrinos as *left-handed* and to anti-neutrinos as *right-handed*. Even though it is theoretically possible to have right-handed neutrinos, so fare no evidence of their existence was found. As a consequence, the distinct handedness of neutrinos does break the $\mathcal{C}$ invariance. A $\mathcal{C}$ transformation converts a neutrino into an anti-neutrino but leaves the spin and the momentum unchanged. Therefore a left-handed neutrino would be transformed into a left-handed anti-neutrino, and since such a particle was not found yet, the $\mathcal{C}$ symmetry is assumed to be broken as well.

As a consequence of the parity violation, a new combined $\mathcal{CP}$ symmetry was defined. The $\mathcal{CP}$ operator successively applies the parity transformation followed by the charge conjugation. Using this weaker symmetry, it could be shown, that the reaction studied by Wu was invariant under the $\mathcal{CP}$ transformation and it was thought, that this new symmetry would hold. E.g., a $\mathcal{CP}$ transformation does convert the left-handed neutrino into a right-handed anti-neutrino. In 1964, *James Cronin* and *Val Fitch* conducted an experiment on kaons which showed that their decay also violates the $\mathcal{CP}$ symmetry, which means that this symmetry does not hold either in the weak interaction. The weak interaction eigenstates of the quarks differ from their mass eigenstates, and the mixing of the latter is described by the ***C****abibbo*-***K****obayashi*-***M****askawa* (CKM) matrix. The elements of the CKM matrix specifies the coupling of charged current to the different quark flavors. It is possible to extract a measure for the amount of $\mathcal{CP}$ violation included in the SM from this matrix. However the predicted upper level is around three orders of magnitude larger than has been found in all experiments so far [5]. For the strong interaction, the QCD Lagrangian of the standard model allows for the addition of a $\mathcal{CP}$ violating term (so-called $\Theta$ term) which can be related to an EDM of the nucleons. From the theoretical side, there is no explanation why the $\Theta$ term has to be very small or even vanish, but no experimental evidence for a $\mathcal{CP}$ violation in the strong interaction has been found so far. This discord between theory and experiment is called the *strong CP problem*.

An even weaker symmetry was introduced at that point using all three symmetries combined. This is called the $\mathcal{CPT}$ theorem and is deeply linked into the quantum field theory. More precisely, any quantum field theory that is Lorentz-invariant, follows the principle of locality (no "spooky action at the distance") and uses a normally ordered hermitian Hamiltonian is by definition $\mathcal{CPT}$ invariant. This means that by successively applying the $\mathcal{C}$, $\mathcal{P}$ and $\mathcal{T}$ transformation to a system it will be found to be in its initial state. So far, this theorem has proven to be true, and no violating cases have been discovered. Stability of the $\mathcal{CPT}$ theorem has consequences on other symmetry violating processes: If a reaction violates the time reversal symmetry, the $\mathcal{CP}$ symmetry is violated as well if the $\mathcal{CPT}$ theorem holds, i.e., $\not{\mathcal{T}} \equiv \not{\mathcal{CP}}$. As the $\mathcal{CP}$ symmetry was experimentally found to be broken, the $\mathcal{T}$ invariance is violated as well. Table 2.1 gives an overview of the preserved physical quantities and the violation of the corresponding symmetry. The information needed to give this brief overview has been found in [6].

| Quantity | Strong | Weak | EM |
|---|---|---|---|
| Energy | ✓ | ✓ | ✓ |
| Momentum | ✓ | ✓ | ✓ |
| Angular Momentum | ✓ | ✓ | ✓ |
| Charge | ✓ | ✓ | ✓ |
| Lepton Number | ✓ | (✓)[1] | (✓)[1] |
| Baryon Number | ✓ | (✓)[1] | (✓)[1] |
| Parity | (✓)[2] | ✗ | ✓ |
| Charge Conjugation | (✓)[2] | ✗ | ✓ |
| Time Reversal | (✓)[2] | ✗ | ✓ |
| CP-Symmetry | (✓)[2] | ✗ | ✓ |
| CPT | ✓ | ✓ | ✓ |

Table 2.1: Overview of the conserved physical quantities and the violation of the corresponding symmetries. [1] could be broken according to a static, non-stable solution of the electroweak field equations of the SM (*Sphaleron* particle, see [7]) but have not been observed. [2] could be broken by adding a term to the QCD Lagrangian ("strong CP problem") but have not been observed

## 2.2 Polarization

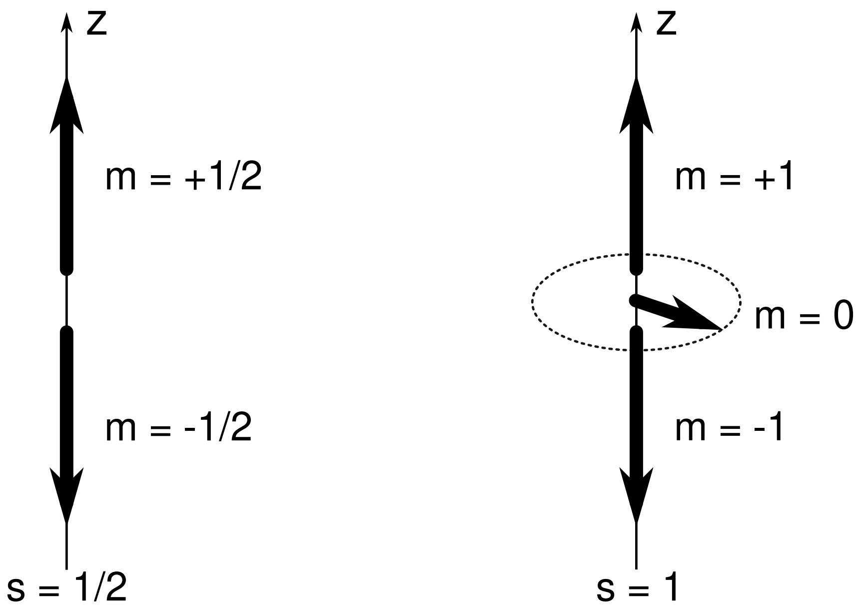


(a) Spin-$\frac{1}{2}$ configuration. (b) Spin-1 configuration.

Figure 2.1: Spin configurations for spin-$\frac{1}{2}$ particles such as the proton and spin-1 particles such as the deuteron.

Since the main task of this works is designated to the development of a polarimeter, i.e., a device that can measure the polarization of a particle beam, it is of great importance to give a formal definition of the polarization here.

The spin of elementary particles such quarks or electrons, as well as composite particles such as neutrons, protons or even nuclei, can be described as an intrinsic angular momentum and its value is given in (full- or half-integers) multiples of the reduced Planck constant $\hbar$. Particles with half-integer spin are called fermions. Hence all quarks and leptons are fermions. Particles with integer spin are called bosons. In a quantum system, the spin defines the only quantization axis which means that other vectorial properties of such a system like the magnetic moment or the electric dipole moment have to be aligned with this axis. The spin itself is given by the quantum number $s$. For a proton, which is a fermion, one has $s = \frac{1}{2}$, and for a deuteron, which is composed of a proton and a neutron and hence is a boson, one has $s = 1$. The spin can have different configuration relative to its quantization axis which is by convention called the z-axis. For a particle with a spin of $s$, $(2s + 1)$ different configurations can be found. These configurations are defined by the quantum number $m$, which can take the following values: $m \in [s, s-1, .., -s+1, -s]$. A schematic picture of these configurations for a spin-$\frac{1}{2}$ and spin-1 particle is given in Figure 2.1.

In a beam of one species of particles, it makes no sense to talk about the spin, as this is a property of the individual particle. Instead one needs a statistical measure that is proportional to the probability of finding a particle with a specific spin configuration in the beam. This beam property is called *Polarization* and can be defined as follows: Assume a beam of spin-$\frac{1}{2}$ particles with $N^{\uparrow}$ particles in the configuration $m = +\frac{1}{2}$ and $N^{\downarrow}$ particles in the configuration $m = -\frac{1}{2}$. The vector polarization is defined in the following way:

$$P_y = \frac{N^{\uparrow} - N^{\downarrow}}{N^{\uparrow} + N^{\downarrow}} = p^{\uparrow} - p^{\downarrow}, \tag{2.1}$$

where $p^{\uparrow}$ and $p^{\downarrow}$ denote the probability of finding a particle with $m = +\frac{1}{2}$ and $m = -\frac{1}{2}$, respectively. For a beam of spin-$\frac{1}{2}$ particles, the vector polarization can take the following value:

$$-1 \leq P_y \leq +1, \tag{2.2}$$

which means that values of the vector polarization between -100 % and +100 % are possible.

For spin-1 particles, the beam can consist of the following fractions: $N^{\uparrow}$ particles in the configuration $m = +1$, $N^{\downarrow}$ particles in the configuration $m = -1$ and $N^0$ particles in the configuration $m = 0$. The vector polarization is defined in the same way as for the spin-$\frac{1}{2}$ particles:

$$P_y = \frac{N^{\uparrow} - N^{\downarrow}}{N^{\uparrow} + N^{\downarrow} + N^0} = p^{\uparrow} - p^{\downarrow}. \tag{2.3}$$

Since the spin-1 particles have a total of three configurations, an additional polarization has to be defined; the tensor polarization:

$$P_{yy} = \frac{N^{\uparrow} - 2N^0 + N^{\downarrow}}{N^{\uparrow} + N^{\downarrow} + N^0} = p^{\uparrow} - 2p^0 + p^{\downarrow} = 1 - 3p^0. \tag{2.4}$$

The vector polarization can take the same values as for the spin-$\frac{1}{2}$ particles, but the tensor polarization can take the following values:

$$-2 \leq P_{yy} \leq +1. \tag{2.5}$$

Due to their definition, the vector and the tensor polarization for the spin-1 particles are connected. This leads to the following restriction of the possible values for the vector polarization in a beam with no tensor polarization:

$$P_{yy} = 0 \Rightarrow -\frac{2}{3} \leq P_y \leq +\frac{2}{3}, \tag{2.6}$$

as can be seen by setting $P_{yy} = 0$ in Equation (2.4) which fixes $p_0 = \frac{1}{3}$ and leads to the expression given above.

All the data that was analyzed in this work was measured using pure vector polarized deuteron beams, which means that the maximum achievable polarization was $\pm 66.66\,\%$. During the database experiment, some measurements with tensor polarized beams were performed as well, but this data was not processed by the author. In all the beam times for the polarimeter development, no tensor polarized beams were used at all. In the subsequent sections, tensor polarization dependent quantities such as the tensor analyzing power will not be discussed as it would go beyond the scope of the thesis. The definitions for the polarization used in this section was taken from [8].

## 2.3 Asymmetries From Elastic Scattering

In this section, an attempt of an explanation for the spin dependence of the elastic scattering of a polarized particle off an unpolarized nucleus will be given. As a first step, the observation of this dependence found in double scattering experiments, that led to the concept of analyzing and polarizing power respectively, will be presented. In a second step, the spin dependence of elastic scattering will be explained using a semi-classical approach.

### 2.3.1 Analyzing Power and Double Scattering

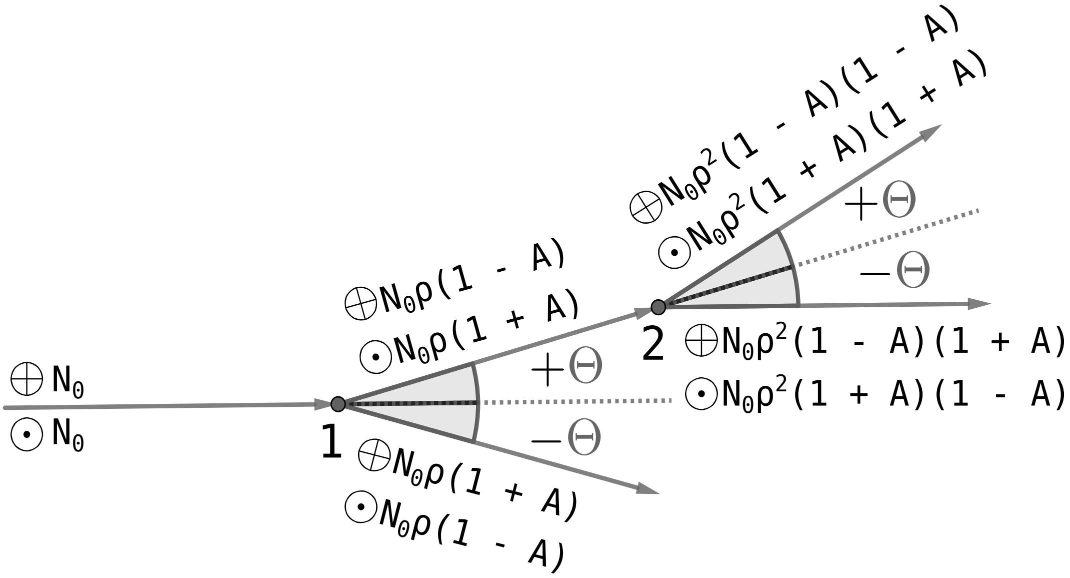


Figure 2.2: Schematic representation of a double scattering experiment. A beam of unpolarized particles scatters elastically off an unpolarized target at position 1. The outgoing particles for a certain scattering angle Θ are scattered a second time off an unpolarized target 2 of the same material as the first one. The angular distribution for the second scattering is recorded.

Assume a double scattering experiment with the following experimental setup: A beam of unpolarized protons was scattered elastically off an unpolarized nucleus such as carbon ($^{12}$C). For a certain scattering angle $\Theta$, another target of the same material was installed, and the protons would undergo a second elastic scattering reaction. The angular distribution was measured after the second scattering. Figure 2.2 shows a schematic drawing of such an experiment. From previous single scattering experiments with unpolarized proton beams scattering of unpolarized nuclei it was found that the number of particles scattered to the left $(N_L(\Theta), \Theta > 0)$ was equal to the number of particles scattered to the right $(N_R(\Theta), \Theta < 0)$ as expected from the $\Phi$-symmetry of the experimental setup. However, for the double scattering experiment, this was not any longer the case [9], i.e., $N_L(\Theta) \neq N_R(\Theta)$. To quantify this inequality, an asymmetry $\epsilon$ can be defined as follows:

$$\epsilon(\Theta) = \frac{N_L(\Theta) - N_R(\Theta)}{N_L(\Theta) + N_R(\Theta)}. \tag{2.7}$$

From first scattering, this asymmetry was found to be $\epsilon_1 = 0$ but for the second scattering $\epsilon_2 \neq 0$.

This result can be explained by adding a spin-dependent term to the elastic cross section. In Figure 2.2, the unpolarized beam is approximated by a beam with $N_0$ particles in a spin-up configuration relative to the plain of scattering (denoted by $\odot$) and the same amount $N_0$ particles in a spin-down configuration (denoted by $\oplus$). The probability for a spin-up particle to scatter to the left ($\Theta > 0$) is larger compared to the probability of the same particle to scatter to the right ($\Theta < 0$). This can be expressed in the expected number of spin-up particles to be found on the left ($N_L^{\odot}$) or the right side ($N_R^{\odot}$) respectively, using the following expression:

$$\begin{aligned} N_L^{\odot} &= N_0\rho(1+A) \\ N_R^{\odot} &= N_0\rho(1-A) \\ \text{with } \rho &= \sigma_0 \cdot \rho_a, \end{aligned} \tag{2.8}$$

with the unpolarized cross section $\sigma_0$ and the areal target density $\rho_a$. For simplicity, the $\Theta$ dependence the quantities $N_{L,R}^{\odot}$, $\rho$ and $A$ are where omitted. Rotating the scattering plane by 180° around the incident beam axis would transform the spin-down into spin-up particles, and thus the same formalism with reversed signs can be used for the spin-down particles:

$$\begin{aligned} N_L^{\oplus} &= N_0\rho(1-A) \\ N_R^{\oplus} &= N_0\rho(1+A) \end{aligned} \tag{2.9}$$

This modification of the cross section for the elastic scattering is compatible with the result of the single scattering as can be seen by calculating the asymmetry $\epsilon$ from Equation (2.7):

$$\epsilon_1 = \frac{N_L - N_R}{N_L + N_R} = \frac{(N_L^{\odot} + N_L^{\oplus}) - (N_R^{\odot} + N_R^{\oplus})}{(N_L^{\odot} + N_L^{\oplus}) + (N_R^{\odot} + N_R^{\oplus})} = 0. \tag{2.10}$$

This means from an experimental point of view, the modification cannot be estimated directly. However if one calculates the polarization of the beam that was scattered to the left according to Equation (2.1), one finds:

$$P_L = \frac{N_L^{\odot} - N_L^{\oplus}}{N_L^{\odot} + N_L^{\oplus}} = A. \tag{2.11}$$

The scattered beam at $\Theta$ gets polarized to a value of $A$ which in this context is called *polarization power*.

Using the same modification for the expected number of scattered spin-up ($N_{LL,LR}^{\odot}$) and spin-down particles ($N_{LL,LR}^{\oplus}$) from the second scattering, one finds the following expression:

$$\begin{aligned} N_{LL}^{\odot} &= N_0\rho(1+A)\rho(1+A) = N_0\rho^2(1+A)^2, \\ N_{LR}^{\odot} &= N_0\rho(1+A)\rho(1-A) = N_0\rho^2(1-A^2), \\ N_{LL}^{\oplus} &= N_0\rho(1-A)\rho(1-A) = N_0\rho^2(1-A)^2, \\ N_{LR}^{\oplus} &= N_0\rho(1-A)\rho(1+A) = N_0\rho^2(1-A^2). \end{aligned} \tag{2.12}$$

To obtain these expressions, a few assumptions have to be made. The targets used in the first and the second have to be identical. Further, it was assumed that the energy loss in the first scattering was negligible. This allows to set $\rho_1 = \rho_2 = \rho$. The scattering angles have to be identical as well such that $A_1 = A_2 = A$ as indicated in Figure 2.2. By calculating the asymmetry according to Equation (2.7)

$$\epsilon_2 = \frac{N_L - N_R}{N_L + N_R} = \frac{(N_{LL}^{\odot} + N_{LL}^{\oplus}) - (N_{LR}^{\odot} + N_{RL}^{\oplus})}{(N_{LL}^{\odot} + N_{LL}^{\oplus}) + (N_{LR}^{\odot} + N_{LR}^{\oplus})} = A^2 > 0, \tag{2.13}$$

the value of $A$ and therefore the magnitude of the polarization after the first scattering can be found. In this context, $A$ is called *analyzing power* even if it describes the same property of spin dependence in the elastic scattering off unpolarized nuclei. Subsequently, it will be referred to $A$ as the analyzing power.

This double scattering experiment can be summarized as follows: An unpolarized beam gets elastically scattered off an unpolarized nucleus. The fraction of the beam that gets scattered under an angle of $\Theta$ gets polarized to a value of $P = A$. Scattering this polarized beam a second time elastically off an unpolarized nucleus results in a left right asymmetry in the number of detected events which is dependent on $A$. The second scattering analyzed the polarization produced in the first scattering reaction. In this experiment where $A_1 = A_2 = A$, the value of $A$ represents the beam polarization after the first scattering as well as the analyzing power which does depend on the beam energy, scattering angle and the target material.

This experiment can now be generalized to a polarized beam that is elastically scattered of an unpolarized target. The cross section of such a reaction was found to be:

$$\sigma_{pol} \sim \sigma_0(1 \pm PA), \tag{2.14}$$

where $P$ denotes the beam polarization, $\sigma_0$ unpolarized cross section, and $A$ the analyzing power. The latter two depend on the scattering angle $\Theta$, the beam energy as well as on the target material. The $+$ in front of the term $PA$ describes the cross section on the left side and the $-$ on the right side. A more detailed description of the polarized cross section is given in Equation (4.4). For a proton beam, which consists of spin-$\frac{1}{2}$ particles, only vector polarization is possible and therefore, $A$ is the *vector analyzing power* and will be denoted as $A_y$. For a deuteron beam, that consists of spin-1 particles, an additional *tensor analyzing power* describes the tensor polarization dependence of the elastic scattering. As stated in the previous section, the tensor polarization is outside of the scope of this work and will be omitted here. The introduction of the analyzing power described in this section followed the arguments given by *Emilio Segrè* in [10].

### 2.3.2 Spin Dependence of Elastic Scattering

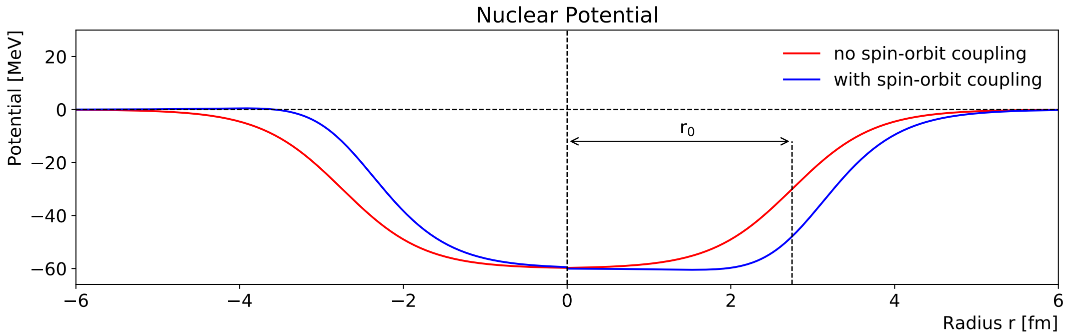


Figure 2.3: Nuclear potential described as a Woods-Saxon potential well (see Equation (2.15)). The red line represents the potential of the strong interaction. A spin-orbit coupling distorts this potential depending on which side of the nucleus the impinging particle was scattered. This is represented with the blue line.

In the previous section, the phenomenon of the spin dependence observed in double scattering was introduced. In this section, an attempt for an explanation of this effect will be given based on a semi-classical approach. The elastic scattering of deuterons and protons with kinetic energies in the order of a few hundred MeV off a carbon target are already dominated by the strong interaction rather than the electromagnetic force, especially for small scattering angles. It is therefore important to understand how the strong nuclear force interacts with the impinging particles in an elastic scattering reaction. According to the shell model of the nucleus, the strong interaction can be modeled as a rotationally symmetric potential well with a negative sign as it describes an attractive force. Depending on the model, this potential is described with a *boxcar*-function (rectangular function), meaning that the edges of this well are of infinite steepness or it is described by a Woods-Saxon potential which allows for smoother edges. The latter is defined as follows:

$$V(r) = \frac{-V_0}{1 + e^{\frac{r-r_0}{a}}}. \tag{2.15}$$

Here $V_0$ defines the maximal potential, $r_0$ describes the radius of the nucleus and $a$ characterizes how fast the potential approaches zero. Typical values for these parameters can be found in [10]:

$$\begin{aligned} V_0 &= (20 - 60)\ \text{MeV}, \\ a &= (0.5 - 0.7)\ \text{fm}, \\ r_0 &= (1.15 - 1.35) \cdot A^{\frac{1}{3}}\ \text{fm}, \end{aligned}$$

where $A$ denotes the mass number of the nucleus, e.g $A = 12$ for $^{12}$C resulting in $r_0 = (2.63 - 3.1)$ fm. The Woods-Saxon potential for carbon is given in Figure 2.3 by the red line.

A particle that enters the nuclear matter gets deflected towards the center of the nucleus due to the attractive strong force. On the other hand, the deeper the impinging particle enters the nucleus, the less of the central force will act on it because the sources of the strong interaction are the nucleons which will attract the particles from all sides. In such a case, the particle dissipates energy in the nuclear matter rather than being just deflected. It should be noted here, that this model for the elastic scattering cannot be used for full head-on collisions as they cannot be considered elastic anymore and the particles would rather be absorbed by the nucleus in an inelastic fashion. For particles that scatter at a reasonable distance from the center, elastic scattering can still be assumed, but some part of the particle flux gets removed from the elastic channel due to inelastic processes. This is described by the use of an *optical model* where an imaginary term is added to the nuclear potential. Solving *Schrödinger's Equation*, the imaginary term of the potential leads to an imaginary part in the wave vector of the particles wave function that can be translated into a damping term. Since the square of the absolute value of the wave function describes the portability density, the damping term decreases the particle flux. $V_0$ in Equation (2.15) will be modified:

$$V_0 \rightarrow V_0(1 + i\xi). \tag{2.16}$$

According to [10], typical values for $\xi$ are in the range of 0.13 to 0.7.

So far the effect of the spin of the impinging particle was not taken into account. However, the shell model of the nucleus introduces a spin-orbit coupling term in analogy to the spin-orbit coupling found to be responsible for the *Zeeman effect* in the shell model of the atom. This spin-orbit interaction can be expressed as a potential as follows:

$$V^{so} \sim \frac{1}{r}\frac{\partial V(r)}{\partial r}\vec{l}\vec{s}, \tag{2.17}$$

with $V(r)$ the nuclear potential as given in Equation (2.15), $\vec{l}$ and $\vec{s}$ the orbital and spin angular momenta, respectively. In the elastic scattering reaction, this spin-orbit potential is generated by the scattering particle when it interacts with the target nucleus and can be described by:

$$V^{so} = V_0^{so}(\nabla V(r) \times \vec{p}\,) \cdot \vec{s} = V_0^{so}\left(\frac{\vec{r}}{r}\frac{\partial V(r)}{\partial r} \times \vec{p}\right) \cdot \vec{s} = \frac{V_0^{so}}{r}\frac{\partial V(r)}{\partial r}(\vec{r} \times \vec{p}\,) \cdot \vec{s}. \tag{2.18}$$

Here $V(r)$ is the nuclear potential as given in Equation (2.15), $\vec{p}$ and $\vec{s}$ the momentum and spin angular momentum of the incoming particle, respectively. The vector $\vec{r}$ points from the center of the nucleus to the point of interaction with the impinging particle, see Figure 2.4. It can be assumed that $\vec{r}$ is orthogonal to $\vec{p}$ and therefore the orbital angular momentum $\vec{l} = \vec{r} \times \vec{p}$ is perpendicular to the plane of scattering. This allows for Equation (2.18) to be simplified to:

$$V^{so} = \pm V_0^{so}\frac{\partial V(r)}{\partial r} \cdot p \cdot s \cdot \cos(\alpha_s). \tag{2.19}$$

$\alpha_s$ denotes the angle between the spin of the scattering particle and the normal vector of the plane of scattering. For the subsequent discussion, this angle can be either $\alpha_s = 0$ (spin-up particles), or $\alpha_s = \pi$ (spin-down particles). The sign of Equation (2.19) depends on which side the particle scatters off the nucleus. Assume a spin-up particle scattering off the left side of the nucleus. According to the right-handed rule of the cross product, the resulting orbital angular momentum vector will point down, i.e., into the plane of scattering. As defined before, the spin of the particle points up, i.e., out of the plane of scattering and therefore the scalar product between spin and orbital angular momentum will be equal to $-1$. For a particle that scatters off the right side of the nucleus, the angular momentum points out of the plane of scattering which results in the $+$ sign of Equation (2.19). If the sign of the nuclear potential (see Equation (2.15)) is taken into account, it can be seen that spin-up particles that scatter on the left side of the nucleus will cause the effective nuclear potential to be increased and for spin-up particles that scatter on the right side, it will be decreased. The blue line in Figure 2.3 shows this deformation of the nuclear potential caused by the spin-orbit coupling of the impinging particles. This asymmetry in the attractive nuclear potential affects by how much an incoming particle gets deflected from its initial straight path depending on which side of the nucleus it scattered. This asymmetry can eventually be observed in the cross section of the elastic scattering of polarized particles off an unpolarized nucleus. The vector analyzing power is, therefore, an experimentalist's measure for the deformation of the nuclear potential.

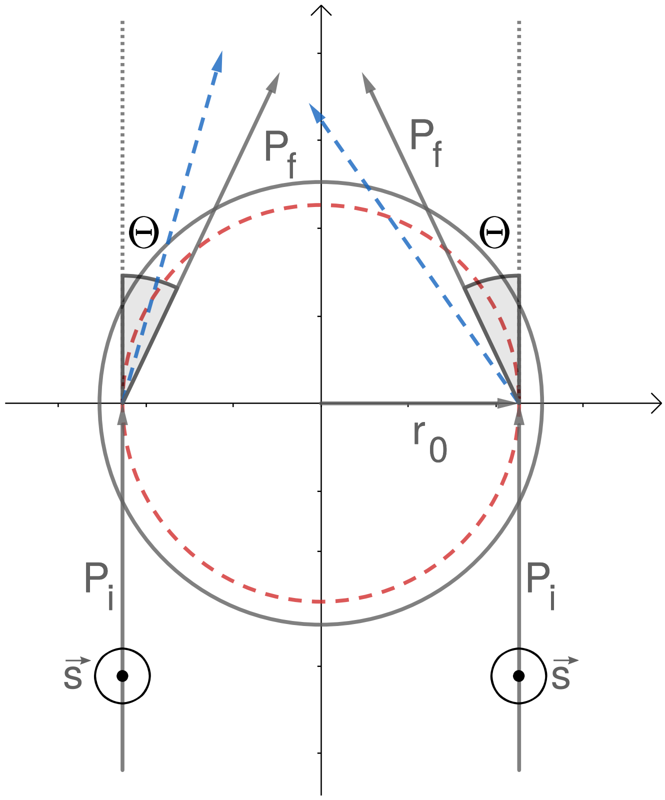


Figure 2.4: Schematic image of the side dependent elastic scattering reaction. The incident particles $P_i$ have a momentum of $p$ and will scatter either on the left or on the right side of the nucleus. The spin of the particles is oriented perpendicular to the plane of scattering and is pointing out of the plane. The scattering process occurs at the fringe of the nucleus and can, therefore, be considered elastic. The scattered particles $P_f$ will have the same magnitude of momentum $p$ as the incident particles, i.e., the recoil momentum on the nucleus is neglected. The gray vectors $P_f$ represent the elastic scattering of a fully symmetrical nuclear potential as given by the red line in Figure (2.3). The blue vectors account for the asymmetry in the nuclear potential that depends on the spin-orbit coupling and is shown as the blue line in Figure (2.3).

In a paper by *Enrico Fermi* [11], he derived a spin-dependent expression for the elastic scattering of protons of nuclei. His approach is based on the considerations given above and will be presented here.

The nuclear potential used for this calculation was given by a simple *boxcar* model rather than by a Woods-Saxon potential:

$$V(r) = \begin{cases} -V_0(1 + i\xi) & \text{for} \quad r < r_0 \\ 0 & \text{for} \quad r > r_0 \end{cases} \tag{2.20}$$

therefore, the derivative of this potential as used in Equation (2.18) was replaced by:

$$\frac{\partial V(r)}{\partial r} = -V_0 \delta(r - r_0). \tag{2.21}$$

The matrix element of the scattering matrix,

$$\mathcal{M}_{if} = \langle \Psi_f | V + V^{so} | \Psi_i \rangle \,, \tag{2.22}$$

was calculated in the *Born approximation*, i.e., $\Psi_i$ and $\Psi_f$ were assumed to be plane waves. Further, it was assumed that the beam consists only of protons in a spin-up configuration. The scattering angle $\Theta$ was defined such that a positive angle corresponds to scattering to the left and a negative angle to scattering to the right. Using Fermi's *Golden Rule No. 2*, the cross section was calculated:

$$\begin{gathered}\frac{d\sigma}{d\Omega} = \frac{m_p^2}{4\pi^2\hbar^4} \cdot |\mathcal{M}_{if}|^2 \\ \Rightarrow \\ \frac{d\sigma}{d\Omega} = \frac{4m_p}{\hbar^4} r_0^6 V_0^2 \left\{ \frac{\sin(q)}{q^3} - \frac{\cos(q)}{q^2} \right\} \left[ 1 + \left( \xi + \frac{15}{2} \left( \frac{p}{m_p c} \right)^2 \sin(\Theta) \right)^2 \right],\end{gathered} \tag{2.23}$$

with $m_p$ being the proton mass and the momentum transfer $q$ given by:

$$q = \frac{2pr_0}{\hbar} \sin\left(\frac{\Theta}{2}\right). \tag{2.24}$$

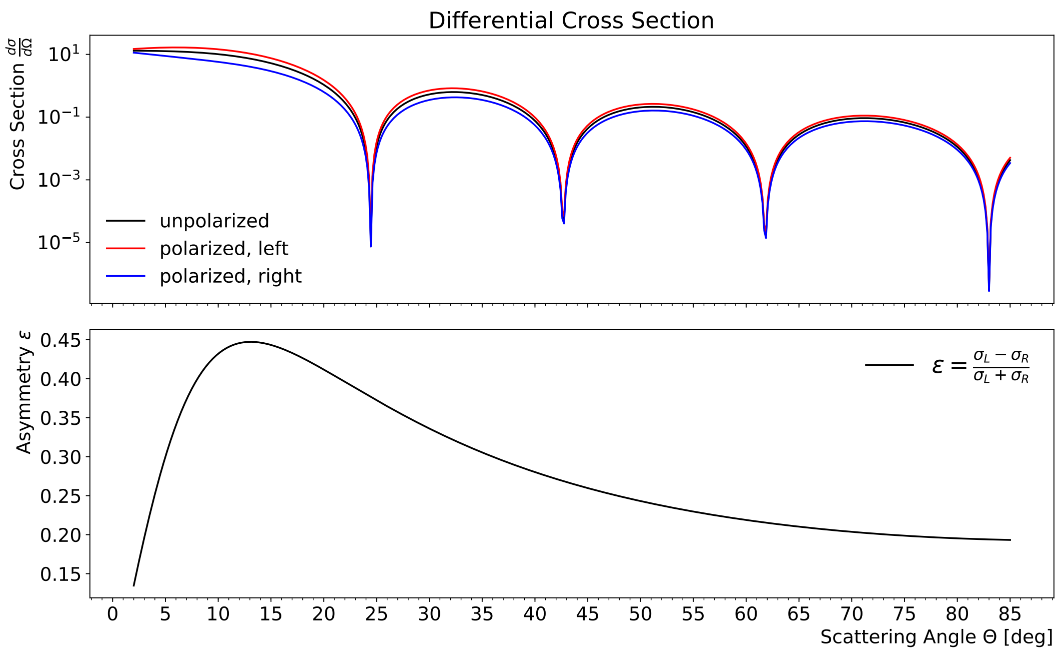


Figure 2.5: Elastic cross section for a polarized beam calculated according to Equation 2.23 for particles that have been scattered to the left or the right, respectively. The left/right asymmetry calculated according to Equation (2.7) is given in the lower section.

The differential cross section given in Equation (2.23) was plotted in Figure 2.5, upper section. The values for the scattering to the left are slightly larger than the values on the scattering to the right. This result is in agreement with the deformed nuclear potential in Figure 2.3 which has a lower value on the right (i.e., is more attractive) which means that more particles are scattered to the left and vice versa. The unpolarized elastic cross section was calculated as the superposition of the cross sections for spin-up and spin-down. As expected, it lies between the two polarized cross sections. The oscillating structure in the cross section origins in the scattering off the nuclear potential and is not a direct consequence of the spin-orbit coupling but is rather generated by the $\{\sin(q)/q^3 - \cos(q)/q^2\}$ term in Equation 2.23. Figure 4.28 in Section 4.3.2.4 shows the measured unpolarized deuteron carbon cross section normalized to the Rutherford cross section. In this figure, a slight oscillating structure is visible as well but much less prominent than in the model shown in Figure 2.5.

Calculating the asymmetry as defined in Equation (2.7) reveals that this model for the cross section does produce a left/right asymmetry as observed in the experiments, see Figure 2.5, lower section. In general, it is important that this is a very simplified model that is not capable of reproducing the measurements presented in this work. The parameters that were entered into Equation (2.23) to produce Figure 2.5 have not been adapted to match the measurements. However, this simple model is able to produce a satisfactory explanation for the observed left/right asymmetry in the experiments and for the vector analyzing power, that will be used to measure the beam polarization with the designated polarimeter whose development is presented in this work.

# Chapter 3

# The Cooler Synchrotron COSY

The ***Co**oler **Sy**nchrotron* COSY accelerator facility is located at the *Forschungzentrum Jülich* in Germany. It consists of three main parts: A source that can produce polarized and unpolarized hydrogen $H^-$ and deuterium $D^-$ ion beams. They are transferred into the injector cyclotron JULIC (***Jül**ich **I**sochronous **C**yclotron*). This machine accelerates the ion beam to kinetic energies up to 45 MeV for $H^-$ beams and up to 76 MeV for $D^-$ beams [12]. From there they are transferred via an injection beam line into the main cooler synchrotron storage ring COSY. On the injection beam line, a small polarimeter (referred to as the ***L**ow **E**nergy **P**olarimeter* (LEP)) is installed that can measure the

ner

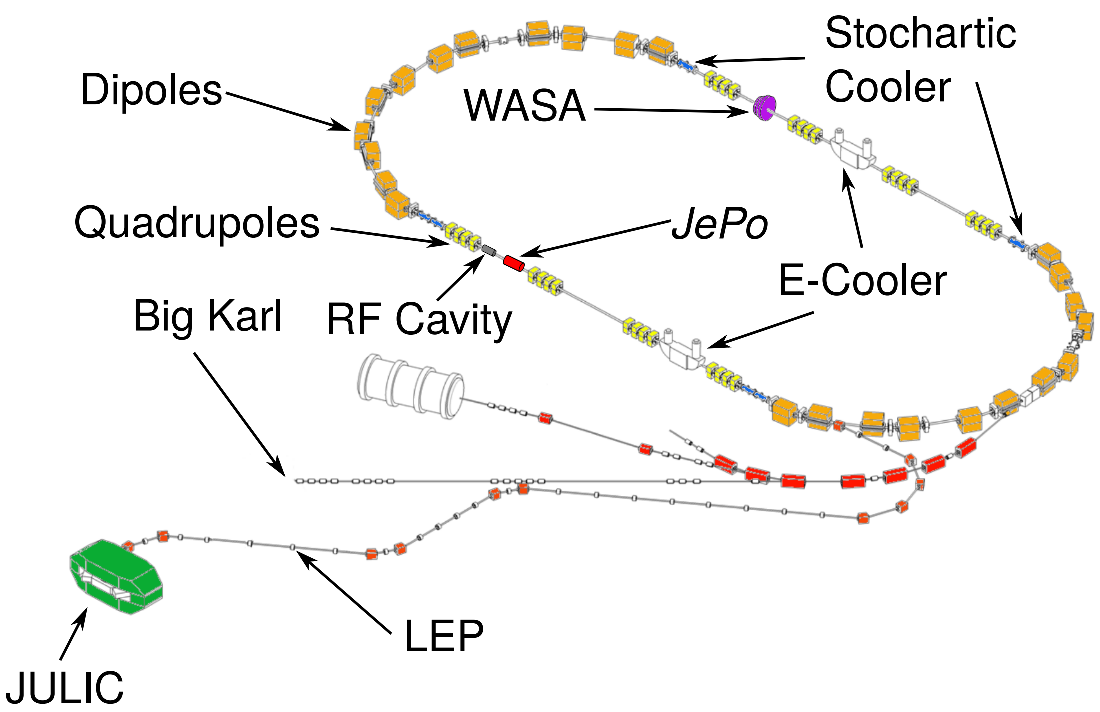


Figure 3.1: Overview sketch of the COSY accelerator facility located at the *Forschungzentrum Jülich* in Germany. The device labeled *JePo* indicates where the LYSO based polarimeter will be installed, see Section 6.2.

beam polarization, see [13]. At the injection, the two electrons from the ions are removed by a stripping reaction in a thin carbon foil. COSY can accelerate deuterons and protons up to a momentum of 3.7 GeV[12] which equals kinetic energies of $\sim$ 2.8 GeV for protons and $\sim$ 2.2 GeV for deuterons. The accelerator has a circumference of 184 m. Two straight sections with a length of 40 m are located between two arc section with a radius of 16.5 m[14]. The magnets that keep the beam in orbit are normal-conducting water cooled dipoles that can reach magnetic fields up to 1.58 T [15]. Groups of four quadrupole magnets in a row form the beam optics. The actual acceleration takes place in a radio wave (RF) driven accelerator cavity installed in the center of a straight section.

What makes COSY unique is its ability to cool the beam. Cooling in this context means that the phase space of the beam gets reduced by removing transversal momentum components from the particles in the beam. This is achieved using two different methods: *Electron Cooling* for beam momentum up to 600 MeV and *Stochastic Cooling* staring from a beam momentum of 1.4 GeV[16]. Two electron coolers are installed, one in each straight section. A beam of electrons of the same velocity as the main beam is injected in a short section of the ring. The electrons scatter elastically with the beam particles and thereby reduce the transversal momentum components of their scattering partners. The electrons are either scattered out of the beam or get removed from the beam at the end of the electron cooler. The stochastic cooling samples the beam positions in very fine packages as they enter through a so-called *pick-up detector*. For each package, the deviation from the ideal orbit is measured, and this information is transferred via a waveguide diagonally across the ring to a device called the *kicker*. The particle package had to travel all the way through the beam pipe, and when it enters the kicker, a correction signal proportional to the deviation measured at the pick-up is applied. This method allows for the reduction of the phase space both in transversal as well as in the longitudinal direction of the beam.

The straight section allows for the installation of experiments in the ring. The WASA detector (see Chapter 4) is installed in such a straight section. The target that is used to produce the elastic scattering reactions can be moved into the beam pipe in front WASA. The beam orbit is set such that it will pass just below the target during the acceleration. When the beam is brought to its final energy, it is excited which causes the beam to be broadened. A small fraction of the beam does now hit the target and scatters into the detector. A feedback loop between the detector rate and the excitation assures that the full beam is slowly extracted on the target.

Another option that COSY provides is to extract the accelerated beam using a magnetic septum and transfer it via the extraction beam line to one of three external experiment places. The whole LYSO based polarimeter development was done at an external beam line in the *Big Karl* experimental hall. At the beginning of 2016, the old Big Karl spectrometer was removed which created space for experiments using an extracted beam.

# Chapter 4

# Database Experiment

The *Database Experiment* was performed from the 2. to 28. November 2016 using the WASA forward detector installed at the COSY facility. In this chapter, the experimental setup, the data analysis procedure, and the results obtained from this experiment will be discussed.

## 4.1 Detector Setup

### 4.1.1 WASA Detector

The WASA (***W**ide **A**ngle **S**hower **A**pparatus*) is actually a rather old device, and there is quite a history attached to it. Originally it was developed and built at the *Department of Radiation Sciences* of the University of Uppsala in Sweden in 1996 [17]. It was then installed at the cooler accelerator and storage ring CELSIUS. Its designed purpose was to detect light mesons such as the $\pi^0$ or the $\eta$. It consisted of two main parts. A central detector that was able to cover a solid angle of almost $4\pi$, which was referred to as the *calorimeter* as it was built from $CsI$ crystal scintillators. In the downstream direction of the beam, the forward detector part was installed. It consisted of multiple layers of plastic scintillators and four layers of gas-filled mylar tubes proportional counters (straw tubes). These straw tube arrays - the ***F**orward **P**roportional **C**hamber* (FPC) - were sandwiched between a thin (0.3 cm) layer of plastic scintillators, the ***F**orward **W**indow **C**ounter* (FWC) and three layers of slightly thicker (0.5 cm) plastic scintillator, the ***F**orward **T**rigger **H**odoscope* (FTH) and eventually followed by another four 11 cm thick plastic scintillator layers, the ***F**orward **R**ange **H**odoscopes* (FRHs). The layers of plastic scintillator layer are segmented into pizza-shaped detector elements with a PMT attached to their ends. The FWC and the FRHs consist of 24 of these elements each, and the FTH of 48 elements. The first two layers of the FTH were constructed from counter-rotating archimedean spirals which together with the straight element formed a pixel like structure.

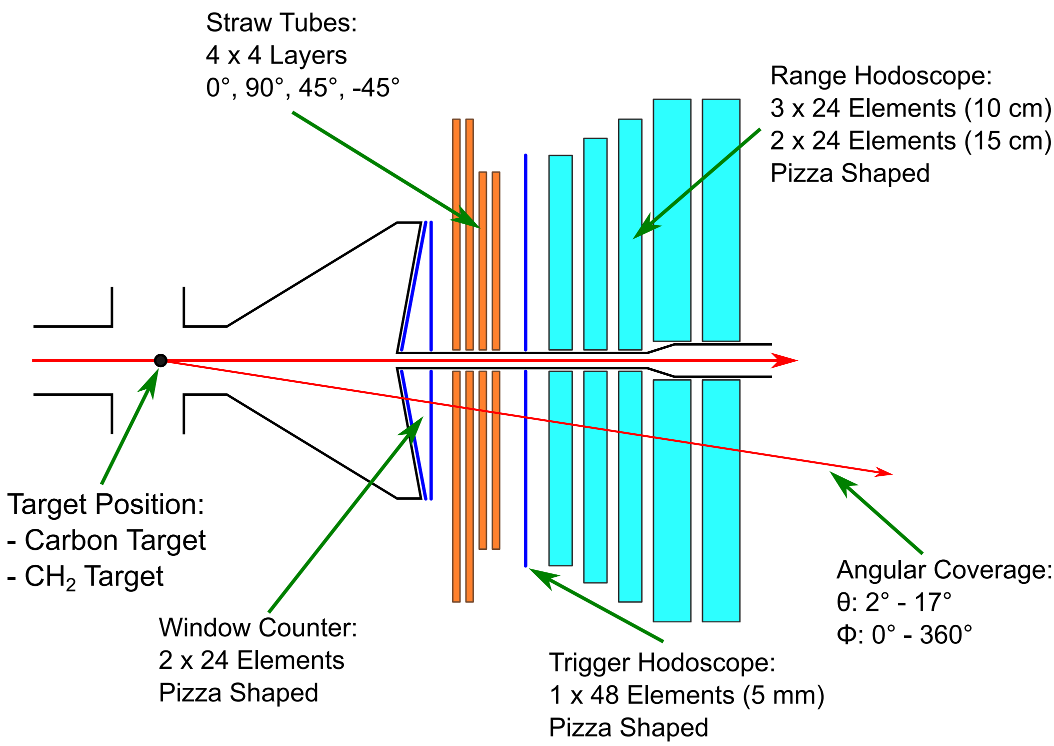


Figure 4.1: Schematic view of the WASA forward detector.

In 2006 the whole WASA detector including its micro-sphere hydrogen pellet target [18] was moved to the COSY accelerator facility of the Forschungszentrum Jülich in the *WASA at COSY* campaign [19], and some upgrades for higher energies and higher count rates were installed. The first layer of the FRH was removed to create more space for the FPC and two additional thicker (15 cm) layers of FRHs were installed after the three remaining original ones. The second layer of window counter was installed as well. In this configuration, the WASA detector was operational and being used for many experiments until 2014.

Between 2014 and end of 2016, the whole detector including the pellet target was removed from COSY and only the forward detector part was then reinstalled, but the first two layers of the FTH (spirals) were not put back. The FPGA based trigger system described below was also developed for this new configuration. The detector elements of the window counter have shown some strange signals and were therefore brought to the lab where they were tested, and some needed a repacking as they were not light tight anymore. The target system needed for the Database Experiment was developed just before the actual experiment took place and is described in the next section.

The final detector setup for the Database Experiment was the following: Two layers of forward window counters (FWC1 and FWC2) with 24 elements each. They are followed by four layers of straw tubes (FPC). These layers of tubes were subsequently rotated by 45° which allowed for a scattering angle resolution of 0.2° [19]. Next, a single layer of the froward trigger hodoscope (FTH) is mounted. It consists of 48 elements which are rotated by 3.75° with respect to the other detector modules. This means, that

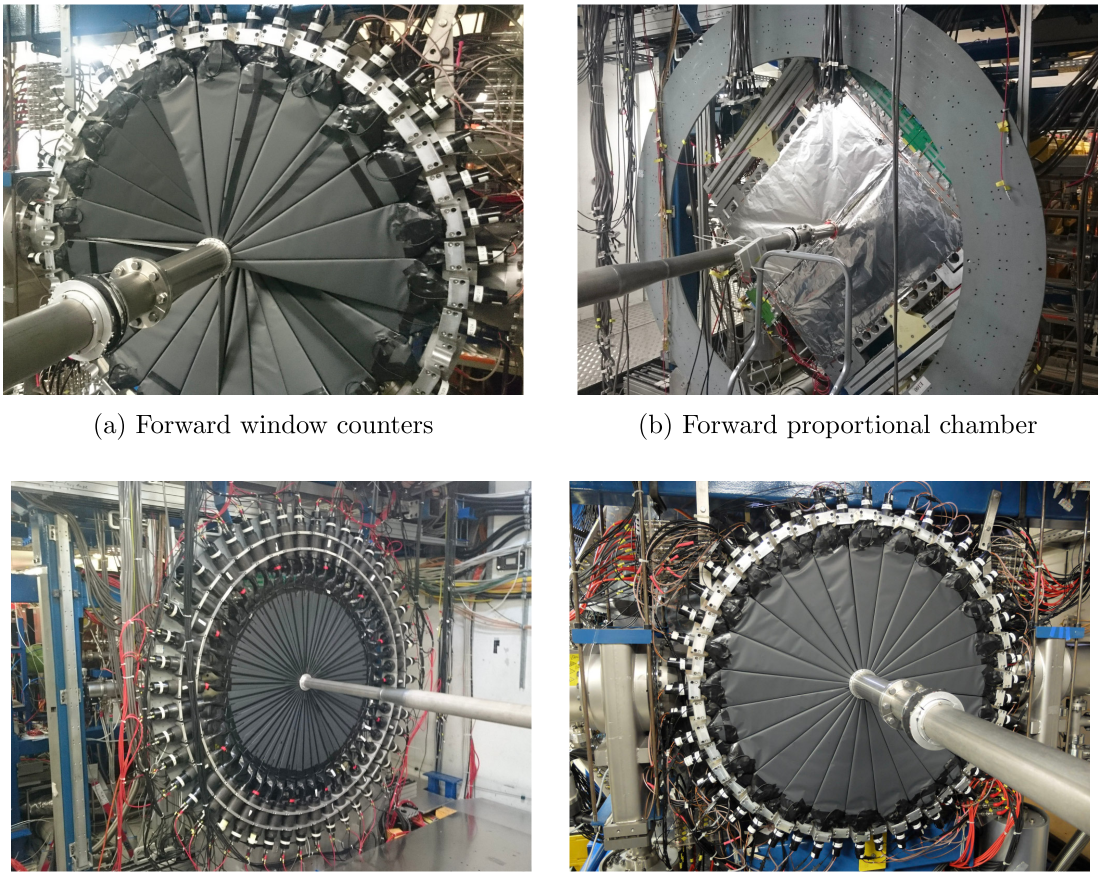

(a) Forward window counters (b) Forward proportional chamber

(c) Forward trigger hodoscope (d) Forward range hodoscope

Figure 4.2: Pictures of the different layers of the WASA forward detector when they were being installed.

each detector module overlaps with three elements of the FTH allowing for finer track reconstruction. The final part of the detector consists of the five layers of the forward range hodoscope with 24 elements in each layer. The first three layers (FRH1, FRH2, and FRH3) are made from 11 cm, and the latter two (FRH4 and FRH5) from 15 cm thick plastic scintillators. A schematic overview of the WASA forward detector is given in Figure 4.1, and the pictures of the individual layers are shown in Figure 4.2.

### 4.1.2 Target Controller

In the old WASA setup, a hydrogen micro-sphere target was used. It was removed for the Database Experiment because it did not suit the experiment as the aim was to measure properties of the elastic deuteron carbon scattering reaction. Hence, a new target needed to be installed in the old interaction point of the pellet target. What was available was a gear rack driven arm in a vacuum-tight enclosure that could be mounted horizontally to the cross flange of the interaction point, see Figure 4.4a. A non-standard stepper motor to drive the rack was already attached to the device, but the motor controller was missing. In order to use this device, a custom made stepper motor driver had to be created, see Figure 4.3.

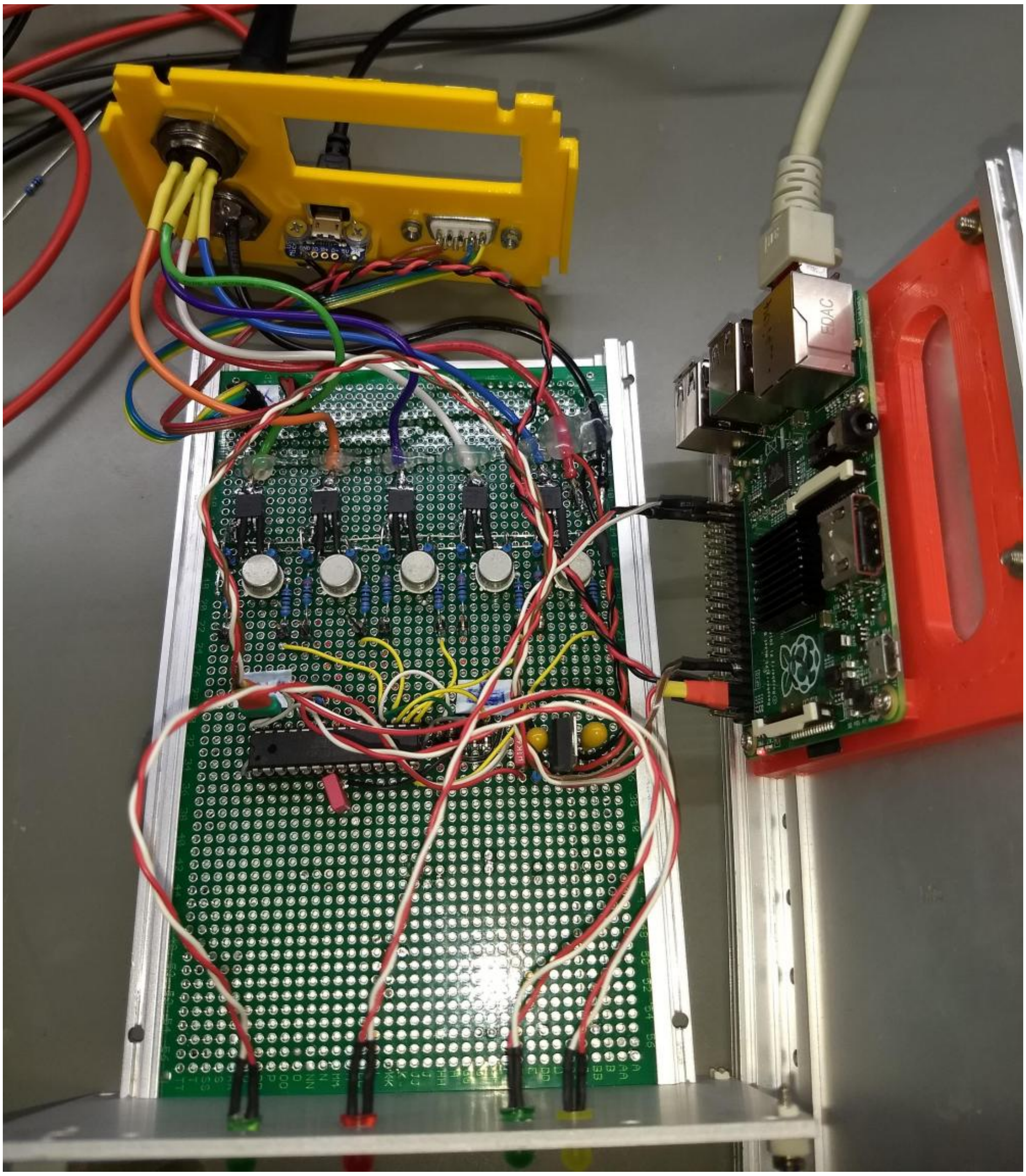

Figure 4.3: Opened housing for the custom made stepper motor driver circuit. The Raspberry Pi running the control software can be seen on the right.

Most of the standard stepper motors use two pairs of coils and can therefore easily be driven with many off-the-shelf driver circuits. However, the stepper motor that was attached to the device, intended to be used to bring the targets into the beam, was a five-coil type which meant that no driver for a reasonable price could be found. The circuit that was built to drive the motor used an ATmega328 [20] microcontroller to generate the step sequence needed to drive the motor. The driving signals were fed into five individual MOSFET half-bridge ICs capable of handling the current needed to energize each coil. With this driver, an accuracy of $\sim$0.1 mm was achieved. The firmware on the microcontroller was designed such that it would calculate a trapezoidal speed profile for each movement in order to minimize fast acceleration and jerking of the gear rack and the targets. Further, it would check the limit switches and prevent movements that could damage the vacuum enclosure of the gear rack. The driver circuit was connected via the I2C bus to a Raspberry Pi which would run a small web server. The target control software was written in Python and could be accessed from any computer connected to the same network via its browser-based user interface.

On the end of the gear rack, three targets were installed. Two strips of polyethylene foils ($CH_2$) and one diamond slab tapered into a very fine tip. Each of the targets had a length of 19 mm, and they were 2 cm spaced apart, see Figure 4.4b. To use one of these targets in the experiment, the gear rack driven arm was moved into the target chamber positioning the target on the center line of the detector. To avoid hitting the target in the acceleration phase of each cycle, a local bump was created at WASA using the steerer magnets of COSY to plunge the beam below the targets. When the beam had reached the desired energy, it was excited in such a way that a tiny fraction would hit the target tip and undergo an elastic scattering reaction. The amount of beam excitation was adjusted to keep the rate in the detector constant and extract as much beam as possible in each cycle.

To be able to install the targets on the arm of the driver, the vacuum enclosure had to be opened. Therefore a shutter was installed between the tube containing the target arm and the cross flange of the target chamber. When this shutter was closed, the tube of the target arm could be opened, and the targets could be installed. Evidently, a separate vacuum pump was needed to recreate the vacuum before the shutter could be opened and the targets could be moved into the chamber. This shutter was part of an interlock system created by the electronics workshop of the IKP. In order to open the shutter, the pressure on both sides of it had to be close to each other. This should, on the one hand, assure that the shutter was not opened accidentally resulting in a catastrophic venting of the COSY beam pipe and on the other hand even if the target arm pipe was sealed, too big of a pressure gradient could "blow" the targets from their mounting points. The interlock system would further prevent the closing of the shutter while the target arm was not fully retracted in order not to damage the arm and/or shutter. Finally, this system would cut the power of the driver circuit as long as the shutter was closed to prevent accidental crushing the target arm into the closed shutter.

A second Raspberry Pi connected to a webcam that was used to visually monitor the movements of the target arm via another web interface. An array of LEDs controlled by the same Raspberry Pi was used to illuminate the target chamber when needed.

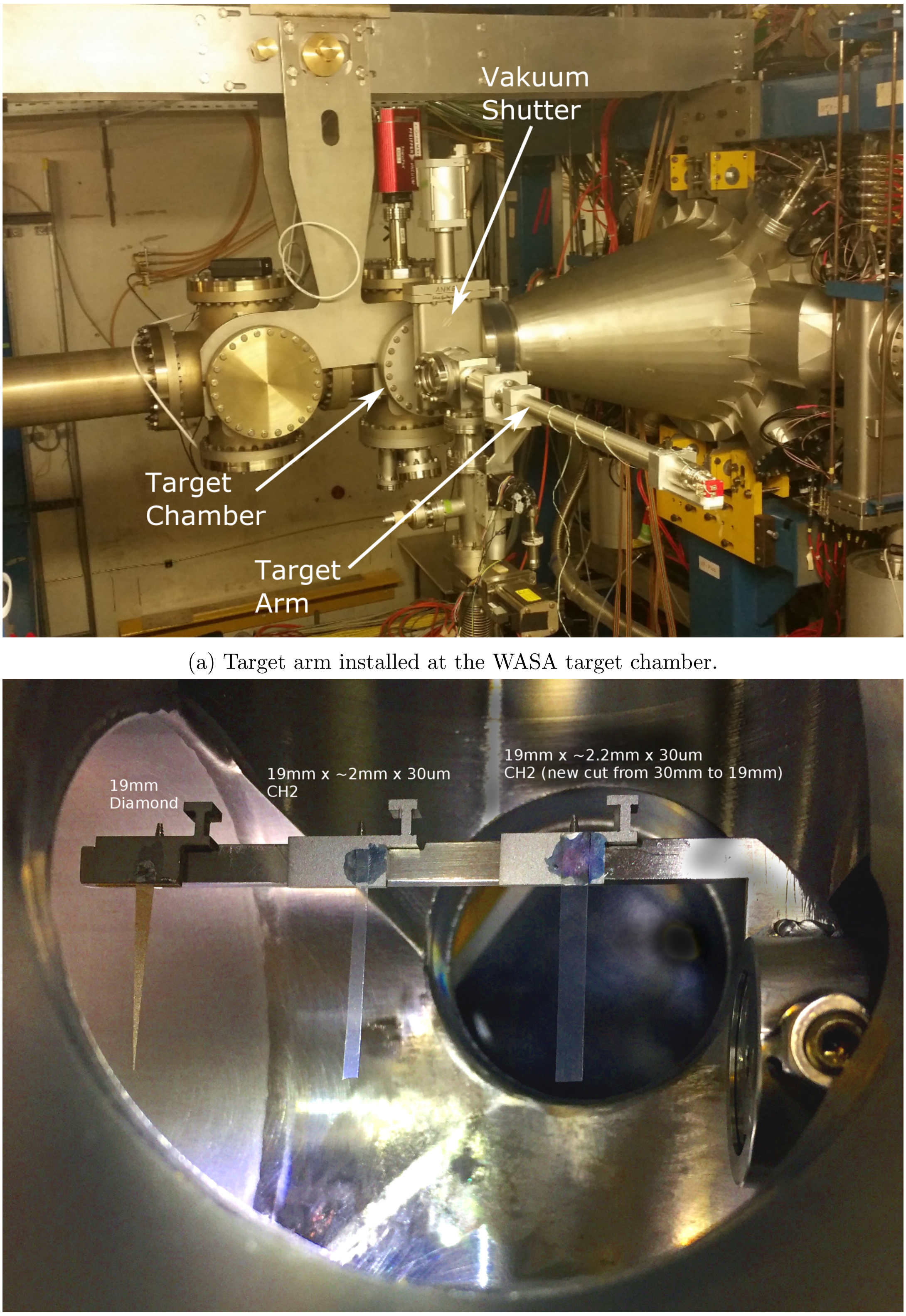


(a) Target arm installed at the WASA target chamber.

(b) The three strip targets installed for the Database Experiment

Figure 4.4: Targets for the Database Experiment

The target controller was upgraded after the experiment in order to control a second target consisting of a carbon block mounted to a rod. Using a magnetic feed-through mechanism, a linear motor could move this block target into the beam from the top.

## 4.2 Calibration

In order to use the measurements from the WASA detector, the raw data had to be calibrated. The main part of this task was done by Maria Żurek when she was employed as a post-doc at IKP-2. She did the whole Monte-Carlo simulation, track reconstruction and the majority of the calibration. The author assisted her with some small tasks, but all the credit for the whole calibration process belongs to her. As a consequence, the calibration will not be described in a very detailed manner, but an overview of the individual steps will be presented.

The trigger requirements for the WASA detector were set in a designated hardware module based on multiple FPGAs that was developed by Volker Hejny. Each detector module of WASA was connected to a fast discriminator that created a logic signal if the signal exceeded a certain threshold. These logic signals were fed into the FPGA-based trigger logic that would create a trigger signal for the ADC if an uninterrupted track was recorded. Here, a track is characterized as a series of subsequent detector elements that have reached the signal threshold in a given time window. For this experiment, the requirement for a trigger was a track reaching FRH1 or further.

The first step of the calibration was to reconstruct connected tracks and consolidated them into event-based ROOT trees. One event could consist of multiple tracks, but most of the events contained only a single track. In order to reconstruct a track, it needed to be checked if the detector modules that had triggered could be connected by a straight line. This was done by testing if the modules of interest were located in a row and if no gaps were present in the track. If a connected track was found, its polar and azimuthal angles were calculated from the straw tube array and attached to the event tree. At least three out of the four straw tube layers have to have created a valid signal, otherwise, the event was rejected. After this step, a ROOT tree was created for each run file, containing the following pieces of information: Number of tracks per event, polar and azimuthal angle, a timestamp, the associated beam energy, and the polarization state. Further, the deposited energy in each detector module associated with the track was stored in raw ADC units.

The second step of the calibration was to perform an energy calibration for each layer. For the beam energy of 380 MeV, the deuterons would reach up to the FRH4 layer representing the most penetrating tracks for this experiment. Therefore this energy was used to do the main calibration, as it covers the energy depositions for all the other beam energies as well. For each layer, a two-dimensional histogram for deposited energy $\Delta E$ versus the polar angle $\Theta$ was created. In order to transform the raw energy information into a physical quantity, it was compared to a Monte-Carlo simulation. To create a linear calibration from such a simulation, a distinct point in the spectra has to be found that could unambiguously be identified in both, data and simulation. This point in the data spectrum can then be scaled to match the Monte-Carlo spectrum. The

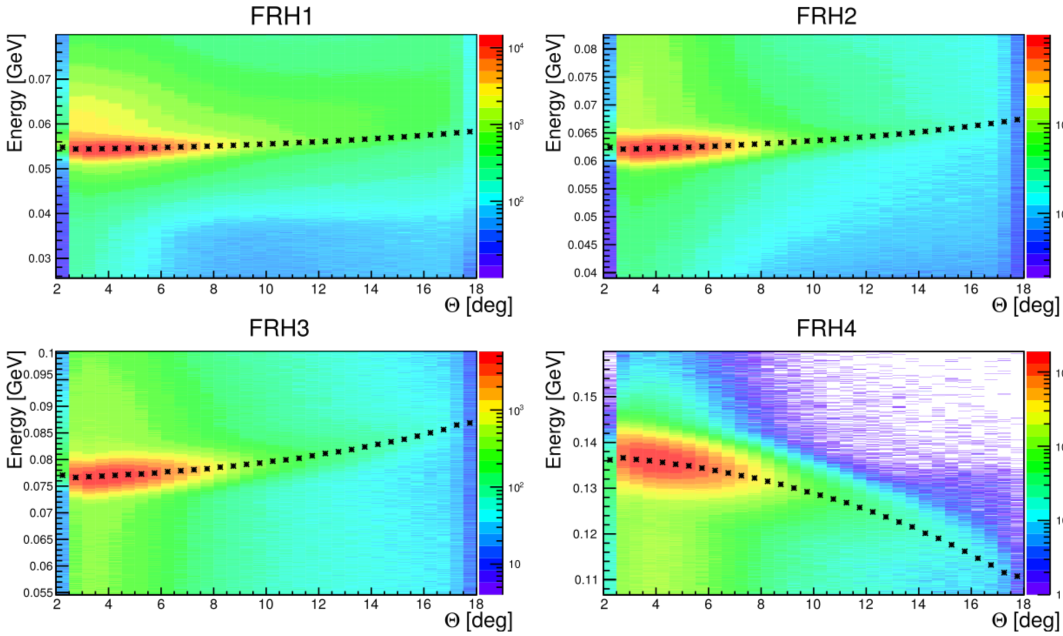


Figure 4.5: Calibrated range hodoscopes for 380 MeV. The elastic peak position from the Monte-Carlo (black points) is plotted on top of the calibrated data to visualize how well the data matches the simulation.

peak from the elastic dC scattering was therefore chosen as a reference. It is represented as a band structure in the $\Delta E$ vs. $\Theta$ spectra which were sliced along the $\Theta$ axis, and the position of the elastic peak was fitted for each $\Theta$-bin individually. This procedure was repeated for the Monte-Carlo simulation and resulted in $\Theta$-depended energy of the peak for elastically scattered deuterons from the simulation as well as from the measured data, see Figure 4.5. From these sets, a $\Theta$-depended linear calibration factor was obtained. The detector modules that make up the WASA detector have a triangular shape (pizza shape, see Figure 4.1) and cover an azimuthal range of 15° for the range hodoscopes (FRHx) and 7.5° for the trigger hodoscope (FTH), respectively. To account for the different gains of each of the detector elements, the linear calibration factor was calculated for each detector element individually. Applying this $\Theta$ and element dependent factor calibrates the value of the deposited energy along with both angular directions. Figure 4.6 shows an example of a $\Delta E$ vs. $\Delta E$ spectrum before and after the linear calibration was applied.

The next step in the calibration procedure was to compensate time dependence of the gain of the individual detector elements. The calibration described above was done for one particular run with a beam energy of 380 MeV. As the gain is not necessarily stable throughout the whole experiment, the elastic peak for $\Theta = 3.75°$ bin was scaled for each run file and each detector element to the corresponding position from the Monte-Carlo simulation. For each beam energy and each detector layer, this process was repeated to obtain a flat time dependence among all the runs. The result of this run-dependent correction is shown in Figure 4.7

So far, all the calibration steps were anchored to the elastic peak in the 380 MeV data. To evaluate the quality of the calibration, another Monte-Carlo simulation of

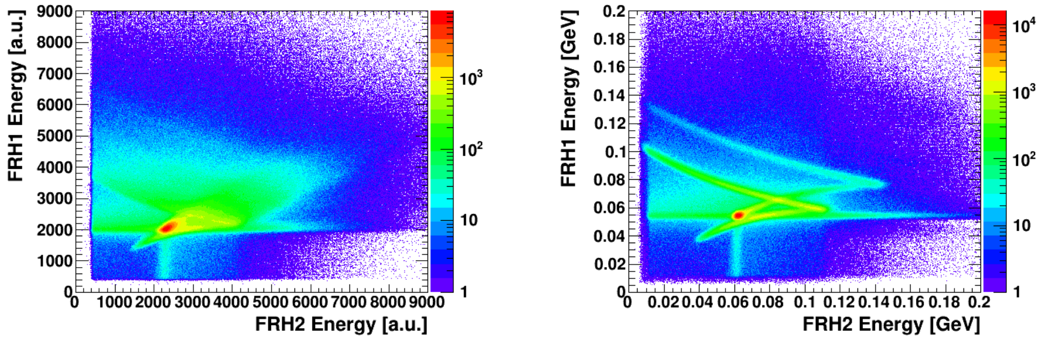


(a) Before the calibration was applied.

(b) After the calibration was applied. Now elastic peak as well as deuteron (upper) and proton (lower) bands get visible.

Figure 4.6: Effect of the linear calibration by way of example of the $\Delta E$ FRH2 vs. $\Delta E$ FRH1 spectra for 380 MeV.

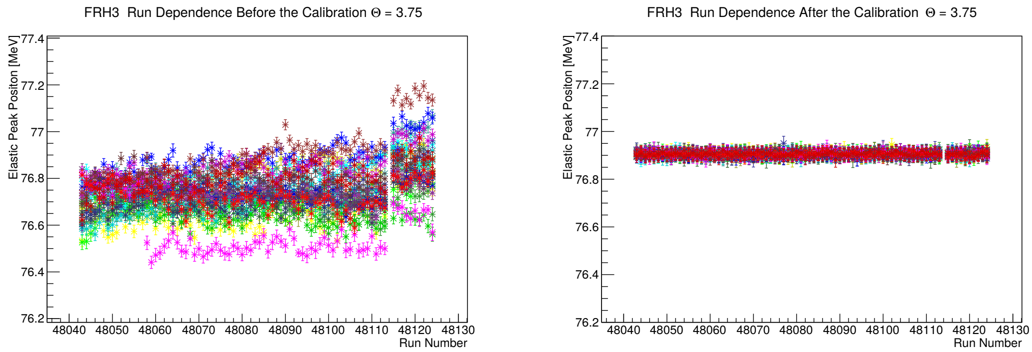


(a) Position of the 380 MeV elastic peak at $\Theta = 3.75°$ as a function of the run number for the FRH3. Each color corresponds to a particular detector module. This plot was obtained before the correction was applied.

(b) Same situation as described above, but this plot was obtained after the correction was applied.

Figure 4.7: Effect of run-dependent correction at a polar angle of $\Theta = 3.75°$ on FRH3 at 380 MeV

deuterons and protons hitting the detector with a uniform energy distribution was created. From this simulation, subsequent $\Delta E$ vs. $\Delta E$ plots were generated for all layers. The deuteron and proton band were fitted and parametrized such that they could be plotted on top of the corresponding $\Delta E$ vs. $\Delta E$ plots created from the measured data, see Figure 4.9a. This revealed that there was a mismatch between data and simulation. To overcome this issue, an additional non-linear calibration was applied on top of the linear one. The deuteron bands in the $\Delta E$ vs. $\Delta E$ plots from the data were fitted and parametrized as well. Non-linear functions were then defined to describe these bands. A third order polynomial function for the FTH and fourth order polynomial functions for the FRHs were assumed. Fixing these functions to the elastic peak ($\Delta E_{FRH1}(\Delta E_{FTH}) \equiv \Delta E^{el.}_{FRH1}$ and $\Delta E_{FRHx}(\Delta E_{FRH(x-1)}) \equiv \Delta E^{el.}_{FRHx}$) as well as to the origin ($\Delta E_{FTH,FRHx}(0) = 0$) reduced the number of parameters to two for the FTH and to three for the FRHs, respectively. Thus, the correction functions were

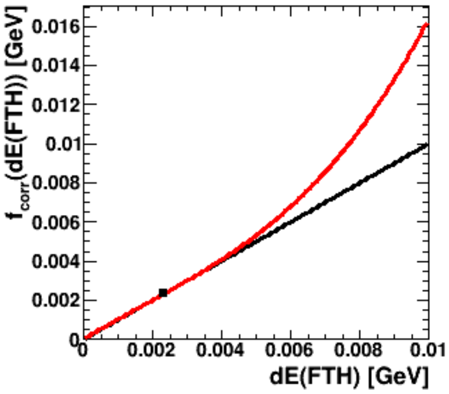


(a) Non-linear correction function for FTH, see Equation (4.1)

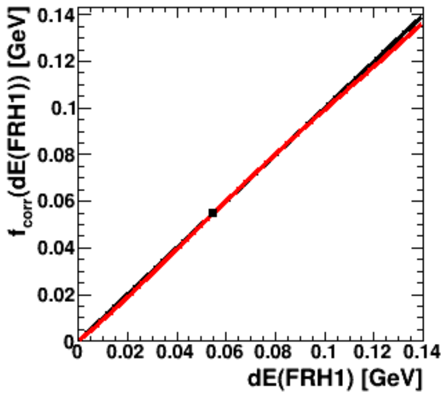


(b) Non-linear correction function for FTH, see Equation (4.2)

Figure 4.8: Non-linear correction functions for FTH and FRH1 in red. In black, the linear calibration function is given. The black dot indicates the elastic peak position that is used as a fix-point in both, the linear as well as the non-linear calibration.

defined as follows:

$$\begin{aligned} f_{corr}^{FTH}(E) &= (1 - p_1(\Delta E_{FTH}^{el.}) - p_2(\Delta E_{FTH}^{el.})^2)E \\ &\quad + p_1E^2 + p_2E^3, \qquad (4.1) \\ f_{corr}^{FRHx}(E) &= (1 - p_1(\Delta E_{FRHx}^{el.}) - p_2(\Delta E_{FRHx}^{el.})^2 - p_3(\Delta E_{FRHx}^{el.})^3)E \\ &\quad + p_1E^2 + p_2E^3 + p_3E^4. \qquad (4.2) \end{aligned}$$

Using this correction functions, a $\chi^2$-sum was defined as follows:

$$\begin{aligned} \chi^2 = &\frac{\left[f_{corr}^{FTH}(\Delta E_{FTH}) - f_{MC.}^{FTH}(f_{corr}^{FRH1}(\Delta E_{FRH1}))\right]^2}{\sigma_{FTH}^2} \\ &+ \sum_{x=1}^{3} \frac{\left[f_{corr}^{FRHx}(\Delta E_{FRHx}) - f_{MC.}^{FRHx}(f_{corr}^{FRH(x+1)}(\Delta E_{FRH(x+1)}))\right]^2}{\sigma_{FRHx}^2}. \qquad (4.3) \end{aligned}$$

Where $f_{MC.}^{FTH,FRHx}$ denote the parametrized Monte-Carlo bands and $\sigma_{FTH,FRHx}$ the width of each point of the parametrized deuteron bands from data. Minimizing Equation (4.3) equals to matching the data to the Monte-Carlo simulation in all five layers simultaneously by determining all 14 free parameters of the correction functions Equation (4.1) and (4.2). For the range hodoscopes, the deviation from the linear calibrations was rather small, but for the trigger hodoscope, the effect of the correction was significant, see Figure 4.8. The non-linear correction was then applied to the data, and the deuteron band was now in alignment with the Monte-Carlo simulation as can be seen in Figure 4.9b.

The full calibration was applied to the ROOT tree files created from the raw data for all seven beam energies. This resulted in a new set of calibrated ROOT tree files that were used for further data analysis.

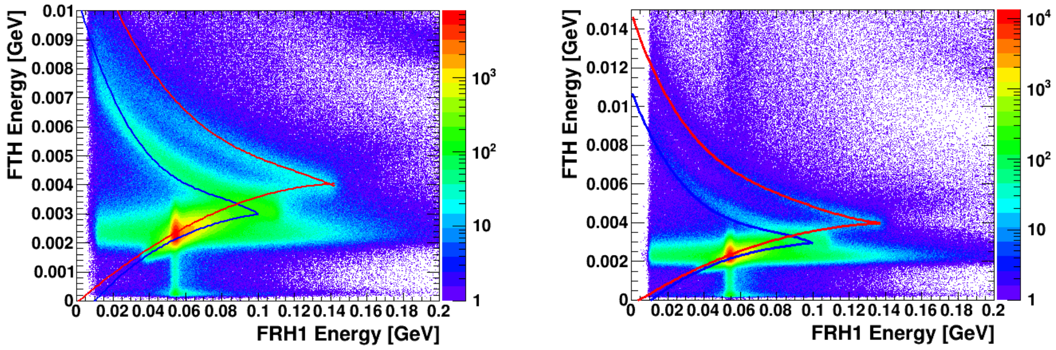


(a) Before the non-linear correction was applied. A mismatch between the data and the simulation is clearly visible, especially for the lower energy range of FRH1.

(b) Non-linear correction applied. The difference between data and Monte-Carlo has vanished.

Figure 4.9: Effect of the non-linear calibration by way of example of the $\Delta E$ FRH1 vs. $\Delta E$ FTH spectra for 380 MeV. The deuteron (red) and proton (blue) bands obtained from the Monte-Carlo simulation are drawn on top of the data.

## 4.3 Results

The elastic cross section for the elastic deuteron carbon scattering with vector polarized deuterons is given by:

$$\sigma^{dC}_{pol.}(\Theta, \Phi, A_y, P_y) = \sigma^{dC}_{unpol.}(\Theta)(1 + \frac{3}{2}A_y(\Theta)P_y\cos(\Phi)) \tag{4.4}$$

where $\Theta$ denotes the polar and $\Phi$ the azimuthal angle respectively [8]. The vector analyzing power $A_y(\Theta)$ is a property of the carbon target, and $P_y$ describes the vector polarization of the incoming deuteron beam. For a deuteron beam, there is an additional factor of $\frac{3}{2}$ in the equation. For a proton, beam this factor is $\frac{1}{2}$. In the subsequent sections, the approach to extract the unpolarized deuteron carbon cross section ($\sigma^{dC}_{unpol.}$ in Equation (4.4)) as well as the vector analyzing power $A_y$ from the data measured during the beam-time of the *Database Experiment* will be presented.

### 4.3.1 Vector Analyzing Power

#### 4.3.1.1 Elastic Event Selection

To obtain the vector analyzing power, the deuteron peaks for the elastic deuteron carbon scattering have to be identified. The elastic deuteron peak was identified by producing a $\Delta E$ vs. $\Delta E$ plot for each $\Theta$-bin of $1°$ in the stopping layer of the corresponding beam energy (see Table 4.1).

In order to remove as much of the non-elastic background contribution as possible, a two dimensional Gaussian was fitted to the elastic deuteron peak in each $\Theta$-bin. The elastic deuteron peak is located on the stopping band and is, therefore, neither parallel to the X- nor to the Y-axis of the plot, but slightly rotated (see Figure 4.10). For this reason, the X- and the Y-component of the Gaussian are correlated, and the following

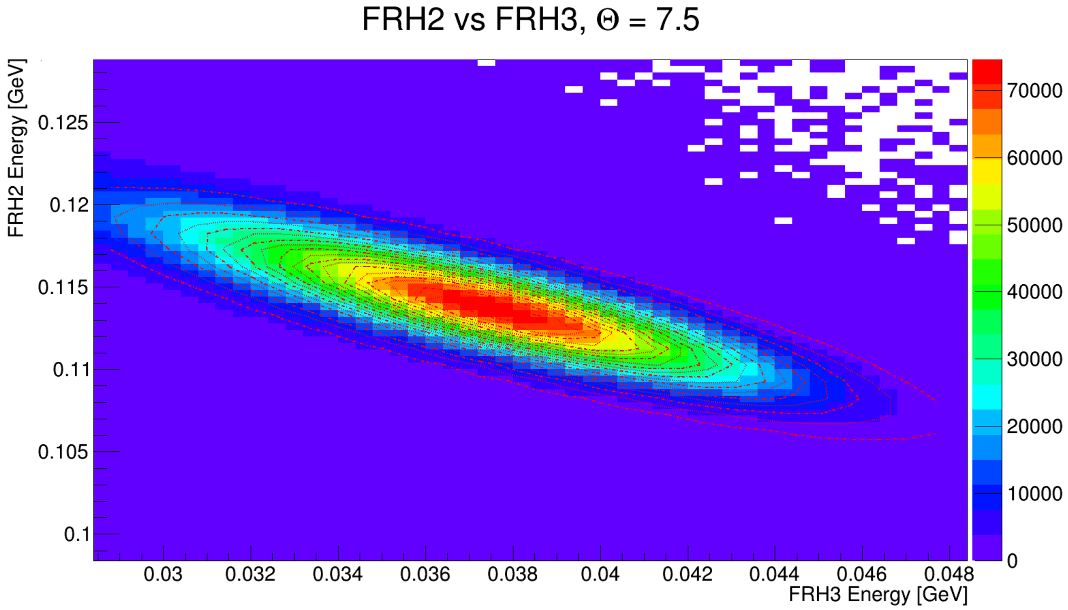


Figure 4.10: Two-dimensional correlated Gaussian fit on the elastic deuteron peak in the $\Delta E$ FRH2 vs. $\Delta E$ FRH3 plot for 270 MeV.

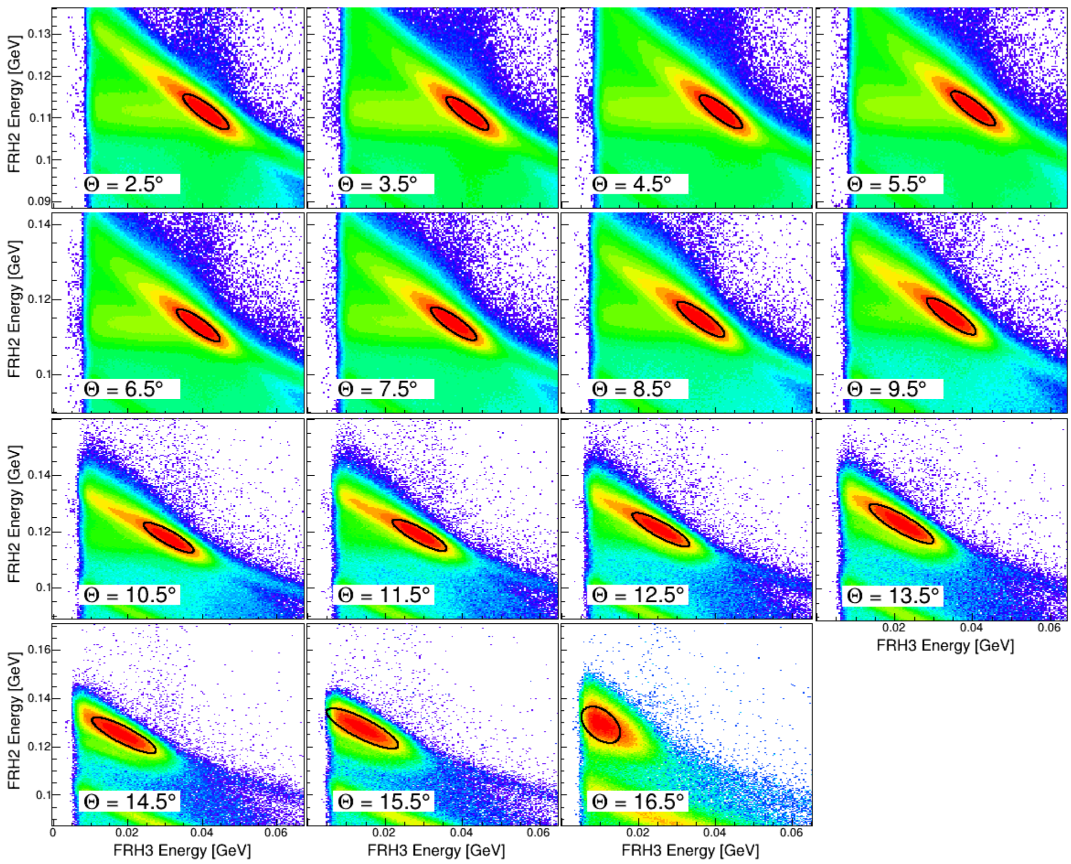


Figure 4.11: Elliptical cuts in each Θ-bin of the $\Delta E$ FRH2 vs. $\Delta E$ FRH3 plot obtained from the correlated two-dimensional Gaussian fit using Equations (4.6), (4.7) and (4.8).

| Energy | Stopping Layer Deuteron | Stopping Layer Proton |
|---|---|---|
| 170 MeV | FRH1 | FRH2 |
| 200 MeV | FRH2 | FRH2 |
| 235 MeV | FRH2 | FRH3* |
| 270 MeV | FRH3 | FRH3 |
| 300 MeV | FRH3 | FRH4 |
| 340 MeV | FRH4 | FRH4 |
| 380 MeV | FRH4 | FRH5 |

Table 4.1: Stopping layers for deuterons and protons for the different beam energies. Note that for 235 MeV, for most of the Θ-bins, the protons are stopped between FRH2 and FRH3.

formula is needed to describe the peak:

$$f(x', y', A_0, \sigma_x, \sigma_y, \rho) = A_0 \cdot e^{-\frac{\frac{x'^2}{\sigma_x^2} + \frac{y'^2}{\sigma_y^2} - \frac{2\rho x' y'}{\sigma_x \sigma_y}}{2(1-\rho^2)}}$$
$$\text{with}$$
$$x' = x - x_0 \text{ and } y' = y - y_0 \tag{4.5}$$

The position of the Gaussian ($x_0$, $y_0$), the widths ($\sigma_x$, $\sigma_y$), the height $A_0$ as well as the correlation parameter $\rho$ was extracted from the fit. These parameters were then used to calculate a rotated ellipse with a $1\sigma$ width relative to the Gaussian:

$$\beta = \frac{1}{2} \arctan\left(\frac{2\rho\sigma_x\sigma_y}{\sigma_y^2 - \sigma_x^2}\right) \tag{4.6}$$

$$a = \sqrt{\frac{4(1-\rho^2)\sigma_x^2\sigma_y^2\cos(2\beta)}{\cos(2\beta)(\sigma_x^2+\sigma_y^2) - (\sigma_x^2 - \sigma_y^2)}} \tag{4.7}$$

$$b = \sqrt{\frac{4(1-\rho^2)\sigma_x^2\sigma_y^2\cos(2\beta)}{\cos(2\beta)(\sigma_x^2+\sigma_y^2) + (\sigma_x^2 - \sigma_y^2)}} \tag{4.8}$$

Here $a$ denotes the semi-major and $b$ the semi-minor axis, respectively, and $\beta$ denotes the rotation of the ellipse. These ellipse parameters were extracted for $\Delta E$ vs. $\Delta E$ plots in each Θ-bin and converted into a graphical cut (see Figure 4.11). Hence, the elastically scattered deuteron had to fulfill the following condition to be taken into account for the calculation of the cross ratio:

1. Only one track per recorded event.
2. The Θ-angle of the track is between 2.45° and 16.45°.
3. The track has to reach the stopping layer.
4. In the stopping layer, the track has to be inside of the elliptical cut.

#### 4.3.1.2 Cross Ratio Method

The asymmetry, the vector analyzing power, the cross sections as well as the number of extracted events described in this section are functions of the polar angle $\Theta$ and will eventually be evaluated in individual $\Theta$-bins. For the sake of readability of the subsequent equations, the explicit $\Theta$-dependence will be omitted.

From Equation (4.4), the asymmetry $\epsilon$ is defined as follows:

$$\epsilon = \frac{3}{2} A_y P_y. \tag{4.9}$$

By limiting $\Phi$ to the range of $[-90°, +90°]$ and exploiting the azimuthal symmetry of the polarized cross section and the fact that $P_y^{\uparrow} = -P_y^{\downarrow}$ the following abbreviations can be defined:

$$\sigma_L^{\uparrow} = \sigma^0 (1 + \frac{2}{3} A_y P_y^{\uparrow} \cos(\Phi)) \tag{4.10}$$

$$\sigma_R^{\uparrow} = \sigma^0 (1 - \frac{2}{3} A_y P_y^{\uparrow} \cos(\Phi)) \tag{4.11}$$

$$\sigma_L^{\downarrow} = \sigma^0 (1 - \frac{2}{3} A_y P_y^{\downarrow} \cos(\Phi)) \tag{4.12}$$

$$\sigma_R^{\downarrow} = \sigma^0 (1 + \frac{2}{3} A_y P_y^{\downarrow} \cos(\Phi)) \tag{4.13}$$

$$\Rightarrow$$

$$\sigma_L \equiv \sigma_L^{\uparrow} = \sigma_R^{\downarrow} \tag{4.14}$$

$$\sigma_R \equiv \sigma_R^{\uparrow} = \sigma_L^{\downarrow} \tag{4.15}$$

where $\uparrow$ denotes an upwards polarized beam, $\downarrow$ a downwards polarized beam, and 0 an unpolarized beam, respectively. By calculating the difference over sum (cross ratio) of Equation (4.14) and (4.15), the asymmetry can be calculated:

$$\epsilon = \frac{\sigma_L - \sigma_R}{\sigma_L + \sigma_R}. \tag{4.16}$$

Hence, the asymmetry can be calculated from the cross sections in the left and the right side of the detector. With the knowledge of the vector polarization, the vector analyzing power can be calculated from the asymmetry:

$$A_y = \frac{2}{3} \frac{\epsilon}{P_y} = \frac{2}{3P_y} \frac{\sigma_L - \sigma_R}{\sigma_L + \sigma_R}. \tag{4.17}$$

The cross section as a function of the number of particles $N$ is defined as follows:

$$\sigma = \frac{N}{\alpha \mathcal{L}_{int}} \tag{4.18}$$

with the detector acceptance $\alpha$ and the integrated luminosity $\mathcal{L}_{int}$. If the assumption holds that the same $\alpha$ can be used for both (left and right) sides of the detector, and $\mathcal{L}_{int}$ does not change for both polarizations, Equation (4.16) can be simplified to:

$$\epsilon = \frac{N_L^{\uparrow} - N_R^{\uparrow}}{N_L^{\uparrow} + N_R^{\uparrow}} = \frac{N_L^{\downarrow} - N_R^{\downarrow}}{N_L^{\downarrow} + N_R^{\downarrow}}. \tag{4.19}$$

However, this assumption is often not valid, and it is, therefore, more convenient to use the full cross ratio $\epsilon_{CR}$:

$$\epsilon_{CR} = \frac{1-r}{1+r} \quad \text{with} \quad r^2 = \frac{\sigma_L^{\uparrow}\sigma_R^{\downarrow}}{\sigma_L^{\downarrow}\sigma_R^{\uparrow}}. \tag{4.20}$$

This method has the significant advantage of being insensitive to differences in $\alpha$ and $\mathcal{L}_{int}$ as can be shown by plugging Equation (4.18) into Equation (4.20) which yields to:

$$r^2 = \frac{N_L^{\uparrow} \cdot N_R^{\downarrow} \cdot \alpha^L \mathcal{L}_{int}^{\downarrow} \cdot \alpha^R \mathcal{L}_{int}^{\uparrow}}{\alpha^L \mathcal{L}_{int}^{\uparrow} \cdot \alpha^R \mathcal{L}_{int}^{\downarrow} \cdot N_L^{\downarrow} \cdot N_R^{\uparrow}} = \frac{N_L^{\uparrow} N_R^{\downarrow}}{N_L^{\downarrow} N_R^{\uparrow}} \tag{4.21}$$

The full cross ratio method does assume both vector polarization states $P_y^{\uparrow}$ and $P_y^{\downarrow}$ to have the same magnitude, i.e., $|P_y^{\uparrow}| = |P_y^{\downarrow}|$. If the two polarization states do not have the same magnitude, the full cross ratio is not a valid measure for the asymmetry.

An alternative approach to remove the dependence of the asymmetry $\epsilon$ on the detector acceptance $\alpha$ and the integrated luminosity $\mathcal{L}_{int}$ is to use the half cross ratio method. If the unpolarized elastic scattering is measured as well it will not show any asymmetry as defined in Equation (4.16):

$$\epsilon^0 = \frac{\sigma_L^0 - \sigma_R^0}{\sigma_L^0 + \sigma_R^0} \stackrel{!}{=} 0 \Rightarrow \sigma_L^0 = \sigma_R^0. \tag{4.22}$$

Using the relation from Equation (4.22), the half cross ratio is defined as follows:

$$\epsilon_{HCR}^{\uparrow} = \frac{1-r^{\uparrow}}{1+r^{\uparrow}} \quad \text{with} \quad r^{\uparrow} = \frac{\sigma_L^{\uparrow}\sigma_R^0}{\sigma_R^{\uparrow}\sigma_L^0} = \frac{N_L^{\uparrow}N_R^0}{N_R^{\uparrow}N_L^0} \tag{4.23}$$

$$\epsilon_{HCR}^{\downarrow} = \frac{1-r^{\downarrow}}{1+r^{\downarrow}} \quad \text{with} \quad r^{\downarrow} = \frac{\sigma_R^{\downarrow}\sigma_L^0}{\sigma_L^{\downarrow}\sigma_R^0} = \frac{N_R^{\downarrow}N_L^0}{N_L^{\downarrow}N_R^0} \tag{4.24}$$

Figure (4.12) shows a comparison between the asymmetries extracted using the full cross ratio as well as with half cross ratio method. It is clear that the magnitude of the polarization $|P|$ is not the same in the two polarization states and therefore it is not justified to use the full cross ratio to extract the asymmetry.

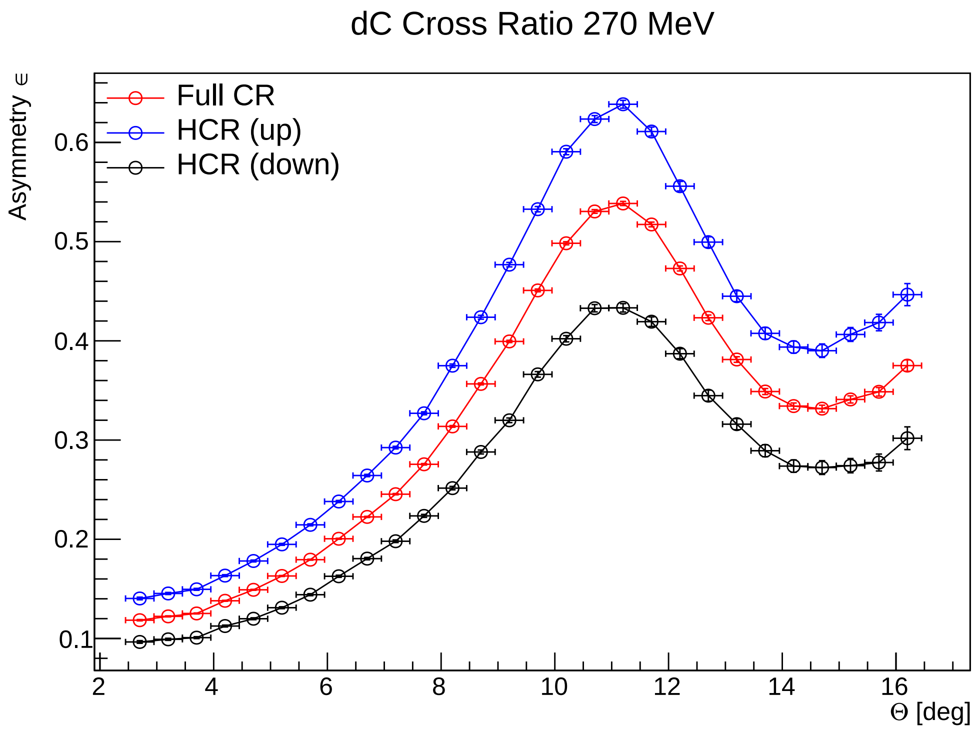


Figure 4.12: Comparison of the asymmetry extracted using the full cross ratio and the half cross ratio method on the 270 MeV data. As the half cross ratio method depends on one polarization state only, it can be stated that as the asymmetries for the up and down polarization states differ from each other and hence the magnitude of the polarization is not equal for both states.

#### 4.3.1.3 Asymmetry Extraction using Weighted and Unweighted Cross Ratios

Using Equation (4.18) as well as Equations (4.10) to (4.13) the following expression can be derived:

$$N_s^p = \mathcal{L}_p \sigma^0 \alpha_s (1 \pm \epsilon^p \cos(\Phi)) \tag{4.25}$$

where $p \in [\uparrow, \downarrow, 0]$ denotes the polarization state and $s \in [L, R]$ the side of the detector. So far, the number of events $N_s^p$ was given for one particular azimuthal angle $\Phi$, i.e., $N_s^p = f(\Phi)$. In reality, the number of events equals the integral over a certain $\Phi$-range and hence its expected value $\langle \cdot \rangle$ is given by:

$$\langle N_s^p \rangle = \mathcal{L}_p \sigma^0 \int_{-\Delta\Phi}^{+\Delta\Phi} \alpha_s (1 \pm \epsilon^p \cos(\Phi)) d\Phi. \tag{4.26}$$

If the acceptance is assumed to be constant within one side of the detector, i.e., $\frac{\partial \alpha(\Phi)}{\partial \Phi} = 0$, this equation can be evaluated to be:

$$\langle N_s^p \rangle = 2\Delta\Phi \cdot \mathcal{L}_p \sigma^0 \alpha_s (1 \pm \epsilon^p \frac{\sin(\Delta\Phi)}{\Delta\Phi}) = 2\Delta\Phi \cdot \mathcal{L}_p \sigma^0 \alpha_s (1 \pm \epsilon^p \langle \cos(\Phi) \rangle). \tag{4.27}$$

Using the expected value for the number of events, the full cross ratio given in Equation (4.21) gets slightly modified to:

$$\epsilon_{CR} = \frac{1}{\langle\cos(\Phi)\rangle}\frac{1-r}{1+r} \quad \text{with} \quad r^2 = \frac{\langle N_L^{\uparrow}\rangle\langle N_R^{\downarrow}\rangle}{\langle N_L^{\downarrow}\rangle\langle N_R^{\uparrow}\rangle}. \tag{4.28}$$

The same modification of the half cross ratio defined in Equation (4.23) and (4.24) yields to:

$$\epsilon_{HCR}^{\downarrow,\uparrow} = \frac{1}{\langle\cos(\Phi)\rangle}\frac{1-r^{\downarrow,\uparrow}}{1+r^{\downarrow,\uparrow}} \quad \text{with} \quad r^{\downarrow,\uparrow} = \frac{\langle N_R^{\downarrow,\uparrow}\rangle\langle N_L^{0}\rangle}{\langle N_L^{\downarrow,\uparrow}\rangle\langle N_R^{0}\rangle}. \tag{4.29}$$

Experimentally, the expected value of the number of events is just the sum of elastically scattered events in the azimuthal range defined by $-\Delta\Phi$ to $+\Delta\Phi$:

$$\langle N_s^p\rangle = \sum_i^{ev(p,s)} 1 = N_s^p. \tag{4.30}$$

This means that the statistical error on the number of events is given by $\Delta N_s^p = \sqrt{N_s^p}$ and using error propagation the uncertainty for the cross ratio is given by:

$$\Delta\epsilon_{CR} = \frac{1}{\langle\cos(\Phi)\rangle}\frac{r}{(1+r)^2}\sqrt{\frac{1}{\langle N_L^{\uparrow}\rangle}+\frac{1}{\langle N_R^{\uparrow}\rangle}+\frac{1}{\langle N_L^{\downarrow}\rangle}+\frac{1}{\langle N_R^{\downarrow}\rangle}} \tag{4.31}$$

$$\Delta\epsilon_{HCR}^{\downarrow,\uparrow} = \frac{1}{\langle\cos(\Phi)\rangle}\frac{2\cdot r^{\downarrow,\uparrow}}{(1+r^{\downarrow,\uparrow})^2}\sqrt{\frac{1}{\langle N_L^{\downarrow,\uparrow}\rangle}+\frac{1}{\langle N_R^{\downarrow,\uparrow}\rangle}+\frac{1}{\langle N_L^{0}\rangle}+\frac{1}{\langle N_R^{0}\rangle}} \tag{4.32}$$

As can be seen from Equation (4.4), the asymmetry term gets smaller and finally vanishes for $\Phi \to \pm 90°$. Therefore, by increasing the range of integration $\Delta\Phi$, the information content about the asymmetry gets diluted at some point even though the number of events increases and subsequently the statistical increases.

In Section 4.3.1.5, an error comparison between different methods of asymmetry calculation will be given. As it turns out, choosing an integration range of $\Delta\Phi > 66.77°$ leads to an increase in the error. To overcome this issue, each event $i$ can be weighted with the $\cos(\Phi_i)$ of the corresponding track. This leads to the following expected value for the measurement:

$$\langle N_s^p\cos(\Phi)\rangle = \sum_i^{ev(p,s)} \cos(\Phi_i). \tag{4.33}$$

Adding the weight to Equation (4.25) and following the same argument for the detector acceptance $\alpha_s$ yields to:

$$\begin{aligned}\langle N_s^p\cos(\Phi)\rangle &= \mathcal{L}_p{\sigma^0}\int_{-\Delta\Phi}^{+\Delta\Phi}\alpha_s\cos(\Phi)(1\pm\epsilon^p\cos(\Phi))d\Phi \\ &= 2\sin(\Delta\Phi)\cdot\mathcal{L}_p{\sigma^0}\alpha_s(1\pm\epsilon^p[\frac{\Delta\Phi+\sin(\Delta\Phi)\cos(\Delta\Phi)}{2\sin(\Delta\Phi)}) \\ &= 2\sin(\Delta\Phi)\cdot\mathcal{L}_p{\sigma^0}\alpha_s(1\pm\epsilon^p\frac{\langle\cos^2(\Phi)\rangle}{\langle\cos(\Phi)\rangle}).\end{aligned} \tag{4.34}$$

Plugging this relation into the definitions of the cross ratios given in Equation (4.21), (4.23) and (4.24) one gets:

$$\epsilon_{CR} = \frac{\langle\cos(\Phi)\rangle}{\langle\cos^2(\Phi)\rangle}\frac{1-r}{1+r} \quad \text{with} \quad r^2 = \frac{\langle N_L^{\uparrow}\cos(\Phi)\rangle\langle N_R^{\downarrow}\cos(\Phi)\rangle}{\langle N_L^{\downarrow}\cos(\Phi)\rangle\langle N_R^{\uparrow}\cos(\Phi)\rangle}, \tag{4.35}$$

$$\epsilon_{HCR}^{\downarrow,\uparrow} = \frac{\langle\cos(\Phi)\rangle}{\langle\cos^2(\Phi)\rangle}\frac{1-r^{\downarrow,\uparrow}}{1+r^{\downarrow,\uparrow}} \quad \text{with} \quad r^{\downarrow,\uparrow} = \frac{\langle N_R^{\downarrow,\uparrow}\cos(\Phi)\rangle\langle N_L^{0}\cos(\Phi)\rangle}{\langle N_L^{\downarrow,\uparrow}\cos(\Phi)\rangle\langle N_R^{0}\cos(\Phi)\rangle}. \tag{4.36}$$

From Equation (A.4) in Appendix A.1, it can be seen that the error for the expected value given in Equation (4.33) is given by:

$$\Delta\langle N_s^p\cos(\Phi)\rangle = \sqrt{\sum_i^{ev(p,s)}\cos^2(\Phi_i)} = \sqrt{\langle N_s^p\cos^2(\Phi)\rangle}. \tag{4.37}$$

The following uncertainty is calculated using simple error propagation:

$$\begin{aligned}\Delta\epsilon_{CR} = {} & \frac{\langle\cos(\Phi)\rangle}{\langle\cos^2(\Phi)\rangle}\frac{r}{(1+r)^2} \\ & \cdot\sqrt{\frac{\langle N_L^{\uparrow}\cos^2(\Phi)\rangle}{\langle N_L^{\uparrow}\cos(\Phi)\rangle^2}+\frac{\langle N_R^{\uparrow}\cos^2(\Phi)\rangle}{\langle N_R^{\uparrow}\cos(\Phi)\rangle^2}+\frac{\langle N_L^{\downarrow}\cos^2(\Phi)\rangle}{\langle N_L^{\downarrow}\cos(\Phi)\rangle^2}+\frac{\langle N_R^{\downarrow}\cos^2(\Phi)\rangle}{\langle N_R^{\downarrow}\cos(\Phi)\rangle^2}}\end{aligned} \tag{4.38}$$

$$\begin{aligned}\Delta\epsilon_{HCR}^{\downarrow,\uparrow} = {} & \frac{\langle\cos(\Phi)\rangle}{\langle\cos^2(\Phi)\rangle}\frac{2\cdot r^{\downarrow,\uparrow}}{(1+r^{\downarrow,\uparrow})^2} \\ & \cdot\sqrt{\frac{\langle N_L^{\downarrow,\uparrow}\cos^2(\Phi)\rangle}{\langle N_L^{\downarrow,\uparrow}\cos(\Phi)\rangle^2}+\frac{\langle N_R^{\downarrow,\uparrow}\cos^2(\Phi)\rangle}{\langle N_R^{\downarrow,\uparrow}\cos(\Phi)\rangle^2}+\frac{\langle N_L^{0}\cos^2(\Phi)\rangle}{\langle N_L^{0}\cos(\Phi)\rangle^2}+\frac{\langle N_R^{0}\cos^2(\Phi)\rangle}{\langle N_R^{0}\cos(\Phi)\rangle^2}}\end{aligned} \tag{4.39}$$

#### 4.3.1.4 Asymmetry Extraction using $\chi^2$-Fit

All the cross ratio methods discussed above depend on the assumption that the acceptance $\alpha$ is constant in $\Phi$ within each side of the detector. However, this is not necessarily the case. To take a $\Phi$-dependence of the detector acceptance $\alpha$ into account, another method using event weighting and a $\chi^2$ minimization can be utilized, see [21]. The $\Phi$-dependent detector acceptance $\alpha(\Phi)$ can be expressed into a Fourier series with a period of $2\pi$:

$$\alpha(\Phi) = a_0 + \sum_{n=1}^{\infty} a_n \cos(n \cdot \Phi) + b_n \sin(n \cdot \Phi). \tag{4.40}$$

By applying this acceptance and $\cos^n \Phi$ weights to Equation (4.25) one can calculate the theoretical expected values from the model:

$$\begin{aligned}
\langle N^p \rangle_{mod.} &= \frac{1}{2\pi} \mathcal{L}_p \sigma_0 \int_0^{2\pi} \alpha(\Phi)(1 + \epsilon^p \cos(\Phi)) d\Phi \\
&= \frac{\mathcal{L}_p \sigma_0 a_0}{2\pi} \int_0^{2\pi} (1 + \sum_{n=1}^{\infty} \frac{a_n}{a_0} \cos(n \cdot \Phi) + \frac{b_n}{a_0} \sin(n \cdot \Phi)) \cdot (1 + \epsilon^p \cos(\Phi)) d\Phi \\
&= \mathcal{L}_p \sigma_0 a_0 \left(1 + \frac{1}{2} \frac{a_1}{a_0} \epsilon^p \right), \qquad (4.41) \\
\langle N^p \cos(\Phi) \rangle_{mod.} &= \frac{1}{2\pi} \mathcal{L}_p \sigma_0 \int_0^{2\pi} \cos(\Phi) \alpha(\Phi)(1 + \epsilon^p \cos(\Phi)) d\Phi \\
&= \frac{\mathcal{L}_p \sigma_0 a_0}{2} \left( \frac{a_1}{a_0} + \epsilon^p \left(1 + \frac{1}{2} \frac{a_2}{a_0}\right)\right), \qquad (4.42) \\
\langle N^p \cos^2(\Phi) \rangle_{mod.} &= \frac{1}{2\pi} \mathcal{L}_p \sigma_0 \int_0^{2\pi} \cos^2(\Phi) \alpha(\Phi)(1 + \epsilon^p \cos(\Phi)) d\Phi \\
&= \frac{\mathcal{L}_p \sigma_0 a_0}{2} \left(1 + \frac{1}{2} \frac{a_2}{a_0} + \frac{\epsilon^p}{4} \left( \frac{a_3}{a_0} + 3 \frac{a_1}{a_0} \right)\right). \qquad (4.43)
\end{aligned}$$

Here, $p \in [\uparrow, \downarrow, 0]$ denotes the polarization state. Equations (A.5) to (A.14) in Appendix A.2 show the relations needed to evaluate these integrals. As stated in Equation (4.22) $\epsilon^0 = 0$, hence:

$$\begin{aligned}
\langle N^{\downarrow,\uparrow} \rangle_{mod.} &= p_0^{\uparrow,\downarrow} \left(1 + \frac{1}{2} p_1 \epsilon^{\downarrow,\uparrow}\right), \qquad (4.44) \\
\langle N^{\downarrow,\uparrow} \cos(\Phi) \rangle_{mod.} &= \frac{1}{2} p_0^{\downarrow,\uparrow} \left(p_1 + \epsilon^{\downarrow,\uparrow} \left(1 + \frac{1}{2} p_2\right)\right), \qquad (4.45) \\
\langle N^{\downarrow,\uparrow} \cos^2(\Phi) \rangle_{mod.} &= \frac{1}{2} p_0^{\downarrow,\uparrow} \left(1 + \frac{1}{2} p_2 + \frac{\epsilon^{\downarrow,\uparrow}}{4} (p_3 + 3p_1)\right), \qquad (4.46) \\
\langle N^0 \rangle_{mod.} &= p_0^0, \qquad (4.47) \\
\langle N^0 \cos(\Phi) \rangle_{mod.} &= \frac{1}{2} p_0^0 p_1, \qquad (4.48) \\
\langle N^0 \cos^2(\Phi) \rangle_{mod.} &= p_0^0 \left(\frac{1}{2} + \frac{1}{4} p_2\right). \qquad (4.49)
\end{aligned}$$

This leads to 9 equations with 8 free parameters: $p_0^{\downarrow,\uparrow} = \mathcal{L}_{\downarrow,\uparrow} \sigma_0 a_0$, $p_0^0 = \mathcal{L}_0 \sigma_0 a_0$, $p_1 = \frac{a_1}{a_0}$, $p_2 = \frac{a_2}{a_0}$, $p_3 = \frac{a_3}{a_0}$ and $\epsilon^{\downarrow,\uparrow}$. Together with the observed weighted expected values from

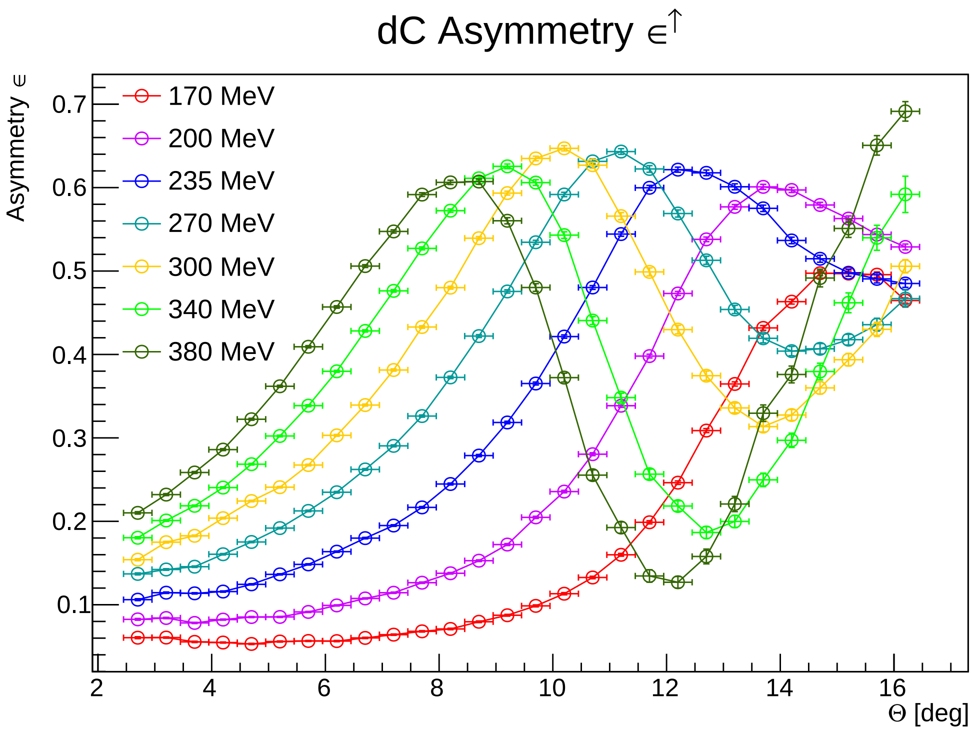


(a) Asymmetries for all energies using upwards polarized events.

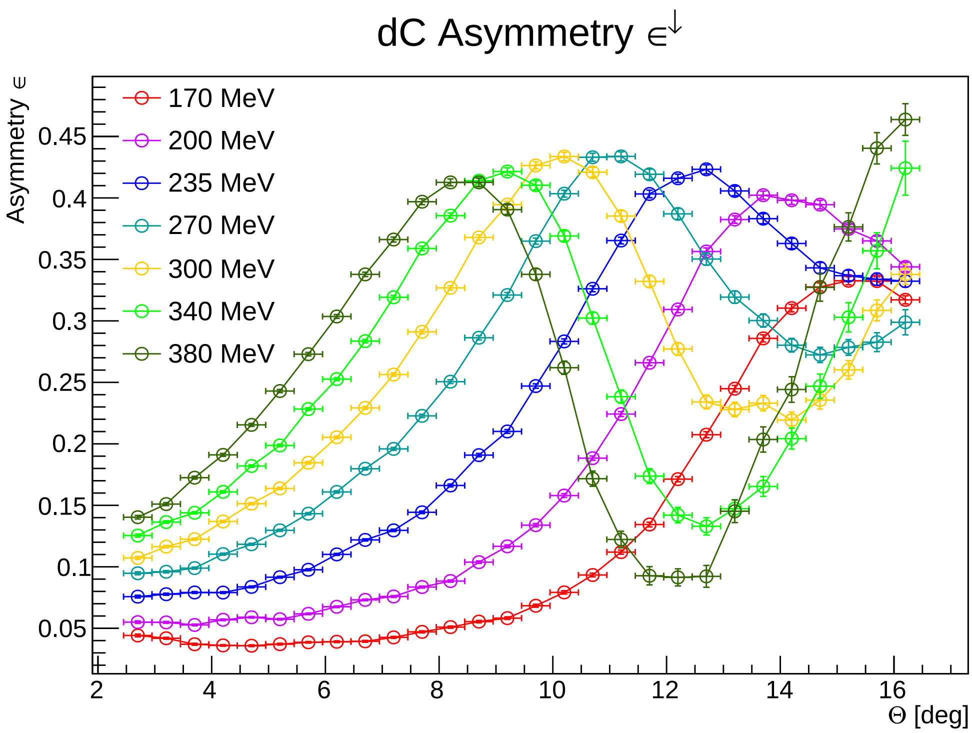


(b) Asymmetries for all energies using downwards polarized events.

Figure 4.13: Asymmetries for both polarization states extracted using the $\chi^2$-fit method for all seven beam energies.

the experiment

$$\langle N^p \cos^n(\Phi)\rangle_{obs.} = \sum_{i}^{ev(p)} \cos^n(\Phi_i) \quad \text{with} \quad n \in [0, 1, 2], \tag{4.50}$$

the $\chi^2$ sum can be calculated:

$$\chi^2 = (\vec{y}_{obs.} - \vec{y}_{mod.})\mathbf{C}^{-1}(\vec{y}_{obs.} - \vec{y}_{mod.})^T \tag{4.51}$$

with

$$(\vec{y}_{obs.} - \vec{y}_{mod.}) = \begin{bmatrix} \langle N^{\uparrow}\rangle_{obs.} - \langle N^{\uparrow}\rangle_{mod.} \\ \langle N^{\uparrow}\cos(\Phi)\rangle_{obs.} - \langle N^{\uparrow}\cos(\Phi)\rangle_{mod.} \\ \langle N^{\uparrow}\cos^2(\Phi)\rangle_{obs.} - \langle N^{\uparrow}\cos^2(\Phi)\rangle_{mod.} \\ \langle N^{\downarrow}\rangle_{obs.} - \langle N^{\downarrow}\rangle_{mod.} \\ \langle N^{\downarrow}\cos(\Phi)\rangle_{obs.} - \langle N^{\downarrow}\cos(\Phi)\rangle_{mod.} \\ \langle N^{\downarrow}\cos^2(\Phi)\rangle_{obs.} - \langle N^{\downarrow}\cos^2(\Phi)\rangle_{mod.} \\ \langle N^{0}\rangle_{obs.} - \langle N^{0}\rangle_{mod.} \\ \langle N^{0}\cos(\Phi)\rangle_{obs.} - \langle N^{0}\cos(\Phi)\rangle_{mod.} \\ \langle N^{0}\cos^2(\Phi)\rangle_{obs.} - \langle N^{0}\cos^2(\Phi)\rangle_{mod.} \end{bmatrix} \tag{4.52}$$

Because of the weighted expected values from the experiment, $\langle\cdot\rangle_{obs.}$ are statistically correlated, and the covariance matrix $\mathbf{C}$ is composed of three blocks describing the covariance between the weighted events from the same polarization state:

$$\mathbf{C} = \left[\begin{array}{c|c|c} \mathrm{Cov}[\uparrow] & 0 & 0 \\ \hline 0 & \mathrm{Cov}[\downarrow] & 0 \\ \hline 0 & 0 & \mathrm{Cov}[0] \end{array}\right]. \tag{4.53}$$

The full covariance matrix $\mathbf{C}$ is given in Appendix A.3, Equation (A.15) to (A.17).

Minimizing the $\chi^2$-sum given in Equation (4.51) in each $\Theta$-bin results in an asymmetry $\epsilon^{\downarrow,\uparrow}$ (see Figure (4.13)) that is independent of the detector acceptance $\alpha$. The acceptance can be extracted from the fit as well, as shown in Figure (4.14).

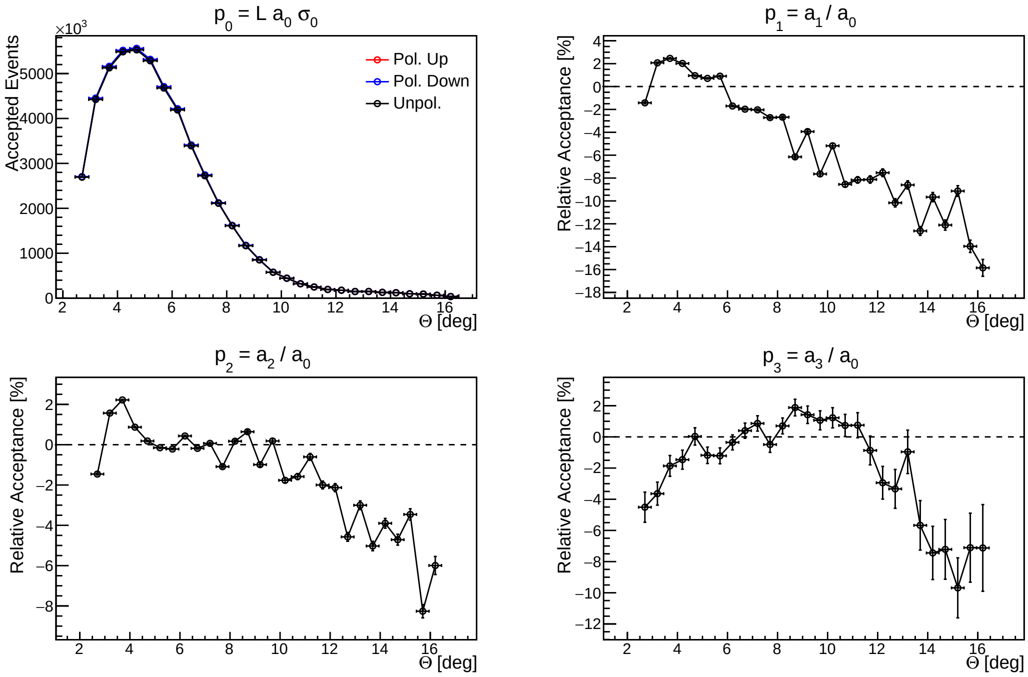

Figure 4.14: The parameters $p_0$ to $p_3$ resulted from the $\chi^2$ minimization of the 270 MeV data. The upper left plot shows parameter $p_0$ which describes the total number of accepted events for all three polarization states, including the zero order detector acceptance $a_0$. The number of accepted events is almost identical for the different polarization states. This indicates that the integrated luminosity remained constant, independent of the polarization as $a_0$ depends on the detector only and $\sigma_0$ does not depend on the polarization per definition. The other three graphs display the higher orders of the detector acceptance. Especially the first order of the detector acceptance $a_1$ is definitely not negligible as it reaches orders of 20%. The second and third orders are relatively small compared to the first order.

#### 4.3.1.5 Asymmetry Extraction: Results and Comparison

In the previous section, three methods to extract the asymmetry were presented. In Figure (4.16), the asymmetries extracted with these methods are plotted together for the 270 MeV data. Generally speaking, the results do not differ a lot between the different methods, especially considering the line-shape as a whole. Nevertheless, there are variations most prominently visible for lager azimuthal angle $\Theta$ where both cross ratio methods seem to underestimate the asymmetry compared to the $\chi^2$-fit method. Both cross ratio approaches assume a flat detector acceptance in $\Phi$ but as can be seen in Figure (4.14) the higher orders of the detector acceptance decrease from the flat acceptance ($a_{n>0} = 0$ in Equation (4.40)). Most of all, this is the case for the first order parameter $a_1$ which leads to a lower detector acceptance for larger $\Theta$ angles. The lowering of the detector acceptance explains the underestimation of the cross ratio methods.

To investigate the influence on the $\Phi$-range of integration on the statistical error of the three methods one can make the following assumptions:

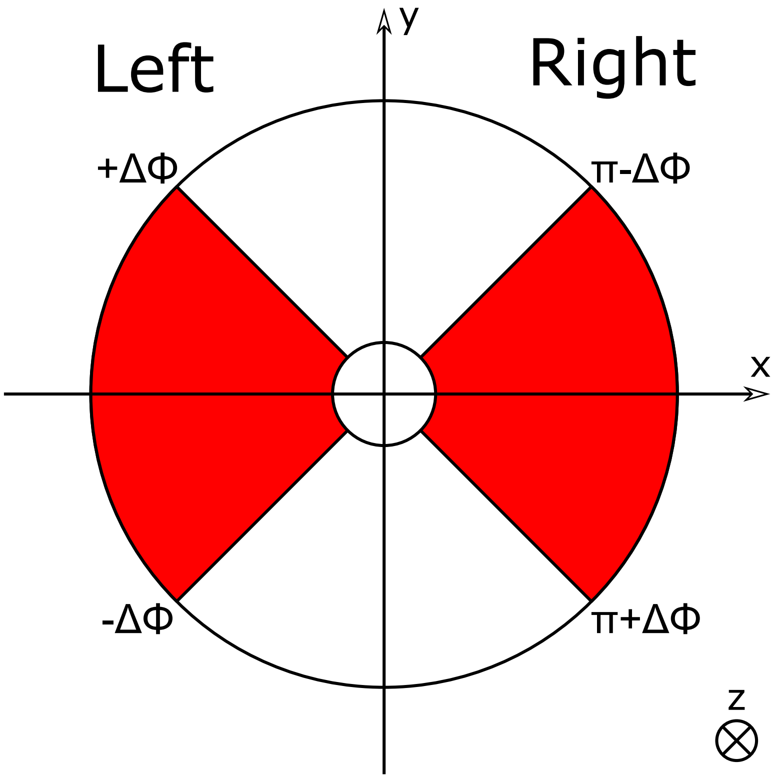


Figure 4.15: Geometry of the WASA detector. The red areas indicate the azimuthal integration range for a given value of $\Delta\Phi$. The beam moves along the z-axis, i.e., into the plane.

1. The asymmetry is small, i.e., $\epsilon \ll 1 \Rightarrow r \to 1$ for $r$ from Equation (4.23) and (4.24).
2. The total number of events is given by $N = N^{\downarrow,\uparrow} + N^0$.
3. The number of events in the polarized and unpolarized states are approximately the same. i.e., $N^{\downarrow,\uparrow} \approx N^0$.
4. As a consequence of the first assumption the number of event in both sides of the detector is almost the same, i.e., $N_L \approx N_R$.

Using these assumptions, the error on the unweighted half cross ratio given in Equation (4.32) can be simplified to:

$$\Delta\epsilon_{HCR} \approx \frac{2}{\langle\cos(\Phi)\rangle\sqrt{N}} \equiv \Delta\epsilon_0. \tag{4.54}$$

For the weighted half cross ratio one can use Equation (A.3) to disentangle the expected values for the number of events $\langle N\rangle$ from the $\Phi$-dependent $\langle\cos^n(\Phi)\rangle$ part. Hence, Equation (4.39) can be rewritten to:

$$\Delta\epsilon_{HCR} \approx \frac{2}{\sqrt{\langle\cos^2(\Phi)\rangle \cdot N}} \equiv \Delta\epsilon_w. \tag{4.55}$$

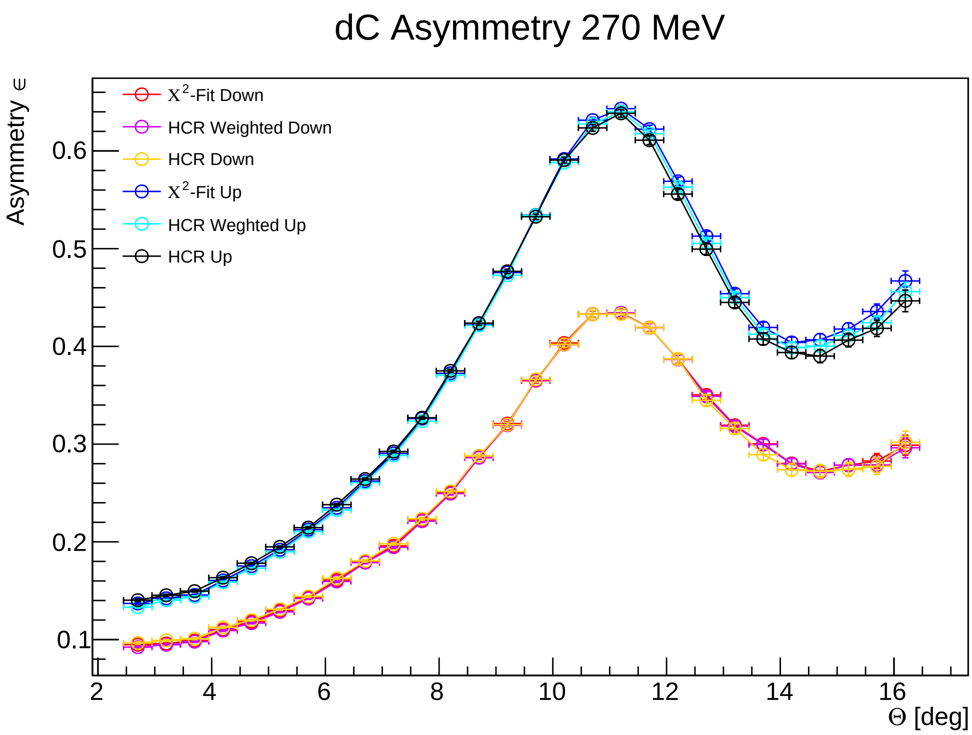


Figure 4.16: Asymmetry extracted using the regular half cross ratio, the weighted half cross ratio and the $\chi^2$-fit method on the 270 MeV data. All three methods used the whole $\Phi$-range of the detector.

In order to compare the $\Phi$-dependence of the error, it is convenient to define a ***Figure of Merit*** (FoM) in the following way:

$$\mathrm{FoM}(\epsilon) \equiv \frac{1}{(\Delta\epsilon)^2}. \tag{4.56}$$

Applying this definition to Equation (4.54) and (4.55) yields:

$$\mathrm{FoM}(\epsilon_0) = \frac{N \cdot \langle\cos(\Phi)\rangle^2}{4}, \tag{4.57}$$

$$\mathrm{FoM}(\epsilon_w) = \frac{N \cdot \langle\cos^2(\Phi)\rangle}{4}. \tag{4.58}$$

The Figure of Merit for the $\chi^2$-fit method was calculated in Appendix A.4 and is given in Equation (A.29). A small asymmetry as stated above (i.e., $\epsilon^{\downarrow,\uparrow} \approx 0$) leads to:

$$\mathrm{FoM}(\epsilon_{\chi^2}) = \frac{N' \cdot \langle\cos^2(\Phi)\rangle}{3}. \tag{4.59}$$

Attention has to be paid to the number of events $N'$ in this equation. Per definition, $N'$ in Equation (4.59) is given as the sum of all polarization states (i.e., $N' = N^{\uparrow}+N^{\downarrow}+N^0$, see Appendix A.4), whereas in Equation (4.57) and (4.58), $N$ is given as $N = N^{\downarrow,\uparrow}+N^0$. To be able to compare the Figure of Merit among the different asymmetry extraction methods, $N$ in Equation (A.28) has to be scaled by a factor of $\frac{3}{2}$ which leads to:

$$\mathrm{FoM}(\epsilon_{\chi^2}) = \frac{N \cdot \langle\cos^2(\Phi)\rangle}{4}. \tag{4.60}$$

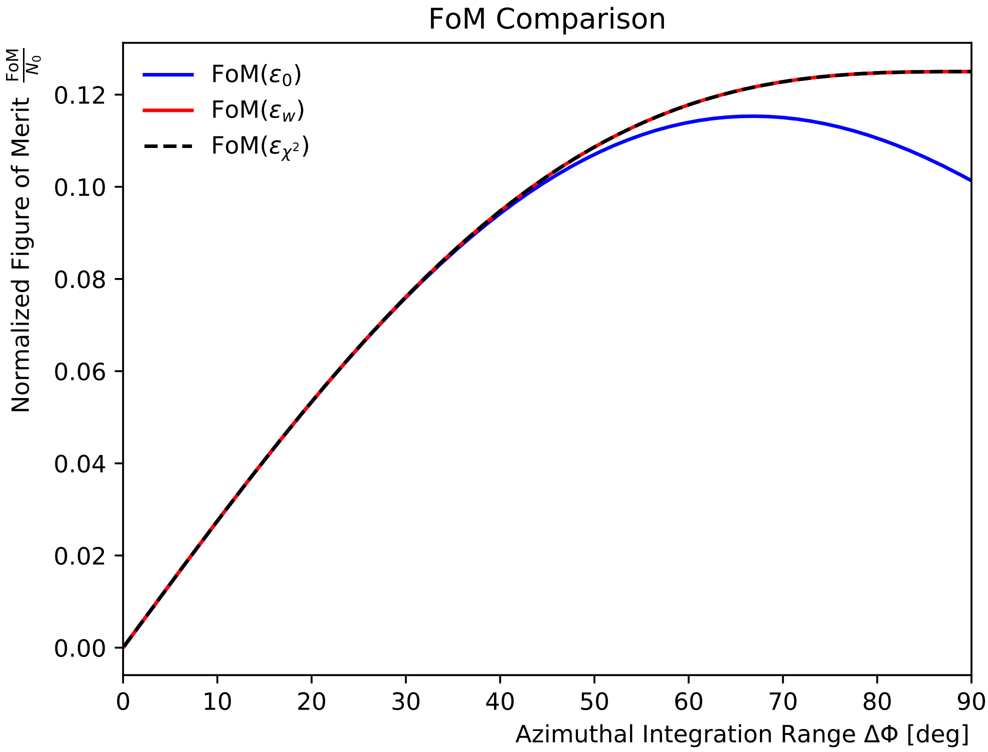


Figure 4.17: Comparison of the Figure of Merit for the three different methods of extracting the asymmetry as a function of the azimuthal integration range $\Delta\Phi$. The FoMs are normalized to the total number of events $N_0$

One has

$$\langle\cos(\Phi)\rangle = \frac{\int_{-\Delta\Phi}^{+\Delta\Phi}\cos(\Phi)d\Phi}{2\Delta\Phi} = \frac{\sin(\Delta\Phi)}{\Delta\Phi}, \tag{4.61}$$

$$\langle\cos^2(\Phi)\rangle = \frac{\int_{-\Delta\Phi}^{+\Delta\Phi}\cos^2(\Phi)d\Phi}{2\Delta\Phi} = \frac{\Delta\Phi + \sin(\Delta\Phi)\cos(\Delta\Phi)}{2\Delta\Phi}. \tag{4.62}$$

If $N_0$ denotes the total number of events recorded by the full $\Phi$-range of the detector, one finds this expression for the number of events $N$ recorded in a $\pm\Delta\Phi$ fraction of the detector:

$$N(\Delta\Phi) = N_0 \cdot \frac{2\Delta\Phi}{\pi}. \tag{4.63}$$

Putting this relation in the Equations (4.57), (4.58) and (4.60) given above, one gets the following analytic expressions for the Figure of Merit:

$$\text{FoM}(\epsilon_0) = N_0 \cdot \frac{\sin^2(\Delta\Phi)}{2\pi \cdot \Delta\Phi}, \tag{4.64}$$

$$\text{FoM}(\epsilon_w) = N_0 \cdot \frac{\Delta\Phi + \sin(\Delta\Phi)\cos(\Delta\Phi)}{4\pi}, \tag{4.65}$$

$$\text{FoM}(\epsilon_{\chi^2}) = N_0 \cdot \frac{\Delta\Phi + \sin(\Delta\Phi)\cos(\Delta\Phi)}{4\pi}. \tag{4.66}$$

Figure 4.17 compares these three FoMs as a function of the integration range $\Delta\Phi$. The Figure of Merit for the unweighted half cross ratio increases until it reaches a maximum. If the integration range is further increased, the Figure of Merit starts to decrease again and subsequently the error increases. This maximum is found to be $\Delta\Phi \approx 1.1655$ rad $\approx 66.77°$ by taking the first derivative of Equation (4.64) with respect to $\Delta\Phi$. This behavior can be explained as follows: By increasing the integration range, more events from the top and the bottom of the detector (i.e., $\Phi \rightarrow \pm 90°$) enter the asymmetry calculation. According to Equation (4.4) these events carry little to no information about the asymmetry and hence dilute the cross ratio. The FoM for the weighted half cross ratio and the $\chi^2$-fit method (Equation (4.58) and (4.60)) take this fact into account by assigning a weight according to its $\Phi$ angle to each event. Therefore, events from the top and bottom of the detector contribute less to the calculation of the asymmetry compared to events from the left and right side of the detector. This leads to a further increase of the FoM by extending the integration to the full detector range as can be seen in Figure 4.17.

The error of the weighted half cross ratio and the $\chi^2$-fit method behave the same with respect to the $\Phi$ integration range. However, as stated above, the $\chi^2$-fit method accounts for a non-flat detector acceptance which is implied by the cross ratio methods. Therefore, of the three approaches to extract the asymmetry the $\chi^2$-fit method was found to be the optimal one and will be used to calculate the asymmetries to be used for the extraction of the analyzing power.

#### 4.3.1.6 Vector Analyzing Power Extraction

The connection between the asymmetry $\epsilon$ and the vector analyzing power $A_y$ is given in Equation (4.9). This equation shows that the magnitude of the vector polarization $P_y$ has to be known in order to disentangle the asymmetry and the vector analyzing power. For the database experiment, it was intended to measure this polarization using the ***L**ow **E**nergy **P**olarimeter* (LEP) which is installed on the injection line of COSY after the cyclotron pre-acceleration stage, see Figure 3.1. The LEP consists of two times three crystal scintillator based detectors that measure asymmetries in elastic dC scattering at the injection energy of 76 MeV (see [13]). As the analyzing power for this energy is known, the polarization in each cycle can be measured. Ideally, the polarization should have been measured on a regular basis, and the values should have been sent via MQTT to a server where they would have been stored. Unfortunately, the storage server was not active during the whole beam time, and therefore no polarization measurement values have been saved. A few screenshots of the LEP graphical user interface were saved into the electronic logbook but they are the result of different arrangement tests of the LEP's detector modules, and hence cannot be used to determine the polarization. In summary, it can be stated that no polarization data from the LEP is available for the entire beam time and therefore another method to calculate the polarization from the measured data had to be found.

A way to calculate the polarization from a measured asymmetry is to fit it to a published reference vector analyzing power for the same energy. From the scaling factor of the fit, the polarization can be extracted. Such a reference for the vector analyzing power for deuteron carbon scattering is available for a 270 MeV deuteron beam by Satou et al. in [22] and another one for 200 MeV by Kawabata et al. in [23]. For 270 MeV, the WASA

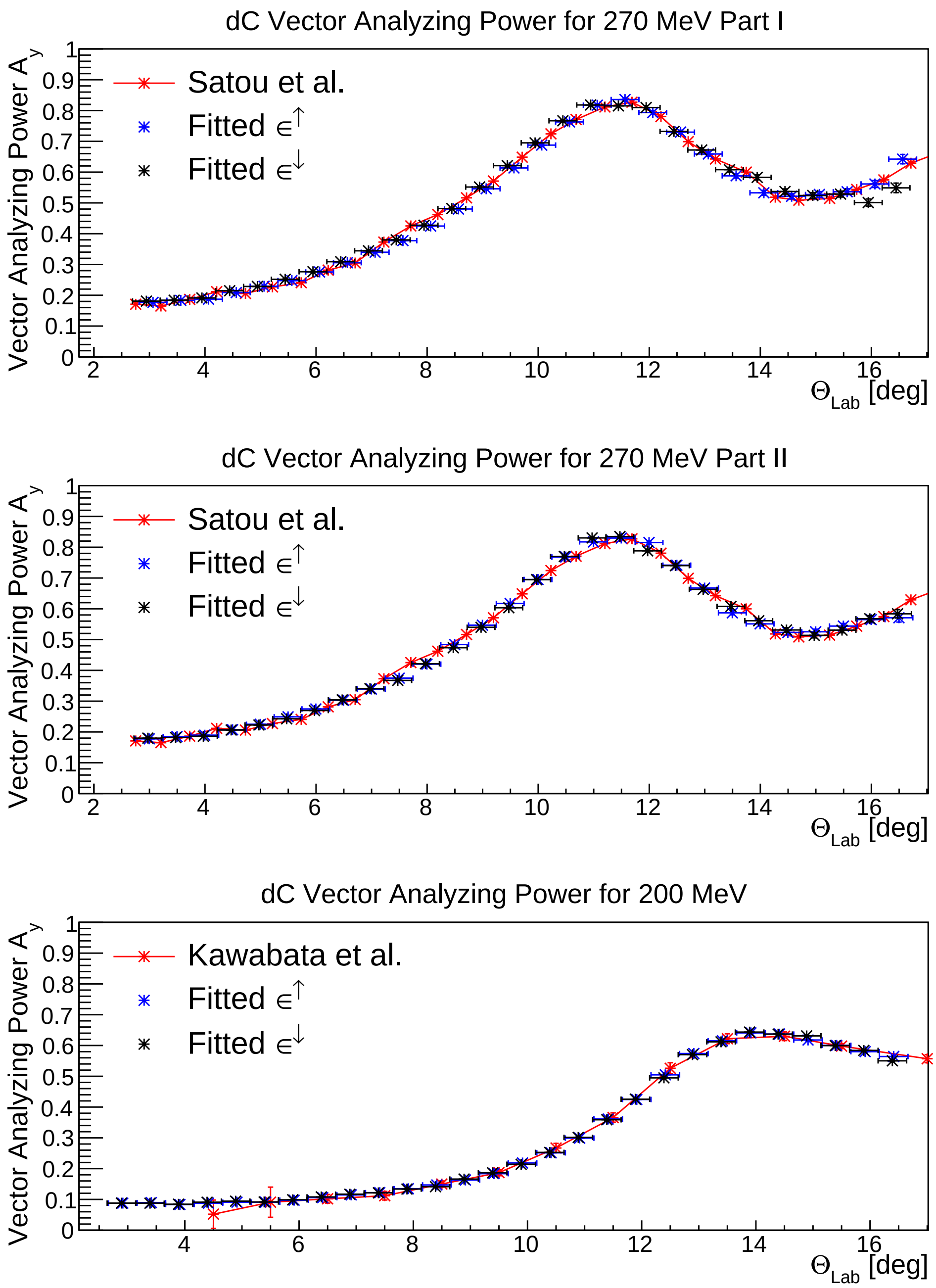


Figure 4.18: Measured asymmetry for the upwards $\epsilon^{\uparrow}$ (blue) and downwards $\epsilon^{\downarrow}$ (black) polarized beam. The asymmetries were fitted to the reference data (red) by *Satou et al.* [22] and *Kawabata et al.* [23] to obtain the beam polarization. The 270 MeV data was measured in two parts that were fitted individually.

| Energy | $P^{\uparrow}$ [%] | $P^{\downarrow}$ [%] |
|---|---|---|
| 200 MeV | $62.50 \pm 0.6$ | $41.67 \pm 0.4$ |
| 270 MeV Part I | $53.66 \pm 0.3$ | $36.84 \pm 0.3$ |
| 270 MeV Part II | $49.90 \pm 0.3$ | $33.66 \pm 0.2$ |
| Average | $55.35 \pm 6.5$ | $37.39 \pm 4.0$ |

Table 4.2: Results from the polarization value extraction for the up state $P^{\uparrow}$ and the down state $P^{\downarrow}$. The errors for the individual energies were taken from the fits. The error for the average was calculated as the unbiased sample standard deviation from the individual results.

data was taken once at the beginning of the beam time and then again in the middle of the experiment. An overview of the asymmetries measurements as a function of the time and the beam energy is given in Figure A.2. Comparing the asymmetries obtained from these two measurement blocks indicate that the beam polarization was not completely stable over the curse of the beam time. For this reason, it was decided to extract the polarization from both measurement blocks individually and later calculate an average. Figure 4.18 shows the result of fitting the asymmetries $\epsilon^{\uparrow}$ and $\epsilon^{\downarrow}$ obtain using the method described in Section 4.3.1.4 to the published reference data for 200 MeV and 270 MeV. The resulting vector polarization is given in Table 4.2. The results of the fits indicate that the line-shape of the asymmetries for 200 MeV as well as for 270 MeV are in good agreement with the published data. The theoretical limit of the magnitude for a pure vector polarized spin-1 particle is $\frac{2}{3}$. The vector analyzing power given in [22] for 270 MeV exceeds the theoretical value of $A_y^{max} = 1.0$ in the range of $\Theta_{Lab} \approx 20° - 22°$ which supports the assumption that this published analyzing power is slightly too large. According to Equation (4.9) this leads to an underestimation of $P_y$ when fitting the asymmetry to this vector analyzing power. This might explain why the values for $P_y$ resulting from this fit have a relative deviation of $\sim 15\%$ from the results of the fit obtained for the 200 MeV data given in [23]. For the 200 MeV reference, there is no way of judging the absolute values of the published vector analyzing power but the result for $P_y^{\uparrow} = 62.50 \pm 0.6\%$ which is close to the theoretical limit hints for the published value being rather too low than too large. In general, one cannot tell which of the results for $P_y$ describes the real beam polarization best, especially because it is not even clear if the polarization was stable during the experiment. For this reason, the best approach is to take the average polarization from the three fits to normalize the asymmetries for all energies and obtain the vector analyzing powers. The unbiased sample standard deviation from the three results was taken to describe the error. This results in a relative error in the order of $\sim 15\%$ that enters the normalized vector analyzing power as a systematic error as described below.

Using the extracted values for the polarization, the vector analyzing power could be calculated from the asymmetries by solving Equation (4.9) for $A_y$. For each energy, this leads to two values for $A_y$ from the two asymmetry-polarization pairs $(\epsilon^{\uparrow}, P^{\uparrow})$ and

$(\epsilon^{\downarrow}, P^{\downarrow})$. They were averaged using:

$$A_y = \frac{1}{3}\left(\frac{\epsilon^{\uparrow}}{P^{\uparrow}} + \frac{\epsilon^{\downarrow}}{P^{\downarrow}}\right). \tag{4.67}$$

As the two values for the asymmetries were obtained from a common fit, they are correlated and the statistical error $\Delta A_y^{stat.}$ on $A_y$ is given by

$$\Delta A_y^{stat.} = \frac{1}{3}\sqrt{\left(\frac{\Delta\epsilon^{\uparrow}}{P^{\uparrow}}\right)^2 + \left(\frac{\Delta\epsilon^{\downarrow}}{P^{\downarrow}}\right)^2 + 2\cdot\frac{\Delta\epsilon^{\uparrow}}{P^{\uparrow}}\cdot\frac{\Delta\epsilon^{\downarrow}}{P^{\downarrow}}\cdot\rho^{\uparrow\downarrow}}. \tag{4.68}$$

$A_y$, $\Delta A_y^{stat.}$ were calculated for each $\Theta$-bin and the uncertainties $\Delta\epsilon^{\uparrow}$ and $\Delta\epsilon^{\downarrow}$ as well as the correlation coefficient $\rho^{\uparrow\downarrow}$ were taken from the $\chi^2$-fit described in Section 4.3.1.4. The uncertainties in the polarization introduce a systematical error $\Delta A_y^{sys.}$ that affects $A_y$ as a whole (no direct $\Theta$-dependence) and is given by

$$\Delta A_y^{sys.} = \frac{1}{3}\sqrt{\left(\frac{\epsilon^{\uparrow}\Delta P^{\uparrow}}{(P^{\uparrow})^2}\right)^2 + \left(\frac{\epsilon^{\downarrow}\Delta P^{\downarrow}}{(P^{\downarrow})^2}\right)^2}. \tag{4.69}$$

The values for polarization and its error were taken from the average section in Table 4.2. The resulting vector analyzing powers for all seven energies are given in Figure 4.19. The statistical errors are drawn on the points using error bars and the systematic uncertainties from the polarization extraction are marked as a red region.

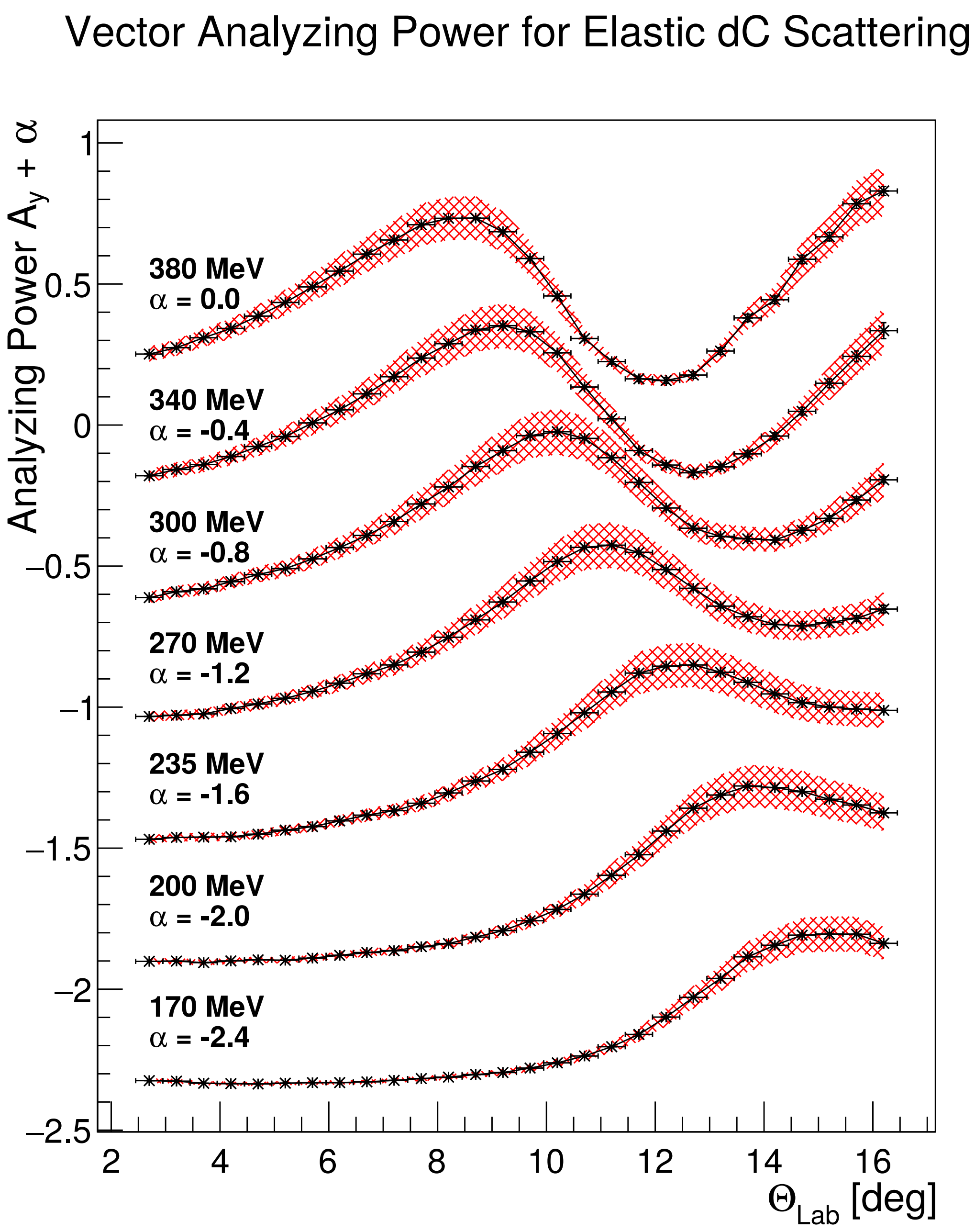


Figure 4.19: Reconstructed vector analyzing power for the deuteron beam energies of (from top to bottom) 380 MeV, 340 MeV, 300 MeV, 270 MeV, 235 MeV, 200 MeV and 170 MeV. The curves are subsequently offset by 0.4 for better readability. The statistical errors are indicated by the vertical error bars on the data points (for most bins, error bars are smaller than the symbol size). The systematic error is drawn as the red regions.

### 4.3.2 Unpolarized Elastic Cross Section

Multiple steps are needed to calculate the unpolarized deuteron carbon elastic cross section. First of all, the number of elastically scattered deuterons have to be identified and extracted. To get the real number of elastic events, the extracted number of deuterons has to be corrected by the detector acceptance which was calculated from a Monte-Carlo simulation. Since it was not possible to place an additional detector to measure the flux of the beam directly, the luminosity could not be calculated from the measured deuteron carbon scattering data. Using the polyethylene target ($CH_2$), the elastically scattered deuterons off the hydrogen in this target were extracted as well. For the energies above 170 MeV, reference data for the unpolarized elastic proton deuteron scattering is available. By scaling the acceptance corrected deuteron proton data to these references, the luminosity could be calculated and used to normalize the acceptance corrected deuteron carbon data in order to obtain the elastic deuteron carbon cross section. For a beam energy of 170 MeV, no proton deuteron reference data was available and an analytical model describing the elastic deuteron carbon cross section had to be used to normalize the extracted events. In the following sections, the process used to obtain the unpolarized elastic deuteron carbon cross section will be described in detail.

#### 4.3.2.1 Elastically Scattered Deuteron Extraction

The first step was to identify the elastically scattered deuteron events in the data. For the asymmetry extraction described above, having tight cuts around the elastic events is not problematic as long as the same cuts are applied for the whole azimuthal range. This works because of the ratio-like nature of the asymmetry which is a relative quantity. For the cross section, on the other hand, it is essential to get the real number of events. An underestimation due to tight cuts would lead to an overall underestimation of the cross section because it is an absolute quantity. For this reason, applying the same elliptical cuts as for the asymmetry extraction (see Section 4.3.1.1) is not feasible for the cross section calculation.

So-called band cuts were used to select the elastically scattered deuterons. From the Monte-Carlo simulations that were used to do the non-linear calibration (see Section 4.2) the parametrized position of the deuteron band in the $\Delta E$ vs. $\Delta E$ plots was available for all layers. From this function, a cut around the deuteron band could be defined. In each $\Delta E$ vs. $\Delta E$ plot, one can distinguish between two types of deuteron bands: A stopping band and a punch-through band. Each $\Delta E$ vs. $\Delta E$ plot describes the energy loss in two succeeding detector layers. The energy loss in the first layer is given on the Y-axis and the energy loss of the second layer is given on the X-axis. The stopping band starts in the top left corner of the plot and moves down and to the right, see Figure 4.6b. This band describes all the deuterons that were stopped in the second layer. Particles that fall in the top left region of this band had a high energy loss in the first layer, but only little energy was left to lose in the second layer. The point at the end of the stopping band describes particles that were more energetic and therefore would lose less energy in the first layer but being slowed down such that they would lose all of their remaining kinetic energy in the stopping layer. Particles with an even higher kinetic energy will fall in the punch-through band starting from the end of the stopping band and curving back down to the bottom left corner of the plot. Particles in the beginning of the punch-through band have just enough kinetic energy not to be stopped by both layers, but their total energy loss in both layers is maximal. The energy loss in matter for ions such as deuterons or protons as a function of their kinetic energy is governed by the *Bethe-Bloch-Equation* as shown in Figure 5.15 and described in Section 5.3.1.1.

The selection criteria for elastically scattered deuterons were the following: For each energy, the particle had to reach the stopping layer as defined in Table 4.1. Next, for all the layers before the stopping layer, the particle had to be inside of the deuteron punch-through band. This criterion assures that the particle is a deuteron but does not yet select only elastics. The last criterion was that in the stopping layer, the particle would be inside of the deuteron stopping band. Purely elastically scattered deuterons will have kinetic energies that are very close to the initial energy of the beam. This means that in the stopping layer, particles that have survived all the previous cuts and remain in the stopping band have to be almost entirely elastically scattered deuterons. From all the deuterons that were recorded, the elastics will always have the largest kinetic energy as process could create particles with higher energy. From the events that have passed all these cuts, the energy loss in all layers was summed up and filled into individual histograms for each polar angle $\Theta$-bin. A bin width of $\Delta\Theta = 1°$ was chosen in the range of $3°$ to $16°$.

Each of these histograms was fitted with a signal + background fit. The signal (i.e., the elastic events) was assumed to be a Gaussian, and the background was modeled as a polynomial with a cut-off described by Gauss error function (*Erf*). As argued above, the background remaining after the band cuts has to be on the low energy side relative to the elastic peak. The fit was therefore restricted such that the Erf cut-off has to be to the left of the elastic peak. Both, the signal and the background functions were initialized independently before the combined fit was performed, see Figure 4.20a. The number of elastically scattered deuterons was then given as the integral of the signal Gaussian divided by the bin width of the energy spectrum. This resulted in the non acceptance corrected number of elastically scattered deuterons as a function of $\Theta$ for each beam energy, see Figure 4.20b.

The exact same procedure was then applied to the Monte-Carlo simulation. By dividing the number of events obtained by applying the cuts and fits on the simulation, by the total number of generated events, the deuteron acceptance was calculated for each energy, see Figure 4.21. The *WASA Monte-Carlo* (WMC) simulation is based on GEANT 3 [24] which is written in FORTRAN. The simulation does include a geometrical model of the WASA forward detector as well as interactions with active and passive detector components like energy losses, multiple scattering, secondary particle decays, and photon conversion [25]. The Monte-Carlo was maintained by Maria Żurek, and the author was running it only as a *user*. Therefore his understanding of all the settings and configuration is very limited. What the simulation did not include was the energy-dependent resolution of the individual detector layers. To add this to the simulation, the elastic peak in each layer was fitted and from the widths of the peaks, a *smearing*

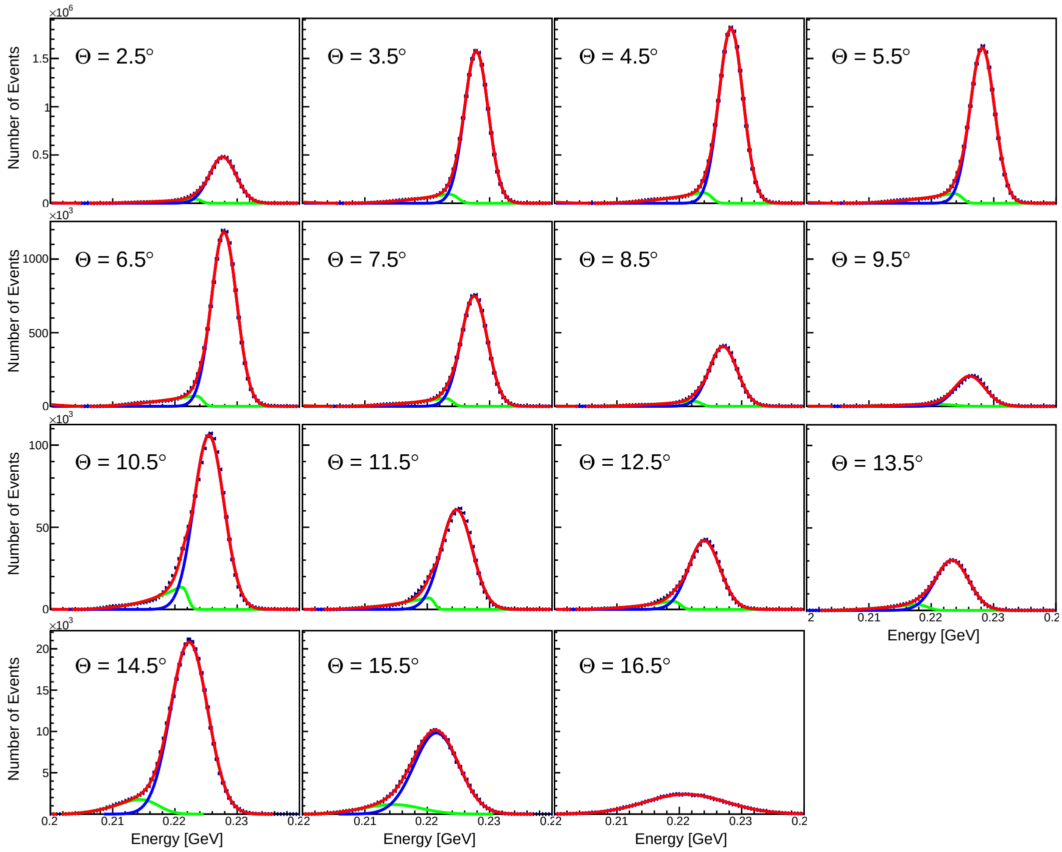


(a) Extraction of the elastically scattered deuterons using a combined signal + background fit (red). The fits were performed for each Θ-bin individually. The integral of the signal part (blue) equals to the number of elastics. The background function is given in green.

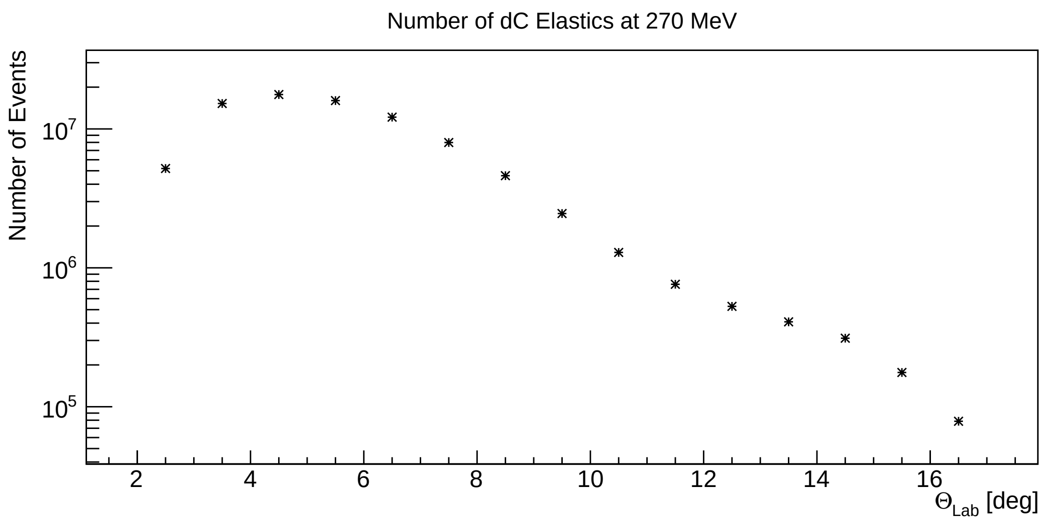


(b) Non acceptance corrected number of elastically scattered deuterons as a function of the scattering angle Θ.

Figure 4.20: Example for the elastic deuteron extraction at a beam energy of 270 MeV.

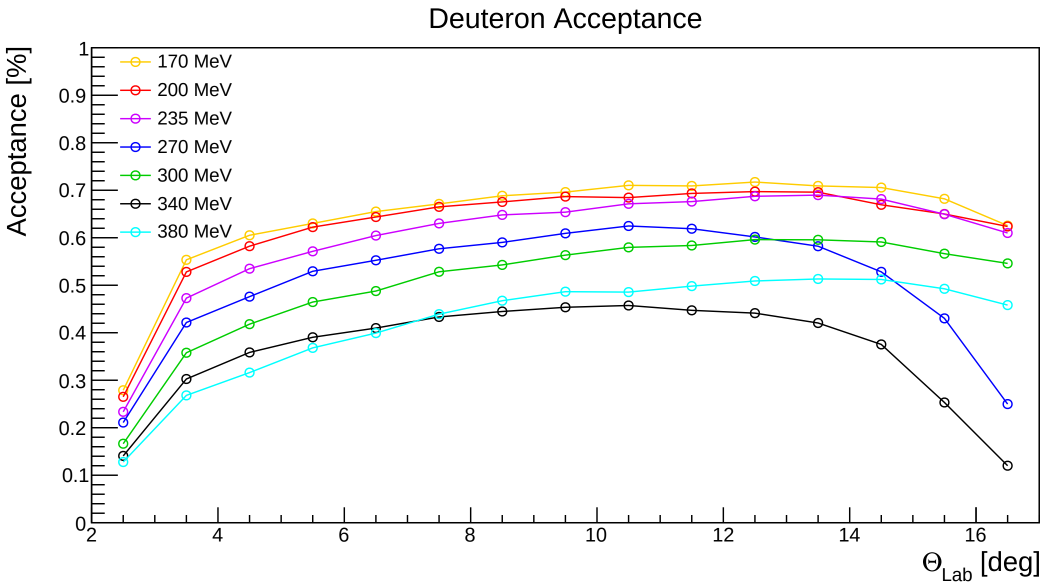


Figure 4.21: Deuteron acceptance for all seven beam energies calculated from the WASA Monte-Carlo (WMC).

parameter was calculated that was added to the simulation. This resulted in a more realistic Monte-Carlo for energy deposition. In many discussions with experts of the WMC Maria Żurek and Volker Hejny, many doubts on the reliability of the simulation were expressed. One major concern was the extremely convoluted configuration files for WMC and the fact that nobody was an expert in FORTRAN. In any case, all the results obtained from the WMC - especially the acceptance - have to be taken with a grain of salt.

#### 4.3.2.2 Proton Extraction from Elastic Deuteron Proton Scattering

The WASA forward detector is installed around the COSY beam pipe and the beam cycles through the target chamber countless times, and therefore no additional detector can be installed in the beam path to measure the flux. The whole beam would have to pass through this detector, and the induced energy loss would destroy the beam orbit. The luminosity needed for the calculation of the deuteron carbon cross section depends on the flux and hence could not be measured with the existing experimental setup. To overcome this issue, a $CH_2$ target was used to measure elastically scattered deuteron proton events off the hydrogen in the target. The recoil protons from this reaction were used to calculate the luminosity using published elastic proton deuteron cross sections as described in Section 4.3.2.3.

The method to extract the recoil protons is almost identical with the elastic deuteron extraction described in the previous section with a few adjustments. The calibration that is explained in Section 4.2 was applied for each energy up to the deuteron stopping layer (see Table 4.1). The succeeding layers were not calibrated for this energy. For some beam energies, the recoil proton from the elastic deuteron proton scattering would be stopped in the last layer as well. This was the case for a beam energy of 200 MeV,

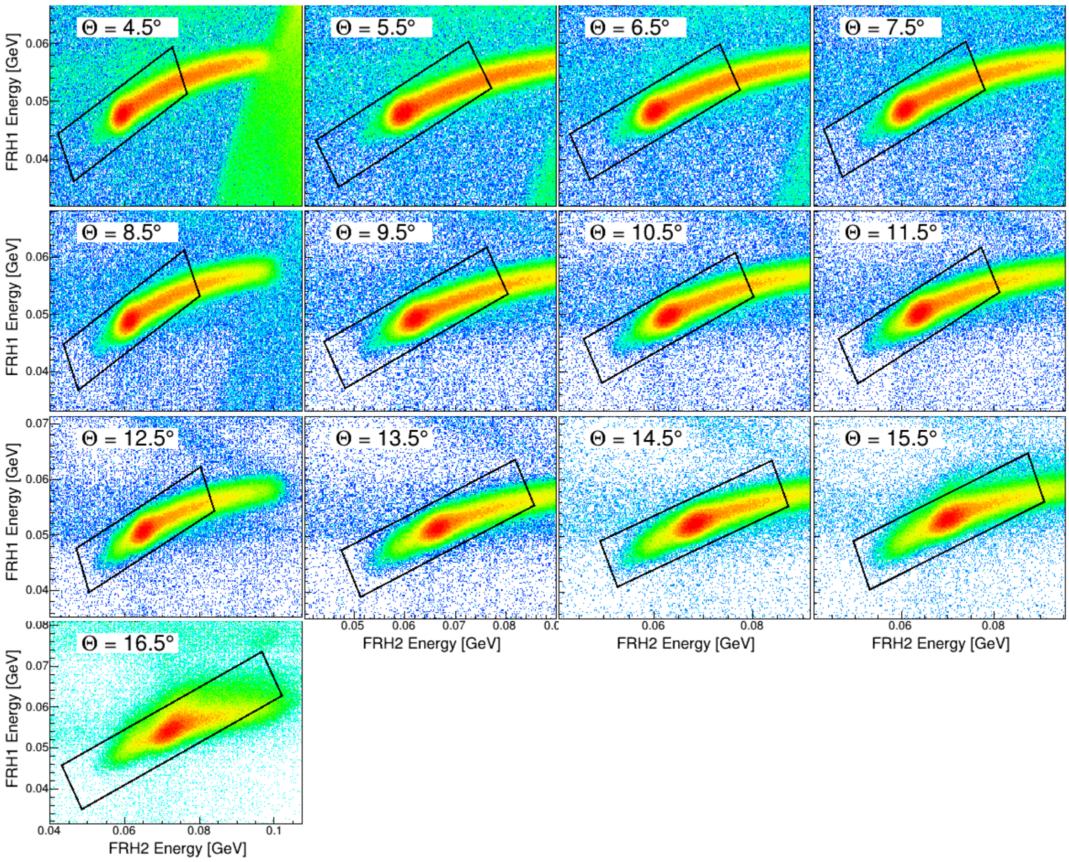


Figure 4.22: $\Delta E$ FRH2 vs. $\Delta E$ FRH1 punch-through plot of each Θ-bin. A graphical box cuts around the elastic recoil proton peak from deuteron proton scattering at 270 MeV was applied.

270 MeV, and 340 MeV. For 170 MeV, 300 MeV, and 380 MeV, the protons were stopped in the layer after the deuteron stopping layer. 235 MeV is a special case because there the protons were mainly stopped between two layers and has, therefore, be treated specially, see Section 4.3.2.4. To keep the analysis as consistent as possible, it was decided to use the last punch-through layer for the proton extraction because their stopping layer was not accessible for all energies.

The first step was to restrict the analysis to unpolarized events and allowing only one particle track per event. Further, it was required for the particles to reach the stopping layer of the protons, see Table 4.1. From the events that have fulfilled these criteria, $\Delta E$ vs. $\Delta E$ spectra from the subsequent layers were generated. Next, a graphical box cut was applied around the elastic proton peak in the last punch-through layer for each Θ-bin. For low theta angles, the proton peak was sometimes obstructed by the deuteron band, and therefore these bins were omitted in the analysis. Figure 4.22 shows the box cuts that were applied for the 270 MeV data. In all spectra from both, the pure carbon as well as the polyethylene target, protons are present. This is due to the break-up reaction of a deuteron into a proton and a neutron inside the carbon target or in the detector itself. From such a break-up, the proton can pick up an arbitrary fraction of the kinetic energy of the original deuteron and hence, the protons are spread over

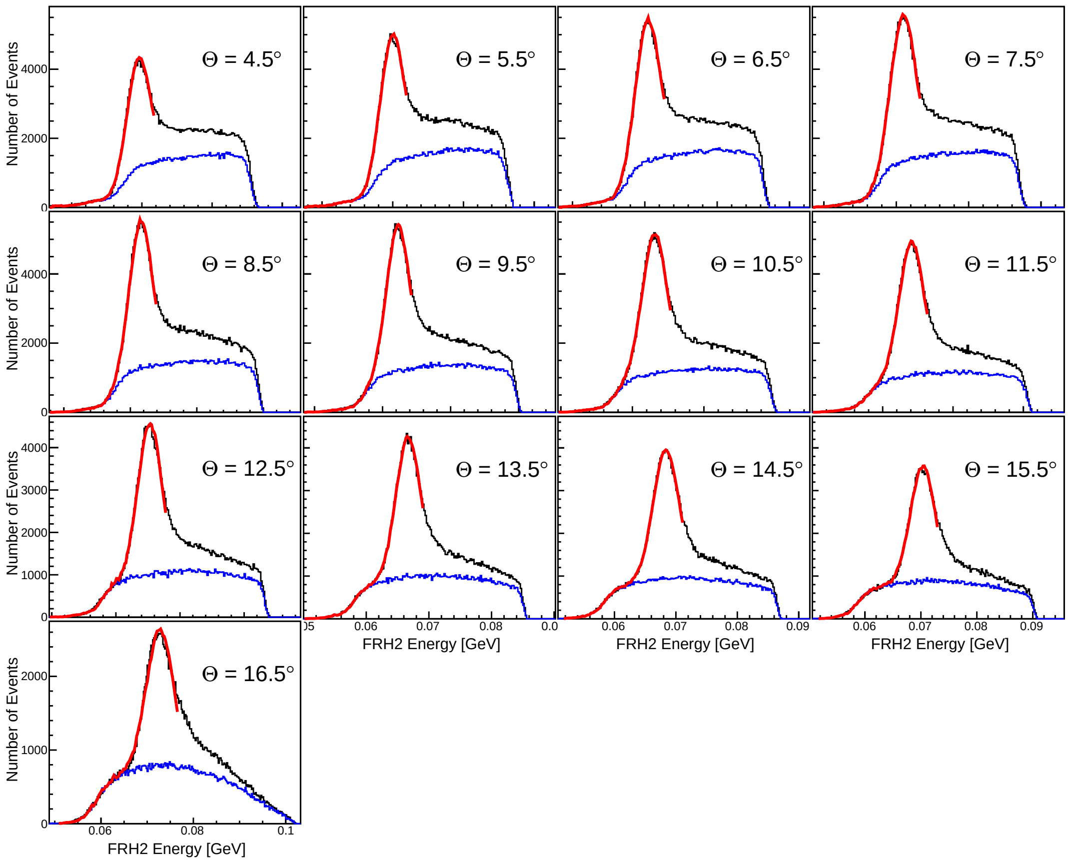


Figure 4.23: Fitting the proton contribution (template) from deuteron break-up for 270 MeV. The proton templates (blue) were measured from the pure carbon target and then fitted to the spectrum of the $CH_2$ target (black). The elastic recoil proton peak (red) was individually described by a Gaussian in each Θ-bin and fitted together with a common scaling factor for the template.

the whole energy spectrum. In the case of the recoil proton from the elastic deuteron proton scattering, its kinetic energy equals almost the kinetic energy of the incoming deuteron beam, especially for smaller scattering angles. The proton peak from elastic deuteron proton scattering is therefore located at the high-energy end of the proton band in a $\Delta E$ vs. $\Delta E$ spectrum. Looking at a punch-through spectrum, the elastic proton peak is located at the bottom left end of the proton band.

To disentangle the protons from break-up reactions from the recoil protons, the same box cut was first applied to the spectra of the pure carbon scattering. This resulted in a *template* describing the proton contribution from the carbon inside the $CH_2$ target. This template was matched to the spectra obtained after the box cut was applied to the $CH_2$ data. A fitting function was created that consisted of an individual Gaussian for the recoil protons in each Θ-bin and a common scaling factor that was applied to the template. Figure 4.23 shows the result of this combined fit for all Θ-bins of the 270 MeV data.

After the contribution from the deuteron break-up off carbon was determined, it was subtracted from the $CH_2$ data, resulting in proton spectra consisting of mainly recoil protons from elastic deuteron proton scattering and some background. The spectrum was described by a fit consisting of a Gaussian signal part and a polynomial background with an Erf-cutoff, see Figure 4.24a. This proton background cannot be shifted to larger kinetic energies as the recoil protons from the deuteron proton scattering. The fit to extract the recoil protons took this into account by restricting the background contribution to the low kinetic energy side of the spectrum. Because this fit was performed on punch-through spectra, the low kinetic energy part results in larger energy losses in this detector layer and is therefore located on the right side of the elastic peak. The number of recoil protons from the elastic deuteron proton scattering was obtained from the integral of the signal part of the fit divided by the bin width of the histogram, see Figure 4.24b.

The detector acceptance for the deuteron proton scattering was obtained exactly like the acceptance for the deuteron carbon scattering described in the previous section. The same cuts and fits as for the data were applied to the proton Monte-Carlo simulation and the result divided by the total number of generated protons led to the acceptance. Initially, it was assumed that the detector setting in WMC would be independent of the particle species, but it turned out that the simulated protons could not be brought into alignment with the data even though the simulation of deuterons was in good agreement with the measurements. Maria Żurek was able to solve this problem by manually adjusting the *quenching* parameter (they describe the relation between the deposited energy and the light yield of a scintillator) for the proton Monte-Carlo.

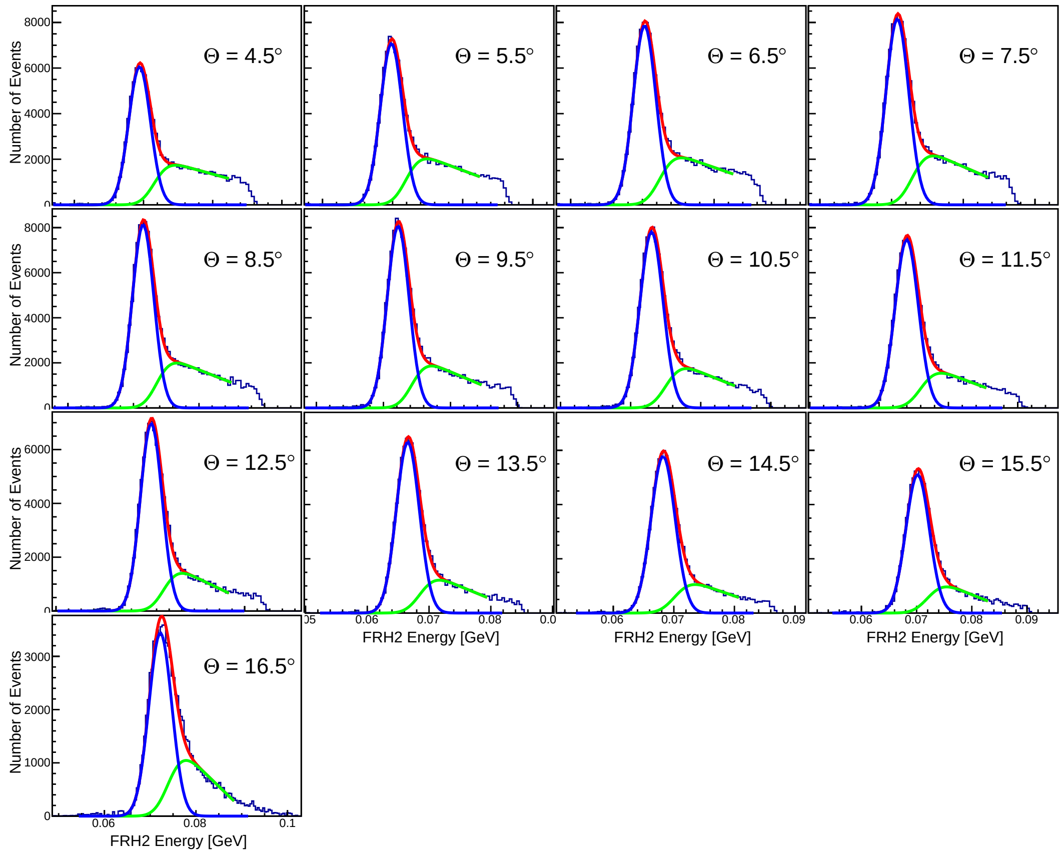


(a) Extraction of the elastically scattered recoil protons from the template subtracted spectra using a combined signal + background fit (red). The fits were performed for each Θ-bin individually. The integral of the signal part (blue) equals to the number of elastics. The background function is given in green.

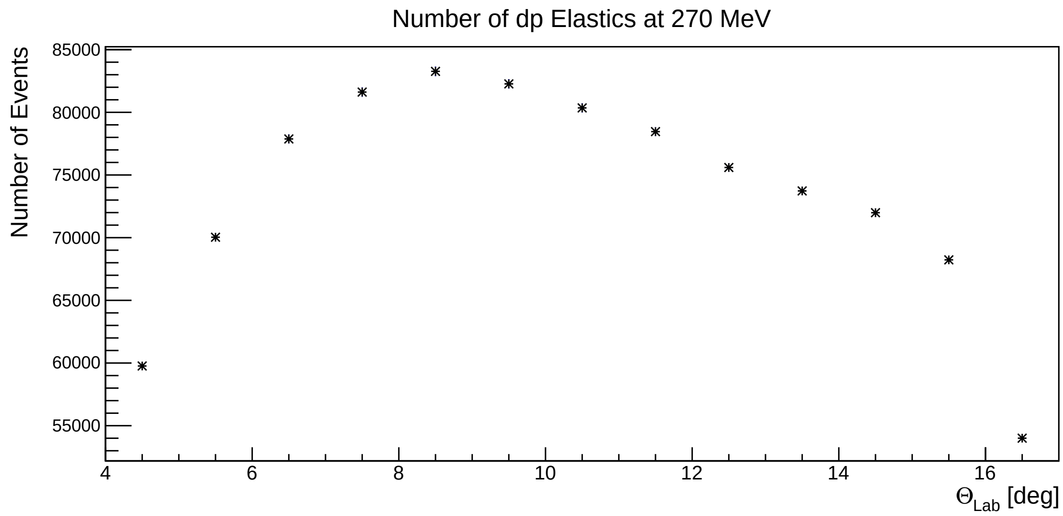


(b) Non acceptance corrected number of elastically scattered recoil protons as a function of the scattering angle Θ.

Figure 4.24: Example for the elastic proton extraction at a beam energy of 270 MeV.

#### 4.3.2.3 Scaling the Elastic Events Using Luminosity

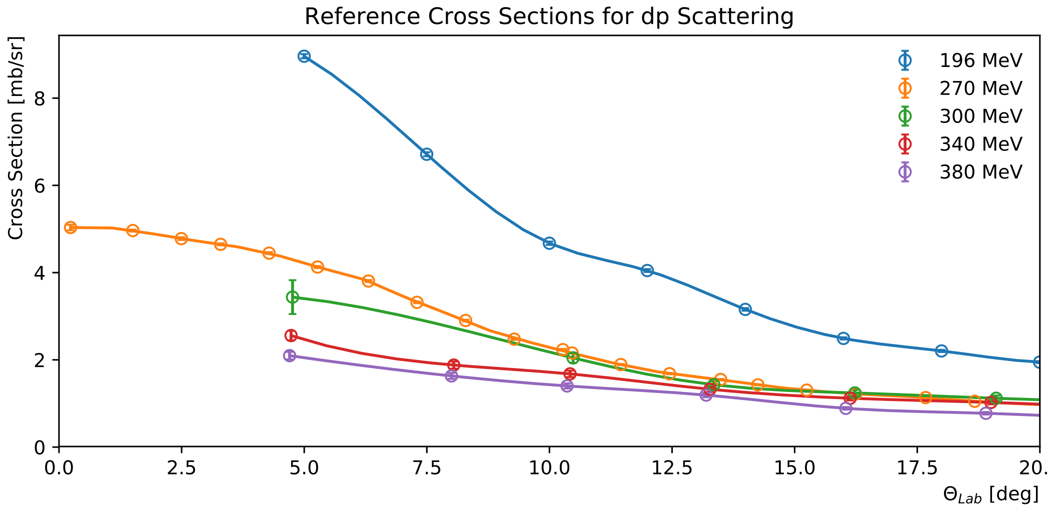


Figure 4.25: Elastic proton deuteron reference cross section boosted into the reference frame of the proton.

The integrated luminosity for the elastic deuteron proton scattering $\mathcal{L}_{dp}^{int}$ can be calculated if the elastic deuteron proton cross section $\sigma_{dp}$ is known:

$$\mathcal{L}_{dp}^{int} = \frac{N_p^{el}}{\alpha_{dp}\sigma_{dp}}, \tag{4.70}$$

where $\alpha_{dp}$ denotes the detector acceptance for deuteron proton scattering. $N_p^{el}$ equals to the number of recoil protons from the elastic deuteron hydrogen scattering calculated in the previous section. There exists reference data for elastic proton scattering off deuteron targets for 98 MeV by K. Hatanaka [26] and for 150 MeV, 170 MeV and 190 MeV by K. Ermisch [27]. These reference cross sections were transformed into the laboratory frame of deuteron scattering off protons. For 270 MeV, K. Sekiguchi et al. [28] have published a direct measurement for elastically scattered deuterons off protons. This means that reference cross sections for elastic deuteron proton scattering are available for the 200 MeV, 270 MeV, 300 MeV, 340 MeV, and 380 MeV data, see Figure 4.25. Using Equation 4.70, The integrated luminosity $\mathcal{L}_{dp}^{int}$ was calculated for these energies for each $\Theta$-bin of the extracted number of scattered recoil protons from the WASA data, see Figure 4.26. In the perfect case, the luminosity should be completely flat as it does not depend on the scattering angle $\Theta$, but unfortunately, this is not the case. Various sources of error might explain this: The recoil proton extraction method described above suffers from a large break-up proton background even though it was tried as good as possible to remove it using the carbon templates. The Monte-Carlo simulation used to calculate the acceptance is affected by the same issues as mentioned in Section 4.3.2.1. Finally, all the uncertainties in the reference data enter the calculation as well. To account for this uncertainties, the luminosity was calculated as the average over the available $\Theta$-range, and the standard deviation from this average enters the subsequent cross section calculations as a systematical error.

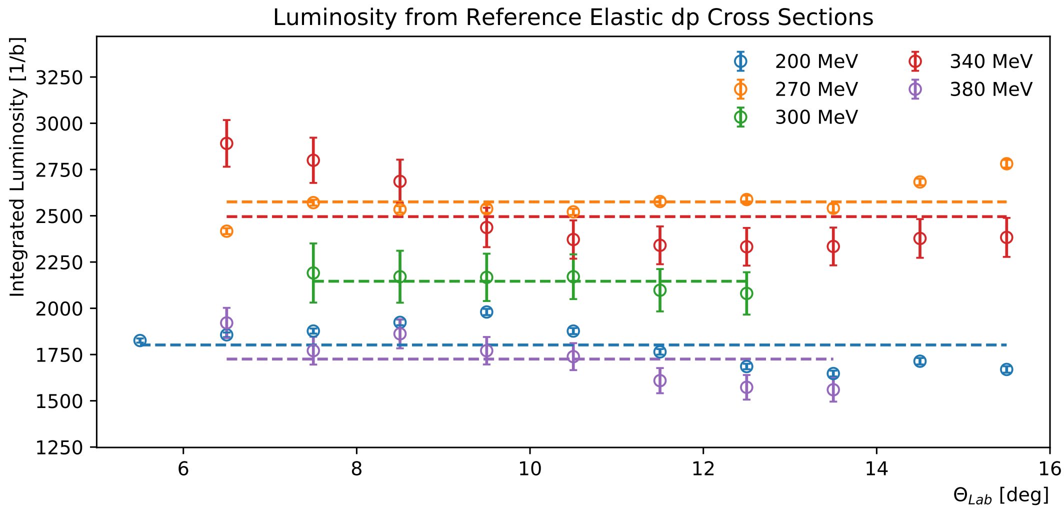


Figure 4.26: Integrated luminosity from the reference dp cross section. It was calculated in the Θ-range were the number of elastically scattered proton as well as the corresponding reference cross section was available. The average over the whole Θ-range is indicated by a dashed line.

The luminosity as a function of the flux $f$ is defined as follows:

$$\mathcal{L} = l \cdot \rho_N \cdot f, \tag{4.71}$$

with the length $l$ and the number density $\rho_N$ (i.e., the number of scattering centers per volume) of the target. The flux does not depend on the actual reaction and hence as the integrated luminosity is known for hydrogen from the data measured using the $CH_2$ target, it needs to be scaled to match the data measured with the pure carbon target. The integrated luminosity for the elastic deuteron carbon scattering is therefore given by:

$$\mathcal{L}_{dC}^{int} = \frac{1}{2} \frac{\mathcal{L}_{dp}^{int}}{\eta_{CH_2 \to C}}. \tag{4.72}$$

The factor $\frac{1}{2}$ scales the luminosity calculated for the scattering off hydrogen to the luminosity off carbon in $CH_2$, and $\eta_{CH_2 \to C}$ describes the scaling from the carbon in the $CH_2$ target to the pure carbon target. The latter factor was obtained by fitting the elastic deuteron peak from the $CH_2$ data to the elastic deuteron peak from the pure carbon data simultaneously in all Θ-bins. For the lower Θ-bins in the $CH_2$ data, the elastic deuteron peak off carbon is superimposed by the elastic deuteron peak off hydrogen and therefore these bins were skipped in the fit. The result is shown if Figure 4.27. Typical values for the scaling factor were found to be around $\eta_{CH_2 \to C} \approx 0.7$.

#### 4.3.2.4 Scaling the Elastic Events Using an Analytical Model

The method of scaling the acceptance-corrected number of events with the luminosity obtained from deuteron proton scattering could not be applied for 170 MeV and

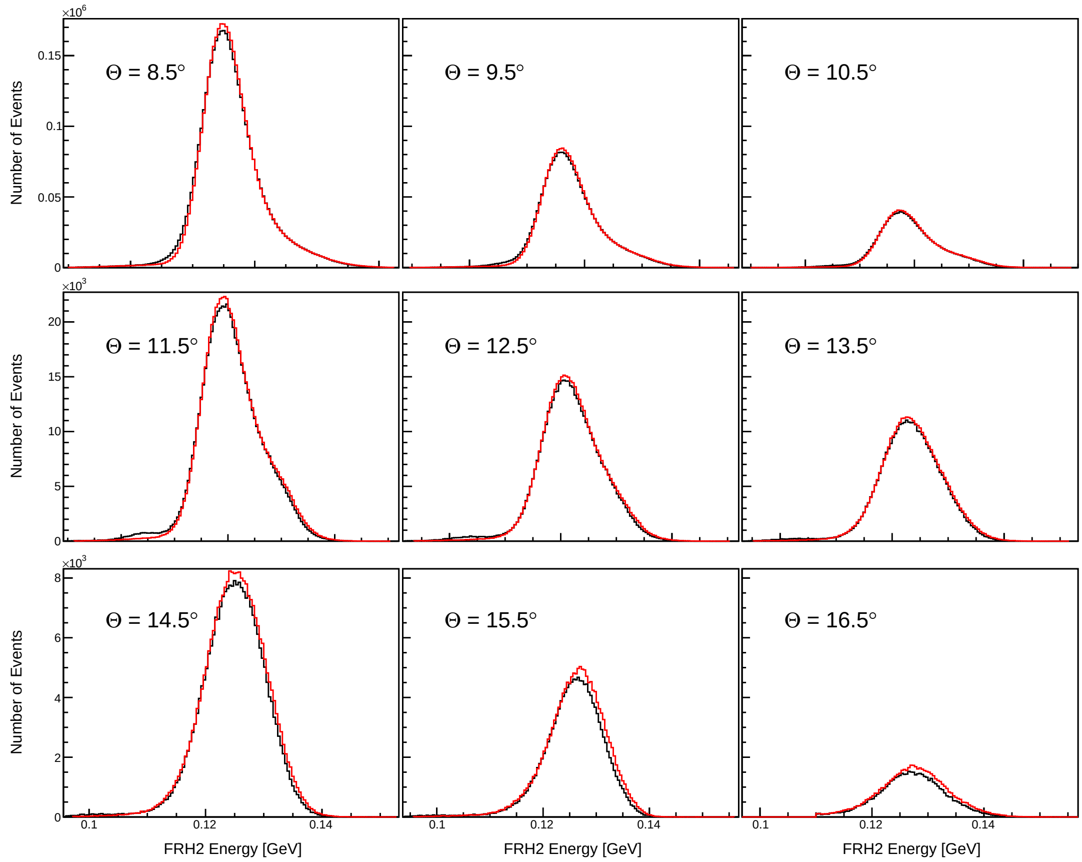


Figure 4.27: Fit to obtain the luminosity scaling factor for integrated luminosity for the pure carbon target data (red) from the $CH_2$ target data (black). The elastic deuteron peak off carbon from pure carbon data was fitted simultaneously in all Θ-bins to the elastic deuteron peak from the $CH_2$ data.

235 MeV. For 170 MeV, no reference cross section was available to extract the luminosity, and for 235 MeV, the recoil proton extraction was not possible as, for most of the Θ-bins, the protons were stopped in the dead material between two detector layers. For this reason, another method of normalizing the acceptance-corrected number of deuterons $N_d(\Theta)$ had to be employed to be able to calculate the cross section.

Edward Stephenson from the University of Indiana and member of the JEDI collaboration has developed an analytical model for the elastic deuteron carbon cross section based on measurements for beam energies from 45 MeV up to 270 MeV. The model describes the dependence of the elastic deuteron carbon cross section as a function of the scattering angle Θ and the beam energy. A detailed description of the model and its parameters can be found in Appendix A.5. The model is purely analytical in the sense that it does not attempt to add any physics to describe the cross sections but uses a phenomenological function that can be fitted to the data points resulting in a smooth representation of the Θ dependence of the cross section. Further, it can be used to interpolate elastic deuteron carbon cross sections for beam energies where no such data was measured. However, it is not suited to do an extrapolation to energies above 270 MeV because it is only anchored to point at lower energies which means that it can predict the cross section between measurements of different energies, but there is no argument to why it should produce reasonable results outside of its sampling range.

Both data points for 170 MeV as well as 235 MeV are located within the sampling range of the model, and therefore it can be used to obtain the normalization factor to get the elastic deuteron carbon cross section from $N_d(\Theta)$. The normalization resulted from fitting $N_d(\Theta)$ to the analytic model. As the cross section drops exponentially for larger scattering angle $\Theta$, a direct fit can cause problems. By just applying a fit to such a steep function it tends to overestimate the first points over the latter ones because the first values are by orders of magnitude larger than the latter ones. By calculating the $\chi^2$-sum for the fit, even small deviations from the first points generate a huge weight especially since the difference between points enters the $\chi^2$-sum quadratically. To reduce the steepness of the fit, $N_d(\Theta)$ was divided by the *Rutherford cross section* given by:

$$\left(\frac{d\sigma}{d\Omega}\right)_{Rf.} = \left(\frac{Z_1 Z_2 \alpha \hbar c}{4E_{kin}\sin^2(\frac{\Theta}{2})}\right)^2, \tag{4.73}$$

with the charge number $Z_1$ of the projectile and $Z_2$ of the target, respectively. $\alpha$ denotes the fine structure constant and $E_{kin}$ the non-relativistic kinetic energy of the projectile. The $\sin^{-4}(\frac{\Theta}{2})$-term flattens the model drastically and allows for the fit to be optimized over the whole $\Theta$-range. Figure 4.28 shows the Rutherford-normalized model and cross sections for all seven energies. For 170 MeV and 235 MeV, the result of the fit is shown and especially for 235 MeV, the accordance is very good. For 200 MeV and 270 MeV, it can be seen that normalizing the deuteron carbon cross section using the luminosity as described in the previous section produces a result that is in good agreement with the analytical model. For the energies above 270 MeV, it is obvious that extrapolating the model does not make sense as the result of the cross sections deviate the more from the model prediction the larger the distance in energy from the last anchor point gets.

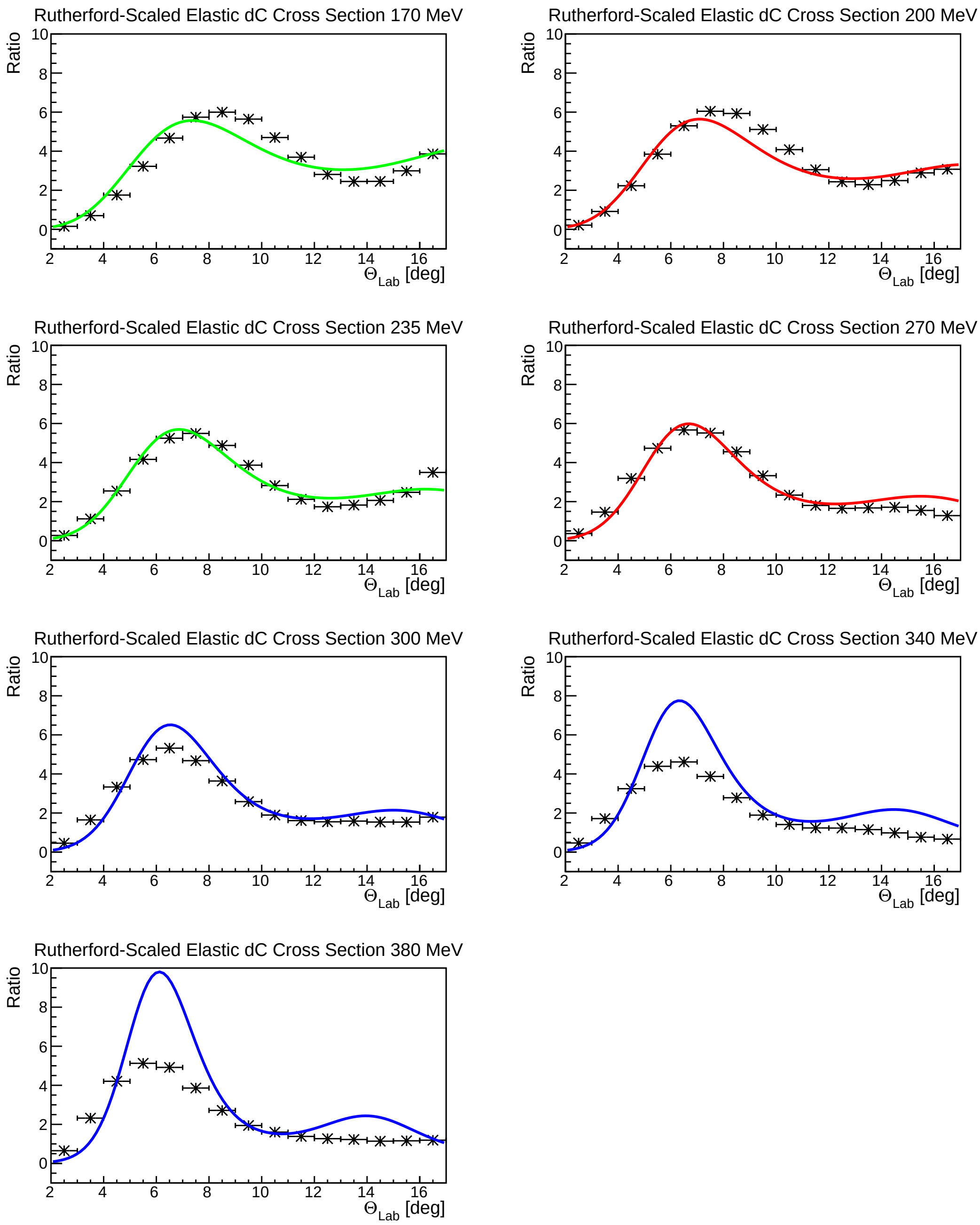


Figure 4.28: Fit to get the normalizing factor for 170 MeV and 235 MeV. The acceptance-corrected number of deuterons, as well as the analytical model, are scaled by the Rutherford cross section. The 170 MeV and 235 MeV data are fitted to the analytical model (green) to get the normalization factor to calculate the elastic deuteron carbon cross section for these energies. To judge the model, the cross sections obtained using the luminosity extraction method are given as well. For 200 MeV and 270 MeV, the cross sections are within the well-defined range of the model (red). For the energies above 270 MeV, the model needs to be extrapolated (blue) and it does not match the measured cross sections anymore.

#### 4.3.2.5 Unpolarized Differential Elastic Deuteron Carbon Cross Section

The unpolarized elastic deuteron carbon cross section was now calculated for all seven energies using the intermediate results from the previous sections. The aim was to obtain the differential elastic cross section as a function of the scattering angle $\Theta$ which means that as a final step, the solid angle coverage of each $\Theta$-bin had to be taken into account. As the WASA forward detector covers the full polar range in $\Phi$, the fraction of of solid angle $d\Omega$ represents a ring around the central $\Theta$-value for each bin and was calculated as follows:

$$\begin{aligned} d\Omega_n &= \int_0^{2\pi} \int_{\Theta_n - \frac{d\Theta}{2}}^{\Theta_n + \frac{d\Theta}{2}} \sin(\Theta) d\Theta d\Phi \\ &= 2\pi \left( \cos(\Theta_n - \frac{d\Theta}{2}) - \cos(\Theta_n + \frac{d\Theta}{2}) \right), \end{aligned} \tag{4.74}$$

where $n$ denotes the index of the $\Theta$-bin and $d\Theta$ its width.

The differential elastic deuteron carbon cross section was calculated using the following equation:

$$\left( \frac{d\sigma(E,\Theta)}{d\Omega} \right)_{dC}^{el.} = \frac{N_{dC}^{el}(E,\Theta)}{\alpha_{dC}(E,\Theta) \cdot \mathcal{L}_{dC}^{int}(E) \cdot d\Omega(\Theta)}, \tag{4.75}$$

with the number of elastically scattered deuterons $N_{dC}^{el}(E,\Theta)$, and the detector acceptance $\alpha_{dC}(E,\Theta)$ calculated as described in Section 4.3.2.1. The luminosity for 200 MeV, 270 MeV, 300 MeV, 340 MeV, and 380 MeV was calculated using the reference elastic deuteron proton scattering as described in Section 4.3.2.3, and for 170 MeV and 245 MeV, it was obtained from the fit to the analytical model described in Section 4.3.2.4. The result for all energies is given in Figure 4.29. The error bars on the points origin form the statistical uncertainties and the red shaded area describes the systematical uncertainties given by the mean of the deviation from the analytical model for 170 MeV and 235 MeV. For the other energies the systematics origin from the normalization by the luminosity.

Measuring a cross section is in general not an easy task as it is an absolute quantity. This means all its contributions have to be determined very precisely and the acceptance of the whole detector setup needs to be known. In comparison to the asymmetry measurement which is a relative quantity and by its nature can cancel many uncertainties directly, i.e., the detector acceptance. In the case of the database experiment, two main challenges made the cross section measurement especially difficult. First of all, the fact that the particle flux was not known. There exist other methods of experiments were each incoming particle can be tagged (labeled) and therefore the flux is precisely known. In the case of our experiment, such a measurement was not possible and methods depending on measurements of other people had to be used. This means that much less control over these references is possible. Secondly, the quality of the Monte-Carlo simulation tool is very hard to judge. For example, it is not entirely clear why the detector acceptance (see Figure 4.21) differ so much for different beam energies and does not follow a clear trend as a function of energy. Rewriting the WMC using the newer Geant4 simulation framework would definitely improve the situation here.

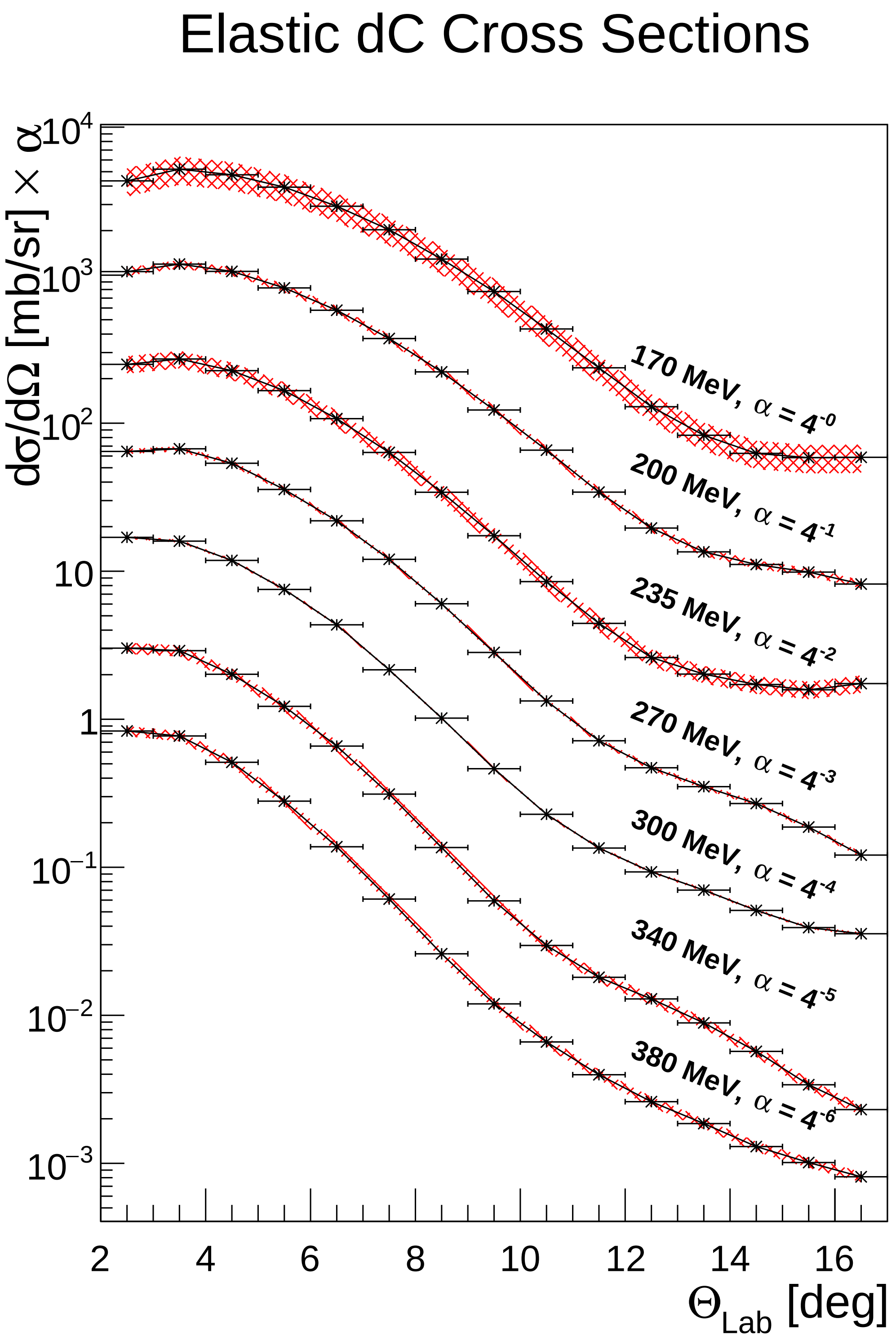


Figure 4.29: Differential elastic deuteron carbon cross section for all seven beam energies. For better readability, the results are subsequently scaled by a factor of four. The statistical uncertainties are smaller than the symbol size. The systematic error due to the luminosity or model normalization respectively is given by the red shaded area.

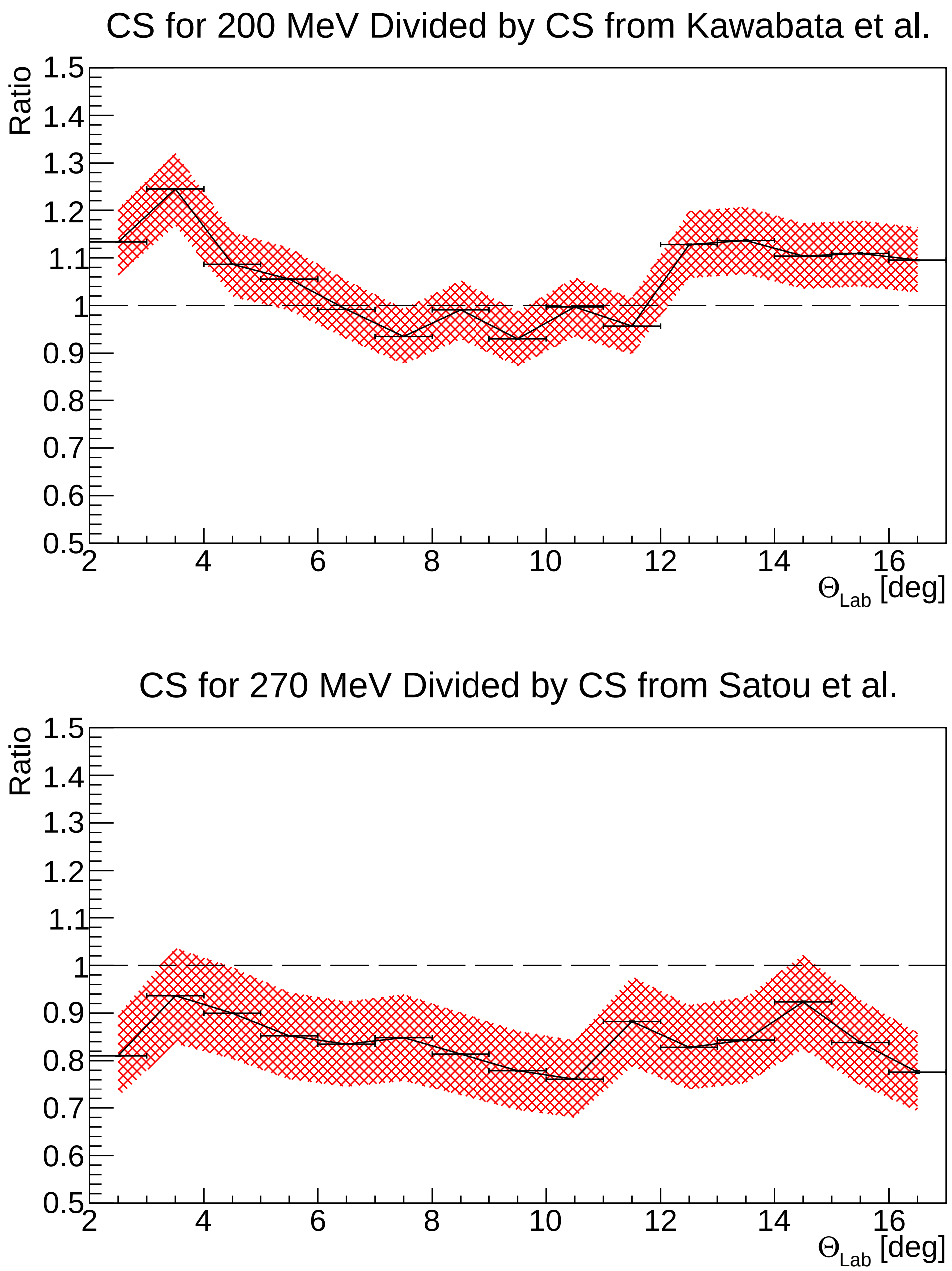


Figure 4.30: Ratio between the measured and the published elastic deuteron cross section for 200 MeV [23] and 270 MeV [22]. The red shaded area represents the systematic error. The systematic error for reference of 270 MeV was estimated to be $\sim 10\%$ in [22] and none was given for 200 MeV in [23]. The statistical uncertainty is too small to be visible.

To check the result, the ratio between the measured and the published elastic deuteron carbon cross section for 200 MeV [23] and 270 MeV [22] was calculated, see Figure 4.30. Assuming the published cross section to be correct, a flat line would indicate a perfect reproduction of the result by our measurement. This comparison reveals a rather flat behavior of the ratio over the whole $\Theta$-range and an overall agreement in the order of $\sim 15\%$. With the tools at our disposal, this seems to be an acceptable result.

### 4.3.3 Figure of Merit of the Polarization

The statistical error of the EDM scales with the statistical error of the vector polarization $\Delta P_y$, as described in [29]. The aim of a designated polarimeter is therefore to minimize this quantity. As shown in Section 4.3.1.5 it is convenient to define a Figure of Merit (FoM) as the inverse square of the error that should get minimized, hence a FoM for the vector polarization is defined as follows:

$$\mathrm{FoM}_{P_y} \equiv \frac{1}{(\Delta P_y)^2}. \tag{4.76}$$

For the vector polarization $P_y$, the underlying distribution function is given by Equation (4.4) which can be rewritten to:

$$n_{L,R}(\Theta, \Phi) = \alpha_{det}\mathcal{L}\left(\frac{d\sigma(\Theta)}{d\Omega}\right)\left(1 \pm \frac{3}{2}A_y(\Theta)P_y\cos(\Phi)\right), \tag{4.77}$$

where $n_{L,R}(\Theta, \Phi)$ denotes the number of scattered particles into an infinitesimal solid angle region defined by $(\Theta, \Phi)$ on the left or right side of the detector, respectively. In this case, $\Phi$ is restricted to $[-\frac{\pi}{2}, \frac{\pi}{2}]$ and the side of the detector is defined by the $\pm$ expression which is $(+)$ for the left side and $(-)$ for the left side, compare Figure 4.15. Equation (4.77) has the form of a differential event distribution:

$$n_{L,R} = \alpha(x)(1 \pm \beta(x)P_y), \tag{4.78}$$

with $x = (\Theta, \Phi)$, $\alpha(x) = \alpha_{det}\mathcal{L}\left(\frac{d\sigma(\Theta)}{d\Omega}\right)$ and $\beta(x) = \frac{3}{2}A_y(\Theta)\cos(\Phi)$. In [30] a detailed discussion about the error on a parameter $P_y$ from a differential event distribution is given. It is shown, that for an arbitrary weight $w$, the FoM as defined in Equation (4.76) for a total number of events $N$ is given by:

$$\mathrm{FoM}_{P_y} \approx \frac{\langle w\beta\rangle^2}{\langle w^2\rangle}N. \tag{4.79}$$

The expected values for an arbitrary function $f(x)$ is here defined to be

$$\langle f\rangle = \frac{\int_{\Delta\Omega(\Delta x)} f(x)\alpha(x)d\Omega}{\int_{\Delta\Omega(\Delta x)} \alpha(x)d\Omega} = \frac{\int_{\Delta\Omega(\Delta\Theta,\Delta\Phi)} f(\Theta,\Phi)\left(\frac{d\sigma(\Theta)}{d\Omega}\right)d\Omega}{\int_{\Delta\Omega(\Delta\Theta,\Delta\Phi)}\left(\frac{d\sigma(\Theta)}{d\Omega}\right)d\Omega}. \tag{4.80}$$

Choosing a weight of $w = 1$ equals to the simplest method of calculating the vector polarization based on the counting rate asymmetry with the following estimator $\hat{P}_{cnt}$:

$$\hat{P}_{cnt} = \frac{N_L - N_R}{\sum_i^{ev(L)}\beta_i + \sum_i^{ev(R)}\beta_i}, \tag{4.81}$$

with $\beta_i = \beta(x_i)$, $N_L = \sum_i^{ev(L)}$ the sum of events recorded in the left side, and $N_R = \sum_i^{ev(R)}$ in the right side of the detector. This method results in a FoM of:

$$\mathrm{FoM}_{P_y}^{w=1} \approx \langle\beta\rangle^2 N, \tag{4.82}$$

with $N = N_L + N_R$. In [30] it is shown that the statistical limit on the error can be reached by choosing a weight of $w = \beta$, i.e., weighing each event by the corresponding vector analyzing power. The estimator for the vector polarization $\hat{P}_\beta$ of this method is found to be:

$$\hat{P}_\beta = \frac{\sum_i^{ev(L)} \beta_i - \sum_i^{ev(R)} \beta_i}{\sum_i^{ev(L)} \beta_i^2 + \sum_i^{ev(R)} \beta_i^2}, \tag{4.83}$$

with a FoM of:

$$\mathrm{FoM}_{P_y}^{w=\beta} \approx \langle\beta^2\rangle N. \tag{4.84}$$

Similar to the calculation of the asymmetries described in Section 4.3.1.3, choosing an integration range $\Delta\Theta$ where the vector analyzing power $A_y$ is low in order to calculate the vector polarization $P_y$ can result in a larger statistical error for the simple counting rate method (Equation (4.81)) compared to the one obtained by choosing the right weight (Equation (4.84)). The explanation is again that by simply counting, events carrying little information about the polarization (low $A_y$) are treated equally to events with a high information content (big $A_y$). This leads to a dilution of the measurement even if the total number of events increases. By applying a weight that is proportional to the information content about the polarization (i.e., $w \sim A_y$), the statistical error gets minimized.

It is important to note that in the previous discussion, the vector polarization was calculated from the difference in the left and the right side of the detector assuming a stable polarization. Alike the asymmetries, the vector polarization can be calculated using only one side of the detector but having two data samples; one measured with a downwards polarized beam (↓) and the second sample of an upwards polarized beam (↑) of the same polarization magnitude. In this case, all the observable with the label (L,R) would be replaced with the corresponding polarization states (↓,↑) (e.g. $N_L \rightarrow N^{\downarrow}$).

Defining the FoM as done in Equation (4.76) has the advantage that when combining multiple sets of vector polarization measurements, their FoMs can be directly summed up. If on the other hand, a comparison between the FoMs of different energies has to be done, it is more convenient to define a Figure of Merit as follows:

$$\mathrm{FoM}_{P_y} = \frac{\langle w\beta\rangle^2}{\langle w^2\rangle}\sigma \sim \frac{1}{(\Delta P_y)^2}. \tag{4.85}$$

Maximizing for this FoM still results in minimizing the statistical error of the vector polarization $\Delta P_y$ but using the integrated cross section $\sigma$ instead of the total number of events $N$, accounts for the difference in luminosity at different beam energies. By employing the definition of the integrated cross section to be:

$$\sigma = \int\limits_{\Delta\Omega(\Delta\Theta,\Delta\Phi)} \left(\frac{d\sigma(\Theta)}{d\Omega}\right) d\Omega = \int\limits_{\Delta\Theta}\int\limits_{\Delta\Phi} \left(\frac{d\sigma(\Theta)}{d\Omega}\right) \sin(\Theta) d\Phi d\Theta, \tag{4.86}$$

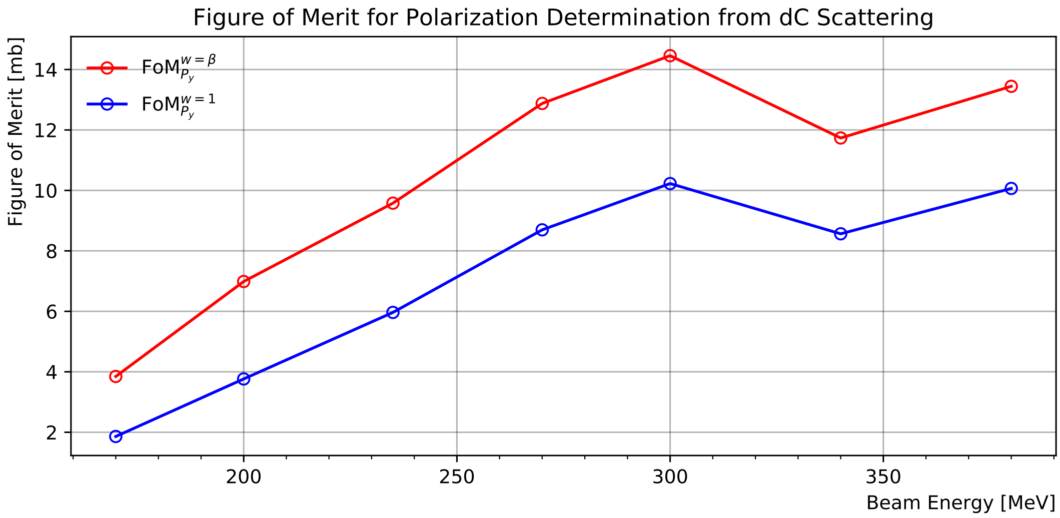


Figure 4.31: FoM for all seven beam energies for a $\Theta$-range from $3.5°$ to $15.5°$ using the simple counting method (blue) and the weighting method (red) to calculate the deuteron vector polarization.

and using the full azimuthal detector coverage $\Delta\Phi = 2\pi$, Equation (4.82) for the simple counting method can be expressed as a function of the polar integration range $\Delta\Theta$ to be:

$$\mathrm{FoM}_{P_y}^{w=1}(\Delta\Theta) = \frac{18}{\pi} \cdot \frac{\left[\int_{\Delta\Theta} A_y(\Theta)\sin(\Theta)\left(\frac{d\sigma(\Theta)}{d\Omega}\right) d\Theta\right]^2}{\int_{\Delta\Theta} \sin(\Theta)\left(\frac{d\sigma(\Theta)}{d\Omega}\right) d\Theta}. \tag{4.87}$$

Equation (4.84) describing the weighing method can be rewritten to be:

$$\mathrm{FoM}_{P_y}^{w=\beta}(\Delta\Theta) = \frac{9\pi}{4} \cdot \int_{\Delta\Theta} A_y(\Theta)^2 \sin(\Theta)\left(\frac{d\sigma(\Theta)}{d\Omega}\right) d\Theta. \tag{4.88}$$

Using the vector analyzing power $A_y$ from Section 4.3.1 and the unpolarized elastic cross section $\left(\frac{d\sigma(\Theta)}{d\Omega}\right)$ from Section 4.3.2, The Figure of Merit for the deuteron vector polarization can be calculated using the two formulas given in Equation (4.87) and (4.88). Figure 4.31 shows this calculation for a polar range of $\Delta\Theta = [3.5°, 15.5°]$ for all seven beam energies. It can be seen that using the weighting method to extract the vector polarization lead to a larger FoM for all seven energies and hence a to a smaller statistical error $\Delta P_y$. The maximum FoM was found at a deuteron beam energy of 300 MeV, see Figure 4.32. The lower limit of the integration range is fixed to $3.5°$ and cannot be reduced further due to the geometry of the WASA detector. With another detector geometry, it would be possible to measure at even lower angles, but as can be seen in Figure 4.19, the vector analyzing power for these small angles is very low, and therefore it does not make sense to include them in the measurement.

To decide for the ideal configuration of a polarimeter for a given beam energy or selecting the ideal beam energy for a polarimeter with a given geometry, a map of the FoM for the weighting method as a function of the beam energy and the integration range is given in Figure 4.33. The beam energy is given on the $y$-axis and the start of

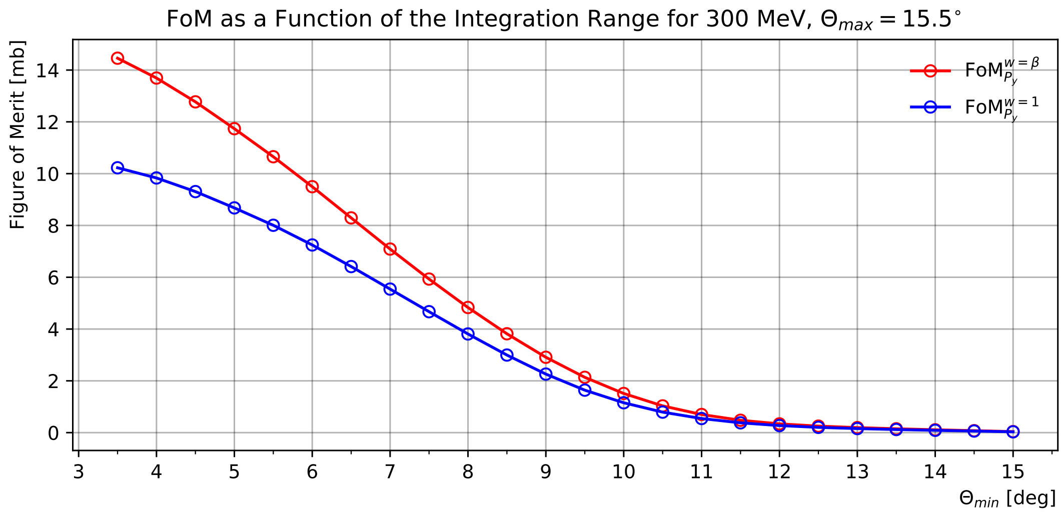


Figure 4.32: FoM for the optimum beam energy of 300 MeV as function of the polar integration range. The upper limit for this range was fixed to 15.5° and the lower limit is given on the X-axis of the plot. The simple counting method is given in blue and the weighting method in red.

the integration range on the $x$-axis starting from 3.5°. The end of the integration range is fixed to 15.5°. Figure 4.31 represents a cut of this map along the $y$-axis at $x = 3.5°$. For a given combination of integration range and beam energy, the corresponding FoM can be found on this map.

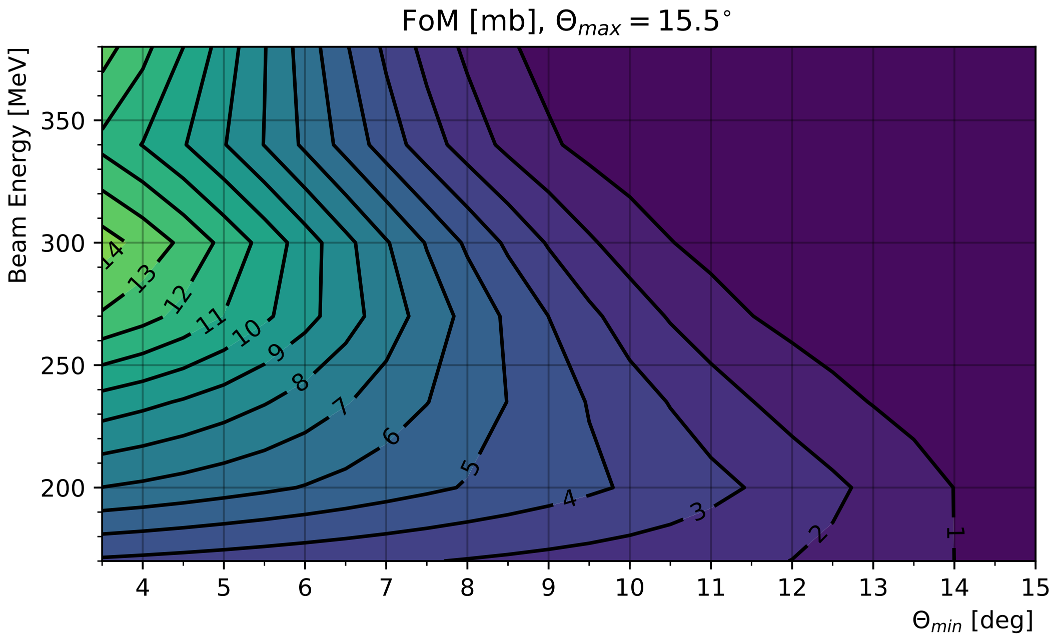


Figure 4.33: FoM as a function of the beam energy and the start of the $\Theta$ integration range. The end of the integration range is set to $15.5°$. The FoM was calculated for the optimal weighting method of extracting the deuteron vector polarization.

### 4.3.4 Polarimeter Efficiency Factor

The statistical uncertainty for a storage ring based EDM measurement of charged particles such as deuterons or protons was found to be [29]:

$$\sigma_{EDM} \approx \frac{2\hbar}{PE\tau A\sqrt{Nf}}, \tag{4.89}$$

with the polarization $P$, the electric field $E$, a spin coherence time $\tau$, the analyzing power $A$, the number of particles in the storage ring $N$, and the polarimeter efficiency factor $f$. Note that Equation (4.89) describes the statistical error for one measurement cycle, i.e., one fill of the storage ring with $N$ particles, horizontally polarized to a degree of $P$ which can keep their spin rotations synchronized for the time $\tau$. During this period, the electric field $E$ will couple to the EDM of the particles and cause a vertical polarization build-up. The particles will be successively extracted on a target that scatters them elastically and their vertical polarization will be calculated using the analyzing power $A$.

The statistical uncertainty given in Equation (4.89) can be related to the Figure of Merit discussed in the previous section and, therefore, to the statistical error of the polarization using Equation (4.76):

$$\sigma_{EDM} \approx \frac{2\hbar}{PE\tau} \cdot \Delta P \quad \text{with} \quad \Delta P = \frac{1}{A\sqrt{N_{el.}}}. \tag{4.90}$$

In this case, $\Delta P$ denotes the statistical uncertainty of the polarization calculation using the simple counting method. This leads to a definition for the polarimeter efficiency factor:

$$f = \frac{N_{el}}{N}. \tag{4.91}$$

The polarimeter efficiency factor $f$ described the fraction of the total beam that can be used for the polarization determination using an elastic scattering reaction. It is possible to approximate this factor from the total elastic cross section for a given detector geometry (assuming 100 % detection efficiency):

$$\begin{aligned} \sigma_{el} = \frac{N_{el}}{\mathcal{L}} \quad &\Leftrightarrow \quad N_{el} = \sigma_{el}\mathcal{L} = N l \rho \sigma_{el} \\ &\Rightarrow \\ f = \frac{N_{el}}{N} &= l\rho\sigma_{el}. \end{aligned} \tag{4.92}$$

Here, $l$ denotes the target length and $\rho$ the target number density, i.e., the number of scattering centers per unit volume. The detector geometry enters this formula via the total elastic cross section $\sigma_{el}$ , see Equation (4.86). For a detector such as WASA which features full azimuthal coverage, it is given by:

$$\sigma_{el} = 2\pi \int_{\Theta_{min}}^{\Theta_{max}} \left( \frac{d\sigma_{el}(\Theta)}{d\Omega} \right) \sin(\Theta) d\Theta. \tag{4.93}$$

To give an estimate for the values that polarimeter efficiency factor can take, a target length of 1 cm is assumed. The mass density of amorphous carbon is $\sim 2\,\mathrm{g/cm^3}$ [31] which equals a number density of $\rho = 1.003 \times 10^{23}\,\mathrm{cm^{-3}}$. Figure 4.34 shows the polarimeter efficiency factor $f$ for a 270 MeV deuteron beam scattering off a carbon target as a function of the polar coverage of a detector with full azimuthal coverage like WASA. Figure 4.35 displays the polarimeter efficiency factor of the WASA detector (i.e., $\Theta = 3.5° - 15.5°$) for the seven deuteron beam energies used in the database experiment. The differential cross section used to calculate the polarimeter efficiency factor was taken from Section 4.3.2.5.

It is tempting to assume, that the efficiency of the polarimeter could be increased by increasing the target length $l$ as, according to Equation (4.92), the efficiency scales with the target length. This is not possible as this formula assumes a thin target, i.e., the energy loss in the target has to be negligible. A longer target would also increase the probability of multiple scattering and consequently break the basic assumptions that the polarization can be extracted by the use of an asymmetry method and the knowledge of the analyzing power. Extending the detector coverage towards lower polar angles is not useful either, as the analyzing power approaches zero in this range and the cross section will be dominated by Coulomb scattering that cannot be used to determine the polarization.

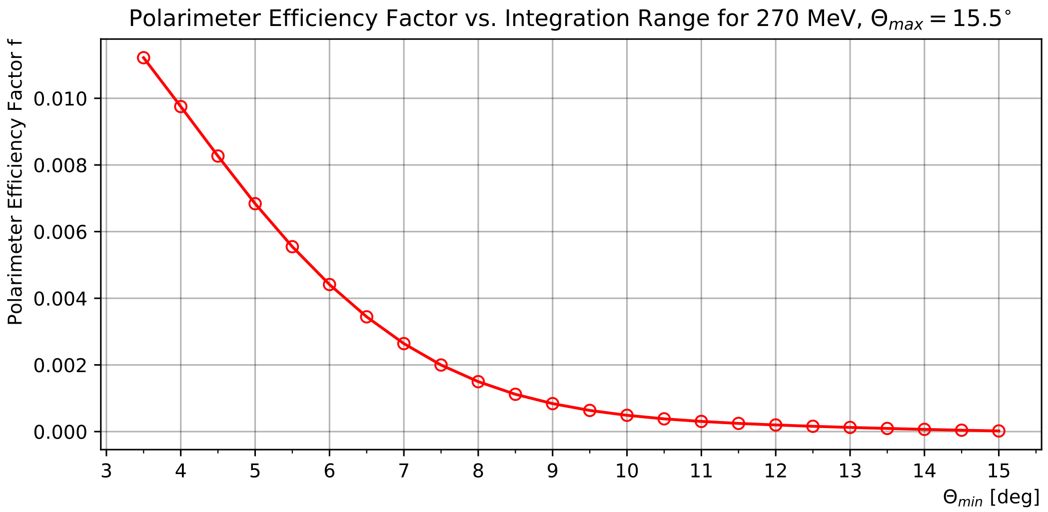


Figure 4.34: Polarimeter efficiency factor for 270 MeV deuteron beam as a function of the polar coverage of the detector.

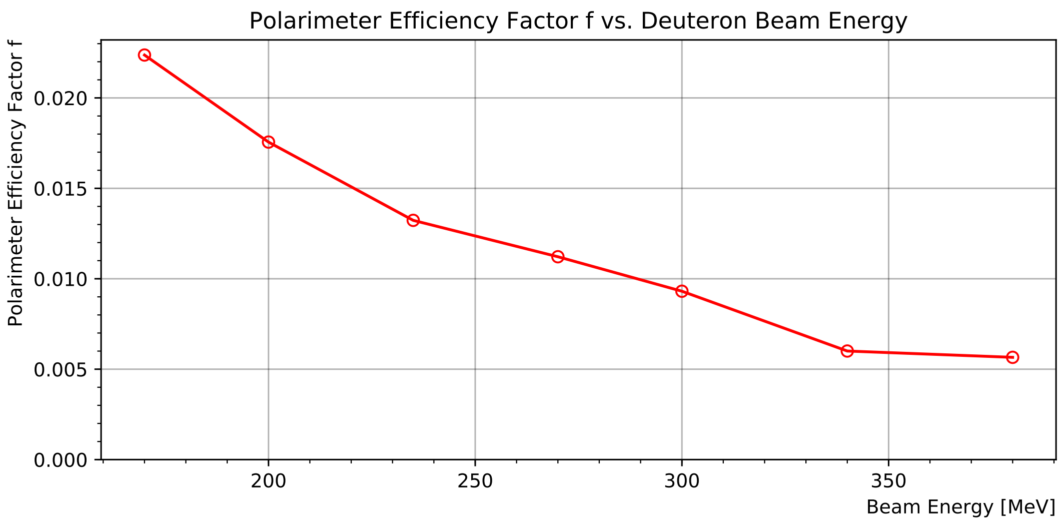


Figure 4.35: Polarimeter efficiency factor as a function of the deuteron beam for a polar coverage of 3.5° to 15.5°.

# Chapter 5

# LYSO Module Development

## 5.1 LYSO Modules

This section will describe the concept and design of the LYSO detector modules developed to be used in the designated polarimeter for the future EDM investigation. Additionally an introduction into inorganic scintillators will be given and the properties of LYSO will be discussed. Since ***S**ilicon **P**hoton **M**ultiplierers* (SiPMs) are used in the final version of the modules, an overview over this photon detector technology will be provided.

### 5.1.1 LYSO Scintillator Material

LYSO ($Lu_{1.8}Y_{0.2}SiO_5 : Ce$) is a Cerium-doped Lutetium based scintillation crystal and therefore belongs to the family of inorganic scintillators. This type of scintillator is built from a crystalline complex and hence forms a band structure in the energy-momentum-space. An ionizing particle striking this crystal can excite an electron from the valence band into the conduction band and, consequently, a hole is left in the valence band. It takes around three times the energy of the band gap to create one electron-hole

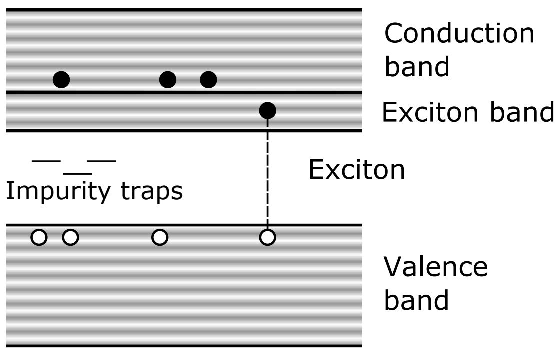


Figure 5.1: Band structure of an inorganic scintillator crystal in the energy-momentum-space. Ionizing particles produce free electrons and free holes which can recombine using the intermediate energy states in the band gap (traps) that are produced by impurities in the crystal lattice. Slightly bound electron-hole pairs called excitons can be formed as well. Since they move as pairs, the recombination occurs faster.

pair [32]. In general, the electrons and holes can move freely in their corresponding bands. If a recombination (i.e., the electron jumps back into the valence band) occurs, a photon is emitted from the scintillator. This mechanism (scintillation) converts the deposited particle energy into light. The photons that are generated by a direct de-excitation from the conductive into the valence band are usually in the ultraviolet spectrum. However, an electron and a hole can only recombine if their individual momentum vectors sum up to zero (momentum conservation). In a pure crystal this could lead to a recombination half-life that renders the scintillator unusable for high rates. To overcome this issue, impurities or dopants are added to the crystal. They add intermediate energy levels in the band gap between the valence and conduction band. These *trap states* can capture a hole from the valence band and keep it until an electron with a matching momentum vector can be trapped and form a neutral but excited state [32]. The de-excitation of this state will produce photons that are, if the dopant material is chosen correctly, in the visible spectrum and can be detected by a photon detector. The most important consequence of this effect is that the absorption and emission spectrum of the scintillator will not overlap and it is therefore transparent for its own scintillation light. Sometimes an electron can be excited into the so-called exciton band where it forms a slight bound system together with the hole which is referred to as an exciton (See Figure (5.1)). If an exciton gets caught by an impurity trap, it can recombine instantaneously which decreases the over-all decay constant of an inorganic crystal even further. Inorganic scintillator are in general still slow compared to organic scintillators such as plastics. A typical plastic scintillator like the NE 104 has a decay constant of 1.9 ns compared to 230 ns for a NaI(Tl) crystal [31].

The main advantages of inorganic scintillator over other type of scintillators such as organic plastics, gaseous, liquids or glasses are the greater stopping power due to the high density of the crystal and the largest light output among all the scintillator types. Unfortunately most of the older types of inorganic scintillator crystal like NaI, CsF, LiI(Eu) and KI(Tl) are hygroscopic and must therefore be carefully enclosed to protect them from the moisture of the air. Other (newer) crystals such as BGO, $BaF_2$ as well as LYSO don't suffer from this problem and can be handled with more ease.

Naturally occurring lutetium is composed by 97.41% from the stable isotope $^{175}_{71}$Lu and by 2.59 % from the isotope $^{176}_{71}$Lu [33]. The latter is a long-lived radioisotope witch undergoes a $\beta^-$-decay with a half-life of $37.6 \times 10^9$ y into $^{176}_{72}$Hf [34]. This decays are visible in the low energy spectra of the LYSO crystals (see Figure 5.22) but since the endpoint energy of the electron from the $\beta$-decay is 1193 keV, this background does not interfere with measurements of deuterons in the hundreds of MeV range.

LYSO is a rather new (patented 2003, see [35]) non-hygroscopic inorganic single crystal scintillator with outstanding properties such as short decay constant, high density, high light yield and a spectral response which matches the sensitivity curve of PMTs with bialkali photocathodes, as well as SiPMs. Further, it is a very radiation hard material. Irradiation test on LYSO samples using gamma radiation doses up to 10 kGy found to cause light output losses at the level of 12% which is considerably less than for other crystal scintillators used in high energy physics. Further is was shown that 300 °C thermal annealing recovers the radiation induced losses. This recovery takes place

| | |
|---|---|
| Density | 7.1 g/cm |
| Wavelength of emission (max) | 420 nm |
| Refractive index @ max emission | 1.81 |
| Decay time | 36 ns |
| Light yield | 33 200 photons/MeV |

Table 5.1: Properties of LYSO crystals from Saint-Gobain [37].

even at room temperature but significantly slower [36]. The properties of the LYSO crystals produced by Saint-Gobain are listed in Table 5.1. All these features make the LYSO scintillator crystal an ideal choice to build compact detector modules as will be described Section 5.1.3.

### 5.1.2 Silicon Photon Multipliers

The foundation of all silicon-based semiconductor photon detectors is the photo-diode. A photo-diode or PIN-diode is built on a silicon wafer that is doped positively on one side (p-layer) and negatively on the other one (n-layer). The center (intrinsic) layer is not or only slightly doped. Contrary to the regular operation principle of a diode, the PIN-diode is reverse biased which creates an electric field in the intrinsic layer. If a photon penetrates the diode through the thin top p-layer and deposits its energy in the intrinsic layer, electron-hole pairs are created. These pairs travel to the opposing poles of the diode along the electric field lines and therefore generates a current that is proportional to the energy of the photon.

An advancement of the PIN-diode is the ***A****valanche* ***P****hoto-***D****iode* (APD). This type of photo-diode is composed of a strongly doped positive layer ($p^+$-layer) on the top side and a strongly doped negative layer ($n^+$-layer) on the opposing side. Just in front of the $n^+$-layer less strongly positive layer (p-layer) is located. The intrinsic layer is sandwiched between the $p^+$-layer and the p-layer. Under reverse bias, this configuration creates a small electric field gradient in the intrinsic layer (drift region) and a strong field gradient between the p-layer and the $n^+$-layer (avalanche region) (See Figure 5.2). As in the PIN-diode, the penetrating photon creates electron-hole pairs in the drift region. The electrons drift along the electric field gradient towards the avalanche region. Due to the high field gradients in this region, the electrons get accelerated until they gain enough energy to create secondary electron-hole pairs which again get accelerated and produce even more electron-hole pairs. This results in an avalanche of charges, and the resulting current is substantially larger compared to a simple PIN-diode. The gain in signal strength of an APD can be hundreds of times larger compared to a PIN-diode [32]. The actual value of the gain is proportional to the reverse voltage applied to the APD. In allusion to gas detectors, the gain is divided into two ranges. In the proportional gain range, the signal produced by the APD is proportional to the number of photons while in the *Geiger-mode* each photon creates the maximal possible current through the diode independent on its energy. In this mode, the current flow remains once triggered by a photon. Therefore a so-called

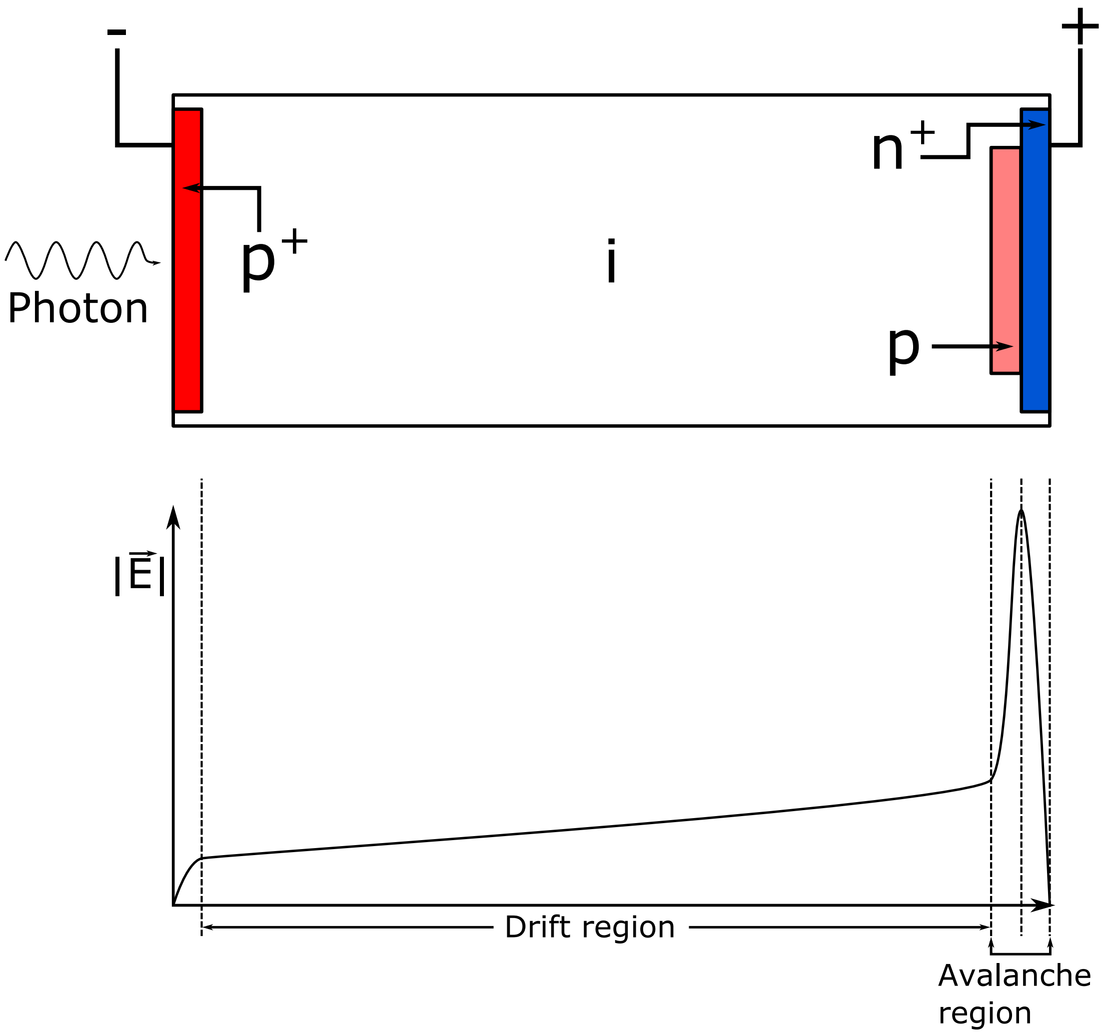


Figure 5.2: Schematic illustration of an APD. Upper figure: Cross section to display the different layers. Lower figure: Electric field inside of the diode.

quenching resistor needs to be added in series with the APD. The current flow through this resistor induces a voltage drop in the reverse bias voltage that subsequently reduces the internal field gradients in the APD which stops the avalanche effect and resets the APD back into an operational state. Since the quantum efficiency of an APD is quite large (around 80% [32]) it makes for an excellent photon detector.

SiPMs consists of a two-dimensional array of tiny cells of APDs (down to 15 µm edge length, see [38]), referred to as microcells. The anodes and cathodes of the individual APDs are connected in parallel, and each APD has a quenching resistor in connected series. The reverse bias voltage applied to the APDs set them into Geiger-mode. In this configuration, each photon that hits a microcell causes it to go into the full current breakdown. The signal from a SiPM is composed of the sum of the signals from each microcell and is therefore proportional to the number of triggered cells and subsequently to the number of registered photons. The number of photons created in a LYSO crystal is proportional to the deposited energy, hence a LYSO scintillator optically coupled to a SiPM creates an assembly that produces a signal that is linearly dependent on the amount of deposited energy within the crystal. The signal created by a SiPM is a current that can be transformed into a voltage signal by adding a resistor in series with the SiPMs, see Figure 5.4b.

In the development of the LYSO modules, different types of SiPMs were used: Two versions from the SensL company and two versions from Ketek. Table B.1 shows the specifications of the different types of SiPMs that were used. All of the SiPMs used in the LYSO based detector module development have in common that they are composed of 8x8 array SiPMs each with an area of 3 mm x 3 mm.

### 5.1.3 LYSO Module Description

The LYSO detector modules were designed with the following criteria in mind:

- Simplicity of the detector modules:
  → The fewer components used to build the modules, the less error-prone are they. Following the same argument, a single detector layer design was chosen as it simplifies the data analysis if the whole energy information is obtained from one single layer.

- Interchangeability:
  → The modules should be exchanged easily in case one fails. This also means that there should be only one type of module in the final polarimeter assembly.

- High resolution:
  → Since the primary purpose of a polarimeter is to identify elastically scattered particle and count them, a high resolution helps to distinguish between elastics and other particles. For the same reason, it was decided against using an absorber in front of the module which would allow using a shorter scintillator but would worsen the resolution.

- Long term stability:
  → As this polarimeter is intended to measure the polarization in a high precision long-running experiment, it is crucial that its performance will not change over time. Therefore LYSO was chosen as a scintillator. It offers excellent radiation hardness and its temperature dependent loss in light yield of 0.28 % $^{\circ}C^{-1}$ in the range of 25 °C to 50 °C is small [37].

- Simplicity of the whole detector setup:
  → In order to keep the whole detector assembly and data acquisition (DAQ) system at a minimum, care was taken that no signal amplifiers were needed between the photon detector and the analog-to-digital converters (ADC) as they were a possible source of noise and non-linearity. Further SiPMs were finally favored over PMTs as the latter would require an individual high-voltage source for each module.

In the process of developing the modules, two different versions were investigated. The first version (see Figure 5.3) was using the dual channel photomultiplier tube

(PMT) R1548-07 from Hamamatsu [39]. To fulfill the interchangeability criterion, it was decided that the module must have a square shaped front face. The R1548-07 tube was ideal for that purpose as its photo-cathode is squared with an edge size of 24 mm which fitted nicely on the first batch of LYSO crystal which had the dimensions of 30 mm x 30 mm x 100 mm. The PMT's photo-cathode was fixed to a 24 mm x 24 mm x 48 mm light guide using a special optical glue. The high voltage divider circuit board for the base of the PMT was designed by Tanja Hahnraths - von der Gracht from the electronic workshop of IKP. The R1548-07 tube provides two channels as the photo-cathode is divided along the center line and it needs a high voltage of 1250 V to operate. The light guide, PMT and the high voltage divider were inserted into a steel tube with the appropriate square cross section and a total length of 185 mm. To avoid any internal reflections, this tube was spray-painted with a dull black color. The high voltage divider was mounted in a 3D-printed designated holder to prevent short connections to the steel tube.

The whole module is held together by a spring-loaded tension device in the 3D-printed end cap of the module. This notched end cap sits on the end of the steel tube, and two wave springs are mounted on either side of it. A hollow nylon screw extends the end cap. It serves as a mounting point of the whole module, a guide for the outer spring and allows the signal and high voltage cables to be lead out of the module. The inner spring pushes on the high voltage divider PCB which in turn presses on the base of the PMT. This mechanism assures a tight fit of the light guide on the LYSO crystal. The outer spring applies a force on a frustum of a pyramid onto which two perpendicular loops of Kapton strips are glued. These two loops revolve around the steel tube and the LYSO crystal and press them together firmly. An additional cap tightened by a nylon nut prevents these strips to get loose. A thin 3D-printed plastic frame is mounted around the rim of the steel tube and the light guide and protects the LYSO crystal from the sharp edge of the steel tube. The scintillator is connected to the light guide using a designated optical grease.

The LYSO crystal was wrapped in two layers. The inner layer was applied to create a surface that reflects most of the photons that leave the crystal back inside. Different materials were tested such as Teflon and Tyvek paper to create a white diffusive surface and metalized Mylar in a wrinkled and flat form to create a shiny, mirror-like surface. The outer layer was made of 20 µm thick black Tedlar film to prevent any light from entering the crystal from outside. Special care was taken to keep the number of overlapping layers as small as possible to avoid dead (non-scintillating) material and still retain light-tightness. To light-seal the sides of the interface between the crystal and the light guide, black electrical insulation tape was used as it proved to be very light tight. In the subsequent test, no differences in the energy spectra were found that could be related to the difference in the reflective wrapping. For the first beam time, four PMT based modules were buily (See Section 5.2.1).

The second version of the LYSO module (see Figure 5.5) was developed after the first beam time and incorporated results that were obtained then. The analysis of the maximal penetration depth (See Section 5.3.1.1) led to the conclusion that a length of 80 mm instead of 100 mm was sufficient. A first experiment using four SiPM arrays

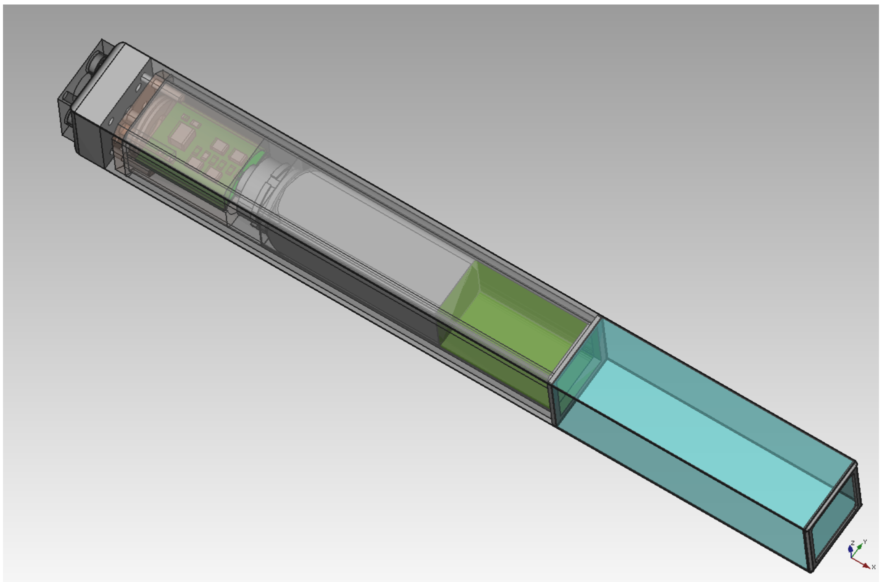

(a) CAD model of the PMT based LYSO module by Nils Demary.

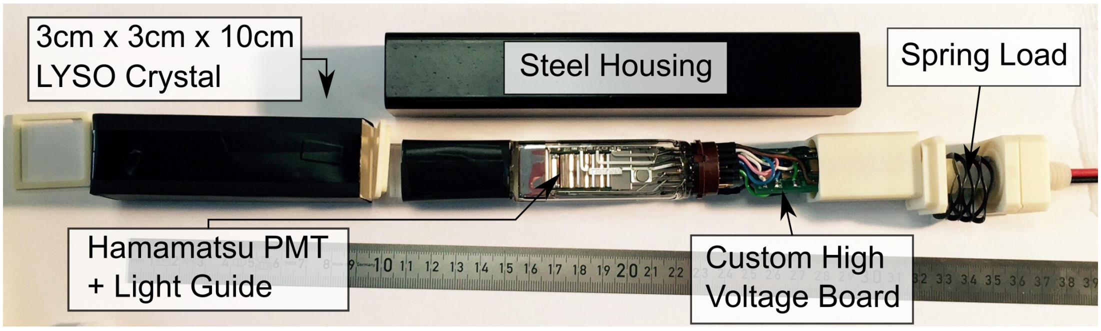


(b) First version of the LYSO detector module using PMTs

Figure 5.3: The first version of the LYSO detector module based on a dual channel PMT.

instead of the PMT was very promising and led to te decision of using SiPMs over PMTs in the new version of the LYSO modules.

Hence the biggest change compared to the previous version affected the scintillation photon detection. As stated in Section 5.1.2, four different SiPM arrays were used throughout the following experiments. The usage of the SiPMs allowed for the creation of a much shorter housing of 40 mm and therefore decreased the overall length significantly. There was no need for a high voltage divider board anymore as the SiPMs can be supplied with a reverse bias voltage in the order of 30 V. The SiPM arrays were delivered with a special connector on their backside that allowed for the access of the common anodes and cathodes of each of the 64 SiPMs. Luca Barion from the University of Ferrara, Italy developed a designated PCB of the same size as the SiPM array where it could be directly plugged, see Figure 5.4a. The circuit is much simpler compared to the previous one for the PMT. The SiPM array and the PCB were installed in an aluminum housing that was painted black on the inside to avoid internal reflections, and one layer of Kapton was stuck in to prevent any electrical connection between the

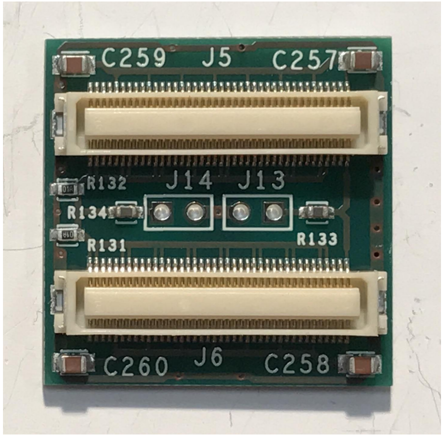


(a) Picture the adapter board developed by Luca Barion.

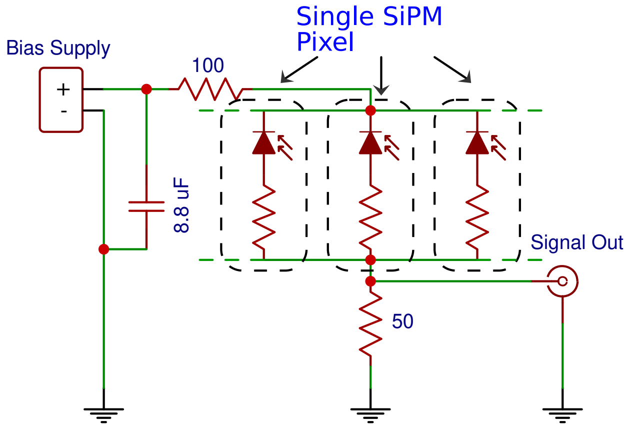


(b) Schema of the adapter board.

Figure 5.4: The adapter board (picture on the left) provides a connector for the SiPM arrays and a few passive components (see schema on the right). The positive reverse bias supply is connected to the cathodes of the SiPM through a series resistor of 100 Ω that acts as a current limiter. The supply voltage is stabilized by four parallel 2.2 µF capacitors (drawn as a single capacitor in the schema). The dashed box represents a single pixel of a SiPM symbolized as a photo-diode and the serial quenching resistor. The anodes of each SiPM pixel are tied together and connected via a 50 Ω resistor to ground. This resistor has a dual purpose: The current from the SiPM creates a voltage drop on this resistor which crates the voltage signal at the output. The value of 50 Ω was chosen to create a proper termination of the coaxial wire that is used to transmit the signal to the ADC, and therefore prevent reflections.

SiPM array, the PCB and the aluminum housing. On the front side of the housing, all four edges taper to a sharp tip. On the LYSO modules, the rear edges are chamfered such that they fit snugly to the edges of the housing. This creates a rigid joint between the two. The spring load mechanism on the end cap was adjusted to the new PCB. To create an optical interface between the SiPM and LYSO crystal, a flexible silicone pad was used. Besides the optical connection is has the advantage of even out any sight height differences among the 64 SiPMs of the array.

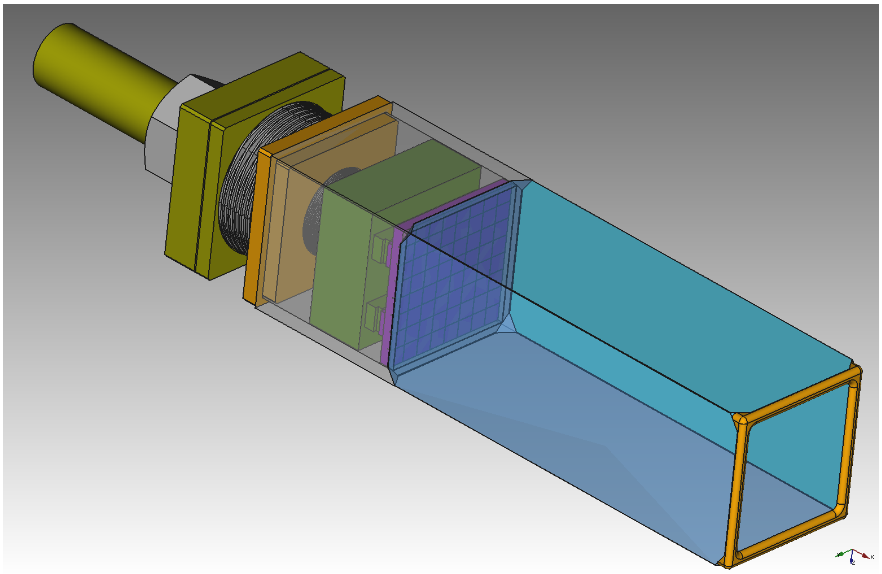

(a) CAD model of the SiPM based LYSO module by Nils Demary.

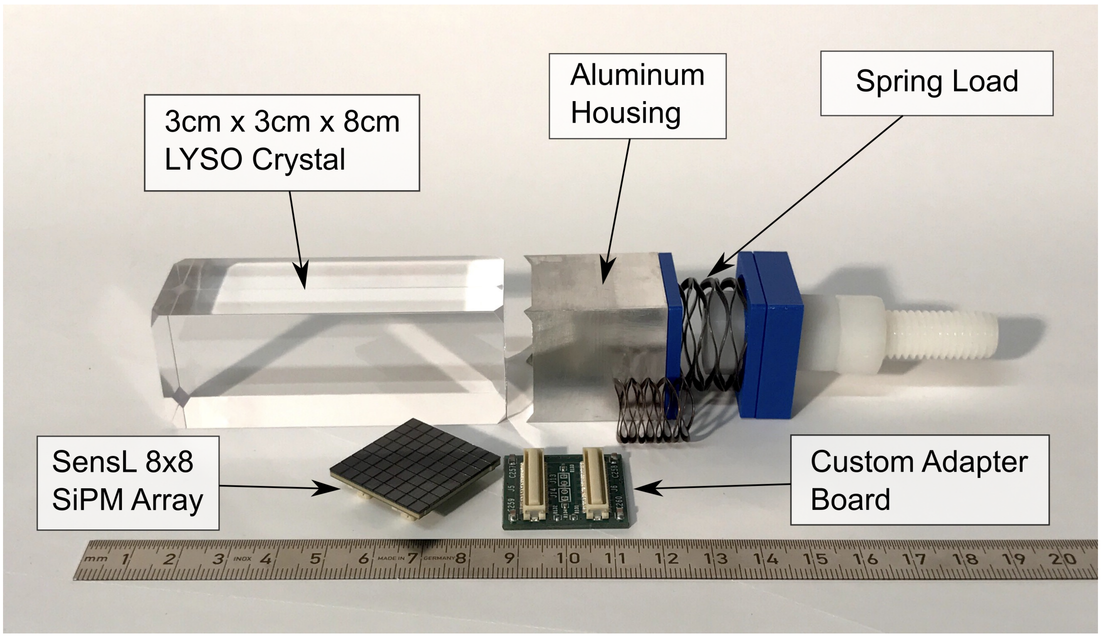


(b) Second version of the LYSO detector module using PMTs

Figure 5.5: The second version of the LYSO detector module based on a 8x8 SiPM array.

## 5.2 Experiments

In order to test and develop the LYSO detector modules, a total of five experiments were performed in the Big Karl experimental hall at the COSY accelerator facility. Each of them was using an extracted deuteron beam with different energies. Three iterations of experimental setups were developed an used. In the subsequent section, these setups will be described. The experimental setups were designed to be cost-efficient while retaining high accuracy. The general concept was to use high quality, state-of-the-art components in the detector modules such as SiPM arrays and LYSO scintillator crystals and modern *Flash-ADC* data acquisition modules but do not waste resources on the experimental setup that might be used for just one experiment. Whenever possible, it was tried to employ open source and open hardware components instead of proprietary solutions which are much more expensive and forces the usage closed source software that is often not flexible and restricted to the Windows operating system. Additionally, many scrap parts and leftover from old experiments were used.

### 5.2.1 1$^{st}$ Iteration

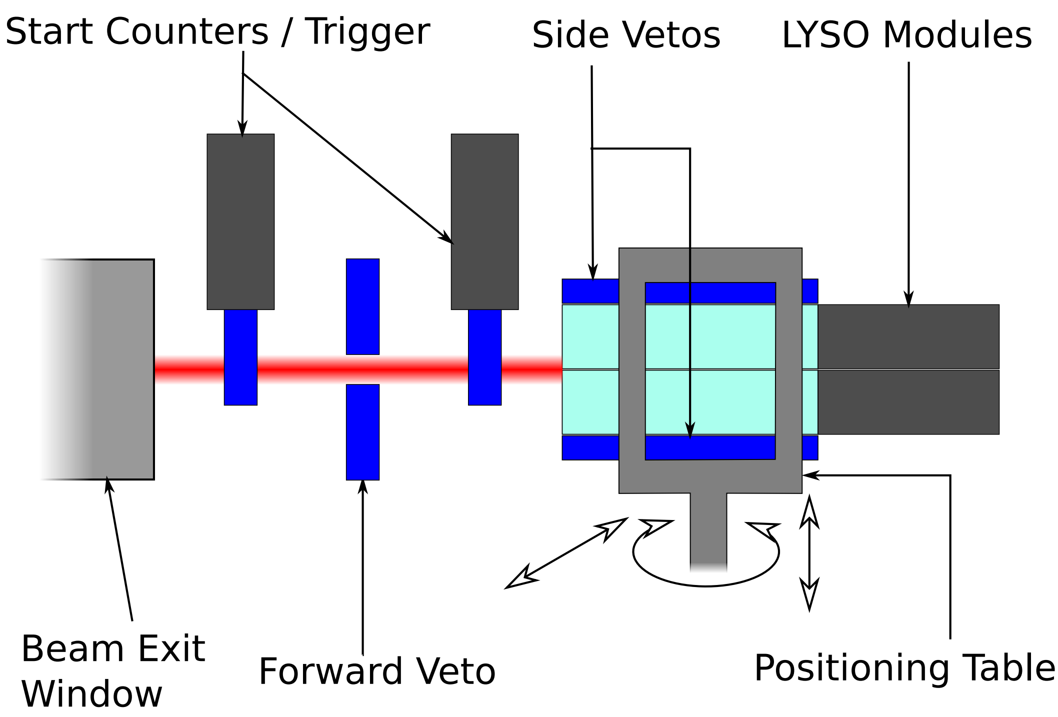


Figure 5.6: Schematic overview of the 1$^{st}$ iteration of the polarimeter development.

The 1$^{st}$ iteration of the LYSO module test setup was used in the beam time from 29. February to 20. March 2016. The main goal of this beam time was to test the concept of the LYSO based detector modules by directly positioning them in a deuteron beam. Therefore, four different beam energies (100 MeV, 200 MeV, 235 MeV, and 270 MeV)

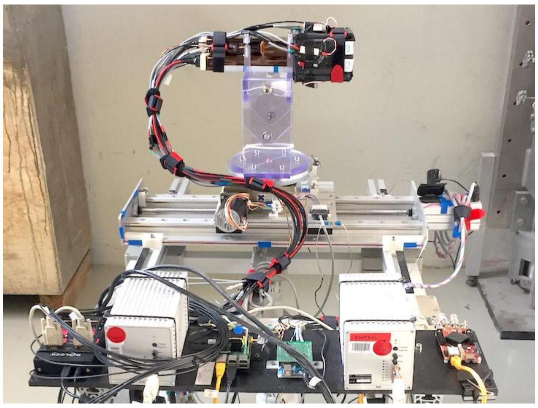

(a) Experimental table.

(b) Full setup at exit window.

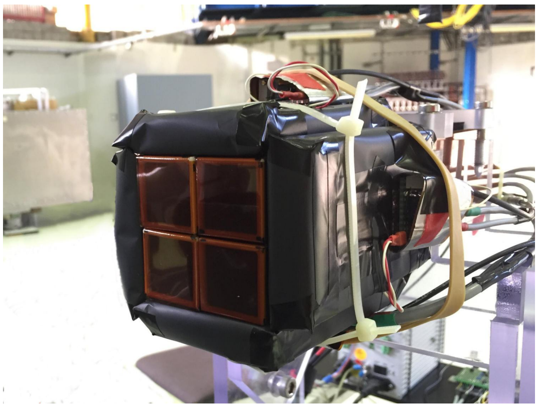

(c) PMT based LYSO modules and SiPM based side vetos.

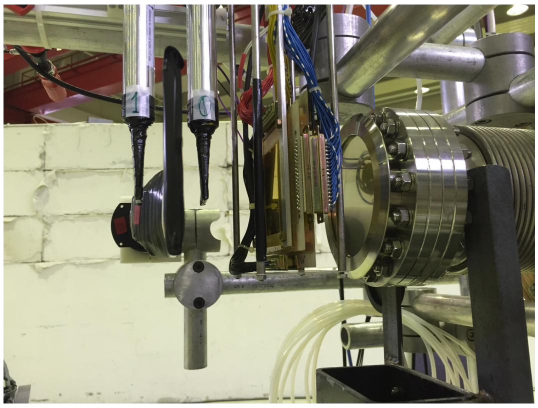

(d) Start counters, forward veto and exit window.

Figure 5.7: Pictures of the experimental setup of the 1$^{st}$ iteration of the polarimeter development installed in the Big Karl area.

were utilized at the extracted beam experimental hall *Big Karl*, see Chapter 3. In this experiment, only unpolarized beams were used.

To test the modules, four PMT-based versions were built for this experiment. Two modules were equipped with the 30 mm x 30 mm x 100 mm LYSO crystal produced by Saint-Gobain [37] and one module used a LYSO crystal of the same dimensions produced by Epic-Crystal [40]. The fourth module was built from two LYSO crystals with a dimension of 15 mm x 30 mm x 100 mm each. These scintillators were arranged side by side and connected to a split light guide that was, in turn, mounted to the PMT in such a way, that the light from each crystal was guided to its own channel of the PMT. This dual channel module was very useful to measure the stopping power of LYSO. In the analysis of the energy spectra obtained from the LYSO crystal produced by Epic-Crystal and Saint-Gobain, there was no difference visible. As the Saint-Gobain crystals are produced in France, it was much easier to order from them as from a seller outside of the European Union. Therefore the crystals for the next iteration were all bought from Saint-Gobain.

The experimental setup consisted of a table frame that could be moved up and down using a hand remote control. David Mchedlishvili built a transistor based adapter that allowed for an Arduino to control the position of the table. The original remote control only allowed to move the table and since it was driven by a DC motor rather than a stepper motor, there was no absolute positioning possible at all. To overcome this issue, a linear potentiometer that could be read by the Arduino was added to the system in order to create a closed-loop feedback system for the vertical positioning of the table. On top of the table, a linear horizontal rail system was installed using extruded aluminum profiles. A stepper motor driven shaft moves a slider along this rail. A rotatable disk was installed on the slider. This disk can be rotated using a second stepper motor. This horizontal rail system including the rotatable disk was a leftover from an old experiment and was provided together with the designated stepper driver by the electronic workshop. Additional limit switches from an old server housing had to be installed using 3D-printed holder in order to provide absolute positioning with the stepper motors. An acrylic mount that holds the four detector modules was mounted on the turning disk. This setup allowed to remotely position each individual module relative to the exit window of the beam pipe and turning the modules enabled to direct the beam not only on to the face of the modules but also to penetrate them at different angles. The closed-loop DC motor driven positioning in the vertical direction as well as the stepper motor driven open-loop positioning along the vertical axis allowed for a positioning accuracy of less than 1 mm. The modules could be rotated with a resolution of less than 1°.

The experimental table was controlled by a designated piece of software that was written for this purpose and was running on a *RaspberryPi*. This is a single board mini-computer running a Linux operating system, and it comes for a very reasonable price tag of around €35 (version 2B, see [41]). The peripherals such as the stepper drivers and the high voltage NIM-module (ISeg 6 channels high voltage PMT driver, NHS 6201p, see [42]) were connected via USB to this computer and the communication with the Arduino was implemented using the UART serial interface that was available on the general purpose input/output (GPIO) pins on the RaspberryPi. The software that controlled all the actuators was written in Python3. As intended by the object-oriented programming paradigm, an individual module was written for each of the hardware components such that they had a software representation in the control program. The main code that controlled all the hardware modules was written using the Flask [43] and socket.io [44] libraries which allows writing interactive browser-based user interfaces. This has the huge advantage, that the remote control software was available on any computer that was connected to the same network as the RaspberryPi. By using the WebSocket based technology provided by Socket.io, the position and status of the high voltage could be displayed on all connected clients without the need to reload the interface webpage.

The four LYSO modules were mounted in the acrylic holder in a 2x2 square configuration, see Figure 5.7c. On four sides of this packet (top, bottom, left, right), 5 mm thick plastic scintillators were attached to serve as a side veto for particles that enter or leave the scintillator crystals from the side. All four top edges of these scintillators were chamfered, and a small SiPM was glued there using an optical glue. The side

| | |
|---|---|
| Number of channels | 16 |
| Resolution [bits] | 14 |
| Sampling speed [MS/s] | 250 |
| Programmable input voltage range [V] | 2 or 5 |
| Programmable analog input offset [V] | ±2 or ±5 |
| Total DDR3 memory [GByte] | 2 |
| Memory buffer per channel [kByte] | 128 |
| Additional inputs | 3: external clock, external trigger, programmable |
| Additional outputs | 3: programmable |
| Trigger | Internal, external or daisy-chaining between multiple modules |
| Readout | Gigabit Ethernet or Multi-Gibabit optical link |

Table 5.2: Key features of the Struck SIS3316-250-14 flash-ADC converter, used in all iterations of the polarimeter development. Information was taken from [45].

vetos were wrapped in Teflon foil to increase reflectivity and in a second layer of Tedlar for light-tightness. The four SiPMs of each veto module were connected in parallel and their signals were amplified through a simple non-inverting operational amplifier circuit build for this purpose, see Appendix B.2. Directly after the exit window of the beam pipe, an additional veto module was installed. An plastic scintillator paddle that was mounted to a PMT by a light guide was utilized. This scintillator was already properly wrapped, and the only change that had to be done was to remove some wrapping from the center and drill a 10 mm hole into the plastic scintillator. This module was sealed again to make it light-tight using electric tape. This veto module was then mounted such that all the deuteron that passed through the hole would not create any signal in the scintillator, but particles that would leave the exit window off axis would hit the scintillator and create a signal that could be used to veto this event in the data acquisition. The veto paddle was mounted between two additional plastic scintillators attached to a PMT. These scintillators had an area of 20 mm x 18 mm and were 2 mm thick. They were used to generate a trigger signal for the data acquisition and were referred to as *start counters*. They could be moved in and out of the beam depending on the test that was performed. When inserted into the beam, they were used to tag each deuteron before it entered the LYSO modules.

To digitize the signals from the LYSO modules, vetos and start counters two high-speed flash analog to digital converter (SIS3316-250-14, [45]) were used. They are produced by the Struck company, and their key features are given in Table 5.2. The flash-ADC technology employs an array of fast comparators (one for each bit) on each channel

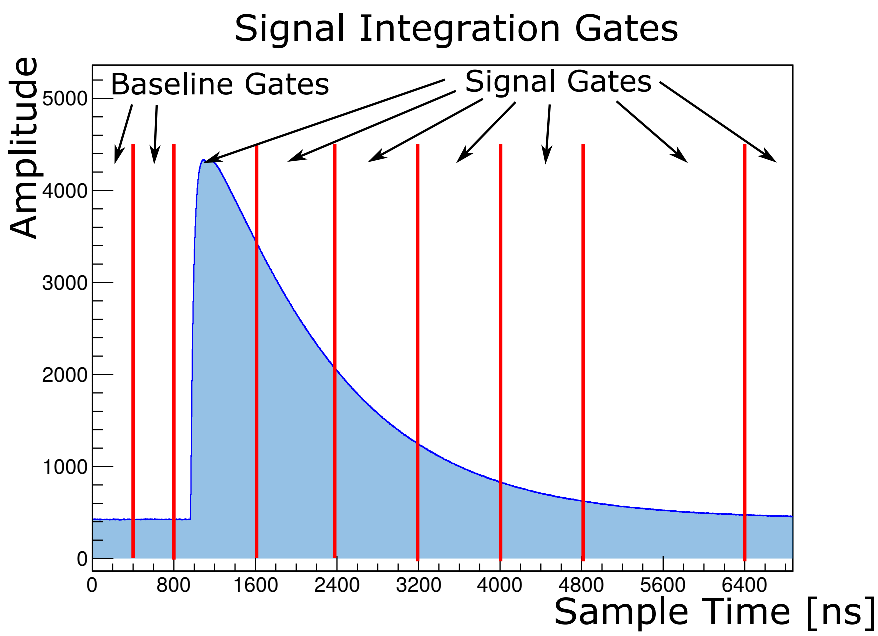


Figure 5.8: Typical signal shape of a LYSO based detector module recorded with the flash-ADC in sampling mode. The ten integration gates are drawn on top of the signal. The first two gates are used to extract the baseline of the signal and the subsequent eight are used to integrate the signal in order to obtain the energy information of the corresponding event.

which allows for much higher sampling rates compared to other ADC types such as the successive approximation controller used in other ADCs. The Struck SIS3316-250-14 can be operated in two basic modes: Sampling mode and integration mode. In the sampling mode, each sample is transferred to the data storage server, and in the offline analysis, the samples can be combined to obtain the waveform of the signal. This mode provides a maximum of information about the signals but creates a lot of data that needs to be transferred to the storage servers which reduces the maximal achievable trigger rate. The information about the energy deposited in the scintillator is represented by the integral of the signal rather than its shape. Therefore, the Struck SIS3316-250-14 offers to do the integration of the signal shape within the module itself on a fast FPGA chip. To retain some information about the waveform, this module offers to set multiple time bins (integration gates or *accumulators*, see Figure 5.8) relative to the trigger and does the integration of the signal in each of this bins individually. The accumulator will be transferred to the storage server, and the integrated signal can be obtained by summing them up. Further, this module allows setting a *pre-trigger* time. One accumulator can be set such that it will be filled before the actual signal arrives. This bin will, therefore, contain the information about the baseline (i.e., the DC offset). This baseline can be obtained by dividing the content of the first accumulator by its width. This means each event will be recorded including its own baseline and shifts in the baseline that can occur over time are automatically corrected. In the first beam time, the flash-ADC was operated in sampling mode only, as the software for the integration mode was not ready to be used yet but starting from the second beam time the flash-ADC was operated in the integration mode. The Struck SIS3316-250-14

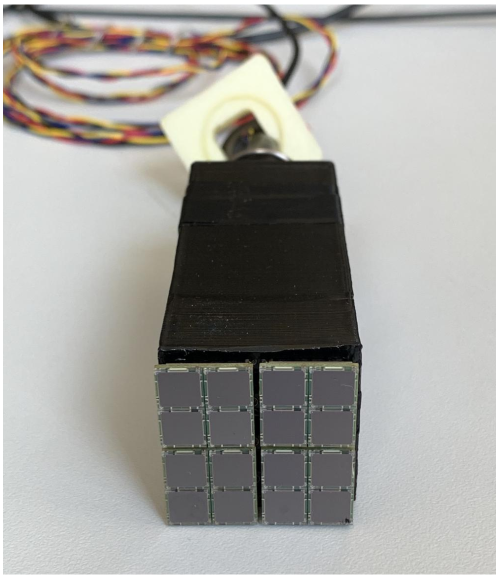

(a) SiPM array used for the first test in 3D-printed housing.

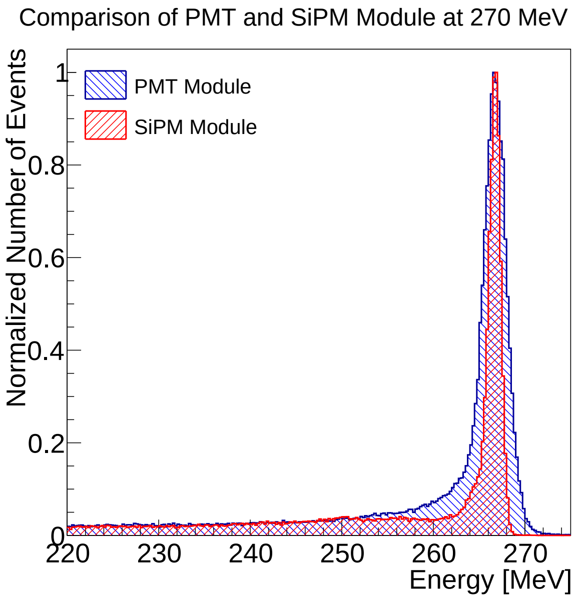


(b) Energy spectrum of a PMT based module in comparison with the SiPM test module.

Figure 5.9: The first test using four 2x2 SiPM arrays (left picture) as a light sensor for a LYSO crystal. A direct comparison of the energy spectrum obtained from the two different light sensors, motivated the usage of SiPM arrays for the next iteration of the LYSO based detector modules.

offers different trigger methods: An external signal can be used to trigger the data acquisition on all channel, or the trigger can be generated internally using the timing stable constant fraction discriminator (CFD) method. This internal CFD can be set to trigger each channel independently or generate a trigger signal that causes all channels to start recording simultaneously. In this beam time, only the external triggers from the start counters were used.

Using this first experimental setup, several different properties of the LYSO module, such as the linearity of the energy response, resolution, stopping power of LYSO and the deuteron break-up probability could be examined. The results are discussed in Section 5.3. At the end of this beam time, one of the LYSO modules was disassembled, and the first prototype of a SiPM based module was assembled and tested, see Figure 5.9. The steel base was removed and replaced by a 3D-printed plastic housing that contained four 2x2 6 mm (type: ARRAYC-60035-4P-EVB, see Table B.1) edge length SiPM arrays that were mounted to DIP sockets soldered to a prototyping PCB. The resulting energy spectrum of this prototype was so promising (see Figure 5.9b) that the decision was made to switch to SiPM as the photon detector in the next version of the LYSO modules.

### 5.2.2 2$^{\text{nd}}$ Iteration

The 2$^{\text{nd}}$ iteration of the LYSO module test setup was used in the beam time from 5. to 18. December 2016 and again from 13. to 26. March 2017. After evaluating the

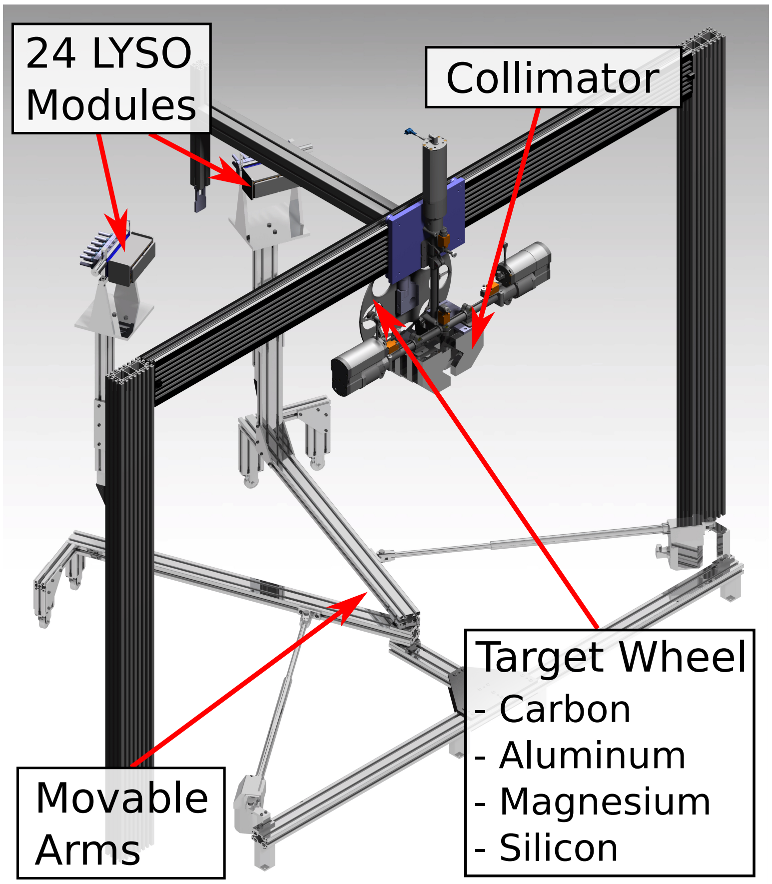


Figure 5.10: Schematic overview of the 2$^{\text{nd}}$ iteration of the polarimeter development. CAD model by Nils Demary.

results from the first beam time, it was decided to build a total of 24 LYSO modules using SiPMs (type: ARRAYJ-30020-64P-PCB, see Table B.1) for the photon detection as described in Section 5.1.3. These new modules were tested in a new experimental setup.

This setup was designed to test the modules in a configuration where they would serve as a polarimeter. As a consequence, this meant that a polarized beam and a target for elastic scattering had to be used. The experimental setup consisted of two parts. A gate and a two-armed module holder. The gate was built from 8 cm x 16 cm extruded aluminum profiles and was 2.0 m high and 2.65 m wide. It was mounted $\sim$ 40 cm away from the exit window with the external beam pipe in the center. To guaranty its stability, it was screwed to the floor of the experimental hall. On the top of this gate, a plate mounted on roller bearings was installed. An adjustable collimator made from iron blades was attached to this plate. It was intended to use it to reduce off-axis particle hits in the detector, but unfortunately, it introduced a lot of scattering surface that led to a very unclean energy spectrum recorded by the modules. Therefore it was decided not to use this collimator at all, and it was moved out of the beam path. In the center of the gate, a motor driven target holder was installed, referred to as the *target flower*. It consisted of an acrylic disk with eight holes. In each of these holes, a different target disk could be mounted on a 3D-printed holder. The target flower was

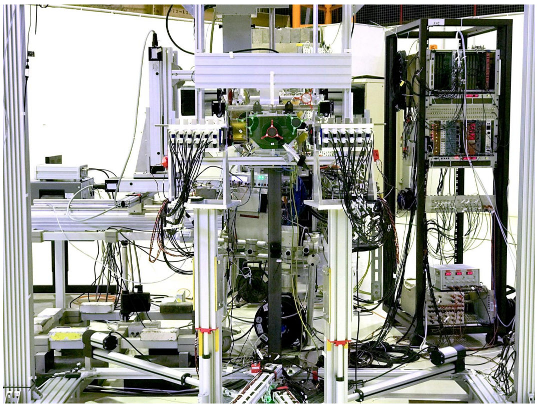

(a) Full setup.

(b) Target flower with installed targets.

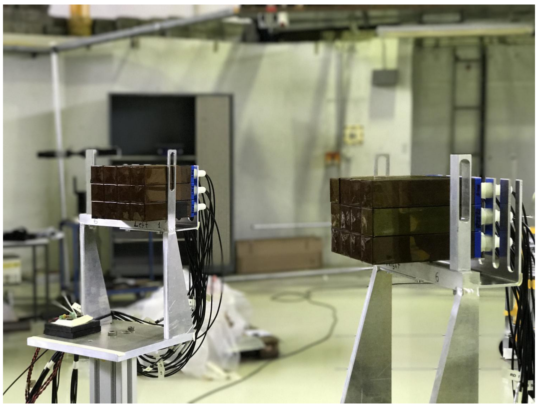

(c) Front view of the two arms with installed modules.

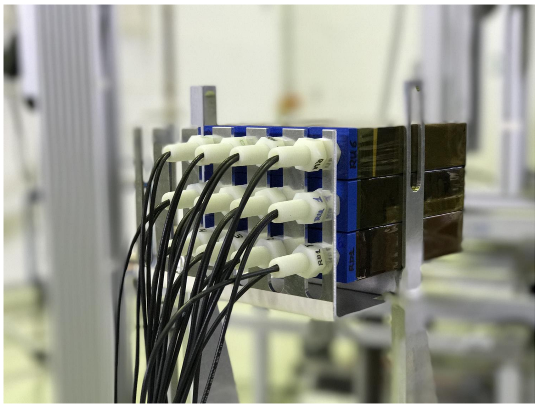

(d) Back view of one arm with slotted aluminum plate to mount the modules.

Figure 5.11: Pictures of the experimental setup of the 2$^{\text{nd}}$ iteration of the polarimeter development installed in the Big Karl area.

mounted on the hub of a stepper motor driven geared device produced by OWIS ([46], [47]) that was incorporated in the second version of the slow control and hence each target could be moved into the beam remotely. The following target materials were installed in the target flower: Silicon (5 mm), Carbon (5 mm and 10 mm), Aluminum (5 mm) and Magnesium (5 mm).

The two-armed module holder was mounted to another extruded aluminum profile that was fixed to the base of the gate on the floor. The Y-shaped two-armed module holder was attached to this profile. The two arms had a common pivot point, and the loose end of each arm was supported on a rubber wheel that allowed the arm to move on a semi-circle. Each of the arms was connected to a DC motor driven linear actuator produced by Rose&Krieger (LZ60P [48]). An encoder built into this actuators in combination with a powerful RoboClaw [49] driver allowed to position each arm with a precision of less than 1° relative to the beam axis. To mount the LYSO modules, another extruded aluminum profile was mounted perpendicular to each arm. This vertical part of the arm consisted of two parts. The lower part was rigidly mounted to the horizontal part of the arm. The second part of the vertical arm was attached to a linear actuator that allowed to set the height of the module holder individually on each arm. This actuator and its designated driver were produced by Pololu. A slotted aluminum plate was installed on top of the vertical part of the arm. This plate allowed to slide-in the LYSO modules in 3 different configurations: 2x6, 3x4 and 4x3. This whole setup enabled to position the modules at different azimuthal and polar angles relative to the beam and the configuration of the modules made different angular range coverage possible. Further, it was possible to position each individual module directly in the beam path in order to do the energy calibration. The length of the arms was chosen such, that the faces of the LYSO modules were at a distance of 1 m from the target point. The control of all four linear actuators was included in the slow control software, and therefore the position of each arm could be set remotely.

One of the start counters from the 1$^{\text{st}}$ iteration of the module test was added to measure the luminosity needed for a cross section calculation, see the thesis of Simone Basile [50]. This start counter was removed for the calibration runs as well as for the asymmetry measurements.

Similar to the side vetos from the first beam time, two types of plastic scintillator based $\Delta E$ detector were built. One version with a thickness of 1 cm and the other one with a thickness of 2 cm. Four SiPMs (PM6660TP-SB0, see Table B.1) were installed on each long side of the plastic scintillator instead of the edges. The wrapping and the signal amplification was done in the same way as for the side vetos. Mounting these $\Delta E$ detectors in front of the LYSO modules allowed for the creation of a particle identification plot as shown in Section 5.3.2.1.

The SiPMs used in the LYSO modules and the $\Delta E$ detectors needed a very stable reverse bias voltage of around 30 V in order to work properly. For this purpose, a designated voltage supply was developed by David Mchedlishvili, Otari Javakhishvili, Mikael Gagoshidze, and Dito Shergelashvili (see his PhD-Thesis). This custom modular power supply consists of a mainboard with a very precise and stable voltage reference and 120 slots for bias voltage generating modules, see Figure 5.12a. For each LYSO module, an individual card is plugged into the mainboard that provides an adjustable voltage. Additionally, each card can be enabled and disabled remotely via an SPI interface on the mainboard. When enabled, the voltage ramps up slowly in order to avoid large currents due to the capacitive nature of the SiPMs. If the bias voltage for one module gets disabled, the SiPMs are discharged in a controlled manner. Figure 5.12b shows an enable/disable trace for a such a bias voltage card. The SPI control interface was connected to the Raspberry Pi that was running the slow control software and hence each module's bias voltage could be turned on and off remotely. A diagnosis line from each card runs through an analog multiplexer IC to a common output connector. A precision digital voltmeter is connected to this diagnosis port of the mainboard, and the voltage on each card is subsequently read. This allows for a continues bias voltage monitoring of all SiPMs. Having a very stable bias voltage is of particular importance as measurements showed that a variation of $\sim$100 mV changes the voltage gain of the SiPMs in the order of 5 %, see Figure 5.24. Measurements performed during the last beam time on these bias voltage generator board showed that the required stability can be achieved, see Figure 5.23.

Staring from the first beam time using the 2$^{\text{nd}}$ iteration of the experimental setup,

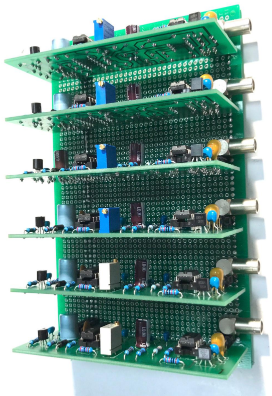

(a) Custom voltage supply generator modules used to create the reverse bias supply for the SiPM version of the LYSO based detector modules. The Voltage of each module can be set on the blue/gray potentiometer.

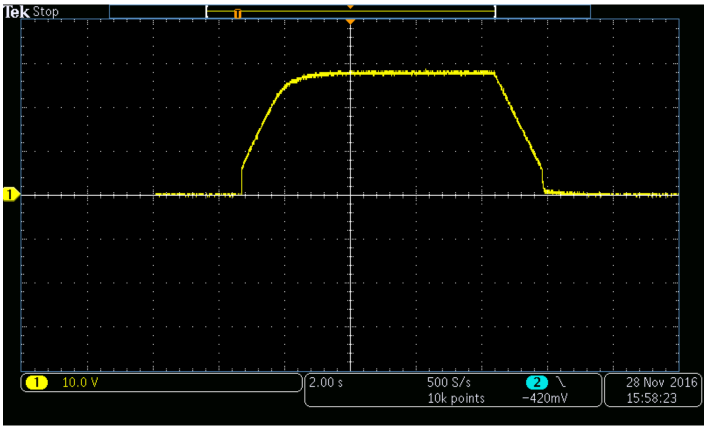


(b) On / off ramp that can be generated for each channel of the custom voltage supply generator. The slow up-ramping of the voltage limits the inrush current due to the capacitive behavior of the SiPMs as well as the actual voltage stabilizing capacitors on the adapter board, see Figure 5.4b. The slow turn-off process ensures a save discharge of these capacitors.

Figure 5.12: A stable supply voltage for the reverse bias voltage for the SiPM arrays is an integral part for of the successful operation of the LYSO based detector modules. A multi-channel supply voltage generator was developed for this purpose. Each detector module is connected to an individual channel of this generator and can be turned on and off via a server that is running on a Raspberry Pi.

David Mchedlishvili improved the DAQ-software in such a way that the flash-ADC could be operated in the integration mode which reduced the amount of data that had to be transmitted to the storage server drastically and therefore increased the maximum trigger rate. Further, it was possible to trigger from each LYSO module individually or switch back to get the trigger signal from the start counter instead.

With the 2$^{\text{nd}}$ iteration of the experiment, properties of the SiPM based LYSO modules such as resolution and linearity could be analyzed. It was proven that the new version on the detector modules based on the shorter (8 cm) LYSO crystal and the SiPM arrays as the photon detector performed well. The custom made power supply for the reverse bias voltage was able to provide stable operation of the LYSO modules. The mechanical two-arms setup allowed to investigate the performance of the LYSO modules in a polarimeter configuration and with the materials mounted in the target flower, it was possible to measure asymmetries for different target materials at different beam energies. By mounting the $\Delta E$ detectors in front of the LYSO modules, it was possible to generate a $\Delta E$ vs. $E$ spectrum for each module that allows for clean particle identification. The results of these measurements are given in Section 5.3.2.1. David Mchedlishvili was able to test his new version of the online analysis software that is not only capable of displaying the energy spectrum of each LYSO module but can calculate the asymmetry in a continuous manner.

### 5.2.3 3rd Iteration

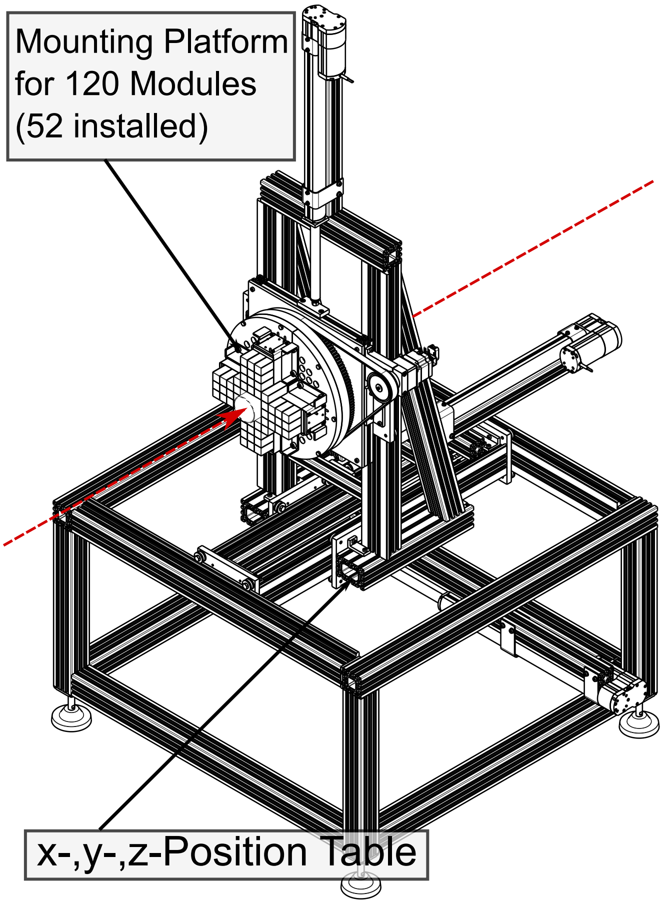


Figure 5.13: Schematic overview of the 3rd iteration of the polarimeter development. CAD model by Nils Demary.

The 3rd iteration of the LYSO modules test setup was used in the beam time from 4. to 17. December 2017 and again from 30. April to 13. May 2018. The evaluation of the performance of the SiPM based LYSO detector module has shown that they are suitable to be used in the final polarimeter setup. Hence it was decided to build a total of 52 LYSO modules. Forty-eight were using the SiPM arrays by SensL used in the 2nd iteration, but since Ketek introduced a new series of SiPMs with the same form factor as the ones by SenseL, it was decided to build four additional modules using the new PA3325-WB-0808 and PA3315-WB-0808 type SiPM arrays by Ketek for comparison. The new model by Ketek promised a better resolution due to the smaller microcell size and a reduced "dead" (non-active) area between the individual SiPMs, see Table B.1.

The experimental setup for this iteration was updated as well. It consisted of a 23 mm thick aluminum disk with a diameter of 480 mm. Since this disk is intended to be used in the final polarimeter it can be separated into two half, and there is a central hole with a diameter of 90 mm to be able to mount it around the beam pipe. There are 120 holes drilled into the disk that allow to install the LYSO modules by sliding them in and fix them with a nylon nut, see Figure 5.14c. This disk allows for the arrangement of the LYSO modules in different patterns in the final polarimeter assembly. For this

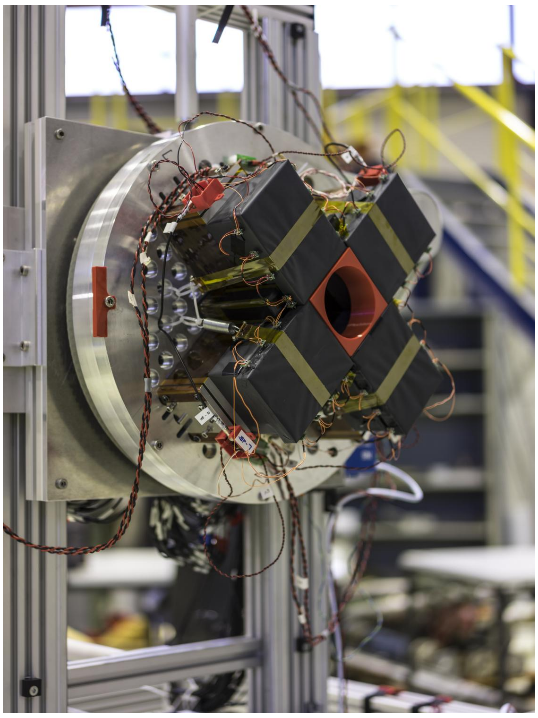

(a) Full polarimeter equipped with $\Delta E$ detectors.

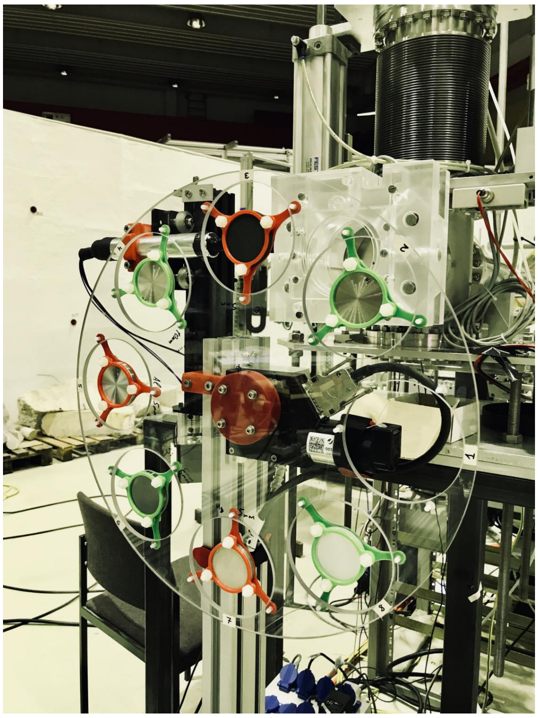

(b) Target flower with all six targets, used for asymmetry measurement, installed.

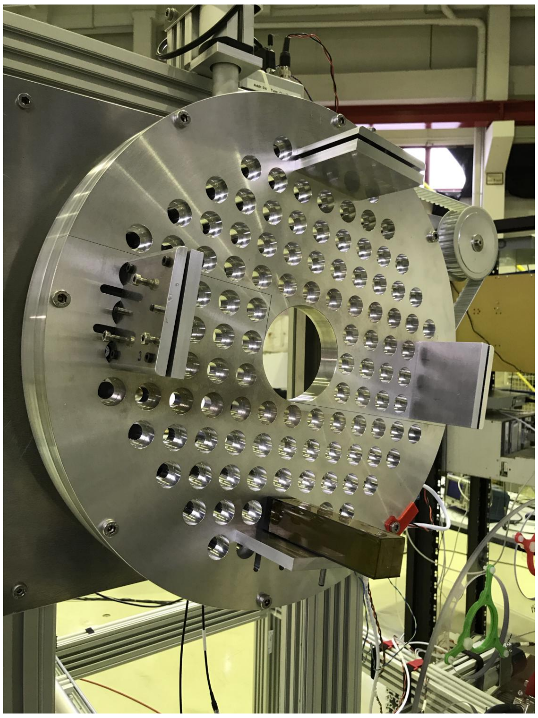

(c) LYSO based detector module support disk made form aluminum.

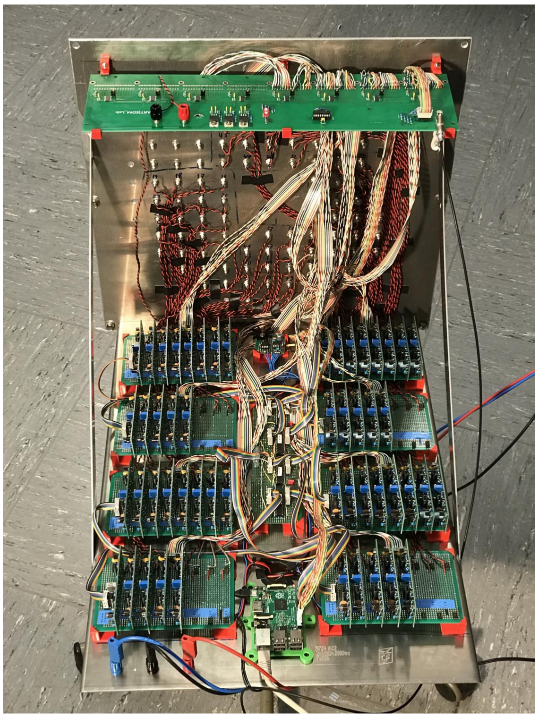

(d) Designated SiPM bias voltage generator.

Figure 5.14: Pictures of the experimental setup of the 3$^{\text{rd}}$ iteration of the polarimeter development installed in the Big Karl area.

iteration, the modules were arranged in a regular cross pattern with 12 modules in each arm of the cross. The additional four Ketek based LYSO modules were installed in the edges of the cross close to the central hole (**C** prefix, see Figure 5.40).

The disk was mounted on a new table made from extruded aluminum profiles installed again in the Big Karl experimental hall in front of the external beam pipe exit window. On the experimental table, a DC motor driven carriage was installed that could be moved perpendicularly with respect to the beam pipe (X-axis). On top of it, a second sled was installed that would allow movements towards the exit window (Z-axis) using another DC linear actuator. On top of this, a frame made from extruded aluminum profiles was mounted perpendicular to the table. A slider on roller bearings could be moved up and down (Y-axis) with a third DC linear motor. The disk holding the LYSO modules was attached to this slider. Figure 5.13 shows the final setup. Being able to move the disk in all three spatial dimensions allowed to position each module directly in the beam path for energy calibration. By moving the disk to the center, i.e., align the central hole of the disk with the exit window of the external beam pipe, the modules could cover different polar angle ranges by moving along the Z-axis. The staff from the IKP's mechanical workshop used optical triangulation to carefully align the whole experimental table with respect to the external beam pipe. The table was precisely leveled using set-screw feet. Two of the DC linear actuator were reused from the 2$^{\text{nd}}$ iteration experimental setup, and the third one of the same type had to be ordered. They were again controlled by RoboClaw drivers and integrated into the third version of the slow control software.

The gate that was installed for the 2$^{\text{nd}}$ iteration experimental setup was used to mount the target flower in front of the exit window. For this iteration, the following target materials with a thickness of 5 mm were installed: Nickel, carbon, tin, aluminum, silicon, magnesium, and $CH_2$ made from multiple layers of polyethylene foil. Between the exit window and the target flower, the PMT-based start counter was installed again. It was attached to a stepper motor driven linear rail that allowed to remotely insert and remove the start counter to/from the beam. The stepper was driven by a custom driver board attached to an Arduino that was in turn connected to the Raspberry Pi running the slow control software.

The disk that holds the LYSO modules was designed to be rotatable. It was mounted on an aluminum gear that was attached via a Teflon bushing to the horizontal slider. The whole disk was intended to be remotely turned using a stepper motor that was belted to the gear behind the disk. Unfortunately, the Teflon bushing was not well chosen to support moment load (angular force relative to the plane of the bushing). Therefore, the bearing would oscillate back and forth between static and sliding friction resulting in strong vibrations of the disk and the LYSO modules attached to it. As this posed a non-tolerable danger to the modules, it was decided to fixate the disk and discard the possibility of rotating it completely.

During the first beam time with this experimental setup in December 2017, the four arms of the cross were equipped with the 2 cm thick plastic scintillator $\Delta E$ detectors built for the 2$^{\text{nd}}$ iteration of the polarimeter development. Using a polarized deuteron beam, asymmetries on different target material were measured. These tests were of particular importance as the LYSO module design as well as the disk for mounting the modules will be used in the final polarimeter setup. For these measurements, the DAQ system consisted of four Struck flash-ADC modules tested in the previous beam times. With this system, it is possible to use up to 64 channels in parallel on a single VME bus. It was crucial to check that all four flash-ADC modules could be synchronized and that the trigger system could be distributed among them. It was possible to set up the modules in such a way that a hit in one LYSO module would trigger the readout of this particular channel or instead cause the digitization of all channels simultaneously. Further, the online analysis system had to be updated to be able to handle all the modules together and calculate the asymmetries as a function of time. All the test were successful and created confidence that the LYSO modules and the DAQ-system were ready to be used in the final polarimeter setup.

However, what the beam time in December revealed was the fact that a finer spatial resolution of the polarimeter would be preferable. In order to keep the final device as compact as possible, the distance between the target and the faces of the LYSO crystal is limited. This means that one crystal face covers a rather large solid angle (see Figure 5.41) and due to the $\Theta$-dependence of the analyzing power, the asymmetry can vary substantially within the coverage of one LYSO face. To overcome this issue, it was decided to test whether it is possible to build a $\Delta E$ detector that would not only provide energy loss information but could be used to improve the spatial resolution as well. Hence the concept of triangular plastic scintillator bars as described in Section 5.3.2.2 was investigated in the second beam time with this iteration of the experimental setup in May 2018. The plan for this last beam time was to test the triangular $\Delta E$ detectors and repeat some asymmetry measurements as well as to test some changes in the DAQ-system. Unfortunately, there were problems to cope with during this beam time. First of all, there were delays in the delivery of the 3D-printed mounting holds that would attach the triangular plastic scintillators and their custom-made signal amplifier PCBs to the aluminum frame. These parts only arrived in the middle of the beam time, and it was not possible to fully assemble both layers of the detector. Nevertheless, some very promising results were obtained in the last days of the experiment as presented in Section 5.3.2.2. The second problem was that the polarized beam source was not working during the entire beam time. This meant that no asymmetry measurement was possible at all. As there was more time for the energy calibration available, it was possible to understand the origin of the double-peak structure that was observed since the first tests of the LYSO modules but could neither be distinctively reproduced nor be explained. Until then it seemed to occur randomly. The result of the double-peak investigation is given in Section 5.3.1.7.

## 5.3 Results

### 5.3.1 LYSO Module and Polarimeter Properties

From the data that was measured in the five beam times, different properties of the individual LYSO based modules and the polarimeter as a whole were calculated. The following sections will present these results and the way they were obtained.

#### 5.3.1.1 Bragg-Peak Measurement

When a particle travels through matter, different processes lead to an energy loss of this particle. These processes depend on the type of particle as well as on the absorber material type. In this section, the discussion of the energy loss of particles will be limited to charged particles heavier than electrons in an absorber material with the average mass of the nuclei larger than the one of the particle. For example: A deuteron that travels through a LYSO scintillator crystal.

For a heavy particle that travels through matter, the following processes lead to losses of its kinetic energy: Inelastic collisions with the electrons of the target material atoms, elastic scattering of the material nuclei, emission of Cherenkov radiation, nuclear reaction and bremsstrahlung. From these processes, the first one contributes by far the most to the energy loss of the particle and was used by *Niels Bohr* to define a classical formula for the *stopping power* of a material. The stopping power of a material defines how much energy a specific particle with given kinetic energy loses when it travels a certain distance through this material. Often it is abbreviated as $\frac{dE}{dx}$ with a unit of energy per distance. Bohr's calculation was then later modified by *Hans Bethe*, *Felix Bloch*, and others to include relativistic and quantum mechanical effects which lead to the famous Bethe-Bloch formula [31]:

$$-\frac{dE}{dx} = 2\pi N_a r_e^2 m_e c^2 \rho \frac{Z}{A} \cdot \frac{z^2}{\beta^2} \left[ \ln \left( \frac{2m_e \gamma^2 \beta^2 W_{max}}{I^2} \right) - 2\beta^2 - \delta - 2\frac{C}{Z} \right], \tag{5.1}$$

with $r_e$ the classical electron radius, $m_e$ the electron mass, $N_a$ the Avogadro's constant, $\rho$ the density of the absorbing material, $Z$ the atomic number, and $A$ the atomic weight of the absorbing material. Further, $z$ the charge number of the incident particle, $I$ the mean excitation potential and $W_{max}$ the maximum energy transfer in a single collision. $\beta$ and $\gamma$ are the relativistic Lorentz factors of the incident particles ($\beta = \frac{v}{c}$ and $\gamma = (1-\beta^2)^{-\frac{1}{2}}$ ). The two correction factors $\delta$ (density correction) and $C$ (shell correction) are only of importance for very high and very low kinetic energies of the incident particles. An extensive discussion of all the factors is given in [31].

For an intermediate energy range of 1 MeV to 100 GeV deuterons, Equation (5.1) can be simplified to:

$$-\frac{dE}{dx} = \pi N_a r_e^2 m_e c^2 \rho \frac{Z}{A} \cdot \frac{z^2}{\beta^2} \left[ \ln \left( \frac{2m_e \gamma^2 \beta^2}{I} \right) - \beta^2 \right], \tag{5.2}$$

because $m_d \gg m_e$ and therefore $W_{max} \approx 2m_e\beta^2\gamma^2$. If the stopping power for a mixed material (with a density $\rho$) such as LYSO has to be calculated, the following scaling rule (*Bragg's Rule*) can be used:

$$\frac{1}{\rho}\frac{dE}{dx} = \frac{w_1}{\rho_1}\left(\frac{dE}{dx}\right)_1 + \frac{w_2}{\rho_2}\left(\frac{dE}{dx}\right)_2 + ... \tag{5.3}$$

Here, $w_n$ describes the fraction of the individual components by weight and $\rho_n$ the individual densities. The weight fractions can be calculated as follows:

$$w_n = \frac{a_n A_n}{A_{tot}} \quad \text{with} \quad A_{tot} = \sum a_n A_n. \tag{5.4}$$

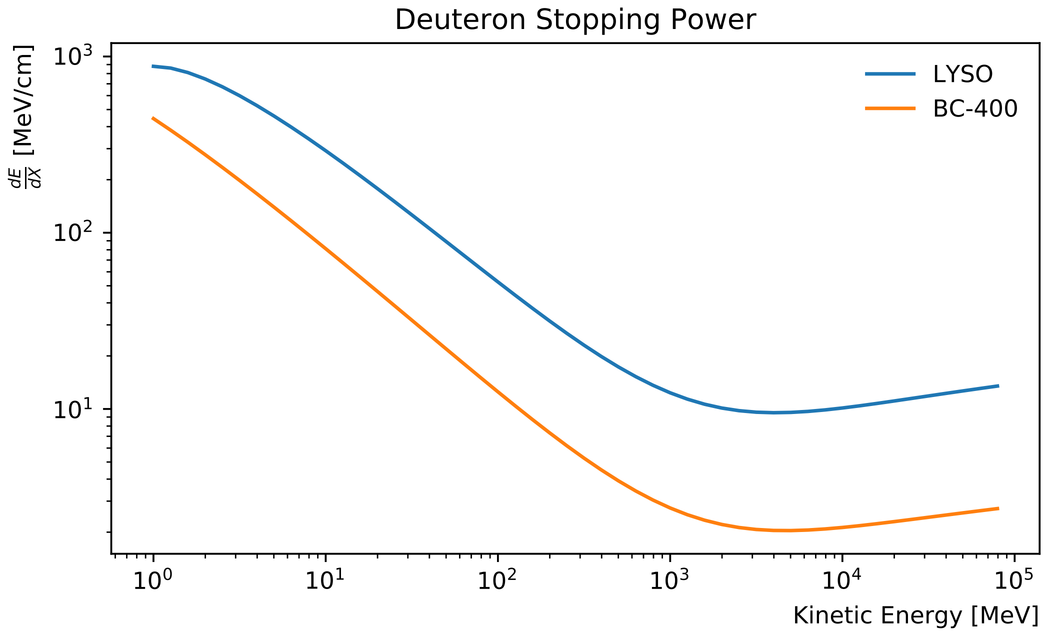


Figure 5.15: Stopping power for deuterons in a LYSO crystal and the plastic scintillator BC-400 as a function of the kinetic energy of the deuteron calculated using the Bethe-Bloch formula from Equation (5.2) and the Bragg rule from Equation (5.3).

$a_n$ denotes the number of atoms with the atomic weight $A_n$ in one molecule of the absorber material. For LYSO, the number of atoms of its constituents is given in Section 5.1.1.

To create a plot of the stopping power of deuterons in LYSO it is more convenient to provide the deuteron kinetic energy $T$ in terms of MeV rather than in terms of $\beta$, i.e., using the relation $\beta^2 = 1 - \frac{m_d}{m_d+T}$. Hence the stopping power of LYSO as a function of the deuteron kinetic energy is given in Figure 5.15. For comparison, the stopping power for a common type of plastic scintillator (BC-400), as used in the $\Delta E$ detectors, is plotted as well. The plastic scintillator material consists mainly of carbon and hydrogen with a H:C ratio of 1.103:1 [51]. The mean excitation potential $I$ for the different components was taken from [52].

The Bethe-Bloch formula has its minimum between 1 GeV and 10 GeV for both absorber materials. Particles in this energy range are called minimal ionizing particles. If the particles kinetic energy gets larger, the stopping power starts to increase again due to relativistic effects. Hence, the high energy range of the Bethe-Bloch formula is referred to as the relativistic tail. On the left of the minimal ionization point, the energy loss per unit length increases with the decrease of the kinetic energy until the particle reaches a full stop.

When a particle with given energy enters an absorber material, the energy loss, in the beginning, is low but it increases as the particle loses more and more of its kinetic energy. By losing kinetic energy it moves up along the Bethe-Bloch curve, and the subsequent loss increases even more. Shortly before the particle comes to a full rest,

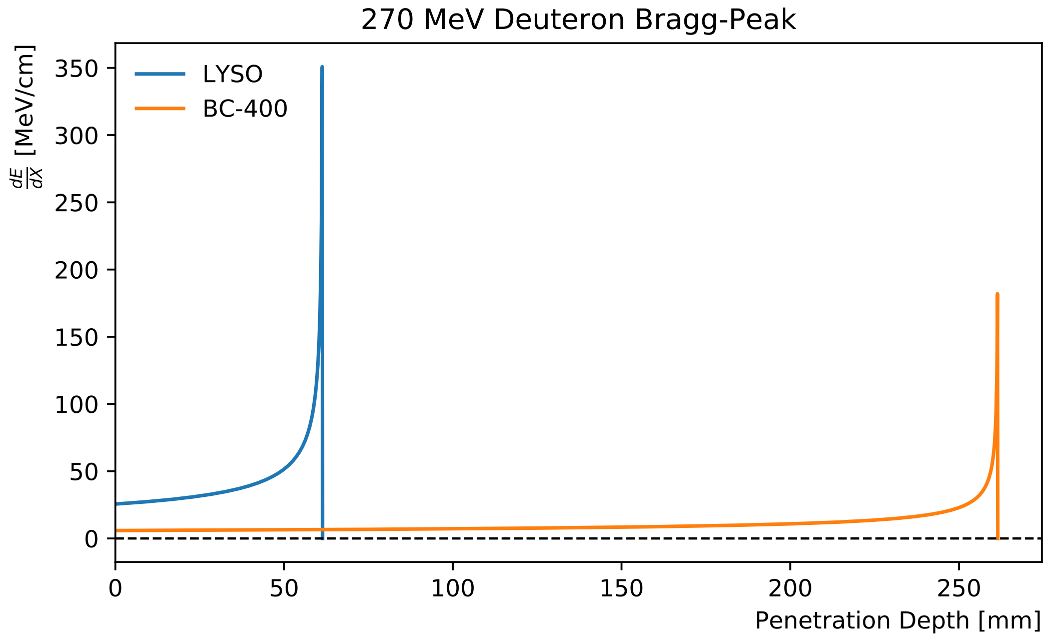


Figure 5.16: Stopping power for 270 MeV deuterons in a LYSO crystal and the plastic scintillator BC-400 as a function of the penetration depth calculated using the Bethe-Bloch formula from Equation (5.2). The point of maximal energy deposition is called Bragg-Peak and the maximal penetration depth is estimated to be 61.3 mm in LYSO and 261.4 mm in BC-400

the energy loss is maximal. If the energy loss per unit length is plotted against the penetration depth, the point of maximal energy loss is called the Bragg-Peak and indicates the maximum penetration depth of a particle with a given initial kinetic energy. In Figure 5.16 the energy loss as a function of the penetration depth is calculated from Equation (5.2). From this plot, the maximal penetration depth for a 270 MeV deuteron in LYSO ($\sim$61.3 mm) and BC-400 ($\sim$261.4 mm) can be estimated. However, calculating the maximum penetration depth just from the Bethe-Bloch formula does oversimplify things a bit. Especially since it is assumed that the particle is just taking a straight path which is known not to true due to *range straggling* , see Section 5.3.1.5. What can be taken from this calculation is the fact that LYSO is a very good choice for a scintillator that should fully stop deuterons. If one had used plastic scintillator cuboid instead of LYSO, the modules would have been longer by a factor of $\sim 4.3$ if they should have been able to stop 270 MeV deuterons.

With the 1$^{st}$ iteration of the detector setup, it was possible to experimentally determine the maximal penetration depth of 270 MeV deuterons in LYSO. To perform this measurement, the module with the split LYSO crystal was used. The module was positioned in such a way in front of the exit window, that the beam would hit the scintillator crystals at an angle (see Figure 5.17) that could be set from the slow control software. The experimental table was moved as close as possible to the exit window of the beam pipe, and a 10 mm x 10 mm x 2 mm plastic scintillator was used as the trigger. By changing the angle $\alpha$ of the module relative to the beam, the effective path

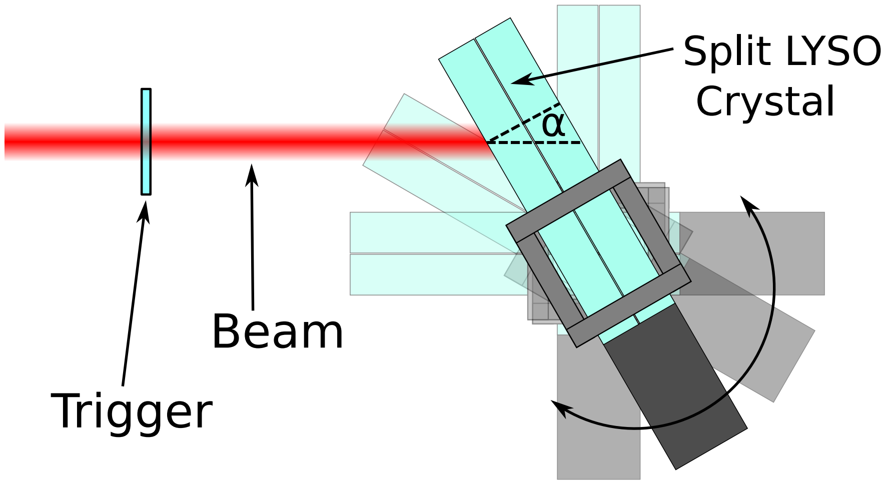


Figure 5.17: Schematic model of the experimental setup that was used to measure the stopping power of 270 MeV deuterons in LYSO.

length of the deuteron in the LYSO crystal could be set. The module was positioned such, that the beam would pass through the first followed by the second 15 mm thick scintillator. For each value of the angle $\alpha$, the deposited energy in the first crystal could be measured simultaneously with the total deposited energy in both crystals. The effective path length as a function of the rotation angle $\alpha$ was therefore given by:

$$x_{1.5cm} = \frac{1.5 \text{ cm}}{\sin(\alpha)} \quad \text{for the first crystal,}$$
$$x_{3.0cm} = \frac{3.0 \text{ cm}}{\sin(\alpha)} \quad \text{for both crystals.}$$

A total of 11 different angles in the range of 20° to 90° could be measured with this setup. This would cover a range of penetration depths of 15 mm to 87.7 mm. For each measurement $i$, two pairs of deposited energy and effective path length ($[x_{1.5\text{cm}}, E_{1.5\text{cm}}]_i$ and $[x_{3.0\text{cm}}, E_{3.0\text{cm}}]_i$) were obtained. By successively calculating the difference between the deposited energy between the measurement $i$ and $i-1$, the stopping power could be calculated as follows:

$$\left(\frac{\Delta E}{\Delta x}\right)_i = \frac{E_{i-1} - E_i}{x_i - x_{i-1}} \quad \text{for} \quad i \in [1, 11]. \tag{5.5}$$

In order to use the first point as well, point zero $[x = 0 \text{ cm.}, E = 270 \text{ MeV}]_0$ had to be included as well. The stopping power according to Equation (5.5) was calculated and is shown in Figure 5.18, for the first crystal only (blue markers) as well as for both crystals together (red markers). The measurement showed that the Bragg-Peak and therefore the maximal penetration depth for 270 MeV deuterons is located between 6 cm and 6.5 cm. Paul Maanen had created a GEANT4 Monte-Carlo simulation that is plotted together with the real measurement in Figure 5.18 and they are in a good agreement.

In the 1$^{\text{st}}$ iteration of the detector development, the LYSO crystals that were used had a length of 10 cm. The result of the Bragg-Peak measurement motivated the decision to use 8 cm LYSO crystals for the next iteration and the final modules as this new length is sufficient to stop deuterons up to 270 MeV as experimentally proven.

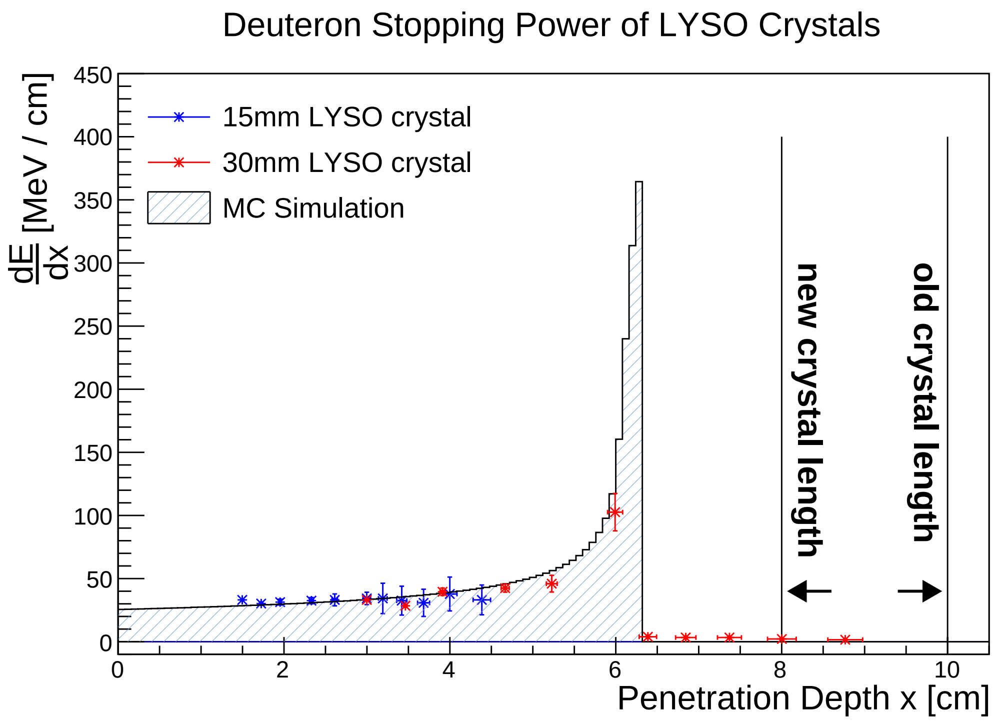


Figure 5.18: Measurement and Monte-Carlo simulation of the stopping power for 270 MeV deuterons in LYSO. The blue data points have been calculated from the first (15 mm thickness) LYSO crystal and the red ones from both (30 mm total thickness) LYSO crystals. The Monte-Carlo simulation was provided by Paul Maanen. The black lines indicate the old crystal length (used in this measurement) and the new length (used starting from the $2^{nd}$ iteration of the detector development).

#### 5.3.1.2 Energy Resolution

One of the most fundamental properties of any detector module is its energy resolution. It decides on how well one can distinguish between different processes such as elastic or inelastic scattering or identify different particle species hitting the detector. In the case of a polarimeter, the main goal is to identify the type of particle as in the elastic scattering process, the particle that is recorded by the detector should be of the same type as the beam particle or the target in the case of inverse kinematics. The kinetic energy of an elastically scattered particle off a given target does only depend on the scattering angle, and thus it is known how much energy it will deposit in a module that is located at a certain angle relative to the target and the beam axis. The LYSO based detector modules were designed to completely stop the scattered particles (see Section 5.3.1.1) and therefore the energy that is deposited in the scintillator crystal equals the full kinetic energy of the particle at the moment of entering the detector module.

The resolution of each detector module was measured by moving it directly into the deuteron beam. The module was positioned as close to the exit window of the beam pipe as the setup allowed. The target and the start counter were removed from the beam path. This procedure was repeated for each installed module at each beam energy that was available in the corresponding beam time. The resulting energy spectra should only contain one peak that corresponds to the deposited kinetic energy of the beam particles. In the case of a deuteron beam, there is a background that is spread over the whole spectrum and origins from deuteron break up reactions inside of the LYSO crystal and is discussed in Section 5.3.1.6. The energy resolution defines how accurately the energy of one particle can be measured, or more precisely whats the minimal energy difference between two particles that can be distinguished by the detector. Hence the resolution is proportional to the width of the peak and its position in the spectrum. For the LYSO based detector modules it is defined as follows:

$$R = \frac{\mathrm{FWHM}}{E_{peak}} \sim \frac{\Delta E}{E}. \tag{5.6}$$

Here, FWHM denotes the full-width at half maximum and $E_{peak}$ the position of the calibration peak in the energy spectrum. For a Gaussian-shaped peak, the relation between the FWHM and the $\sigma$ is given by:

$$\mathrm{FWHM} = 2\sqrt{2\ln(2)} \cdot \sigma \approx 2.355\sigma. \tag{5.7}$$

In the case of a perfectly Gaussian-shaped calibration peak, the resolution could be obtained by fitting a Gaussian to the peak and calculate the resolution from the fit result. Unfortunately, this approach turned out to be impossible for the LYSO based detector modules due to the double-peak issue discussed in Section 5.3.1.7. Therefore another approach was chosen: A histogram was filled with all the events recorded for a given calibration. The position of the calibration peak was given by the center of the maximum bin in the spectrum. Starting from this position, the bin on the left and the right of maximum was found where the peak decreased below half of the maximum value for the first time. The distance between these two bins resulted in the FWHM for this peak. This method worked for the clean peaks as well as for the broaden or double-peaks. Figure 5.19 shows examples of the two calibration peak for a 150 MeV deuteron beam in two different modules. Figure 5.19a is an example of a module with a very clean peak where the resolution could have been extracted using a Gaussian fit ad Figure 5.19b shows a module with a clear double-peak where even a double Gaussian fit does not describe the shape well. The black lines indicate the FWHM range. For modules that display a double-peak, this method of calculating the resolution does lead to an underestimation of the actual resolution of the module. Another possibility would have been to extract the resolution from only one of the two peaks, but it was decided that the resolution extraction should reflect the actual situation when the modules are used in the final polarimeter and in this case, it is better to describe the worst case scenario.

The resolution was calculated for all LYSO based detector modules using all available beam energies. Figure 5.20 shows the average of the energy-dependent resolution for both versions of the LYSO based detector modules. Due to the difference in the peak shape mentioned before, the spread of the resolution of the modules at the same energy can be quite large which is reflected in the big error bars. The resolution of the SiPM based detector modules is better than for the PMT based version. With an increase of the beam energy, the value of the resolution decreases, i.e., the larger the energy, the better the resolution gets. The measurement for both versions of detector modules was

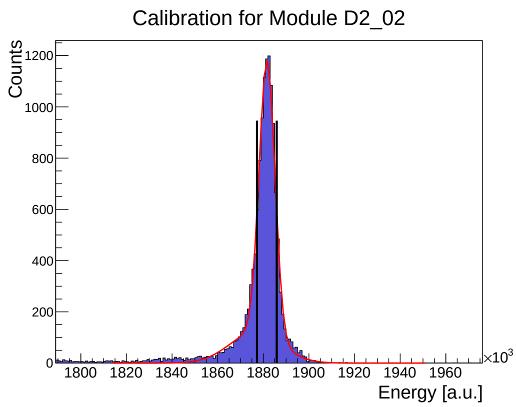


(a) Example of module a clean single peak.

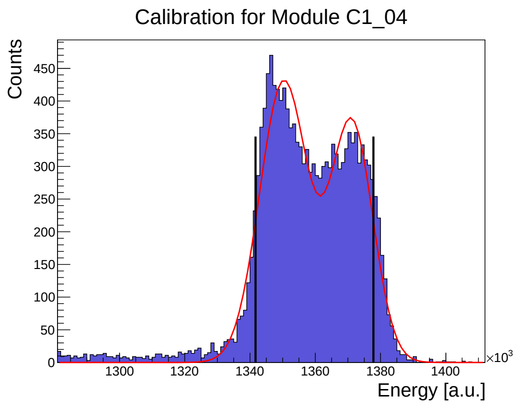


(b) Example of module with a double-peak.

Figure 5.19: Zoomed-in energy spectra for calibration peaks of two LYSO based detector modules in a 150 MeV deuteron beam. The black lines indicate the region for the FWHM. The red line shows the attempt to fit the peaks using a single and double Gaussian fit, respectively.

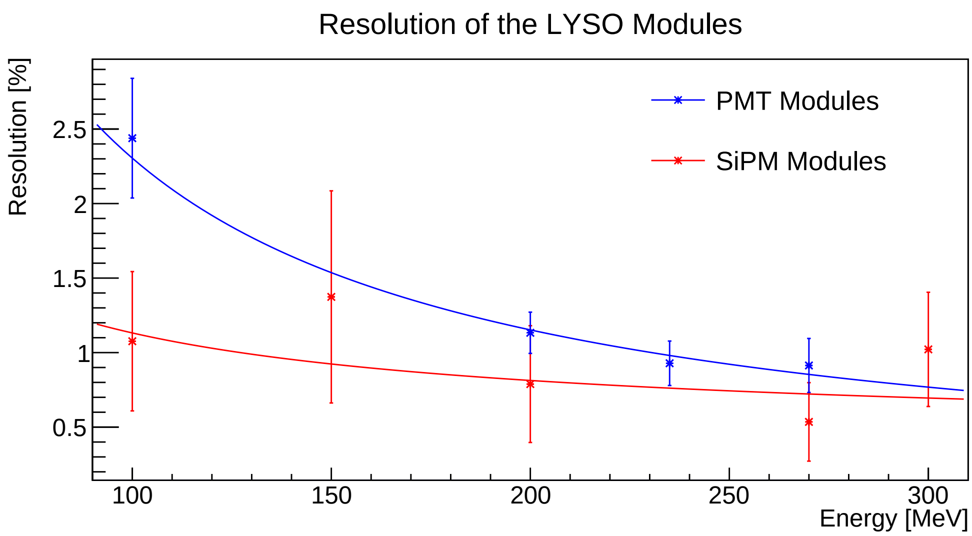


Figure 5.20: Mean of the energy resolution of both versions of the LYSO based detector modules as a function of the deuteron beam energy. The solid lines represent a fit using Equation (5.8). The error bars indicate the width of the distribution of the resolution.

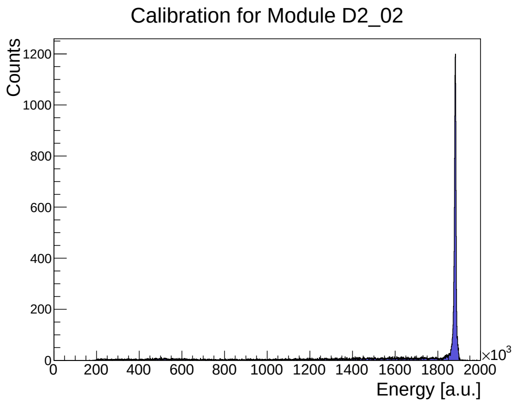


(a) Example of a single peak.

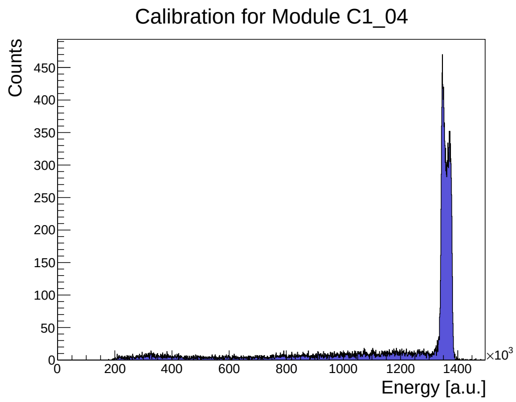


(b) Example of a double-peak.

Figure 5.21: Full energy spectra for calibration peaks of two LYSO based detector modules in a 150 MeV deuteron beam.

fitted with the following formula for the energy dependent-resolution:

$$R(E) = \frac{A}{\sqrt{E}} \oplus \frac{B}{E} \oplus C. \tag{5.8}$$

This equation is usually used to describe the resolution of a calorimeter and can, therefore, be applied to the LYSO based detector modules as they can be considered to be calorimeter modules since they absorb the whole energy of the detected particle. The $\oplus$ operator is an abbreviation for the quadratic sum. The parameters $A$, $B$ and $C$ can be used to describe different properties of a calorimeter. $A$ is called the stochastic term and includes the statistical fluctuation of the detector module while $B$ and $C$ are more influenced by the readout electronics and non energy-dependent contribution such as noise. Analyzing the individual terms would go beyond the scope of this work. However, the fits can be used to interpolate the resolution for beam energies between the measured points.

The most important result of the resolution measurement is the fact that the SiPM version of the LYSO based detector modules have a very high resolution of around or less than 1% over the whole measured energy range. With this resolution, the main task of the modules which is the identification and counting of elastically scattered particles can be done without a problem. Even in the case of the modules that show the double-peak behavior, particle identification is still possible without any issues. It can be argued, that the double-peak issue could have only be discovered because of the high resolution of the modules. Figure 5.21 show the calibration peaks from Figure 5.19 again but this time, not zoomed-in. The very narrow peaks illustrate how good the resolution of the modules is.

Before a LYSO based detector module was used in the experimental setup, it was tested for light tightness and general performance in the lab. David Mchedlishvili developed a test setup based on a *Red Pitaya* data acquisition board [53]. After each module was assembled, it was connected to this test setup, and a low energy spectrum was measured. A LYSO crystal contains the radioactive lutetium $^{176}$Lu isotope which decays via a $\beta^-$ decay into the hafnium $^{176}$Hf isotope. The emitted electron, as well as the $\gamma$-lines

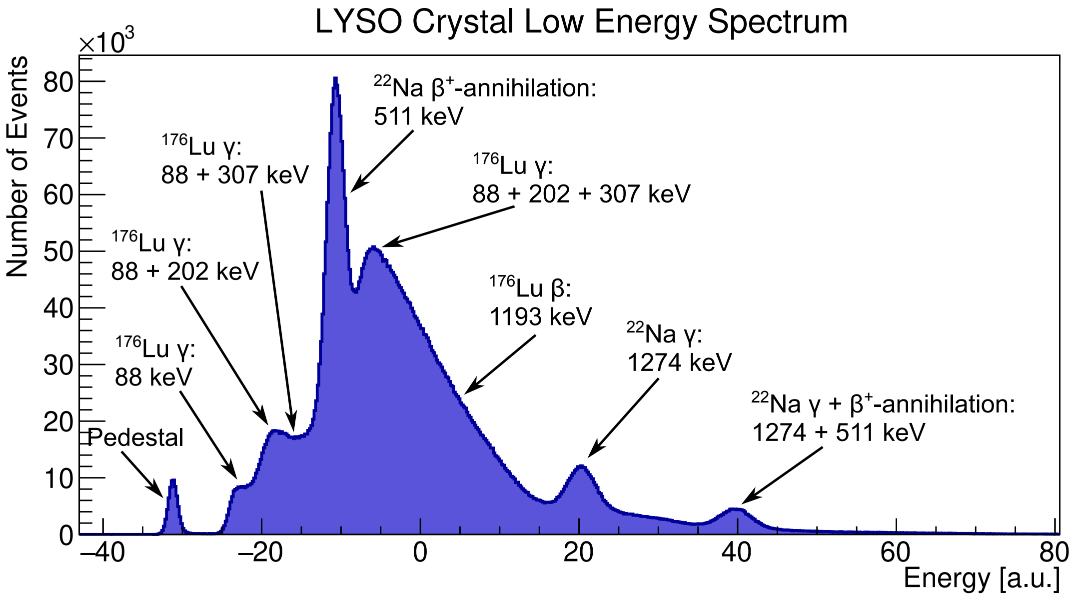


Figure 5.22: Low energy spectrum of a LYSO based detector module recorded in the lab. Three $\gamma$-peaks from the $^{176}$Hf deexcitation as well as the continuous $\beta$ tail are clearly visible. The energy values are taken from [54]. In addition to the internal radiation, a $^{22}$Na source was placed on the module. $^{22}$Na is a $\beta^+$ emitter and the most distinct peak in the spectrum comes from one of the photos created in the $\beta^+ + \beta^-$ annihilation and is therefore located at 511 keV. The $^{22}$Na decay creates one $\gamma$-line at 1274 keV [55] which is also clearly visible. Since the LYSO crystal provides a large volume, the probability of catching multiple $\gamma$ particles in the same event is rather large and this leads to the peaks that represent the sum of multiple $\gamma$ energies.

from the deexcitation of the $^{176}$Hf isotope, are visible in the low energy spectrum if the module is light tight and the scintillator crystal is properly connected to the SiPM array. In addition, a $^{22}$Na and $^{60}$Co source were used to test the modules. Figure 5.22 is an example of such a spectrum. If the module is not well packed or the interface between the LYSO crystal is not perfect, it can be found out from this measurement, and the module had to be taken apart and be reassembled. The structures in the low energy spectrum that origin from the lutetium decay matches the description from the LYSO crystal datasheet given in [37]. Performing this lab test, assured that the LYSO based detector modules perform well in the actual experiments using the deuteron beam and in all three iterations of the polarimeter development, no modules showed any sign of light leakage. An evaluation of the low energy resolution of the LYSO based detector module using the 511 keV peak results in a value of $\sim 15.3\%$. This explains why no double-peaks structures can be seen in the low energy spectra.

#### 5.3.1.3 Gain Stability of the LYSO Based Detector Modules

To quantify the requirement of long term stability of the LYSO based detector modules, it is important to investigate the different sources that can influence the overall gain of the modules. The main source of gain variation can come from the temperature dependence of light yield of the LYSO scintillator and the gain of the SiPM arrays as

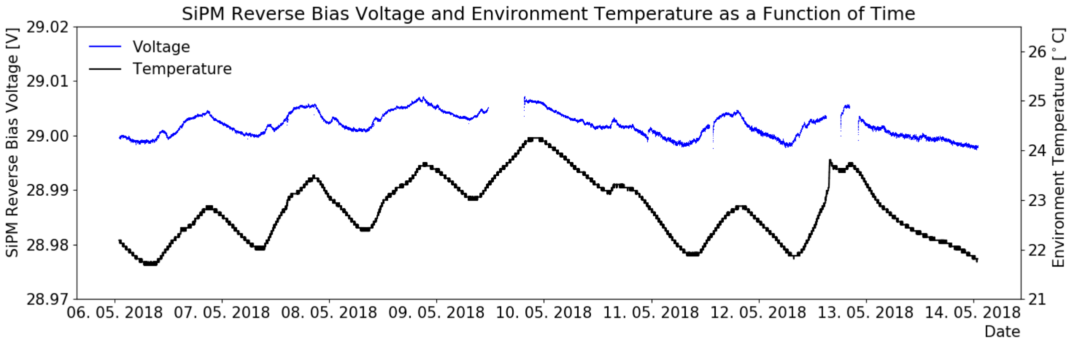


Figure 5.23: Measurement of the environment temperature in the Big Karl area (black) as well as the reverse bias voltage (blue) that was applied to the SiPM array of a LYSO based detector module as a function of time. This graph comprises the eight days of measurement done in the last beam time. The supply voltage for the SiPMs had to be turned off several times in this period, hence the gaps in the measurement.

well as the gain dependence of the latter on the reverse bias voltage. According to the manufacturer of the LYSO crystals, the variation in light yield accounts to $-0.28\,\%\,\mathrm{K}^{-1}$ in a temperature range of 25 °C to 50 °C. It is thereby one order of magnitude smaller than comparable crystal scintillators such as BGO or LSO, see [37]. For SiPMs, the gain dependence on the temperature is given by $-0.8\,\%\,\mathrm{K}^{-1}$ for the SenseL types [56] and $-0.3\,\%\,\mathrm{K}^{-1}$ for the Ketek types, both at 21 °C. For a silicon-based sensor, this is a very low value. The APD type that was used for the *Crystal Barrel* detector upgrade at the ELSA accelerator has a temperature dependent gain variation of around $-2.3\,\%\,\mathrm{K}^{-1}$[57]. The fact that the individual APD pixels in a SiPM are operated in the Geiger-mode makes the whole device much less sensitive to temperature changes compared to an APD that is operated in the proportional mode.

In the last beam time using the 3$^{\text{rd}}$ iteration of the experimental setup. The environment temperature in the Big Karl area was measured using a DS18B20 temperature sensor with an accuracy of ±0.5 K and a resolution of ∼0.1 K [58]. Simultaneously, the reverse bias voltage for the SiPM arrays of the LYSO based detector modules generated by the designated power supply was measured as well. The result of the eight days of temperature and voltage measurement is given in Figure 5.23. This measurement showed an average temperature of $22.80 \pm 0.65$ °C with a peak-to-peak variation of 2.56 K. By comparing the curves for the temperature and the reverse bias voltage, a correlation between the two is evident. The voltage was set to 29 V at the beginning of the experiment and the measurement showed an average voltage of $29.0018 \pm 0.0022$ V and a peak-to-peak variation of 9.842 mV. To put these numbers into perspective, one needs to know by how much the gain of the SiPM array changes as a function of the reverse bias supply voltage.

For this purpose, the gain of a SiPM array (type ARRAYJ-30020-64P-PCB, see Table B.1) was measured as a function of the reverse bias voltage. The SiPM array was placed in a light-tight box together with a green LED that was illuminating the array through a diffusor foil. The LED was driven by a frequency generator that generated 10 ns flashes at a repetition rate of 10 kHz. The signals from the SiPM array were

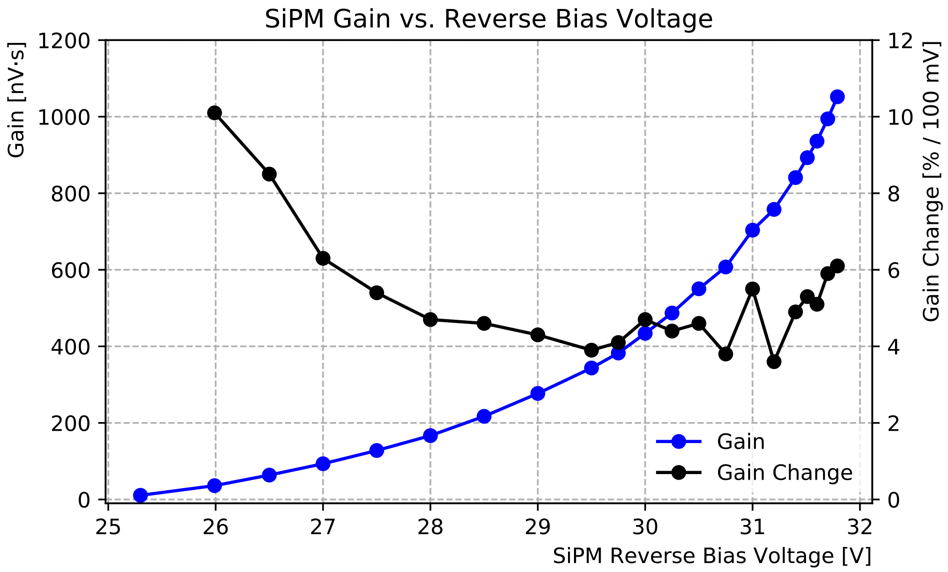


Figure 5.24: Measurement of the gain dependence of a SiPM array on the reverse bias voltage (blue) and the corresponding relative gain change per 100 mV variation (black). The data for this graph was measured in the lab using a green LED pulser with 10 ns flashes at a repetition rate of 10 kHz.

captured with an oscilloscope, and the signal shape was integrated as a measure of the gain of the SiPM. The reverse bias voltage was then successively increased from 25.3 V up to 31.8 V. The result is given in Figure 5.24. The relative gain change was calculated for each voltage step by taking the derivative and is given in the same plot. This measurement revealed that at 29 V, the relative gain change amounts to 4.3 % for a voltage change of 100 mV. Applied to the voltage measurement given in Figure 5.23, a peak-to-peak variation of 9.842 mV equals to a gain variation of 0.423 %. Comparing this result to the temperature peak-to-peak variation of 2.56 K, a rough approximation for the temperature dependent gain variation of the LYSO based detector modules based on the temperature variation of the reverse bias supply generator can be given by $+0.165\,\%\,\mathrm{K}^{-1}$.

The gain dependence of the final signal $S$ on the deposited energy $E$ can be described as follows:

$$S = E \cdot G_{LYSO} \cdot G_{SiPM} \cdot G_{Supply}, \tag{5.9}$$

where the $G$ factors denote the absolute gains of the LYSO crystal, the SiPM array, and the SiPM dependence on the reverse voltage supply. The temperature dependent relative gain variations ($\Delta G$) discussed above can be included in this equation:

$$\begin{aligned} S = E \cdot \\ G^0_{LYSO}(1 + \Delta G_{LYSO}\Delta T)\cdot \\ G^0_{SiPM}(1 + \Delta G_{SiPM}\Delta T)\cdot \\ G^0_{Supply}(1 + \Delta G_{Supply}\Delta T), \end{aligned} \tag{5.10}$$

where $\Delta T$ denotes the temperature changes relative to an absolute temperature $T^0$ at which the gain $G^0$ is defined. By factoring out Equation (5.10) and keeping only the terms linear in $\Delta T$, it can be simplified to:

$$S \approx E \cdot G^0_{LYSO} G^0_{SiPM} G^0_{Supply} \cdot \\ (1 + [\Delta G_{LYSO} + \Delta G_{SiPM} + \Delta G_{Supply}] \Delta T) \tag{5.11}$$

By combining temperature dependent effects as stated in Equation (5.11) to calculate an overall temperature dependence of gain of the LYSO based detector modules, one finds a value of approximately $\Delta G \approx -0.915\,\%\,\mathrm{K}^{-1}$ for the SensL based modules and $\Delta G \approx -0.415\,\%\,\mathrm{K}^{-1}$ for the Ketek based types. A 1 K temperature variation results in less variation in the energy spectrum than expected from the energy resolution of the modules. These results show that the LSYO based modules can be operated without the need of active temperature regulation on the modules if it is possible to keep the environment temperature stable within 1 K. If the environment temperature varies more than that, it will affect the resolution of the LYSO based detector modules. Nevertheless, even a variation in the order a few Kelvin is not enough to significantly affect the ability of the polarimeter to identify elastic events. One option to make the detector modules less sensitive to temperature changes is to add a feedback-loop to the reverse bias voltage generator that would compensate the gain loss of the LYSO crystal and SiPM with a temperature increase by increasing the bias voltage accordingly. This option is being investigated at the moment by David Mchedlishvili at the SmartLab in Tbilisi.

#### 5.3.1.4 Linearity in Detector Response

In the last beam time in May 2018, a total of 52 detector modules have been installed. All the modules in the four arms of the cross (see Figure 5.40) were equipped with 20 µm SensL SiPM arrays, and the four edge modules (prefixed with **C**) used two versions of Ketek arrays with a SiPM pixel size of 15 µm and 25 µm, respectively. The linearity of the modules was specified by plotting the peak position as a function of the deuteron beam energy, as shown in Figure 5.25. To perform this measurement, the module was positioned such that the deuteron beam would penetrate it directly and all targets and the start counter were removed from the beam path. In the case of a completely linear module, the integral of the detected signal is directly proportional to the beam energy and thus can be described by a linear fit. This works fine for the modules equipped with a Ketek SiPM array, but in the case of the SenseL SiPM arrays, the module deviates from a linear behavior for higher energies.

For the Ketek based modules, the linear fits were anchored at the origin and the measurements at 150 MeV and 200 MeV for the 15 µm and at the origin and the measurement at 200 MeV for the 25 µm version. The result of the linear fit was then extrapolated up to a beam energy of 300 MeV, and it turned out that the extrapolated function was in good agreement with the measurement at 300 MeV. This indicates that these modules are very linear.

In the case of the SensL based modules, the linear fit (dashed line) was anchored at the origin and at the measurement at 150 MeV. The extrapolation of this fit disclosed the

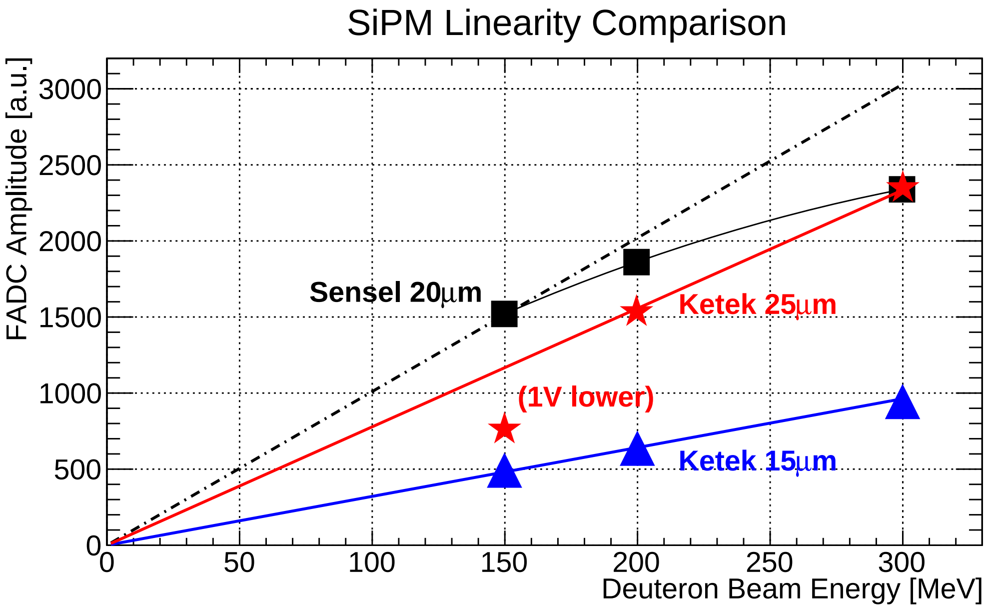


Figure 5.25: Linearity of LYSO based detector modules equipped with different types of SiPM arrays. The amplitude of the recorded signal is plotted as a function of the deuteron beam energy. The relation between the amplitude and the beam energy can be described by a linear function in the case of the Ketek based modules (solid line). Note that the point at 150 MeV for the 25 µm Ketek based module was measured with a bias voltage that was lowered by one volt compared to the other point and can therefore not contribute to the linearity fit. The SensL based modules deviate from the linear behavior (dashed line) with increasing beam energy. Plot by courtesy of Irakli Keshelashvili.

non-linear trend for higher energies. The full range of the measurements done with the SenseL version was fitted again with a quadratic function (solid line) that was able to describe the energy dependence of these modules. At 300 MeV, the relative deviation of the measurement from the linear function equals to $\sim$ 23% and evaluating the quadratic fit function suggests that this module will be fully saturated (slope approaches zero) at $\sim$400 MeV. The slight saturation of the SensL based detector module is a possible explanation of the small increase of the resolution value at 300 MeV in Figure 5.20, as 48 of the 52 SiPM based detector modules were equipped with SensL sensors.

A possible explanation for this non-linear trend for the SensL arrays compared to the Ketek SiPMs can be found in the difference in the PCB layout of the manufacturer. The SensL SiPM array provides an additional, capacitive decoupled output (*Fast Output*) on each of the individual pixels of their SiPMs, see [38]. On each of the 64 SiPM of the array, all the anodes, cathodes as well as the fast outputs are tied together. The SiPM array is equipped with two 80-pin connectors that allow for the connection to the baseboard of the detector modules (see Figure 5.4a). A total of 160 pins is not enough to provide an individual connection to all three inputs on each of the 64 SiPMs on the array. SensL designed their array such that all the cathodes are interconnected on the array itself (common cathode) and an individual path was provided for each anode and fast output of each SiPM. The copper traces on the array are very thin and therefore their resistance is not as small as for the wider traces on the baseboard of the modules. When a LYSO based detector module that is equipped with such a SensL array is exposed to a high energy deuteron beam, the number of photons created by the scintillator crystal can be quite large (33200 photons per MeV of deposited energy, see [37]). This large number of photons trigger almost all SiPM pixels simultaneously, and hence the current draw of the whole array can be rather large during a very short time. The current enters the array through the common cathode and causes a voltage drop on the trace itself. This voltage drop reduces the effective reverse bias voltage of the individual pixels and eventually causes a reduced gain of the SiPM array as a whole. In the case of the Ketek arrays, there is no fast output available. The array uses the same 2 x 80 pins connector but provides an individual trace for both, anode and cathode of each of the 64 SiPMs. When a large number of pixels fires in this array, the current draw on one cathode is therefore reduced by a factor of 64 compared to the common cathode of the SenseL arrays and the voltage drop on each cathode is too small to cause a significant reduction of the gain.

This non-linear trend of the SensL based detector modules is unfortunate, but since they are used as a polarimeter it should not affect their ability to identify elastically scattered events. However, if in the future new modules will be added to the polarimeter, it makes sense to use Ketek SiPM arrays over the ones from SensL.

#### 5.3.1.5 Detection Efficiency

Due to the high density of the LYSO scintillator crystal, it is safe to assume that whenever a particle hits the crystal, it will produce a scintillation flash. The large number of photons being produced assures that the signal will be recorded by the SiPM array especially due to the large quantum efficiency of each APD pixel and the densely packed surface of the SiPM array. It can, therefore, be stated that a LYSO based detector module has a detection efficiency of approximately 100% when a deuteron hits the module straight in the center of the detector.

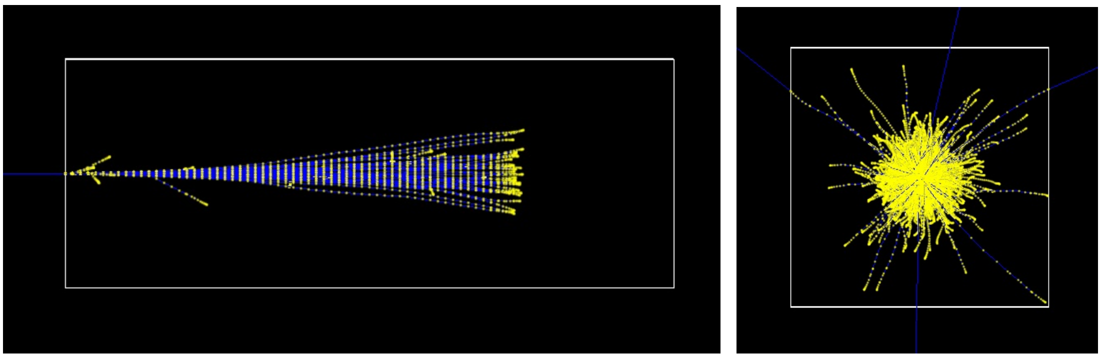

(a) Side view. (b) Front view.

Figure 5.26: GEANT4 simulation of 270 MeV deuterons being stopped in a LYSO crystal by Giorgi Macharashvili

For particles that hit the fringe of a module, the situation is different. A particle that hits the scintillator will not necessarily travel on a straight path within the crystal

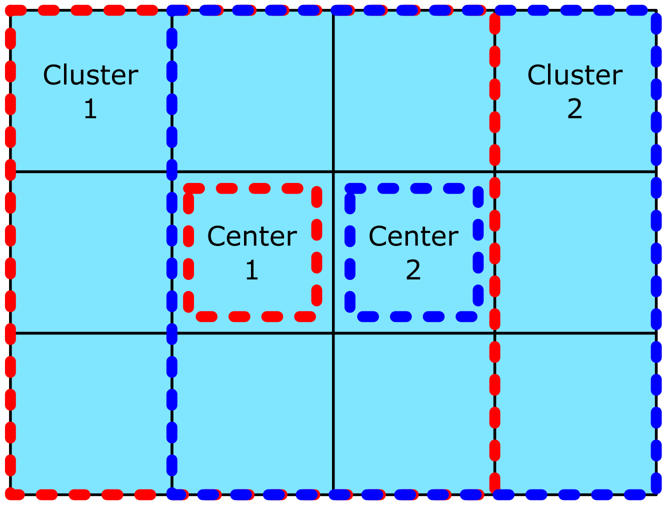


Figure 5.27: Schematic representation of the LYSO based detector module arrangement and the two clusters that can be formed on each arm of the detector.

until it comes to a full stop, but instead can be deflected from its straight path due to scattering off the nuclei of the crystal material. This process is known as *range straggling* [31]. The expected value of the volume in which the particle is stopped can be described by a cone with the tip pointing towards the point of entrance of the particles. Figure 5.26 shows a GEANT4 simulation by Giorgi Macharashvili for the paths of multiple 270 MeV deuterons being stopped in a LYSO crystal. If a deuteron hits the scintillator crystal close to its fringe, it is possible that the particle leaves the first module and enters a neighboring one. In this case, the first module will still record parts of the kinetic energy of the particle, but this event will not be in the elastic peak in the energy spectrum of this module and effectively reduce the number of detected deuterons and therefore the detection efficiency.

To evaluate the magnitude of this effect, the number of events in one module was compared to a cluster including this module and all of its direct neighbors, see Figure 5.27. In the 2$^{\text{nd}}$ iteration of the experimental setup, the modules on each arm were arranged such, that two center modules were surrounded by eight neighbor modules. This setup allowed for the calculation of the ratio between the number of events in the center crystal and the number of events of the corresponding cluster for all four center modules. To assure that the entrance points of the deuterons were spread evenly over the whole cluster, the data from runs with different targets were combined. Additionally, each arm was moved to different positions to get an even more even coverage of the modules with scattered deuterons. The result can be seen in Figure 5.28.

The center histograms contain all the events that have triggered this module. The cluster histogram contains the energy sum of all modules of the corresponding cluster when the center module generated a trigger. In the cluster histograms for Center Left 1 and Center Left 2, a high energy tail is visible. It is not clear why these tails are there but they might origin from pile-up. In any case, the results from these modules have to be treated with caution because additional events in the cluster histogram will lead to a decrease of the fringe efficiency. The spectra of the Center Right 2 modules look very

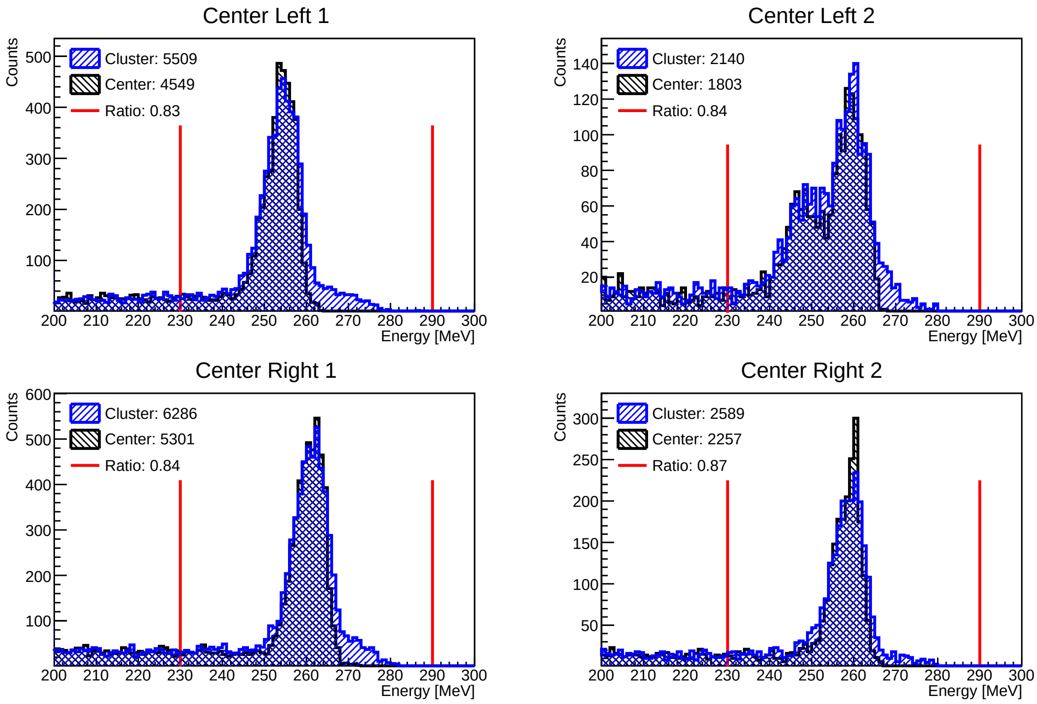


Figure 5.28: Comparison of the four spectra of the center crystals with their corresponding clusters at a deuteron beam energy of 270 MeV. The ratio between the number of events in the spectra of the center crystal and the clusters equals to the fringe efficiency of the module, i.e., the fraction of events that are identified as deuterons when the module face is evenly bombarded. The integration range to obtain the number of events was the same for the center crystals and the clusters and is indicated by the red lines.

reasonable, and the fringe efficiency from this module is also slightly larger than for the other modules. On average, a fringe efficiency of $\sim 84.5\%$ was measured at 270 MeV. This means, when the scintillator face is evenly covered by deuteron hits, $\sim 84.5\%$ are within a region where they can be identified as deuterons by just applying a cut to the energy spectrum. On the other hand, if the number of events within a specific cut is known, the actual number can be obtained by applying this fringe efficiency correction. Applied to the 30 mm x 30 mm face area of the LYSO based detector module, this number can be translated into a geometrical fringe with a width of $\sim$1.2 mm around the border of the module face.

In the case of a polarimeter with the detector modules at a fixed place, the previous correction cannot be applied to calculate the actual number of events, because due to the strong polar angle $\Theta$ dependence of the unpolarized cross section, the hits will not be evenly spread over the face of the detector modules. However, the geometrical interpretation of the fringe is still valid and it will reduce the effective covered area of the modules. If the detector is used in its intended polarimeter application, the fringe efficiency does not need to be known as it will cancel out if a cross ratio method is used to calculate the polarization.

#### 5.3.1.6 Deuteron Reconstruction Efficiency

The deuteron is a very light bound system of a proton and a neutron. Its binding energy amounts to 2.224 MeV [59] which is only $\sim 0.11\%$ of its mass-energy of $m_d =$ 1875.612 MeV [60]. When a deuteron scatters off another nucleus, it is rather likely that it breaks-up into its constituents nuclei. In the case of a polarimeter that uses a carbon target for the polarimetry reaction and a heavy scintillator crystal, there are different places where such a break-up reaction can occur. The first place where this reaction can take place is the target itself. Dependent on the setup, the deuteron beam will pass the exit window of the beam pipe before it hits the target as was the case in the different iterations of the polarimeter development in the Big Karl area. When the polarimeter will be installed inside of the COSY accelerator, the target will be inside of a vacuum chamber, and the scattered deuterons will pass the exit window before they hit the LYSO based detector modules. In any case, a break-up reaction can take place at the exit window as well. Finally, the deuteron will penetrate the scintillator crystal and can break within the LYSO material.

When a deuteron undergoes a break-up reaction, the kinetic energy can be randomly distributed between the proton and the neutron. The neutron is usually undetectable with the detector modules of the polarimeter, but the proton on, the other hand, can be detected. The energy spectrum of break-up protons is spread over the whole energy range up to the endpoint energy equal to the kinetic energy of the projectile deuteron. However, it is very unlikely that the proton takes the full kinetic energy of the original deuteron and therefore the break-up proton peak does not or only slightly overlap with the elastic deuteron peak. The angular distribution of the proton after a break-up reaction does not reflect the original deuteron scattering angle anymore. Generally speaking, a proton from the break-up reaction of a deuteron will not carry the asymmetry information from the elastic deuteron carbon scattering anymore and has to be removed from the analysis. Removing the proton contribution from the energy spectrum of the elastic deuteron scattering can be done by either applying a tight cut on the elastic deuteron peak or using a cut in the $\Delta E$ vs. $E$ plot where the deuterons and the protons occupy different bands, see Section 5.3.2.1.

For deuterons that break within the LYSO crystal, the situation is different. As they enter the detector module as a deuteron, they carry the asymmetry information from the polarimetry reaction and can be used to calculate the polarization as well. The problem is the identification of these events. In the $\Delta E$ vs. $E$ plot, they are located on a band that overlaps the proton band from the break-up protons off the target and cannot be disentangled. By applying a cut on the elastically scattered deuteron, the break-up protons from inside of the scintillator are removed as well.

A possible approach to overcome this issue is to measure the fraction of deuterons that undergo a break-up reaction within the LYSO scintillator in a setup were almost no contamination from other protons exists. This was done in the 1$^{\text{st}}$ iteration of the polarimeter development where the experimental setup allowed the LYSO based detector modules to be placed close to the exit window of the beam pipe. A very thin plastic scintillator with the dimensions of 10 mm x 10 mm x 2 mm was placed in front

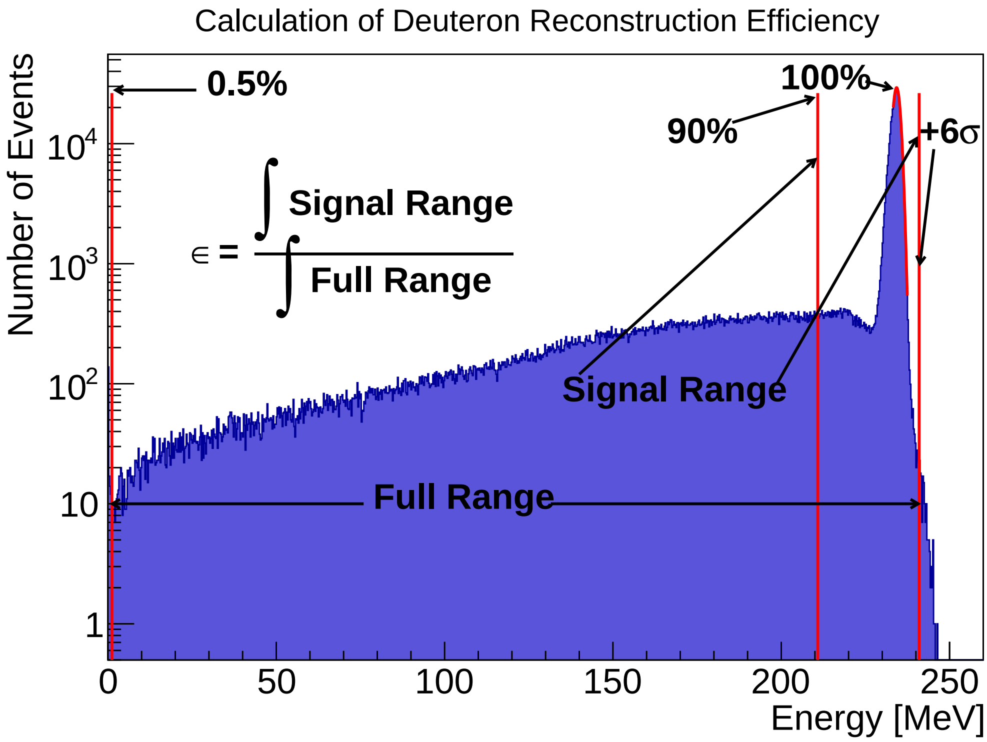


Figure 5.29: Energy spectrum for a LYSO based detector module in a 235 MeV deuteron beam. The ranges for the calculation of the deuteron reconstruction efficiency are indicated with the red lines.

of the detector module to act as a trigger. This trigger selected only deuterons that hit the LYSO scintillator in the very center and removed events that would hit the modules at the edges and assured that all deuterons would be stopped fully within the crystal. The energy spectrum that was recorded with this setup consisted of only deuterons and protons that underwent a break-up reaction inside the LYSO crystal. Since the exit window consists of very thin (0.4 mm) stainless steel, its break-up proton contribution can be neglected. Figure 5.29 shows this spectrum for 235 MeV deuterons. It is dominated by a large deuteron peak at the energy of the beam and a rather flat background from the break-up protons. To calculate the number of deuterons that underwent a break-up reaction, the spectrum was divided into two ranges. The deuteron peak was fitted with a Gaussian and the peak value was defined as 100%. The *signal range* was defined as the range between 90% and $+6\sigma$ of the Gaussian. This assured that the whole peak was in the signal range. The 90% point as the lower end is rather arbitrary, but as long as this definition is applied to the spectra of all measured beam energies the results can be compared among each other. The second range, the *full range*, was defined between the 0.5% point to exclude any pedestal effects, up to the end of the signal range. By dividing the number of events in these two ranges, the deuteron detection efficiency was defined and describes what fraction of the deuteron did not break up when being stopped by the LYSO crystal. Like any other efficiency correction, the deuteron detection efficiency can be multiplied with the number of events after a cut on the elastically scattered deuterons was applied to obtain

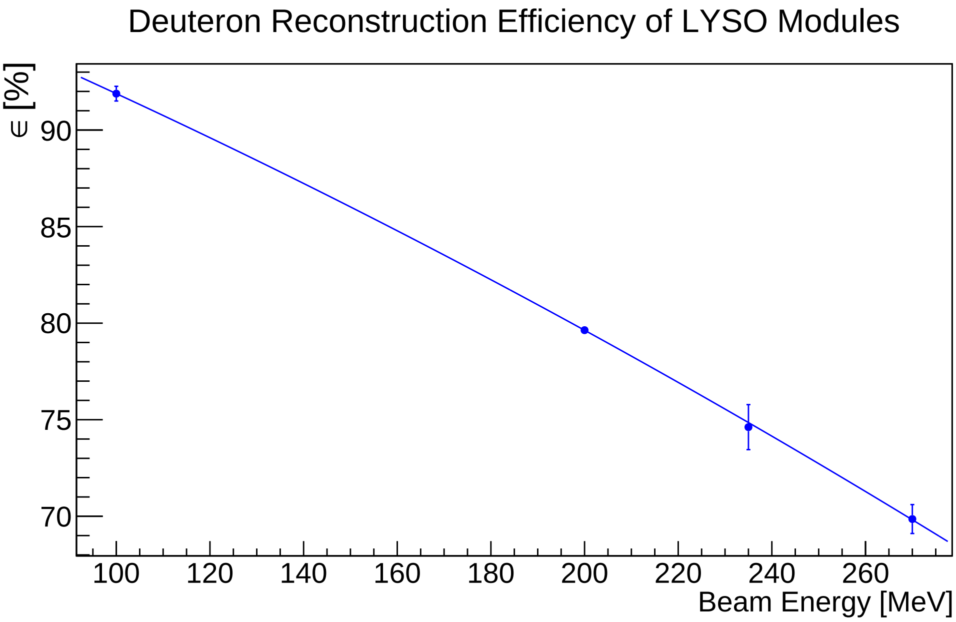


Figure 5.30: Deuteron reconstruction efficiency in LYSO as a function of the beam energy. The measurements from the four PMT based detector modules are averaged and the error bars represent the statistical variation and indicate that the number of recorded events was not equal for all energies. The energy dependence can be described by a quadratic fit function (solid line).

the actual number of deuterons that have hit the corresponding detector module.

This measurement was done for all four beam energies used in the first beam time, and the result is given in Figure 5.30. The measurements can be described by a quadratic fit (solid line). The measurements show that for increasing beam energy, the probability for a break-up reaction within the LYSO material increases and therefore the deuteron reconstruction efficiency decreases. As for any other module dependent efficiency correction, the deuteron reconstruction efficiency gets canceled when the polarization is calculated using a cross ratio method. However, this efficiency could be used if the LYSO based detector modules will be modeled in a GEANT4 simulation.

#### 5.3.1.7 Double-Peaks

The double-peak issue became evident when the 2$^{\text{nd}}$ iteration of the LYSO based detector modules was tested in the deuteron beam. The modules started to show a double-peak in the energy spectrum (see Figure 5.21b) in situations where only a single peak was expected, i.e., when the module was placed directly in the beam for resolution measurements. At first, it was thought that it would affect only certain modules, but it turned out that all modules were affected by this issue under certain conditions. The main problem was that it was not possible to figure out what settings in the detector setup or the beam control would cause the double-peak to appear or disappear for a given module.

Many different theories have been found to try to explain the problem. At first, it was assumed that the deuterons would scatter or lose part of their energy in the iron from the collimator, that was intended to be used at the beginning of the 2nd iteration of the detector development. The removal of this part did not change anything. What made this problem very hard to figure out was the fact that there were two distinct peaks visible. This ruled out a lot of possible sources such as variations in the gain of the SiPMs and their supply voltages as well as any temperature dependent effects. If any of these effects were present, it would have led to a broadening or smearing of the peak as there was no obvious reason why the gain would jump between distinct values. Analyzing the energy spectrum of a module showing a double-peak as a function of time showed, that the double-peaks were present at any point of the measurement and that there were no jumps from one peak to the other one visible. Another theory was that there was some loose material inside the beam-pipe. If one part of the deuterons would pass through this material they would lose part of their kinetic energy, and this could explain the observed double-peaks.

The explanation of the issue was found accidentally during the last beam time. In order to measure the resolution of the detector modules, the detector was moved as close to the exit window of the beam-pipe as possible. The detector was then moved in such a way that one module after another was positioned in the beam and an energy spectrum was recorded. The exact same procedure was applied in the other beam times as well with one small difference: In the other beam times, the data acquisition was turned off while the detector was moving and one individual file was taken for each module. In the last beam time, it was decided that the data acquisition could be left running and the spectra of all modules could be stored in one file. After the spectrum of the first module was recorded, the detector was moved to place the next module in the beam. While the detector was moving the module through the beam, one peak appeared on the online spectrum and as the detector was continuing to move the module a second peak appeared. To confirm the observation, two spectra were taken with the beam hitting either side of the module and one with the beam hitting the center of the module. The first two spectra showed a single peak but at different positions but the center spectrum had two peaks, each one on the position found in the side spectra. This observation led to the decision to scan the face of the modules with the beam and check how the module position affected the peak position.

The slow control software allowed to write a script that would automatically move the modules in a way that the beam penetrated them on defined grid points and take an energy spectrum measurement for each of the points. Each module was scanned in a 5 x 5 grid with 5 mm distance between the points. From the spectra, the peak position was extracted and filled into a two-dimensional histogram. This procedure was repeated for the available beam energies of 150 MeV, 200 MeV, and 300 MeV. Figure 5.31 shows an example for the maps that were measured using this procedure. To see the how much the peak position differs for each grid point, the obtained positions were scaled to the maximum peak position measured for this crystal and the individual grid points show the relative deviation from the maximum peak position in percentage. In addition, the summed spectrum for all the grid points is shown as well. For 150 MeV and 200 MeV, the two peaks, origin from the two regions in the crystal, are clearly visible. For 150 MeV this module showed variations in the upper half in the order of

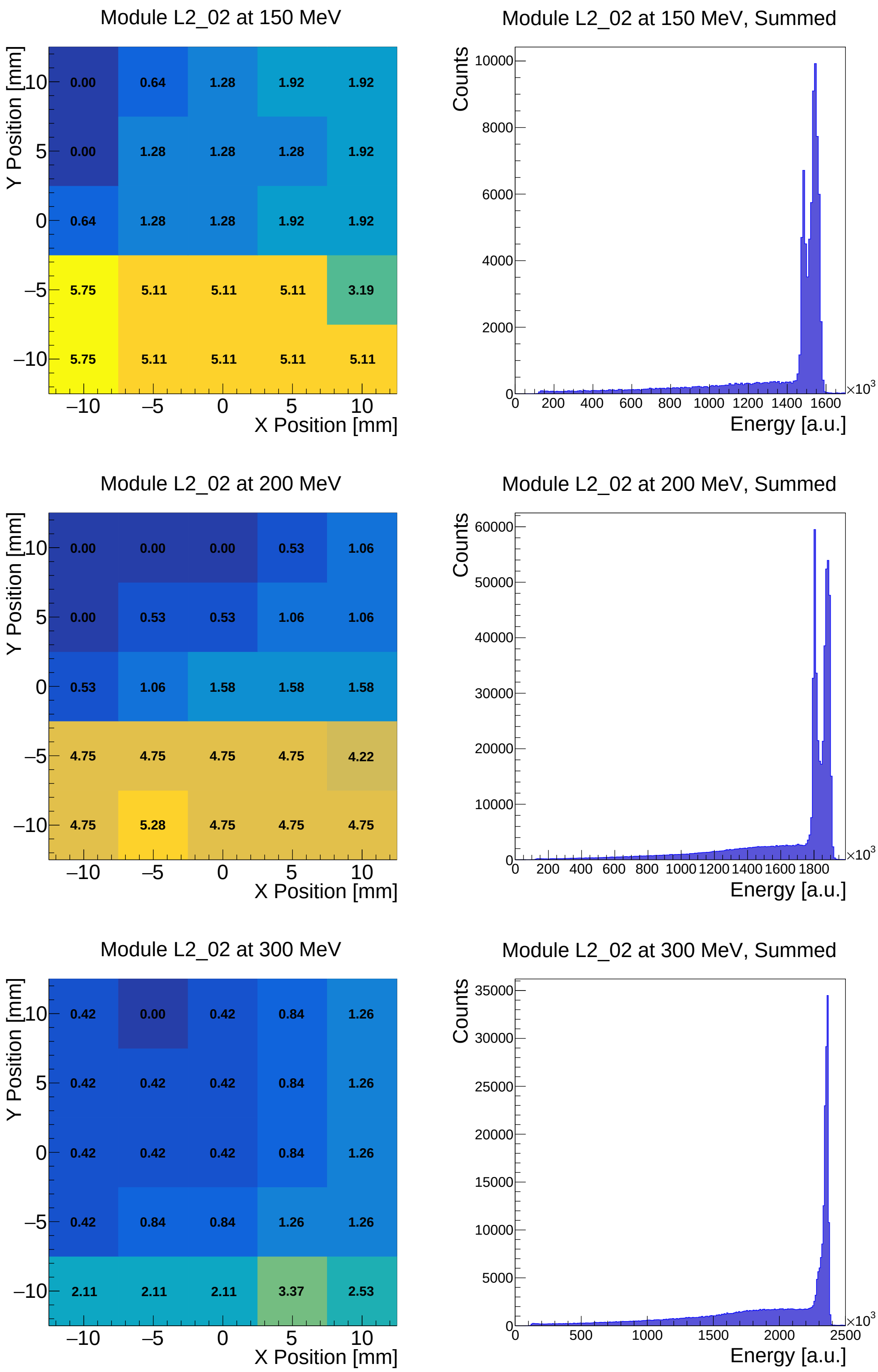


Figure 5.31: Left column: maps of the relative peak position in module L2_02 for deuteron beam energies of 150 MeV, 200 MeV, and 300 MeV . The peak position for each grid point was scaled to the maximum peak position and the values given for each grid point represent the relative deviation from this maximum given in percentage. Right column: summed histogram of all the individual grid points. These histograms show the situation when the deuterons hit the crystal face evenly distributed.

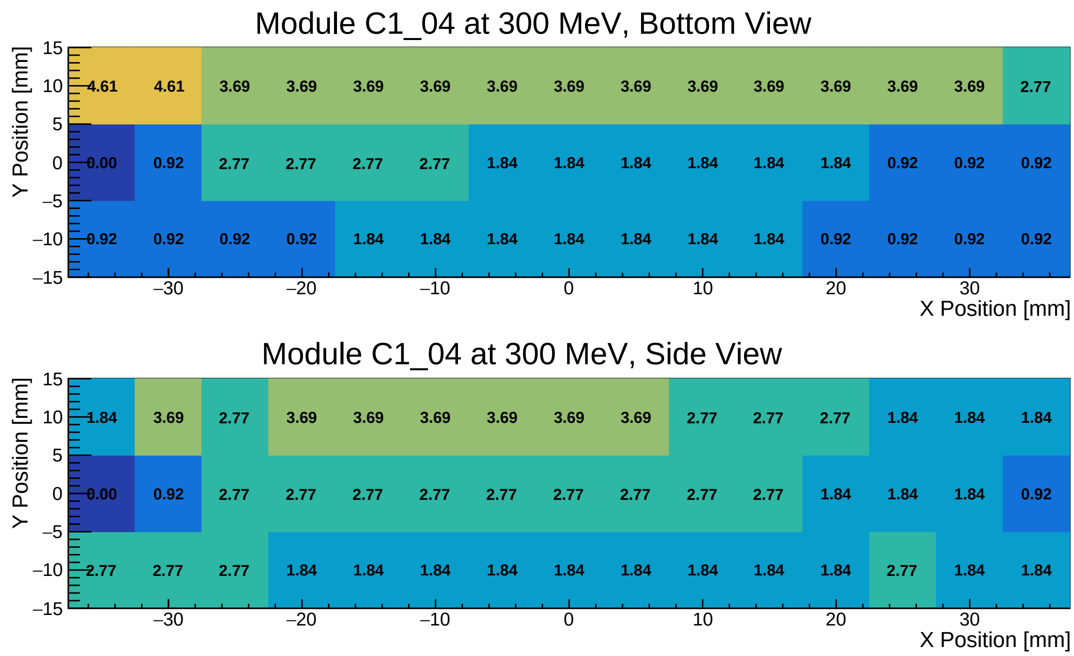


Figure 5.32: Grid scan of the long sides of the module C1_04 with a 300 MeV deuteron beam. 15 x 3 points were measured with a horizontal spacing of 5 mm and a vertical distance of 10 mm. The peak position that was obtained from the energy spectrum obtained in for each of the grid points was scaled to the maximum peak position, and therefore each grid point shows the relative deviation from this maximum. The top map was measured by scanning the bottom of the module, i.e., the long side pointing downwards when the module is installed in the polarimeter. For the lower map, the crystal was rotated by 90°.

$\sim 1.5\%$ which leads to a broadening of the right peak in the summed spectrum. In the lower half of the module, the variations between the grid points are smaller which is reflected in a more narrow left peak in the summed spectrum. The same result can be seen in the example at 200 MeV as well. At 300 MeV, there was no clear step measured in the grid measurement of the crystal face and since most of the variations are in the order of the module resolution, the summed spectrum shows only one peak. However, the lowest row of the grid measurement shows a $\sim 2\%$ deviation from the maximum, and again a broadening on the low energy edge of the peak can be observed.

The map measurement was repeated for all 52 LYSO crystals at all three beam energies. An all of them showed differences in the peak position as a function of the beam position similar to the example shown in Figure 5.31. The LYSO crystal of module C1_04 was measured along both long sides as well, see Figure 5.32. For this purpose, the module was removed from the detector assembly and mounted on top of the experimental table which allowed to move the module in the beam and scan the sides.

The conclusion from this measurement was that the LYSO crystals are inhomogeneous in their light yield depending on the position of the volume inside the crystal where most of the energy was deposited. As described in Section 5.3.1.1, the majority of the energy is deposited in a rather small volume of the scintillator crystal. By using different energies, one probes different depths regions in the crystal. According to Equation (5.2), 150 MeV corresponds to a penetration depth of 22.1 mm, 200 MeV to 36.5 mm and 300 MeV to 73.5 mm. This measurement together with the side measurement shown in Figure 5.32 indicates that the difference in light yield cannot be described by a simple yield line dividing the crystal into two regions but that the inhomogeneities within the LYSO scintillators follow a much more complicated three-dimensional pattern. It is important to note that it can be excluded that the inhomogeneity origin from the SiPM arrays for two reasons: First, the light that hits the SiPM array from the scintillator consists only of a small fraction from a direct cast but most of it reaches the sensor after multiple internal reflections. This means that the scintillation light is evenly spread over the whole SiPM sensor independent of the origin of the light within the scintillator. Second, this was also experimentally checked. For this purpose, one module was opened after the map was measured and the SiPM array was rotated by 90° while the LYSO crystal orientation remained unchanged. After the module was reassembled with the SiPM array in its new orientation, the map was remeasured, and the result was the same as before, i.e., the position dependence of the peak did not change with the reorientation of the SiPM array.

The question that remains is, how does the double-peak issue affect the performance of the LYSO based detector modules in the final polarimeter setup. It is obviously not ideal, and there is nothing that can be done to remove these inhomogeneities from the LYSO crystal nor would it make sense to order new crystals. One can argue, that the issue was only visible because of the very high resolution of the SiPM array based design of the modules. This means that by using another light detector this would have never been disclosed and the crystals would have been used without someone knowing that the light yield is not homogeneous throughout the whole scintillator. As the most crucial part of the polarimeter is to identify and count elastically scattered particles, this ability is not affected by the double-peaks. Instead of counting the number of events in one peak one needs to integrate over both peaks to get the number of elastic events from the spectrum. In theory, it would be possible to remove the double-peaks by applying a position dependent calibration map to each of the modules. This would require having a high-resolution angular tracker in front of the LYSO based detector modules. The first measurements of the position reconstruction from the triangular $\Delta E$ detector (see Section 5.3.2.2) suggest a rather high spatial resolution of less then 5 mm that would be enough to create such a calibration map.

### 5.3.2 $\Delta E$ Detectors and Particle Identification

Having an additional layer of plastic scintillator mounted in front of the LYSO based detector modules allows for the creation of $\Delta E$ vs. $E$ spectra. From these spectra, the type of the particle can be identified, and it is, therefore, an essential tool to select the elastically scattered deuteron needed to calculate the polarization of the beam. In the following sections, this method of particle identification will be discussed. Further, the first result of a test using triangular $\Delta E$ detectors, that not only provide the information for particle identification but can be used for position reconstruction of the tracks for the individual events will be presented.

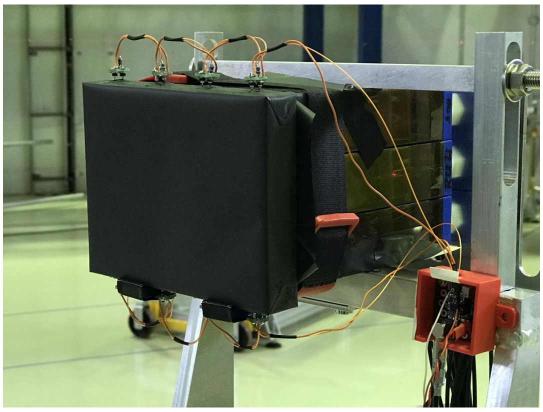

(a) 2 cm $\Delta E$ detector installed in the 2nd iteration of the polarimeter development. The custom pre-amplifier (see Appendix B.2) is installed in the red box.

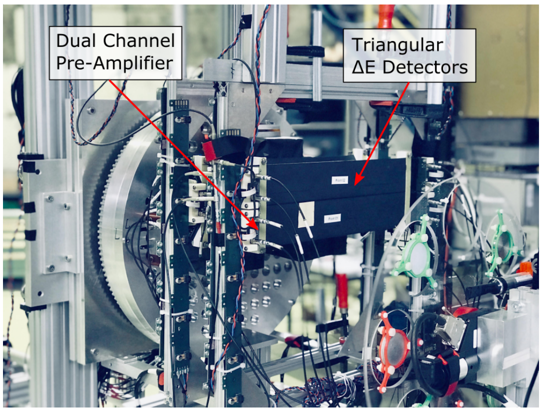


(b) Two layers on triangular $\Delta E$ detectors as tested in the last beam time using the 3rd iteration of the experimental setup.

Figure 5.33: Examples of $\Delta E$ detectors used in the polarimeter development.

#### 5.3.2.1 Particle Identification

A $\Delta E$ vs. $E$ spectrum can be created when an additional detector is installed in front of the detector that fully stops the particle. In the case of our polarimeter, plastic scintillators were installed in front of the LYSO based detector modules. In the two-armed version of the detector setup used in the 2nd iteration, one plastic scintillator was used on each arm and in the 3rd iteration, a plastic scintillator for each quadrant was installed. A particle travels through this scintillator and loses part of its kinetic energy before it gets fully stopped in the following LYSO crystal.

For each event that is recorded by the detector, the energy loss in the plastic scintillator can be plotted against the total kinetic energy deposited in the LYSO crystal in a two-dimensional histogram. How much energy is deposited in the plastic scintillator depends on the type of the particle as well as on its kinetic energy and is described by the Bethe-Bloch formula given in Equation (5.1). Figure 5.34 shows such a $\Delta E$ vs. $E$ spectrum measured in the 2nd iteration with a 2 cm thick plastic scintillator mounted in front a LYSO based detector module that was located at a polar angle $\Theta$ of 10° relative to the beam axis. A 10 mm carbon target was inserted into the beam path, and the deuteron beam energy was 300 MeV. Independent on the kinetic energy of a particle, its position on the $\Delta E$ vs. $E$ spectrum is restricted to a particle specific band. In the case of protons and deuterons, these bands resemble the shape of a banana and are therefore sometimes referred to as *the proton-banana* and *the deuteron-banana*, respectively. The heavier the particle, the more its corresponding band is shifted up-right in the $\Delta E$ vs. $E$ spectrum, as can be seen in Figure 5.34 where the deuteron band is located above the proton band. The most energetic particles will be located at the right end of their respective band and hence, elastically scattered deuterons off the carbon target are located at the end of their band. All the other events located in this band are deuterons as well, but they have not been elastically scattering off the target but have lost their kinetic energy somewhere else before they hit the detector. A lot of events are located in the proton band. The combination of a rather thick target, high

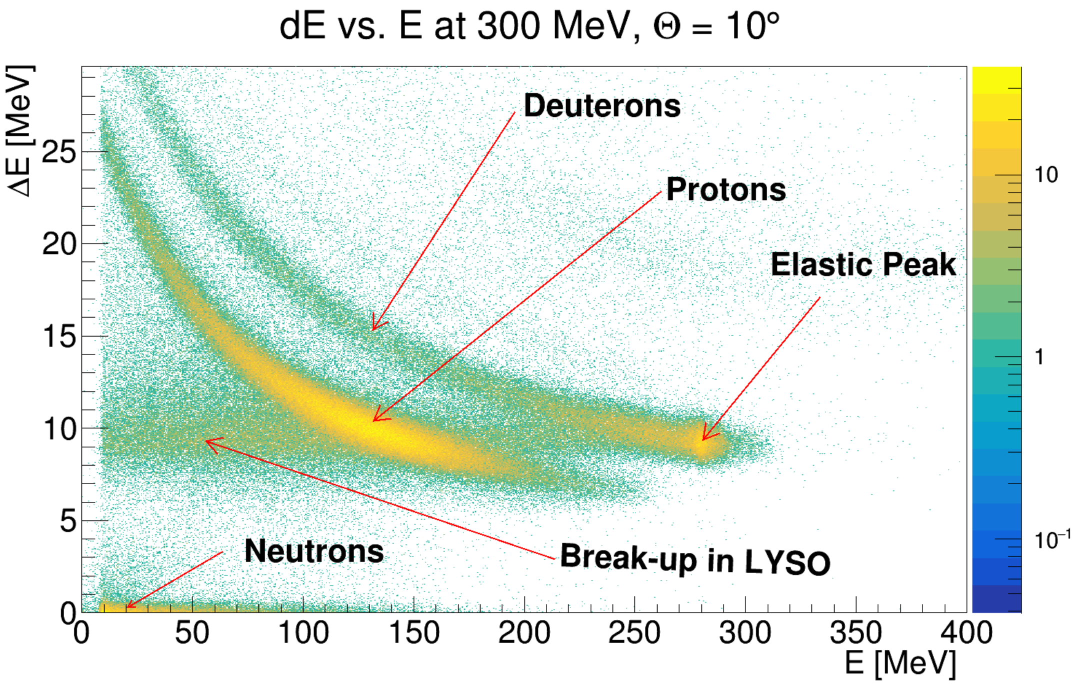


Figure 5.34: $\Delta E$ vs. $E$ spectrum measured for a 300 MeV deuteron beam and a 10 mm carbon target.

energy and the large polar angle of the detector led to a lot of protons (from deuteron break-up in the target) to be recorded. As stated in Section 5.3.1.6, the protons from a break-up reaction can take any fraction of the initial kinetic energy of the deuteron and are therefore spread over the whole proton band. The deuterons that undergo a break-up reaction within the crystal are also visible in this spectrum. As they enter the LYSO scintillator as deuterons, they are registered by the plastic scintillator as such. When they break inside of the crystal, only the proton is detected and as the case for the break-up protons from the target, the energy deposited by the internal break-up protons is spread over the full energy range up to the kinetic energy of the initial deuterons. In the $\Delta E$ vs. $E$ spectrum, they occupy the region that the deuteron band projects on the $\Delta E$ axis. Since the majority of internal break-up reactions origins from elastically scattered deuterons, a band formed by the projection of the elastic peak onto the $\Delta E$ axis is most pronounced. The last particle species that can be found in this plot are neutrons from the deuteron break-up reaction in the target. Neither LYSO nor plastic scintillators are suited to detect neutrons, but in a heavy material such as LYSO, neutrons can deposit some energy mainly due to elastic scattering off the crystal nuclei. The energy loss from these reactions is usually rather small, and therefore the neutron events can be found at the lower end of the energy spectrum of the LYSO scintillator. The energy deposition of a neutron in a plastic scintillator is much smaller than in LYSO and therefore, the neutron event can be found only in the lower left corner of the $\Delta E$ vs. $E$ spectrum.

To select elastically scattered deuterons for the calculation of the polarization, having an additional layer of plastic scintillator in front of the LYSO based detector module, can be very useful. It is possible to select the elastically scattered deuterons only form the LYSO energy spectrum by applying a cut around the elastic peak. However, as can be seen from Figure 5.34, the tail of the proton band reaches up to the elastic peak and if only the projection of this spectrum on the abscissa is available. This is the case if no $\Delta E$ detector is installed. It is tricky to define the lower position of the cut if no elastic deuteron events should be removed and still all protons have to be excluded. If a $\Delta E$ vs. $E$ spectrum can be used, a simple box cut around the elastic peak maximizes the number of elastically scattered deuterons that enter the analysis while simultaneously the proton contamination can be minimized. In addition, a second region around the internal deuteron break-up band, on the left of the proton band, can be defined to increase the number of valid events even further. Following these arguments, it is evident that some form of $\Delta E$ detector has to be installed in the final polarimeter setup.

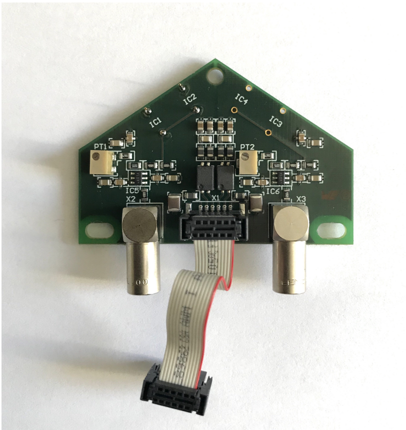

(a) Picture of the dual channel pre-amplifier.

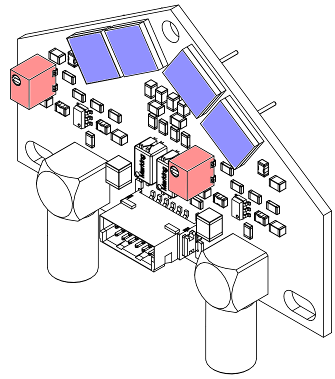

(b) Model of the dual channel pre-amplifier.

Figure 5.35: Dual channel pre-amplifier that was custom designed for the triangular $\Delta E$ detector by Kai Cremer from the company *QS Electronics* in Hückelhoven, Germany. The SiPM arrays are colored in blue. In this model, they are drawn on the front side, but they were eventually mounted on the back side of the PCB such that they could be brought in contact with the plastic scintillators. The component that is colored in red is a potentiometer that allowed to set the gain individually for each channel.

#### 5.3.2.2 Triangular $\Delta E$ Detector

The angular coverage of each of the LYSO based detector modules is rather large as can be seen in Figure 5.41. It would be desirable to have a smaller angular binning for the calculation of the polarization because the unpolarized angular cross section is assumed to be constant over the polar angle $\Theta$ range of one module, see Section 5.3.3.1. For this reason, it would be good to have an additional tracking detector in front of the LYSO based detector modules to obtain the angular information of each event. Adding another detector layer to the polarimeter would be contrary to the basic design requirement stated in Section 5.1.3 and is therefore not feasible. However, as discussed in the previous section, a $\Delta E$ detector is needed in the final version of the polarimeter and therefore the idea of having a combined $\Delta E$ and tracking detector was born.

This detector consists of two layers of plastic scintillator made from triangular bars that are arranged in such a way that the form an even surface. The bars in the first layer are oriented perpendicular to the ones in the second layer. The central bars in both layers have to be shortened to allow the beam pipe to pass through. Two types of triangular plastic scintillator bars will be used. One type features a cross section of an equilateral triangle with a base length of 6 cm and a height of 2 cm while the other type has a cross section of an oblique triangle with the base length of 3 cm and a height of 2 cm as well. The length of both bars is 39 cm. The shorter bars will have to be cut to length in order to fit around the beam pipe. Custom designed pre-amplifier boards with a triangular cross section (see Figure 5.35) will be mounted on each face of the bars. These boards provide two independent op-amp driven channels that can be equipped with two SiPM arrays per channel. The sensors used are 6 mm x 6 mm SiPM arrays from Ketek (PM6660TP-SB0, see Table B.1). The plastic scintillator bars are covered in one layer of Teflon for the enhancement of internal reflection followed

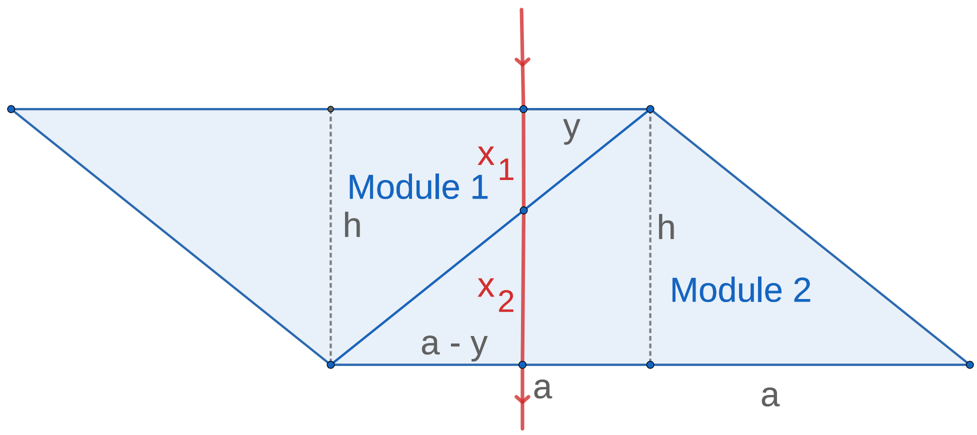


Figure 5.36: Schematic drawing of two triangular $\Delta E$ detectors to discuss the geometrical consideration needed for the calculation of the position reconstruction. A particle (red line) hits the first module at the incident position $y$ and travels a distance of $x_1$ in module 1 before it enters module 2 and travels a distance of $x_2$. The dimensions of the triangles are known: The height $h$ is equal to 2 cm and the half of the base of the triangle $a$ amounts to 3 cm

by a second layer of Tedlar foil for light tightness. The faces of the bars are not covered as the pre-amplifier boards with the SiPMs will cover them. A thin, white 3D-printed mask is sandwiched between the pre-amplifier board and the SiPM arrays allowing them to sit flush in a reflective flat surface. The pre-amplifier with SiPMs are mounted on an aluminum frame with a 3D-printed mount that allows the scintillator bars to be pressure-fit between them. The optical interface between the SiPM arrays and the triangular bars is implemented using a thin silicone pad which also prevents the plastic scintillators from slipping out of the frame. The amplified SiPM signal from each channel is fed out of the pre-amplifier using a LEMO connector while a common voltage supply rail is attached on each side of the frame that allows to plug in each of pre-amplifier to provide the necessary dual supply voltage. In the last beam time of the 3$^{\text{rd}}$ iteration of the detector development, two frames each equipped with three plastic scintillator bars were installed and tested.

To obtain the $\Delta E$ information needed for the particle identification, the energy loss for each event in all the triangular bars can be summed. This means that all the bars act as one solid layer of scintillator. The position information can be extracted from the energy losses in the individual bars. The amount of deposited energy in one scintillator depends on the position where the particle passed through the scintillator as the triangular cross section of the bar leads to an incident position $y$ dependent effective path length $x_1$ or $x_2$ within the scintillators, see Figure 5.36. The beam hits the first module and loses a fraction of its kinetic energy $\Delta E_1$ while traveling a distance $x_1$ in this module then it hits module 2 where it loses $\Delta E_2$ of its kinetic energy while traveling a distance of $x_2$. The amount of deposited energy is proportional to this distance and is described by the Bethe-Bloch formula given in Equation (5.1). The energy loss in the plastic scintillator material is rather small, and the maximal path length is limited to 2 cm by the thickness of the triangular bars. Therefore, the distance-dependent energy loss can be approximated to be a linear function of the path length given by:

$$\Delta E_n(x) \approx k_n \cdot x_n, \tag{5.12}$$

where $k$ describes the energy loss per distance and the index $n \in [1, 2]$ denotes the first or the second module as drawn in Figure 5.36. By assuming that the energy loss in the first module is small compared to the total kinetic energy of the particle it can be assumed, that the energy loss constant $k_n$ is the same for both modules, i.e., $k_1 \approx k_2$. Under these assumptions, one can build the following ratio from Equation (5.12):

$$\eta = \frac{\Delta E_1 - \Delta E_2}{\Delta E_1 + \Delta E_2} = \frac{x_1 - x_2}{x_1 + x_2}. \tag{5.13}$$

From the triangle shown in Figure 5.36, the following geometrical relation can be found using the theorem of intersecting lines:

$$\begin{aligned}
\frac{y}{x_1} = \frac{a}{h} \quad &\Leftrightarrow x_1 = \frac{h}{a} \cdot y, \\
\frac{a-y}{x_2} = \frac{a}{h} \quad &\Leftrightarrow x_2 = \frac{h}{a} \cdot (a-y), \\
&\Longrightarrow \\
\frac{x_1 - x_2}{x_1 + x_2} &= y \cdot \frac{2}{a} - 1.
\end{aligned} \tag{5.14}$$

Combining Equation (5.13) and (5.14) the following expression for the incident position $y$ can be found:

$$y = \frac{a}{2} \cdot (\eta + 1) = \frac{a}{2} \cdot \left( \frac{\Delta E_1 - \Delta E_2}{\Delta E_1 + \Delta E_2} + 1 \right). \tag{5.15}$$

This means that the incident position of a particle can be reconstructed from the deposited energy in two stacked triangular bars. The position that is found using this method is given relative to the tip of the lower triangular bar (module 2), but since its absolute position is known, the absolute position of the particle can be calculated as well. Having one layer of triangular bars allows for the calculation of the incident position along the axis that is perpendicular to the orientation of the bars and it is, therefore, necessary to have two layers of triangular $\Delta E$ detectors to calculate incident coordinates of a particle.

Figure 5.37 shows the measurement procedure that was applied during the last beam time using the 3$^{\text{rd}}$ detector development setup. The first frame equipped with three scintillator bars was fixed relative to the exit window of the beam pipe and positioned such that the beam would penetrate the scintillators between the first (F_01) and the second (F_02) module. The energy that was deposited in these two modules was plotted against each other in a $\Delta E$ vs. $\Delta E$ spectrum as can be seen in the left two-dimensional histogram of Figure 5.38. The 270 MeV deuteron beam used for this test showed some angular dispersion even as the frames holding the scintillator bars were moved as close as possible to the exit window. This resulted in a band structure in the left $\Delta E$ vs.

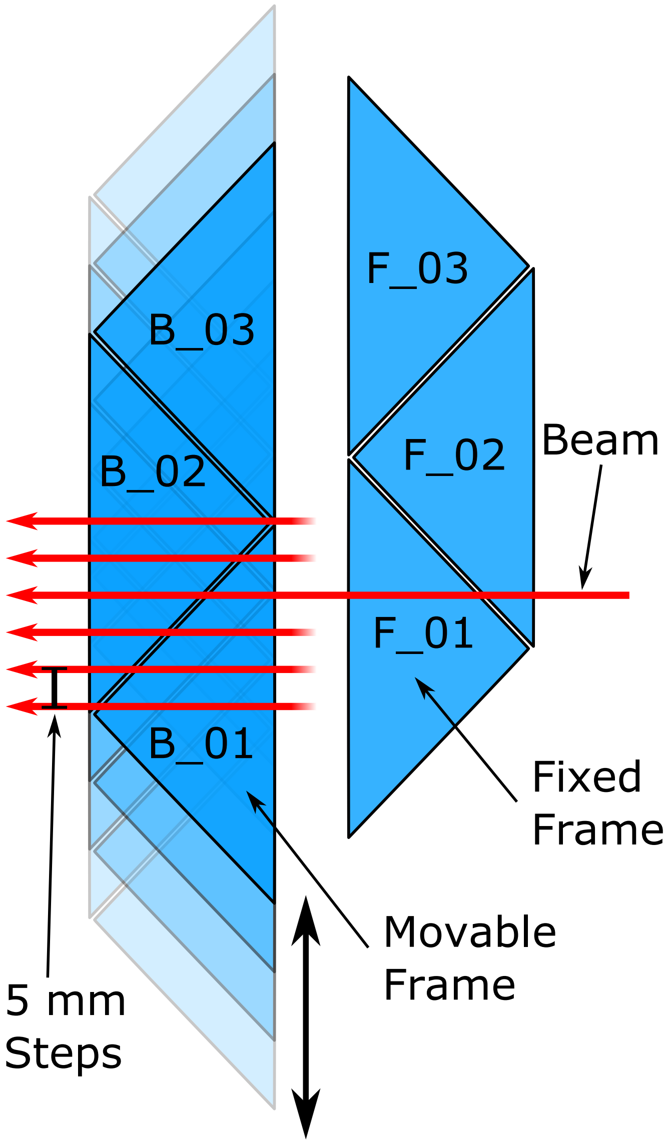


Figure 5.37: Schematic model of the measurement procedure used to test the position reconstruction using the triangular $\Delta E$ detectors. Two frames with three scintillator bars each were mounted in the beam path. The first frame (modules prefixed with **F**) was fixed relative to the beam pipe while the second frame (modules prefixed with **B**) was mounted on the experimental table allowing it to be moved vertically. The second frame was moved to six different positions with a vertical spacing of 5 mm.

$\Delta E$ spectrum rather than a single point. Each point in this spectrum corresponds to a different incident position of a beam particle and therefore by applying a cut to this spectrum (red lines) the range if incident positions was restricted. Only events that were located in this cut region were considered in the second layer which effectively created an almost point-like beam. The experimental table was then moved until only a minimal number of events were recorded in the modules B_03 and B_01 and the number of events in B_02 was maximal. This meant that the beam was hitting the tip of the B_02 triangular bar. from this position, the detector was successively moved up six times in 5 mm steps and a $\Delta E$ vs. $\Delta E$ spectrum was recorded at each position. These spectra were then summed up, and the result is shown in the right histogram of Figure 5.38. Each of the six measurements is represented by a distinct point in the resulting band.

To prove that the individual detector positions could be resolved, the difference over sum $\eta$ was calculated as defined in Equation (5.13) for each of these spectra and the result is given in Figure 5.39. Each of the measurement resulted in a clearly distinguish-

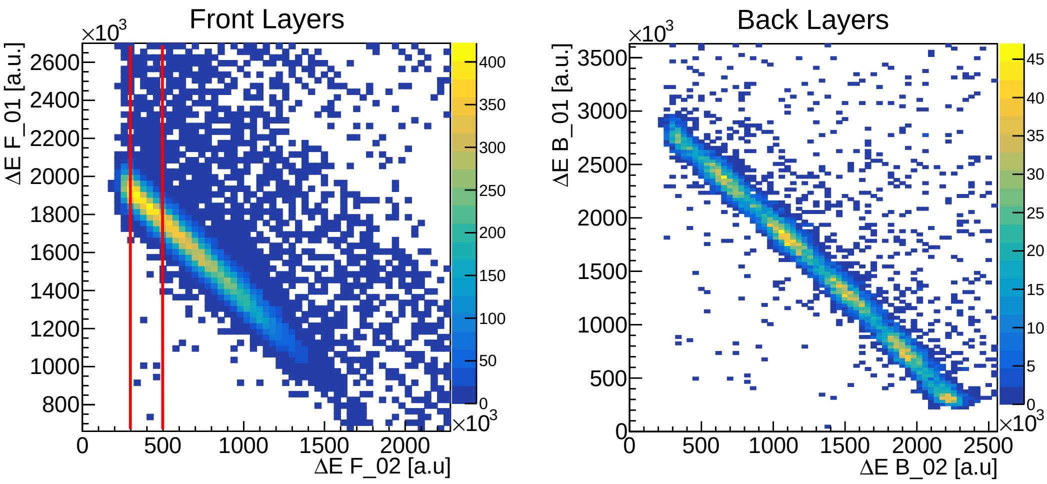


Figure 5.38: $\Delta E$ vs. $\Delta E$ spectra for the deposited energy in module F_01 and F_02 for the first, fixed layer on the left. The same spectrum is given for the second, movable layer with the modules B_01 and B_02 on the right. The first layer acted as a filter to narrow the beam. Only events located within the cut range (red lines) in the left spectrum were considered in the right spectrum. This plot contains the measurements taken at the six different vertical positions which is represented by the distinct points in the band.

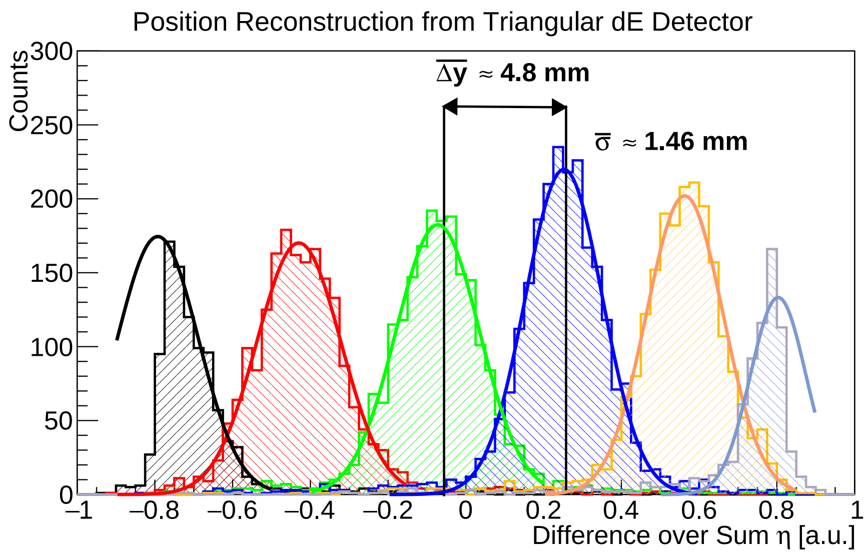


Figure 5.39: The difference over sum ratio $\eta$ as defined Equation (5.13) that can be used for the position reconstruction. From this plot, it is clearly visible that the measurements that were taken with a 5 mm spacing can be separated from each other. The average reconstructed spacing between the peaks is indicated as well as the average width of the peaks obtained from the Gaussian fits.

able peak that was fitted with a Gaussian. The result of measurements that were taken with the beam hitting the very edges of the module B_01 and B_02, respectively are located at the leftmost (black peak) and rightmost (gray peak) position of Figure 5.39. In these two cases, not all the particles that penetrated the second layer deposited their energy in the modules B_01 and B_02, and this is reflected in a cut-off Gaussian at these points. The other measurement showed a clear Gaussian peak shape. The average width $\bar{\sigma}$ obtained from the fits was calculated to be 1.46 mm. The incident position for each peak was calculated according to Equation (5.15). The average of the distance between the peak positions $\bar{\Delta y}$ was found to be 4.78 mm.

The results from this first test look very promising and suggest that creating a combined $\Delta E$ and position detector is feasible. How accurate the position could be reconstructed has to be further investigated. The accuracy in positioning the experimental table that was used to perform these measurements did influence the result given for the average peak distance, and there is for sure room for improvement. The width of the peaks in Figure 5.39 is not only defined by the resolution of the plastic scintillator bars but also by the width of the deuteron beam that was used. By narrowing the cut shown in the left spectrum of Figure 5.38, the effective beam size could be decreased but would cause a loss in statistics as the number of events would be decreased as well. This issue could be overcome by increasing the measurement time for spectra that were taken at each position of the experimental table. The performance of having both layers installed has to be further investigated. If this detector should be installed at the final polarimeter setup, the effect of having particles penetrating the surface at a certain angle compared to this measurement where all the particles hit the scintillator surface in a perpendicular fashion, has to be studied as well.

### 5.3.3 Asymmetry Measurements

In the first beam time with the 3$^{\text{rd}}$ iteration of the detector development setup, it was possible to measure asymmetries using the final geometry of the polarimeter with all 52 LYSO based detector modules installed. The modules were arranged in a symmetrical pattern, see Figure 5.40. Having identical detector modules installed on the left and right, or on the top and bottom side of the polarimeter, respectively, is very important to reduce the systematic error in the final polarization measurement, as the cross ratio methods depend on this symmetries. In [61] it was shown, that this symmetric arrangement allows to calculate and compensate up to second order error contribution from beam misalignment, provided a proper detector calibration.

Due to some error in the event reconstruction section of the data acquisition system, the four $\Delta E$ detectors could not be used for the asymmetry measurements. However, it was possible to measure the asymmetries for the elastic scattering of 200 MeV and 270 MeV deuterons of a 5 mm carbon target with good statistical accuracy. In addition, some lower statistic runs were taken for the elastic scattering of deuterons off different target materials. In order to measure the asymmetries, the detector was moved as close as possible to the exit window of the beam pipe which led to a distance between the target and the center of the polarimeter of $z = 360$ mm. Figure 5.41 displays the angular coverage of each LYSO based detector module in this detector setup. In

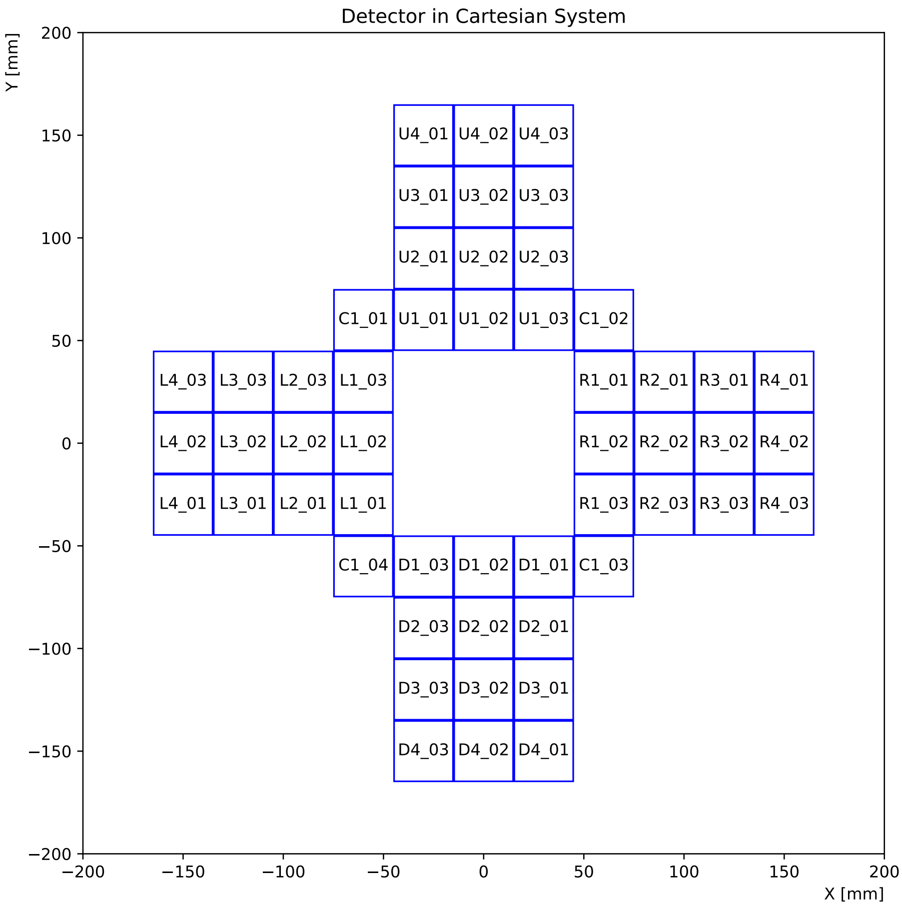


Figure 5.40: Arrangement and naming convention for the LYSO based detector modules as used in the 3rd iteration of the polarimeter development. The names consist of a prefix that indicates in which of the four arms the module is located. The prefixes can be **L** (left), **R** (right), **U** (up), **D** (down) and **C** (central). The number following this prefix indicates the $\Theta$ segment, i.e., defines how far from the center of the detector the particular model is located. The number 1 means that the module is placed next to the beam-pipe while the number 5 represents the outer most position where a LYSO based detector module can be installed on the aluminum support disk. The number that follows the underline denotes the $\Phi$ index. This number starts at 1 in each of the four arms and is increased in a clockwise manner. Modules with the same $\Theta$ and $\Phi$ index, and the opposing prefix form the pairs needed for symmetry calculation.

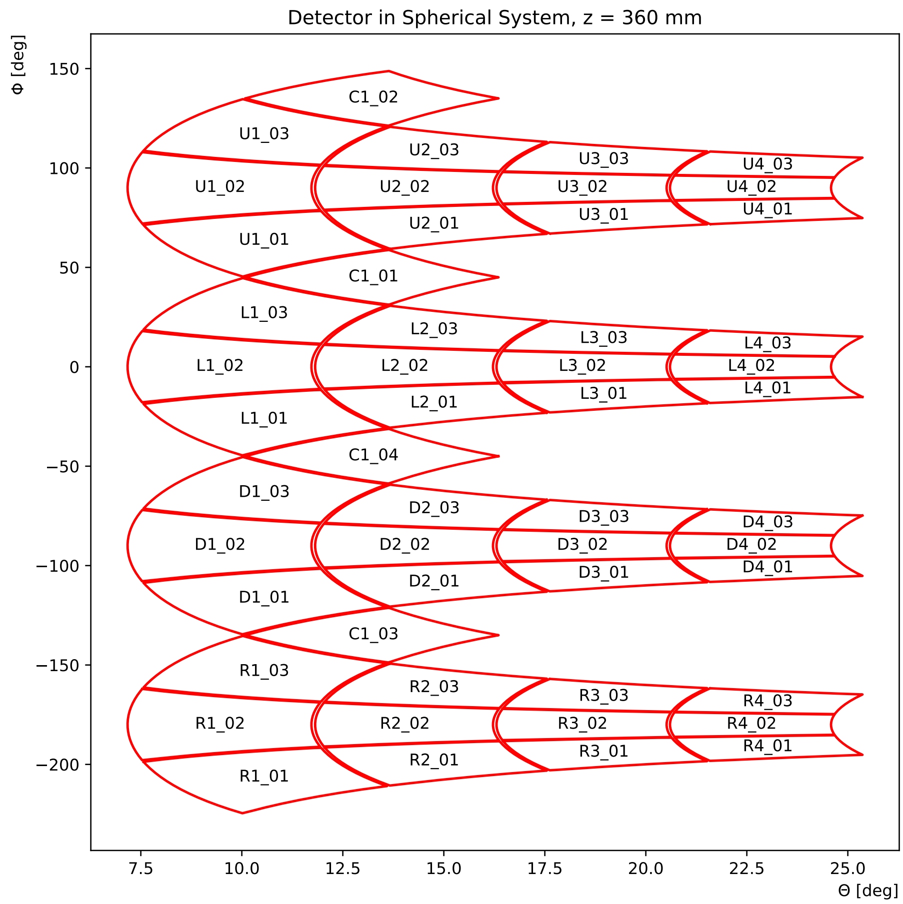


Figure 5.41: Representation of the modules in the spherical coordinate system that is used to describe the scattering process is given. The actual solid angle that is covered by each module depends on the distance from the origin (the target) and is given for $z = 360\,\mathrm{mm}$ as was used in the asymmetry calculation described in Section 5.3.3.1.

the subsequent sections, the extraction of the beam polarization using the measured asymmetry from the elastic deuteron carbon scattering will be presented as well as the attempt to extract the vector analyzing power from the elastic deuteron scattering off the different target materials.

#### 5.3.3.1 Polarization Measurement

The first step in the asymmetry calculation was to extract the number of elastically scattered events in each LYSO based detector module. The approach used here was very minimalist as the exact same procedure should be possible to use in the online analysis and calculation of the online asymmetries. For each module, the elastic peak was identified by searching for the first peak starting from the high energy side of the spectrum. This method assures that the actual deuteron peak was selected. By defining the elastic peak as the maximum peak in the spectrum, for large $\Theta$ angles, the proton peak from deuteron break-up reactions in the target might exceed the elastic deuteron peak, and therefore this method should not be applied. When the location of the elastic deuteron peak was found, a cut with a width of $-5\%$ and $+15\%$ relative to the peak location was defined. It was visually checked that this range would include the full elastic deuteron peak in all modules. When this cut positions are defined, they can be used to create a look-up table for each module and used for the online analysis.

To calculate the asymmetry, the half cross ratio method described in Section 4.3.1.3 was chosen. The deuteron beam was cycling through three polarization states: Up, down and unpolarized. The up and the down polarization state represent pure vector polarized states with an opposing sign. In theory, their magnitude should be the same, but the experience from the WASA beam time suggested that this will not be the case. Since unpolarized cycles were available, the half cross ratio method was the right choice.

The LYSO based detector modules were assigned to either the left or the right side of the polarimeter. The left side of the polarimeter included all modules with the **L** prefix, the modules U1_01 to U4_01, D1_03 to D4_03 as well as C1_01 and C4_01. The right side of the polarimeter included all modules with the **R** prefix, the modules U1_03 to U4_03, D1_01 to D4_01 as well as C2_01 and C3_01. The central modules U1_02 to U4_02, and D1_02 to D4_02 cannot be assigned to either side and are therefore removed from the analysis.

The asymmetry for each of the polarization state was calculated from the formula of the half cross ratio given in Equation (4.29) for each pair of opposing LYSO detector module, i.e., the modules with the same $\Phi$ index from both sides of the polarimeter. By calculating the asymmetry individually for each pair of opposing modules, it can be assured that the difference in acceptance origin from the module itself or from the elastic cut would cancel out. The error according to Equation (4.32) was calculated as well. The asymmetry from all the modules that cover the same $\Theta$ range were averaged and the error of this average was calculated using simple error propagation. The result for 200 MeV is given in Figure 5.42a and for 270 MeV in Figure 5.42b, respectively.

The vector analyzing power for 200 MeV as well as for 270 MeV was measured in the database experiment, see Figure 4.19 and was used to calculate the polarization from each $\Theta$-bin individually, according to Equation (4.9). The resulting polarization was fitted with a constant for both beam energies individually. The result is given in Figure 5.43. The values obtained for the polarization were used to up-scale the vector analyzing power functions measured by the WASA detector and plot them together with the asymmetries measured by the LYSO polarimeter to check the line shapes, see dashed lines in Figure 5.42.

The results of the fit for the polarization extraction differ by $\sim 4\%$ for both polarization states which is well in agreement with the uncertainties of the vector analyzing power. Unfortunately, no direct measurement of the vector polarization was provided by the ***L****ow* ***E****nergy* ***P****olarimeter* (LEP) during this beam time, but three measurements of the asymmetry were provided. The asymmetry at the LEP is calculated using a simple left/right method as described in Section 4.3.1.2 with the effect that any differences in the acceptance between the left and the right detectors will not cancel. To compare the results of the polarization obtained from the setup using the LYSO based detector modules to the asymmetry measured by the LEP, the ratio between the asymmetries

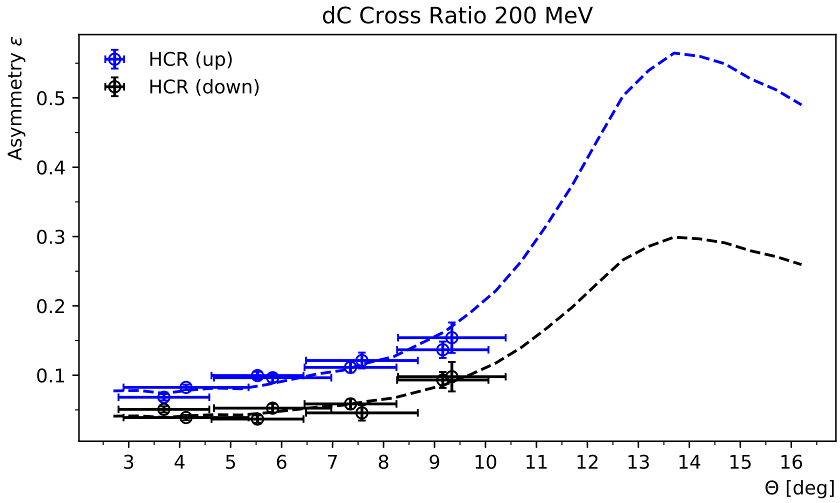


(a) Asymmetry measurement at 200 MeV.

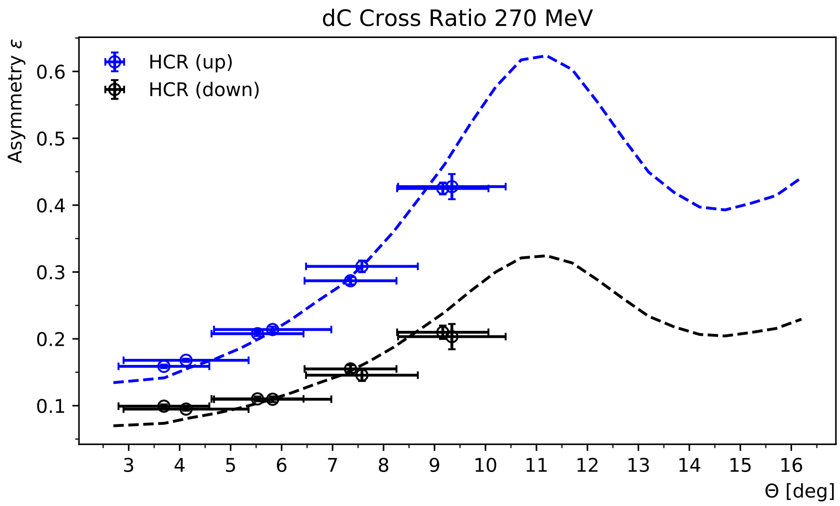


(b) Asymmetry measurement at 270 MeV.

Figure 5.42: Asymmetries measured from the elastic deuteron carbon scattering at 200 MeV and 270 MeV for the polarization state up (blue) and down (black). The dashed lines represent the vector analyzing power measured in the database experiment up-scaled by the polarization that was extracted for each state, see Figure 5.43

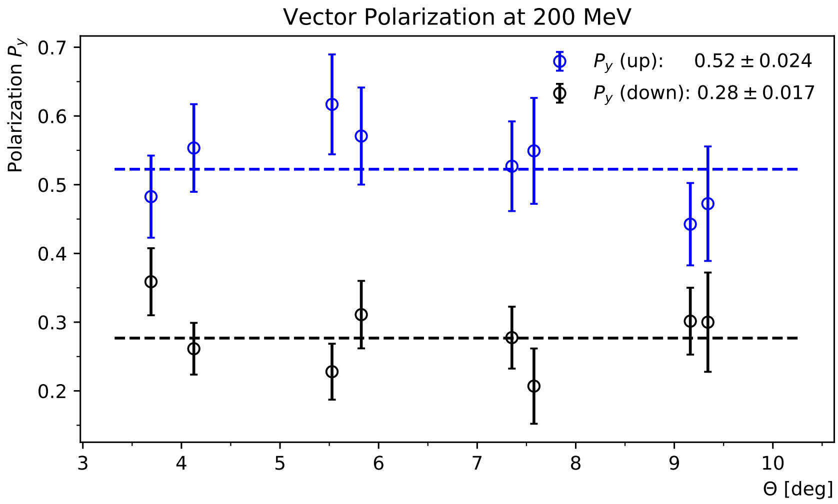


(a) Polarization extraction at 200 MeV.

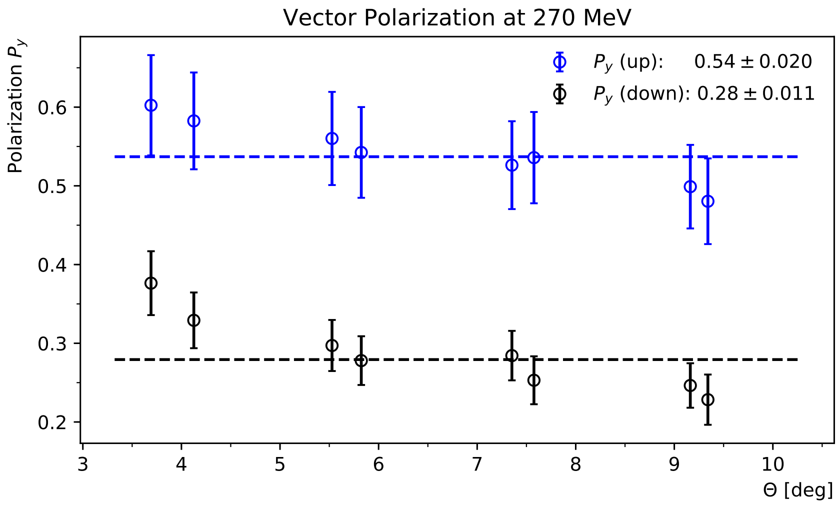


(b) Polarization extraction at 200 MeV.

Figure 5.43: Extraction of the vector polarization according to the Equation (4.9) for each Θ-bin using the measured asymmetry given in Figure 5.42 and the vector analyzing power measured in the database experiment, see Figure 4.19. The individual polarization values from each Θ-bin were fitted with a constant (dashed line) to obtain the average polarization for each state.

for the up and down polarization state measured by the LEP can be compared to the ratio of the polarization values obtained in this section. This is possible because the LEP measures the asymmetry at one angle and therefore the ratio

$$r = \frac{\epsilon^{\uparrow}}{\epsilon^{\downarrow}} = \frac{\frac{3}{2}A_y P_y^{\uparrow}}{\frac{3}{2}A_y P_y^{\downarrow}} = \frac{P_y^{\uparrow}}{P_y^{\downarrow}}, \tag{5.16}$$

can be calculated using Equation (4.9). The average ratio from the LEP is given by $\bar{r}_{LEP} = 2.106$ and for the LYSO polarimeter by $\bar{r}_{LYSO} = 1.893$ which means that they differ by $\sim 10\%$. It is worth mentioning that the ratio $r_{LEP}$ can vary in the order of $\sim 2.5\%$ from one measurement to another. It is not clear why there is this difference between the two detectors. There can be a source of systematic error in the asymmetry calculation done by the LEP as well as by the LYSO polarimeter. Using the $\Delta E$ detector to improve the cuts on the elastic peak is definitely a good idea. Another issue is that the measurements at the LEP were not done simultaneously with the LYSO polarimeter measurements. Even if the beam polarization is assumed to be stable over time, the database experiment has shown that this is not entirely the case.

Overall, this first test of the performance of the final setup with the LYSO based detector modules as a polarimeter is very promising and the final conclusion can only be made once the polarimeter gets installed at its final place inside of the COSY ring equipped with the designated target and $\Delta E$ detectors.

#### 5.3.3.2 Vector Analyzing Power for Different Target Materials

As mentioned before, some additional measurements were made using different targets materials during this beam time. The materials that were examined were aluminum, magnesium, silicon, nickel, and tin. A disk with a thickness of 5 mm and a diameter of 50 mm made from each of these materials was installed in the target flower and could be remotely positioned in the deuteron beam.

For each of these targets, the elastically scattered deuterons were extracted in the same way as described in the previous section. The asymmetry was then calculated and by using the average beam polarization of $P_y^{\uparrow} = 0.489 \pm 0.0190$ and $P_y^{\downarrow} = 0.255 \pm 0.0114$ obtained from the carbon runs, the vector analyzing power was extracted. The results for 200 MeV and 270 MeV are given in Figure 5.44. The error bars were omitted in this plot as they were in the order of 20% and would, therefore, obstruct the plot. The measurement of these analyzing powers suffers from a few issues: First of all, the statistics for each of the target is much too low to create a meaningful result. Second, the geometry of the LYSO polarimeter in the configuration used in this beam time led to a much too big binning in $\Theta$. To resolve the structure of the vector analyzing power for the different materials, a much finer binning is necessary, e.g., the one available at the WASA detector. If the line shape of the vector analyzing power is known for a specific reaction, like deuteron carbon scattering, the results from the LYSO polarimeter can be compared to this line shape. From this comparison, it is possible to state whether the LYSO polarimeter is able to reproduce the vector analyzing power as it was the case in Figure 5.42. However, if the line shape of the vector analyzing power is completely unknown, Figure 5.44 is a perfect example of *undersampling*. This means that it can

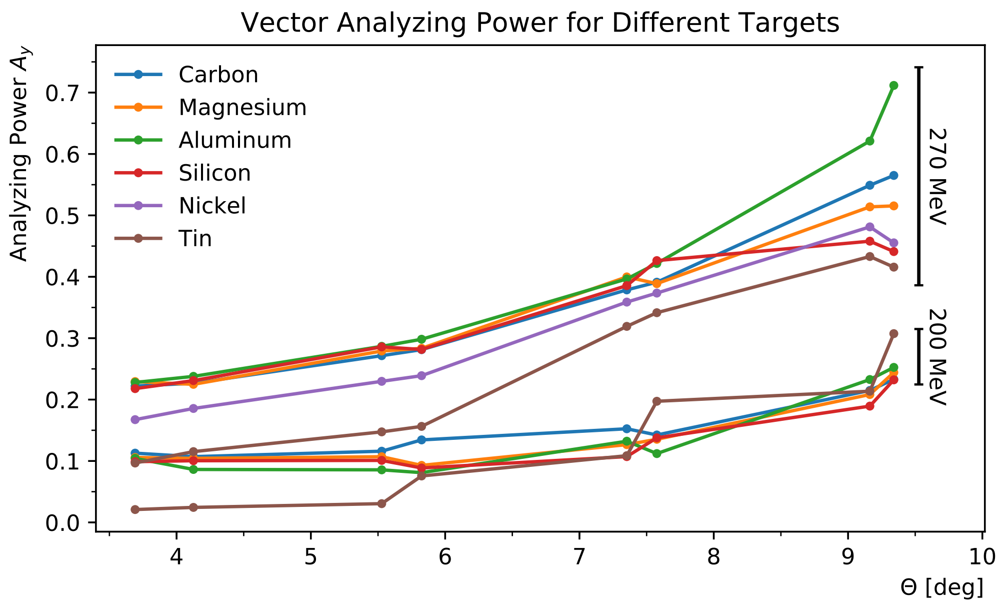


Figure 5.44: Vector analyzing power for elastically scattered deuterons off different target material. The analyzing power was extracted from the asymmetries measured with a 200 MeV and 270 MeV deuteron beam. The vector polarization calculated from elastic deuteron carbon scattering was used to normalize these asymmetries.

not be known how the line shape behaves between the measurement point and the assumption that it follows a straight line is not valid. Despite these issues, the results of the vector analyzing power for these various materials in this energy range are novel and therefore interesting.

The initial question that led to these test was the following: Does choosing a target material other than carbon, lead to a much higher vector analyzing power and therefore increase the FoM (assuming a cross section similar to one for elastic deuteron carbon scattering) of the polarization measurement (see Section 4.3.3) or should the beam energy be used to find an optimum FoM? Despite the uncertainties in the plots given in Figure 5.44, this question can be somewhat answered. It seems to be the case that for the same deuteron beam energy, the vector analyzing powers of the different target materials are rather similar. At 200 MeV, this is even more the case than at 270 MeV where aluminum shows a significant increase in the vector analyzing power for larger angles and tin is located below all the other materials in the whole angular range. On the other hand, it is quite evident that by going from 200 MeV to 270 MeV, the vector analyzing power can be increased more than by choosing another target material and staying at the same energy.

For the development of the polarimeter, a good strategy seems to be to use carbon as the target that provides the polarimetry reaction and adjust the energy to optimize the FoM. Independent of this strategy, it would be interesting to examine the analyzing power of other material using a designated detector setup and to collect enough statistics especially as aluminum shows this large increase in the vector analyzing power for larger angles.

# Chapter 6

# Discussion

## 6.1 Summary and Conclusion

The aim of this work was to present the development of a designated polarimeter to be used in an EDM measurement of deuterons and protons that aims to reach a statistical sensitivity down to $10^{-29}\,e\,\mathrm{cm}$. This EDM experiment will be performed on polarized beams in a storage ring. The thesis is structured in two main parts. The first part described the measurement of the vector analyzing power and differential cross section in elastic deuteron carbon scattering that was performed in the *database experiment* using the WASA forward detector installed at COSY at the *Forschungszentrum Jülich*. The knowledge of these quantities is crucial as they provide the physical base that is needed to measure the beam polarization which is needed to calculate the EDM. The second part was devoted to the development and hardware testing of a polarimeter based on LYSO crystal scintillator modules. This polarimeter is designed to provide the stability and accuracy that is needed to measure an EDM.

### 6.1.1 Database Experiment

The database experiment was conducted with the intention of creating a solid set of vector analyzing powers for the deuteron carbon elastic scattering. This was achieved for seven different beam energies between 170 MeV and 380 MeV. The data was taken using the well served WASA detector installed in the COSY ring. A lot of detail work went into the preparation and calibration of the measured data. The multilayer design of the WASA detector did, on the one hand, allow for careful selection of the elastic events but complicated the whole analysis and calibration process.

Different approaches for the asymmetry extractions have been discussed and examined. The final method used, employed a sophisticated procedure that took advantage of the full $\Phi$ coverage of the WASA detector and accounted for the amount of asymmetry information associated with each event. This was accomplished by adding a $\Phi$-dependent weight to each event and then perform a combined fit on the polarized and unpolarized data simultaneously, see Section 4.3.1.4. The resulting asymmetry was a very smooth function of the scattering angle $\Theta$, and its line shape was in good agreement with reference data that was available for 200 MeV[23] and 270 MeV[22].

To calculate the vector analyzing powers, the beam polarization has to be known. Unfortunately, this information was not available for this experiment, due to the lack of continues measurements from the LEP. To circumvent this issue, it was decided to use the reference vector analyzing power for 200 MeV and 270 MeV to extract the beam polarization that could, in turn, be used to obtain the vector analyzing power for the other energies. Even though this worked, it also introduced a quite large systematic error into the resulting analyzing power measurements, see Figure 4.19.

A general description of the methods to be used to measure a charged particle EDM in a storage ring are given in [62], and the statements made in this paragraph are related to this source. Generally, it can be stated that a non-zero EDM would cause the polarization of a proton or deuteron beam to oscillate at a frequency $\Omega_{EDM}$ when interacting with a properly aligned electric field. The frequency of this oscillation is directly proportional to the value of the EDM and the strength of the electric field. If the experiment designed such, that multiple full oscillations could be observed, $\Omega_{EDM}$ could be calculated from the zero-crossing of this oscillation without the need to know the actual value of the beam polarization. However, the design parameters for the designated prototype ring predict a value for $\Omega_{EDM}$ in the order of a few nHz for a proton EDM of $10^{-29}\,e\,\mathrm{cm}$. This means that in the actual EDM experiment, a small polarization build-up will be measured in order to calculate $\Omega_{EDM}$, and, therefore, the uncertainties in the polarization determination will enter the result for the EDM directly. In both cases, the error on the polarization has to be taken into account for the estimation of the uncertainties of the EDM itself.

This work concentrated solely on the elastic deuteron carbon scattering to extract an asymmetry that can be used to calculate the vector polarization. There exists other reactions that could potentially be used to measure the polarization. These reactions belong to the group of *inelastic reactions*. The proton and the neutron that compose the deuteron can undergo a *quasi-free* reaction with nucleons of the carbon target that produce light mesons. E.g., $p + p \to d + \pi^+$, $n + n \to d + \pi^-$ or $p + n \to d + \pi^0$. From these mesons, the $\pi^\pm$ feature a decay length of $\sim$7.8 m [63] that would allow them to reach the polarimeter and could be detected directly. However, even for the 380 MeV deuteron beam, the production energy threshold cannot be reached, and therefore these mesons are not available for a polarimeter reaction. Another inelastic reaction is given by the excitation of the carbon nucleus by the impinging deuterons. In [64], an overview over the excited states of $^{12}C$ is given. The states at 4.433 MeV and 9.36 MeV can be produced by deuteron scattering. Both of these states should be visible in the energy spectra where they would form peaks that are shifted towards lower energies relative to the elastic peak. The excited state at 4.433 MeV is so close to the elastic peak that it is not possible to disentangle them with the WASA detector. The LYSO based polarimeter should be able to resolve it due to its resolution of $\sim$1 % but the double peak issue (see Section 5.3.1.7) would obscure the peak anyway. In any case, since the peak of this state is located so close to the elastic peak, it is very likely that it is included in the latter when the number of elastic events was extracted. The second peak which is located 9.36 MeV away from the elastic peak could be resolved in both detectors but no visible peak was found in any spectra of neither the WASA nor the LYSO based detector. This indicates that the cross section for the excitement of this state is very small compared to the elastic scattering cross section. The third inelastic reaction is given by the deuteron break-up in the target. The protons from this reaction contribute significantly to the total number of recorded events. Therefore, it would make sense to measure the analyzing power of the break-up protons to see if they could be used measure the polarization. The data from the database experiment would allow for the extraction of this quantity but it would be more complicated than for the deuterons as the break-up protons do not form a discrete peak but are distributed over the whole energy range.

The extraction of the differential deuteron carbon cross sections was much more sensitive to the calibration of the data as they are absolute quantities. In comparison to the asymmetries, where the detector acceptance cancels from the calculation, it needs to be known for the differential cross sections. To obtain these acceptances, a Monte-Carlo simulation of the WASA detector was used. This simulation software is rather old and written in FORTRAN which makes it hard to judge its quality. There are concerns about the accuracy of the detector description built into this software. A further difficulty was imposed on the analysis by the fact that the experimental setup would not allow for a direct measurement of the luminosity of the beam. The elastic deuteron proton scattering reaction was therefore used to calculate the luminosity by comparing the extracted number of events from this reaction to published proton deuteron cross sections, see Section 4.3.2.3. This procedure was applied for five out of the seven beam energies, but for 170 MeV and 235 MeV, the final cross sections were calculated by the usage of a normalization factor obtained from an analytical model, see Section 4.3.2.4. Despite all these difficulties, the results, given in Figure 4.29 were still comparable in the order of $\sim 15\,\%$ with published cross sections, see Figure 4.30.

Using the differential cross sections together with the vector analyzing power, it was possible to calculate a Figure of Merit as a measure of the statistical error of the polarization extraction as a function of different angular coverage of a polarimeter and the beam energy. The result from this calculation states, that the lowest statistical uncertainties on the polarization are to be achieved at a beam energy of 300 MeV with an angular coverage of $3.5° \leq \Theta \leq 15.5°$, see Figure 4.33. This result, has to be taken with a grain of salt because only a certain angular range was accessible due to the geometry of the WASA detector and Figure 4.31 indicates that the FoM could potentially further increase with increasing beam energies. A strong effect of the statistical error of the polarization was found by employing the weighting method described in [30]. This increases the FoM just by choosing a smart weight as a function of the scattering angle $\Theta$. It is also important to notice that in the framework of an experiment designed to measure an EDM, parameters such as the beam energy cannot be selected solely by considerations to optimize the FoM of the polarization measurement but will rather depend on the design of the designated storage ring.

### 6.1.2 LYSO Based Polarimeter Development

The development of a polarimeter started with a list of requirements that such a device had to fulfill (see Section 5.1.3) in order to be used in the framework of the EDM investigation. The key requirements were simplicity, long term stability as for the final EDM experiment a year of continuous data taking is intended to reach the required statistical accuracy[29]. For this reason, it was decided to create a polarimeter that follows a simple design that would still allow a provide a high resolution. The later is important because an elastic scattering reaction off a carbon target will produce the polarimetry reaction and therefore the clean selection of elastically scattered particle is the most important feature of the polarimeter. The best solution was found to use an inorganic crystal scintillator such as LYSO to fully stop the particles and obtain the kinetic energy information. An additional layer of plastic scintillator in front of the LYSO crystals would allow for the selection of a particle species using $\Delta E$ vs. $E$ particle identification plots.

The basic element of the polarimeter is a LYSO based detector module with a SiPM array to convert the energy-dependent scintillation light into an electric signal that can be in turn digitized by a fast flash-ADC. Using a modular approach allows for an arrangement of the LYSO based detector modules that can be adapted to the requirement of the final experiment. The modules and the final structure of the polarimeter were developed, tested and improved in an iterative process that involved a total of five experiments with deuteron beams of different energies at the external beam place in the Big Karl hall. During these experiments, different types of light sensors such as PMTs and SiPM arrays, different lengths of the LYSO crystals, various arrangements of the modules as well as different target materials have been tested and evaluated.

This experiments allowed for the characterization of the modules by measuring different properties of the entire module like energy resolution or linearity. The LYSO crystal was further analyzed by measuring its stopping power and deuteron break-up probability. Two different $\Delta E$ detectors were tested. A simple version consisting of a single layer of plastic scintillator was used to demonstrate the particle identification ability of the polarimeter setup. A more sophisticated prototype, made from triangular plastic scintillator bars, was tested as well. This type would not only provide a $\Delta E$ information but in addition, can be used to obtain position information for each track. This would allow for a much finer granularity of the final polarimeter compared to position information that can be obtained only from the LYSO modules.

The whole development process was done in close collaboration with the SmartLab in Tbilisi, Georgia. Their members developed a custom made power supply that creates a very stable reverse bias supply voltage that is needed to maintain the gain stability of the SiPM arrays. For the final iteration, a total of 52 LYSO based detector modules have been built and tested. An aluminum disk used in the last iteration provides the base for the LYSO based detector modules and allows them to be arranged in different configurations. Each module is connected to an individual channel on a flash-ADC and has an individually controllable supply voltage channel. The status of the polarimeter at the moment of writing is such that it is almost ready to be installed and tested in the COSY ring. The LYSO based detector modules, their mounting base, the simple version of the $\Delta E$ detectors as well as the custom power supply and the data acquisition system are prepared and ready to use. The main mounting structure including the vacuum flight chamber with a thin exit window is being assembled at the moment.

In general, the development of the polarimeter was quite successful. However, there was one major issue present in the LYSO based detector modules. The energy spectrum of all of the modules showed a double-peak structure in situations where from the physics it was clear that only a single peak should be present, see Section 5.3.1.7. It took until the last beam time to figure out that this issue was caused by inhomogeneities of the light yield inside of the LYSO crystals. Taking a grid-based set of measurements with a deuteron beam on the surface of the crystal revealed that depending on the position of penetration of the beam, the LYSO crystals produce a different amount of scintillation light. There are regions of similar light yield within the crystals which produced the distinct double-peaks. This issue cannot be solved directly as it is connected to the LYSO crystals itself. On the other hand, this problem was most probably only disclosed because the general resolution of the SiPM arrays is so good that the separation between the two peaks is visible. This also means that the double-peak issue does not affect the ability of the polarimeter to identify elastically scattered particles. Once it is known that both peaks origin from particles with the same energy, both peaks can be used when counting the number of elastics. A theoretical possibility to circumvent this issue would depend on a fine position resolution from the triangular $\Delta E$ detector. By creating a position dependent calibration, i.e., having multiple different calibration functions depending on the position of an event on each crystal face, the position dependence of the gain could be compensated.

## 6.2 Outlook

The database experiment described in this work did only measure the vector analyzing power of the deuteron carbon scattering. Of course, it is also very desirable to have measurements of the proton carbon vector analyzing power as well. For this reason, the *WASA proton database experiment* was conducted in August 2019 at COSY using again the WASA detector. The following proton beam energy where used: 160 MeV, 190 MeV, 200 MeV, 210 MeV, 232.8 MeV and 250 MeV. From the experiences of the deuteron database analysis, a few things were improved significantly in this experiment. Most importantly, the polarization of the beam at the injection energy was monitored on a regular base using the LEP. This will allow getting much smaller errors on the analyzing power compared to the deuteron results. Hoyong Jeong from the “Center for Axion and Precision Physics Research” at the *Institute of Basic Research* in Daejeon, Korea who is a member of the JEDI collaboration is working on the analysis of the proton run data. He is currently developing a new version of the Monte-Carlo software that was used to calculate the calibration of the WASA detector. His new version is called ***W****ASA* ***M****onte*-***C****arlo 4* (WMC4) and, as the name implies, will be written fully in Geant 4 which is not using FORTRAN anymore. If this new software will be successfully used in the analysis of the proton data, there would be the option to re-analyze the deuteron data using the new WMC4 to calculate the calibration and the detector acceptance. This would probably allow getting rid of a few issues in the previous analysis such as the detector acceptance calculation. The results from the deuteron and proton database experiments will form a solid base for the polarimetry at various energies.

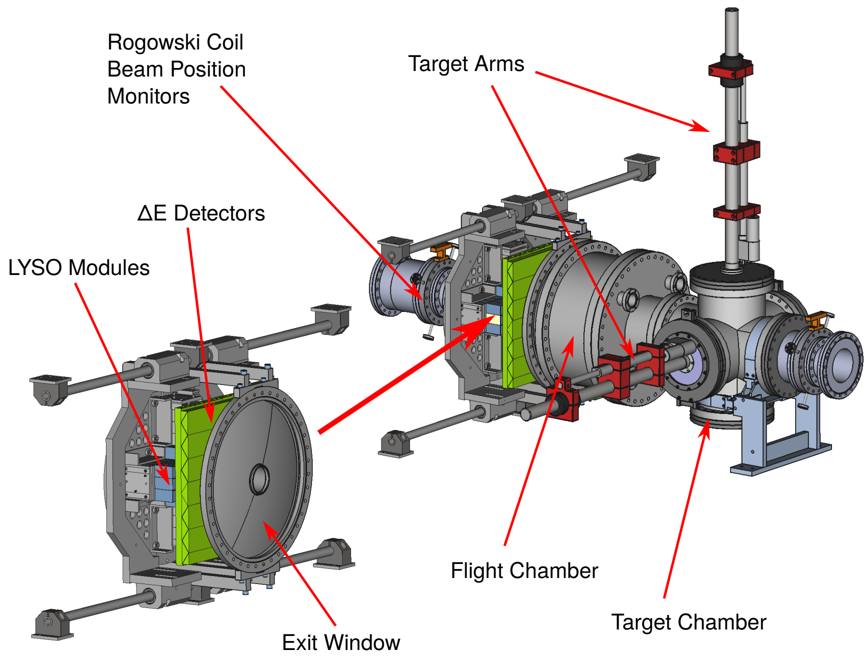


Figure 6.1: Model of the final polarimeter (working title: ***JE****DI* ***Po****larimeter* (JEPO)) that will be installed in the COSY ring by the end of the summer of 2019. CAD drawing by Berthold Klimczok

On the polarimeter side, a lot of future activity can be expected. For the end of the summer of 2019, it is planned to install the polarimeter in the ring of COSY and perform the first experiment. The individual components of the polarimeter are already and at our disposal. The 0.8 mm steel exit window is welded in a frame that can be attached to the vacuum flight chamber, see Figure 6.1. The vacuum parts are assembled and being tested at the moment of writing. A clone of the carbon block target system developed for WASA will be used for the first experiment. The PhD thesis of Otari Javakhishvili will be about the development of a diamond-pellet target that should allow for the measurement of a polarization profile of the beam. Nicola Canale just started his PhD with the intent to continue the development of the triangular $\Delta E$ detectors and Dito Shergelashvili and David Mchedlishvili will work on further improvement of the stability of the reverse bias supply for the SiPM arrays. All in all, a continuous rate of improvements on the LYSO based polarimeter can be expected until it will be used in the final EDM experiment.

# Appendix A

# Database Experiment

## A.1 Variance and Covariance of Weighted Sums

In order to calculate the statistical error and the covariance of weighted sums, the subsequent consideration can be made. Assuming an arbitrary function $f(x)$ with $x$ distributed according to a probability density function $n$ with $\langle N\rangle = \int n(x)dx$. Thus, the expected value of $f$ is given by:

$$\langle f\rangle = \frac{\int f(x)n(x)dx}{\int n(x)dx} = \frac{1}{\langle N\rangle}\int f(x)n(x)dx. \tag{A.1}$$

For a discrete values of $x_i$ with $f_i = f(x_i)$, the following substitution can be made:

$$\sum f_i \approx \int f(x)n(x)dx$$

and Equation (A.1) can be rewritten:

$$\begin{aligned} \langle f\rangle = \frac{\sum f_i}{\langle N\rangle} &\Rightarrow \langle f\rangle\langle N\rangle = \sum f_i \\ &\Rightarrow \langle \sum f_i\rangle = \langle\langle f\rangle\langle N\rangle\rangle = \langle f\rangle\langle N\rangle \end{aligned} \tag{A.2}$$

where the last equal sign implies statistical independence between $f$ and $n$, which can be assumed without loss of generality. From the expected value given in Equation (A.2) an expression for the covariance can be derived. Let $f_i$ and $g_i$ be two statistically independent functions distributed according to the probability density function $n$ defined above. For the covariance one gets:

$$\begin{aligned} \mathrm{Cov}\left(\sum f_i, \sum g_i\right) &= \langle\left(\sum f_i\right)\left(\sum g_i\right)\rangle - \langle\sum f_i\rangle\langle\sum g_i\rangle \\ &= \langle\sum_{i=j} f_i \cdot g_j + \sum_{i\neq j} f_i \cdot g_j\rangle - \langle N\rangle^2\langle f\rangle\langle g\rangle \\ &= \langle N\rangle\langle fg\rangle + (\langle N(N-1)\rangle)\langle f\rangle\langle g\rangle - \langle N\rangle^2\langle f\rangle\langle g\rangle \\ &= \langle N\rangle\langle fg\rangle + (\langle N^2\rangle - \langle N\rangle^2 - \langle N\rangle)\langle f\rangle\langle g\rangle \end{aligned}$$

with $N$ from a counting experiment, i.e., being Poisson-distributed, one can use

$$\langle N^2\rangle - \langle N\rangle^2 = \langle N\rangle$$

and therefore

$$\mathrm{Cov}\left(\sum f_i, \sum g_i\right) = \langle N\rangle\langle fg\rangle = \sum f_i \cdot g_i. \tag{A.3}$$

From this equation, one can directly derive the error on a weighted sum by choosing $f = g$:

$$\Delta^2\left(\sum f_i\right) = \mathrm{Cov}\left(\sum f_i, \sum f_i\right) = \sum f_i^2. \tag{A.4}$$

## A.2 Identities for the $\chi^2$ Calculation

In order to calculate the integrals from Section 4.3.1.4, Equations (4.41) to (4.43) the following identities are used:

$$\int_0^{2\pi} \cos(x)\ dx = 0 \tag{A.5}$$
$$\int_0^{2\pi} \cos^2(x)\ dx = \pi \tag{A.6}$$
$$\int_0^{2\pi} \cos^3(x)\ dx = 0 \tag{A.7}$$
$$\int_0^{2\pi} \cos^4(x)\ dx = \frac{3}{4}\pi \tag{A.8}$$
$$\int_0^{2\pi} \cos(x)\cos(2x)\ dx = 0 \tag{A.9}$$
$$\int_0^{2\pi} \cos^2(x)\cos(2x)\ dx = \frac{1}{2}\pi \tag{A.10}$$
$$\int_0^{2\pi} \cos^2(x)\sin(2x)\ dx = 0 \tag{A.11}$$
$$\int_0^{2\pi} \cos(nx)\cos(mx)\ dx = \delta_{nm}\pi \tag{A.12}$$
$$\int_0^{2\pi} \sin(nx)\sin(mx)\ dx = \delta_{nm}\pi \tag{A.13}$$
$$\int_0^{2\pi} \cos(nx)\sin(mx)\ dx = 0 \tag{A.14}$$

## A.3 Covariance Matrix for the $\chi^2$ Calculation

The full version of the covariance matrix given in Section 4.3.1.4, Equation (4.53) was calculated using the expression given in Equation (A.3):

$$\mathbf{C} = \left[\begin{array}{c|c|c} \mathrm{Cov}[\uparrow] & 0 & 0 \\ \hline 0 & \mathrm{Cov}[\downarrow] & 0 \\ \hline 0 & 0 & \mathrm{Cov}[0] \end{array}\right]$$

with

$$\mathrm{Cov}[\uparrow] = \begin{bmatrix} \sum_i^{ev(\uparrow)} 1 & \sum_i^{ev(\uparrow)} \cos(\Phi_i) & \sum_i^{ev(\uparrow)} \cos^2(\Phi_i) \\ \sum_i^{ev(\uparrow)} \cos(\Phi_i) & \sum_i^{ev(\uparrow)} \cos^2(\Phi_i) & \sum_i^{ev(\uparrow)} \cos^3(\Phi_i) \\ \sum_i^{ev(\uparrow)} \cos^2(\Phi_i) & \sum_i^{ev(\uparrow)} \cos^3(\Phi_i) & \sum_i^{ev(\uparrow)} \cos^4(\Phi_i) \end{bmatrix} \tag{A.15}$$

$$\mathrm{Cov}[\downarrow] = \begin{bmatrix} \sum_i^{ev(\downarrow)} 1 & \sum_i^{ev(\downarrow)} \cos(\Phi_i) & \sum_i^{ev(\downarrow)} \cos^2(\Phi_i) \\ \sum_i^{ev(\downarrow)} \cos(\Phi_i) & \sum_i^{ev(\downarrow)} \cos^2(\Phi_i) & \sum_i^{ev(\downarrow)} \cos^3(\Phi_i) \\ \sum_i^{ev(\downarrow)} \cos^2(\Phi_i) & \sum_i^{ev(\downarrow)} \cos^3(\Phi_i) & \sum_i^{ev(\downarrow)} \cos^4(\Phi_i) \end{bmatrix} \tag{A.16}$$

$$\mathrm{Cov}[0] = \begin{bmatrix} \sum_i^{ev(0)} 1 & \sum_i^{ev(0)} \cos(\Phi_i) & \sum_i^{ev(0)} \cos^2(\Phi_i) \\ \sum_i^{ev(0)} \cos(\Phi_i) & \sum_i^{ev(0)} \cos^2(\Phi_i) & \sum_i^{ev(0)} \cos^3(\Phi_i) \\ \sum_i^{ev(0)} \cos^2(\Phi_i) & \sum_i^{ev(0)} \cos^3(\Phi_i) & \sum_i^{ev(0)} \cos^4(\Phi_i) \end{bmatrix} \tag{A.17}$$

## A.4 Error Calculation of the $\chi^2$-Fit Method

The statistical errors on the asymmetries $\epsilon^{\downarrow,\uparrow}$, calculated using the *method of least squares* given in Equation (4.51), can be calculated using the approach described in [63]. A similar method using only polarized states is described in [21]. As in section 4.3.1.5 some assumptions have to be made:

1. The number of events in all three polarization states is equal: $N^{\uparrow} \approx N^{\downarrow} \approx N^0 \approx \frac{N}{3}$.
2. The acceptance of the detector is flat: $a_n = 0\ \forall n > 0$ in Equation (4.40).
3. The asymmetry is small: $\epsilon^{\downarrow,\uparrow} \ll 1$.

As a first step, the expected values given in Equation (4.41) to (4.43) have to be recalculated as a function of the azimuthal integration range $\Delta\Phi$. Note: For each value of $\Delta\Phi$ there are two sectors (one on the left and one on the right side of the detector, see Figure (4.15) with a size of $2 \cdot \Delta\Phi$ each. Hence:

$$\begin{aligned} \langle N^p \cos^n \rangle = \frac{\ell^p}{4 \cdot \Delta\Phi} \cdot \\ \Bigg[ \int_{-\Delta\Phi}^{+\Delta\Phi} \cos^n(\Phi) + \epsilon^p \cos^{n+1}(\Phi) d\Phi \\ + \int_{\pi-\Delta\Phi}^{\pi+\Delta\Phi} \cos^n(\Phi) + \epsilon^p \cos^{n+1}(\Phi) d\Phi \Bigg], \end{aligned} \tag{A.18}$$

with the polarization state $p = [\downarrow, \uparrow, 0]$ and $\ell^p = \mathcal{L}_p \sigma_0 a_0$. One has

$$\cos^n(\pi + x) = \begin{cases} + \cos^n(x) & \text{for even } n, \\ - \cos^n(x) & \text{for odd } n. \end{cases} \tag{A.19}$$

Using this relation, Equation (A.18) reduces to:

$$\langle N^p \cos^n \rangle = \begin{cases} \ell^p & \text{for } n = 0, \\ \ell^p \epsilon^p \langle \cos^{n+1}(\Delta\Phi) \rangle & \text{for odd } n > 0, \\ \ell^p \langle \cos^n(\Delta\Phi) \rangle & \text{for even } n > 0. \end{cases} \tag{A.20}$$

As a next step, these equations have to be linearized. This is done using the first order Taylor expansion $T[\cdot]$ around $(\ell_0^p, \epsilon_0^p)$:

$$T[\langle N^p \cos^n(\Phi) \rangle] = \begin{cases} \ell_0^p + \Delta\ell^p & \text{for } n = 0, \\ \ell_0^p \epsilon_0^p c_{n+1} + \Delta\ell^p \epsilon_0^p c_{n+1} + \ell_0^p \Delta\epsilon^p c_{n+1} & \text{for odd } n > 0, \\ \ell_0^p c_n + \Delta\ell^p c_n & \text{for even } n > 0, \end{cases} \tag{A.21}$$

where $\Delta\ell^p = \ell^p - \ell_0^p$, $\Delta\epsilon^p = \epsilon^p - \epsilon_0^p$ and $c_n = \langle \cos^n(\Delta\Phi) \rangle$.

By defining a parameter vector (note that $\epsilon^0 = \epsilon_0^0 = 0 \;\Rightarrow\; \Delta\epsilon^0 = 0$)

$$\vec{x}_{par.} = \left[ \Delta\ell^\uparrow, \Delta\ell^\downarrow, \Delta\ell^0, \Delta\epsilon^\uparrow, \Delta\epsilon^\downarrow \right]^T, \tag{A.22}$$

one can rewrite the linearized version of $\vec{y}_{mod.}$ from Equation (4.51) as follows:

$$\vec{y}_{mod.} = \mathbf{A} \vec{x}_{par.} + \vec{y}_0 \tag{A.23}$$

with

$$\mathbf{A} = \begin{bmatrix} 1 & 0 & 0 & 0 & 0 \\ \epsilon_0^\uparrow c_2 & 0 & 0 & \ell_0^\uparrow c_2 & 0 \\ c_2 & 0 & 0 & 0 & 0 \\ 0 & 1 & 0 & 0 & 0 \\ 0 & \epsilon_0^\downarrow c_2 & 0 & 0 & \ell_0^\downarrow c_2 \\ 0 & c_2 & 0 & 0 & 0 \\ 0 & 0 & 1 & 0 & 0 \\ 0 & 0 & 0 & 0 & 0 \\ 0 & 0 & c_2 & 0 & 0 \end{bmatrix}, \tag{A.24}$$

and

$$\vec{y}_0 = \left[\ell_0^{\uparrow},\ \ell_0^{\uparrow}\epsilon_0^{\uparrow}c_2,\ \ell_0^{\uparrow}c_2,\ \ell_0^{\downarrow},\ \ell_0^{\downarrow}\epsilon_0^{\downarrow}c_2,\ \ell_0^{\downarrow}c_2,\ \ell_0^{0},\ 0,\ \ell_0^{0}c_2\right]^T. \tag{A.25}$$

The third step is to transform the covariance matrix given in Equation (4.53) into a linearized form. The weighted sums in the blocks described by Equation (A.15) to (A.17) can be replaced by their expected values as stated in Equation (4.50) and their linearized form given in Equation (A.21), respectively. As defined in the 1. assumption at the beginning of this section, the number of events is considered equal in all three polarization states. Since $\ell^p = N^p$, the following substitution is valid: $\ell^{\uparrow} = \ell^{\downarrow} = \ell^0 = \frac{N}{3}$. Further, it was assumed that $\frac{\Delta\ell^p}{\ell_0^p} \approx 0$ as well as $\Delta\epsilon^p \approx 0$ in the covariance matrix. This yields to:

$$\mathbf{C}_{lin.} = \frac{N}{3}\cdot\begin{bmatrix} 1 & \epsilon_0^{\uparrow}c_2 & c_2 & 0 & 0 & 0 & 0 & 0 & 0 \\ \epsilon_0^{\uparrow}c_2 & c_2 & \epsilon_0^{\uparrow}c_4 & 0 & 0 & 0 & 0 & 0 & 0 \\ c_2 & \epsilon_0^{\uparrow}c_4 & c_4 & 0 & 0 & 0 & 0 & 0 & 0 \\ 0 & 0 & 0 & 1 & \epsilon_0^{\downarrow}c_2 & c_2 & 0 & 0 & 0 \\ 0 & 0 & 0 & \epsilon_0^{\downarrow}c_2 & c_2 & \epsilon_0^{\downarrow}c_4 & 0 & 0 & 0 \\ 0 & 0 & 0 & c_2 & \epsilon_0^{\downarrow}c_4 & c_4 & 0 & 0 & 0 \\ 0 & 0 & 0 & 0 & 0 & 0 & 1 & 0 & c_2 \\ 0 & 0 & 0 & 0 & 0 & 0 & 0 & c_2 & 0 \\ 0 & 0 & 0 & 0 & 0 & 0 & c_2 & 0 & c4 \end{bmatrix} \tag{A.26}$$

Now one can calculate the covariance matrix of the parameters as follows:

$$\begin{aligned}\mathbf{C}_{par.} &= (\mathbf{A}^T\mathbf{C}_{lin.}^{-1}\mathbf{A})^{-1} \\ &= \begin{bmatrix} \frac{N}{3} & 0 & 0 & 0 & 0 \\ 0 & \frac{N}{3} & 0 & 0 & 0 \\ 0 & 0 & \frac{N}{3} & 0 & 0 \\ 0 & 0 & 0 & \frac{3\left(c_2-\left(\epsilon_0^{\uparrow}\right)^2 c_4\right)}{Nc_2^2} & 0 \\ 0 & 0 & 0 & 0 & \frac{3\left(c_2-\left(\epsilon_0^{\downarrow}\right)^2 c_4\right)}{Nc_2^2} \end{bmatrix}.\end{aligned} \tag{A.27}$$

The diagonal of this matrix denotes the variance and the off-diagonal entries show the covariance among the parameters. On sees that all the parameters are non-correlated. The variance for $\Delta\ell^p$ is given by the expression $\frac{N}{3}$ witch is in agreement with a Poissonian error $\Delta N = \sqrt{N}$. As the quantities $\Delta\ell^p$ and $\Delta\epsilon^p$ represent just a shift by a constant value $(\ell_0^p, \epsilon_0^p)$ from the original observable $(\ell^p, \epsilon^p)$, the variance of $\Delta\ell^p$ represents the variance of $\ell^p$ and $\Delta\epsilon^p$ of $\epsilon^p$, respectively. Thus, the error for $\epsilon^{\uparrow,\downarrow}$ as a function of the azimuthal integration range $\Delta\Phi$ is given by:

$$\Delta\epsilon^{\uparrow,\downarrow}(\Delta\Phi) = \sqrt{\frac{3\left(\langle\cos^2(\Delta\Phi)\rangle - \left(\epsilon_0^{\uparrow,\downarrow}\right)^2\langle\cos^4(\Delta\Phi)\rangle\right)}{N\langle\cos^2(\Delta\Phi)\rangle^2}}, \tag{A.28}$$

and the Figure of Merit by:

$$\mathrm{FoM}(\epsilon^{\uparrow,\downarrow}, \Delta\Phi) = \frac{N}{3}\cdot\frac{\langle\cos^2(\Delta\Phi)\rangle^2}{\langle\cos^2(\Delta\Phi)\rangle - \left(\epsilon_0^{\uparrow,\downarrow}\right)^2\langle\cos^4(\Delta\Phi)\rangle}. \tag{A.29}$$

## A.5 Analytical Model of the Elastic Deuteron Carbon Cross Section

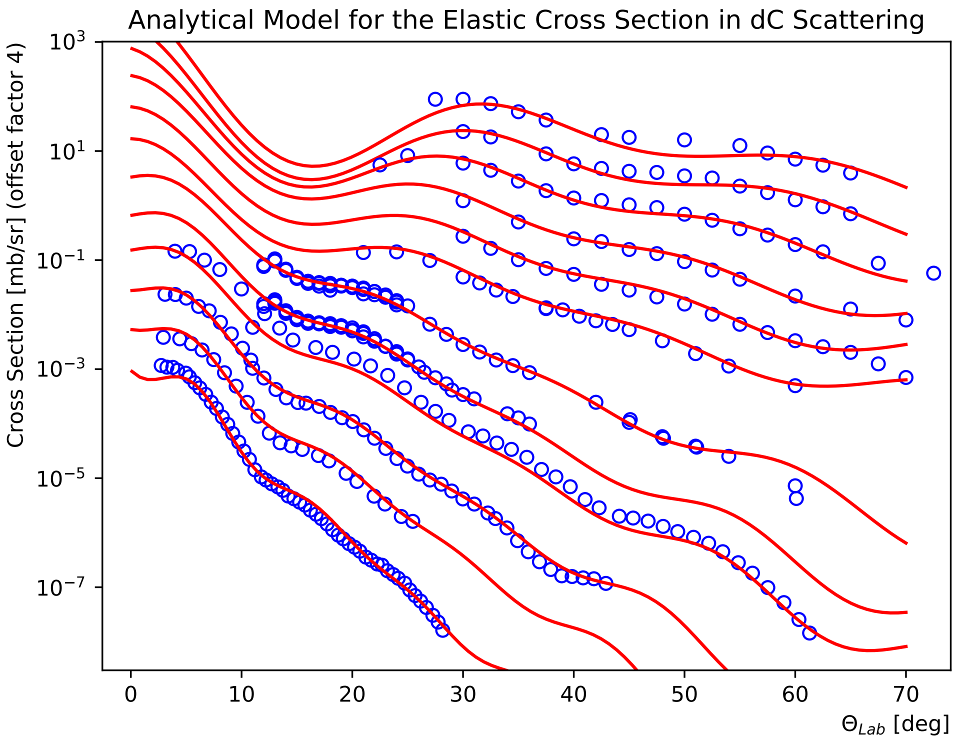


Figure A.1: Analytical model of the elastic deuteron carbon cross section (red) as a function of the deuteron beam energy and the scattering angle Θ. There reference data used as the input to the model is given in blue, from top to bottom for 45 MeV, 49 MeV, 54 MeV, 65 MeV, 70 MeV, 76 MeV, 113 MeV, 133 MeV, 140 MeV, 170 MeV, 200 MeV and 270 MeV. Each cross section is subsequently scaled down by a factor of four for better readability.

The analytical model of the elastic deuteron carbon cross section developed by Edward J. Stephenson uses reference data for this cross sections for the following energies: 45 MeV, 49 MeV, 54 MeV, 65 MeV and 70 MeV from [65], 76 MeV from [66], 113 MeV from [66] and [67], 133 MeV from [67], 140 MeV from [68], 170 MeV from [69], 200 MeV from [23] and 270 MeV from [22]. The energy and scattering angle dependent cross section is described by:

$$\sigma(E,\Theta) = 10^x \quad \text{with}$$
$$x = a_1 + a_2 q + (1 + a_5 q)\left[a_3 \sin(a_6 q) + a_4 \cos(a_6 q)\right]. \tag{A.30}$$

Here $q = q(E,\Theta)$ denotes the momentum transfer and is given in units of GeV/c. $a_1$ to $a_6$ are polynomials of $w = \ln(E)$ with E given in MeV. The parameters of these polynomials were to be determined using a minimization on all reference data points simultaneously and the result is given in Table A.1. A comparison of the model and the reference data is given in Figure A.1.

| | $p_0$ | $p_1$ | $p_2$ | $p_3$ |
|---|---|---|---|---|
| $a_1$ | -74.99 | 43.96 | -8.111 | 0.4966 |
| $a_2$ | 53.76 | -23.02 | 2.073 | 0.0 |
| $a_3$ | -25.22 | 12.65 | -1.905 | 0.07993 |
| $a_4$ | 17.78 | -6.375 | 0.5565 | 0.0 |
| $a_5$ | -3.822 | 0.2481 | 0.0 | 0.0 |
| $a_6$ | 14.37 | 2.772 | 0.0 | 0.0 |

Table A.1: Parameters for the polynomials $a_1$ to $a_6$ in Equation (A.30). Each of this polynomials has the form $a_x = p_0 + p_1 w + p_2 w^2 + p_3 w^3$ with $w = \ln(E)$

## A.6 Time-Based dC Asymmetries

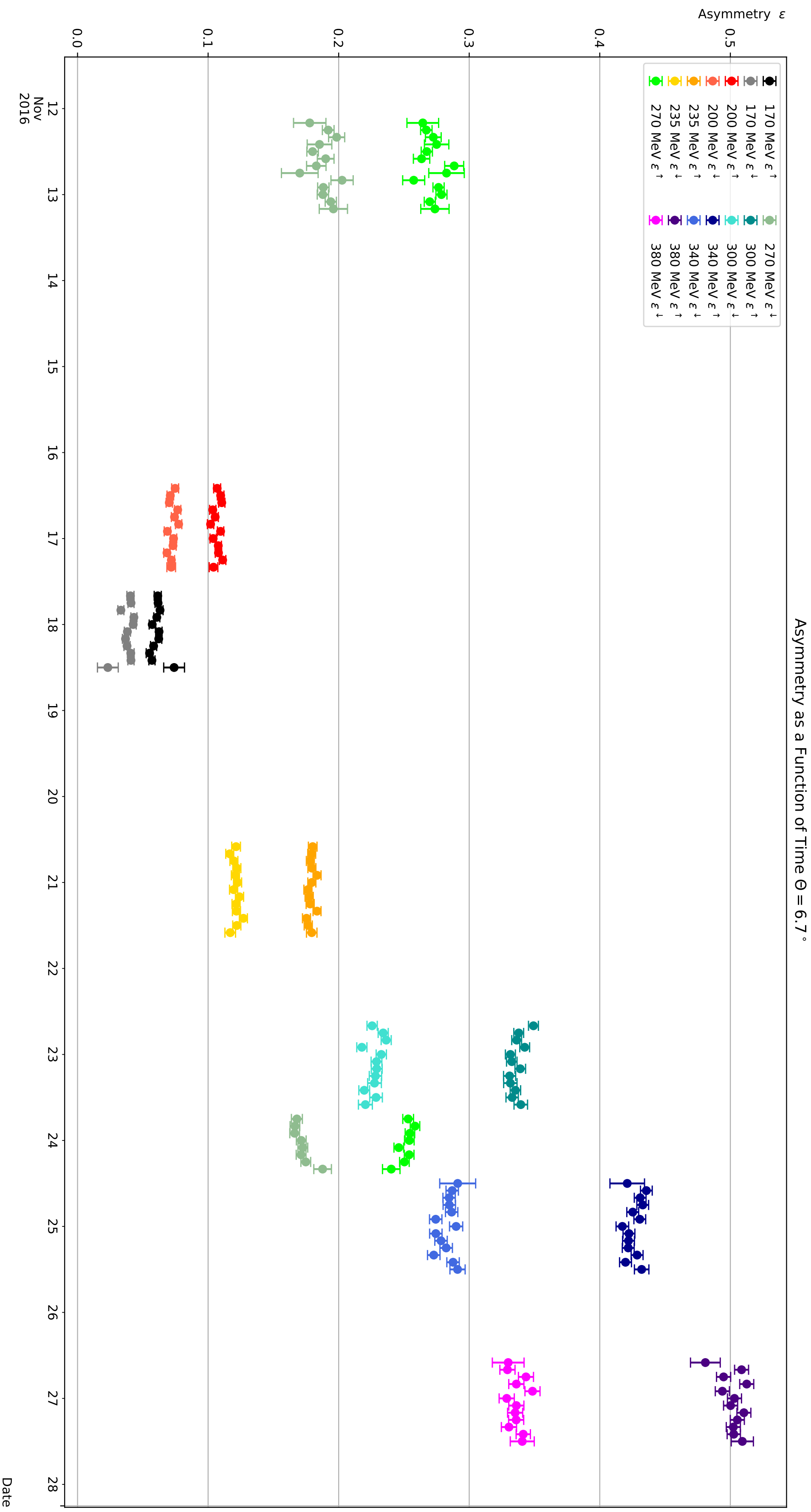


Figure A.2: Asymmetries as a function the date of measurement during the database experiment. The asymmetries were calculated form data that was binned in two hour bins.

# Appendix B

# LYSO Module Development

## B.1 Overview of SiPMs used in the Polarimeter Development

| | ARRAYC-60035-4P-EVB | ARRAYJ-30020-64P-PCB | J-Series 60035 |
|---|---|---|---|
| Application | 1st test with LYSO | LYSO based detector modules | Veto Scintillators, 1st iteration |
| Manufacturer | SensL | SensL | SensL |
| SiPM sensor type | C-Series 30035 | J-Series 30020 | J-Series 60035 |
| Bias voltage range [V] | 25.2 - 29.7 | 25.2 - 30.7 | 25.2 - 30.7 |
| Spectral range [nm] | 300 - 950 | 200 - 900 | 200 - 900 |
| Peak sensitivity [nm] | 420 | 420 | 420 |
| Pixel size [$\mu$m] | 35 | 20 | 35 |
| Pixel per SiPM | 18'980 | 14'410 | 22'292 |
| SiPM fill-factor [%] | 64 | 65 | 75 |
| SiPM area [mm] | $6^2$ | $3^2$ | $6^2$ |
| SiPMs per array | 2x2 | 8x8 | single SiPM |
| Array area [mm$^2$] | $12.46^2$ | $26.68^2$ | - |
| Array fill-factor [%] | $\sim 90$ | $\sim 90$ | - |
| Total pixel per array | 75'920 | 922'240 | - |
| Connector | 8-Pin DIL | 2x Hirose-80 | solder pads |

| | PA3325-WB-0808 | PA3315-WB-0808 | PM6660TP-SB0 |
|---|---|---|---|
| Application | LYSO based detector modules | LYSO based detector modules | $\Delta E$ detectors |
| Manufacturer | Ketek | Ketek | Ketek |
| SiPM sensor type | PM3325-WB | PM3315-WB | PM6660 |
| Bias voltage range [V] | 24.4 - 31.0 | 26.6 - 33.2 | 26.6 - 33.2 |
| Spectral range [nm] | 300 - 900 | 300 - 900 | 300 - 900 |
| Peak sensitivity [nm] | 430 | 430 | 430 |
| Pixel size [$\mu$m] | 25 | 15 | 60 |
| Pixel per SiPM | 13'920 | 38'800 | $\sim 6600$ |
| SiPM fill-factor [%] | $\sim 95$ | $\sim 97$ | $\sim 66$ |
| SiPM area [mm] | $3^2$ | $3^2$ | $6^2$ |
| SiPMs per array | 8x8 | 8x8 | single SiPM |
| Array area [mm$^2$] | $26.84^2$ | $26.84^2$ | - |
| Array fill-factor [%] | $\sim 80$ | $\sim 80$ | - |
| Total pixel per array | 890'880 | 2'483'200 | - |
| Connector | 2x SAMTEC ST4-40 | 2x SAMTEC ST4-40 | 2x single pin |

Table B.1: Overview over all SiPMs used in the complete polarimeter development process. The information was taken from [70], [56] and [71] for the SensL SiPMs and from [72], [73] and [74] for the Ketek SiPMs.

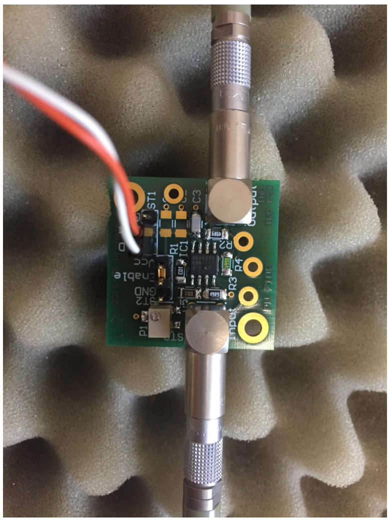

(a) Picture of the $\Delta E$ pre-amplifier.

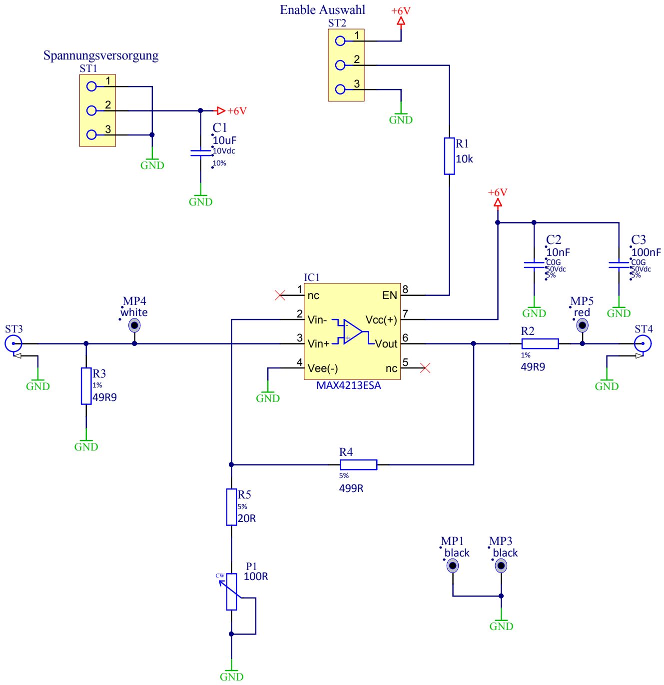


(b) Schema of the $\Delta E$ pre-amplifier.

Figure B.1: $\Delta E$ pre-amplifier being tested using a signal generator on the left and its schema on the right.

## B.2 Pre-Amplifier for the $\Delta E$ Detectors

The signals created by the SiPMs that were glued to the plastic scintillators used in all three iterations of the polarimeter development, were to small to be directly fed to the ADC. For this reason, a simple pre-amplifier had to be developed. A simple design based on a non-inverting op-amp was chosen for this purpose. By having a non-inverting configuration, the pre-amplifier could be designed using a single supply voltage. The reverse bias voltage for the SiPMs of the $\Delta E$ detectors was taken from the same designated power supply that was used to generate the bias for the LYSO based detector modules and was, therefore, a positive voltage. The circuit was designed around the *MAX4213* op-amp, see [75]. This op-amp was chosen for its high speed of up to 300 MHz, its large slew rate of 600 V µs$^{-1}$ and its single supply rail-to-rail capability. Rail-to-rail means that the output can go up to the positive supply voltage rail and in the case of the single supply operation down to the ground rail. The circuit was designed by the author as a sketch which was given to Tanja Hahnraths - von der Gracht from the electronic workshop of IKP who created a PCB layout that was then ordered. The schema of the pre-amplifier is shown if Figure B.1b. The gain of the pre-amplifier can be set to a value between 5.2 and 25.9 using a potentiometer. The output is terminated with 50 Ω series resistor and can, therefore, drive a standard coaxial line. The input is 50 Ω terminated as well which allows the connection of coaxial wires at the input which can be directly connected to the anode of a positive reverse biased SiPM. The *MAX4213* allows a supply voltage of up to 12 V but was connected to the 6 V rail of a NIM crate.

The SiPMs that were glued to the plastic $\Delta E$ detectors were connected all in parallel using a very thin coaxial cable that was then connected to the pre-amplifier that was secured in a 3D-printed box and mounted next to the detectors.

# Bibliography


[1] Laurent Canetti, Marco Drewes, and Mikhail Shaposhnikov. Matter and Antimatter in the Universe. *New Journal of Physics, Focus Issue on the Origin of Matter*, Vol. 14 (095012), 2012.

[2] W. Bernreuther. CP Violation and Baryogenesis, 2002.

[3] A. D. Sakharov. Violation of CP Invariance, C Asymmetry and Baryon Asymmetry in the Universe. *Pisma Zh. Eksp. Teor. Fiz.*, Vol. 5, Nr. 1, 1967.

[4] JEDI Collaboration. Homepage. http://collaborations.fz-juelich.de/ikp/jedi/, 2019.

[5] Thomas Mannel. Theory and Phenomenology of CP Violation. In *The 7th International Conference on Hyperons, Charm And Beauty Hadrons (BEACH 2006)*, volume 167 of *Nuclear Physics B*. Lancaster: Elsevier, 2006.

[6] Dr. J. F. J. van den Brand. Discrete symmetries. Vrije Universiteit, Amsterdam, The Netherlands. Introductory Course.

[7] F. R. Klinkhamer and N. S. Manton. A Saddle-Point Solution in the Weinberg-Salam Theory. *Physical Review D*, 30:2212–2220, 1984.

[8] Dr. Dieter Fick. *Einführung in die Kernphsik mit polarisierten Teilchen, Nachdruck*. MPI für Kernphysik, 1991.

[9] C. L. Oxley, W. F. Cartwright, I. Rouvina, E. Baskir, D. Klein, J. Ring, and W. Skillman. Double scattering of high-energy protons by hydrogen and carbon. *Physical Review*, Vol. 91, Nr. 2:419–420, 1953.

[10] Emilio Segrè. *Nuclei and Particles, Second Edition*. The Benjamin / Cummings Publishing, Inc., 1977.

[11] E. Fermi. Polarization of High Energy Protons Scattered by Nuclei. *Il Nuovo Cimento*, Vol. 10, Nr. 4, 1954.

[12] H. Stein et al. Current Status of the COSY Electron Cooler (Jülich, Germany) . *Atomic Energy*, Vol. 94, No. 1, 2003.

[13] N. Hempelmann. *Polarization Measurement and Manipulation for Electric Dipole Moment Measurements in Storage Rings*. PhD thesis, RWTH Aachen University, 2018.

[14] R. Maier et al. Cooler Synchrotron COSY. *Nuclear Physics A*, Vol. 626:395 – 403, 1997.

[15] U. Bechstedt et al. Field Measurement of the Magnets for COSY - Jülich. In *EPAC 92, Third European Particle Accelerator Conference*, 1992.

[16] D. Prasuhn et al. Electron and Stochastic Cooling at COSY. *Nuclear Instruments and Methods in Physics Research A*, Vol. 441:167 – 174, 2000.

[17] H. Calen et al. Detector Setup for a Storage Ring with an Internal Target. *Nuclear Instruments and Methods in Physics Research A*, Vol. 379:57–75, 1996.

[18] B. Trostell. Vacuum Injection of Hydrogen Micro-Sphere Beams. *Nuclear Instruments and Methods in Physics Research A*, Vol. 362:41–52, 1995.

[19] H. H. Adam et al. Proposal for the Wide Angle Shower Apparatus (WASA) at COSY-Julich. *(WASA-at-COSY)*, nucl-ex/0411038, 2004.

[20] Atmel/Microchip. ATmega 328P. http://ww1.microchip.com/downloads/en/DeviceDoc/ATmega48A-PA-88A-PA-168A-PA-328-P-DS-DS40002061A.pdf, 2018. [Online; accessed 01. 03. 2019].

[21] J. Pretz and F. Müller. Extraction of Azimuthal Asymmetries Using Optimal Observables. *The European Physical Journal C*, Vol. 79:47, 2019.

[22] Y. Satou et al. Three-body dN interaction in the analysis of the $^{12}C(\vec{d}, d')$ reaction at 270 MeV. *Physics Letters B*, Vol. 549:307–313, 2002.

[23] T. Kawabata et al. Isovector and isoscalar spin-flip $M1$ strengths in $^{11}B$. *Physical Review C*, Vol. 70:034318, 2004.

[24] R. Brun et al. CERN-W5013: GEANT Detector Description and Simulation Tool. https://cds.cern.ch/record/118715?ln=en, 1994. [Online; accessed 01. 03. 2019].

[25] M Żurek. *Investigation of the Charge Symmetry Breaking Reaction $dd \rightarrow\ ^4He\pi^0$ with the WASA-at-COSY Facility*. PhD thesis, Universität zu Köln, 2017.

[26] K. Hatanaka. courtesy of E. J. Stephenson.

[27] K. Ermisch. *Search for Three-Nucleon Force Effects in Proton-Deuteron Elastic Scattering*. PhD thesis, University of Groningen, 2003.

[28] K. Sekiguchi et al. Complete Set of Precise Deuteron Analyzing Powers at Intermediate Energies: Comparison With Modern Nuclear Force Predictions. *Physical Review C*, Vol. 65:034003, 2002.

[29] F. Abusaif et al. Feasibility Study for an EDM Storage Ring. *arXiv e-prints*, page arXiv:1812.08535, Dec 2018.

[30] J. Pretz. Comparison of Methods to Extract an Asymmetry Parameter From Data. *Nuclear Instruments and Methods A*, Vol. 659:456–461, 2011.

[31] Dr. William R. Leo. *Techniques for Nuclear and Particle Physics Experiments, A How-to Approach*. Springer-Verlag, 1994.

[32] Dr. Glenn F. Knoll. *Radiation Detection and Measurement, Fourth Edition*. John Wiley & Sons, Inc, 2010.

[33] J. R. De Laeter, J. K. Böhlke, P. De Bièvre, H. Hidaka, H. S. Peiser, K. J. R. Rosman, and P. D. P. Taylor. Atomic Weights of the Elements: Review 2000. *Pure and Applied Chemistry*, Vol. 75, No. 6:683–800, 2003.

[34] G. Audi, F.G. Kondev, M. Wang, B. Pfeiffer, X. Sun, J. Blachot, and M. MacCormick. The NUBASE 2012 evaluation of nuclear properties. *Chinese Physics C*, Vol. 36, No. 12:1157–1286, 2012.

[35] US Patent. US 6,624,420 Bl. https://pdfs.semanticscholar.org/b644/9bab5c4fee95381ec1da732e79b2c48f9d93.pdf, 2003. [Online; accessed 11. 01. 2019].

[36] Jianming Chen, Rihua Mao, Liyuan Zhang, and Ren-Yuan Zhu. Gamma-Ray Induced Radiation Damage in Large Size LSO and LYSO Crystal Samples. *IEEE Transactions on Nuclear Science*, Vol. 54, No. 4:1319–1326, 2007.

[37] Saint-Gobain. LYSO Scintillation Material. https://www.crystals.saint-gobain.com/sites/imdf.crystals.com/files/documents/lyso-material-data-sheet_1.pdf, 2018. [Online; accessed 11. 01. 2019].

[38] SensL - Technical Note. An Introduction to the Silicon Photomultiplier. http://www.sensl.com/downloads/ds/TN%20-%20Intro%20to%20SPM%20Tech.pdf, 2017. [Online; accessed 11. 01. 2019].

[39] Hamamatsu. Photomultiplier Tubes. https://www.hamamatsu.com/resources/pdf/etd/PMT_TPMZ0002E.pdf, 2016. [Online; accessed 11. 01. 2019].

[40] Epic-Crystal. LYSO (Ce). http://www.epic-crystal.com/data/upload/20181120/5bf3cf6c2ebf5.pdf, 2018. [Online; accessed 11. 01. 2019].

[41] The Raspberry Pi Foundation. Raspberry Pi 2 Model B. https://www.raspberrypi.org/products/raspberry-pi-2-model-b/, 2015. [Online; accessed 11. 01. 2019].

[42] iseg. NHS series - Versatile High Precision HV Module in NIM Standard. https://iseg-hv.com/files/media/iseg_manual_NHS_en_20.pdf, 2018. [Online; accessed 11. 01. 2019].

[43] Flask. Web Development, One Drop at a Time. http://flask.pocoo.org/, 2018. [Online; accessed 11. 01. 2019].

[44] socket.io. Featuring the Fastest and Most Reliable Real-Time Engine. https://socket.io/, 2018. [Online; accessed 11. 01. 2019].

[45] Struck - Innovative Systeme. SIS3316-250-14. https://www.struck.de/sis3316-2014-03-20.pdf, 2014. [Online; accessed 11. 01. 2019].

[46] OWIS. Rotary Measuring Stages - DMT 65. https://www.owis.eu/fileadmin/user_upload/owis.eu/products/pdf/pi_dmt_65.pdf, 2017. [Online; accessed 01. 04. 2019].

[47] OWIS. Position Control Units - PS 10. https://www.owis.eu/fileadmin/user_upload/owis.eu/products/pdf/pi_dmt_65.pdf, 2017. [Online; accessed 01. 04. 2019].

[48] Rose&Krieger. Elektrozylinder LZ 60 - Linearzylinder. https://www.rk-rose-krieger.com/fileadmin/catalogue/lineartechnik/lt_zyl_leistungskl2_d.pdf, 2018. [Online; accessed 01. 04. 2019].

[49] Basicmicro. RoboClaw 2x15A, 34VDC Dual ChannelBrushed DC Motor Controller. http://downloads.basicmicro.com/docs/roboclaw_datasheet_2x15A.pdf, 2016. [Online; accessed 30. 03. 2019].

[50] S. Basile. *Development of a High Precision LYSO Polarimeter for EDM Search at COSY Storage Ring* . PhD thesis, Università degli Studi di Ferrara, 2019.

[51] Saint-Gobain. BC-400, BC-404, BC-408, BC-412, BC-416 - Premium Plastic Scintillators. https://www.crystals.saint-gobain.com/sites/imdf.crystals.com/files/documents/bc400-404-408-412-416-data-sheet.pdf, 2018. [Online; accessed 26. 03. 2019].

[52] M. J. Berger et al. Report 49. *Journal of the International Commission on Radiation Units and Measurements*, Vol. 25, No. 2, 1993.

[53] StemLab. Red Pitaya v1.1. https://www.redpitaya.com/f130/STEMlab-board, 2018. [Online; accessed 04. 04. 2019].

[54] The Lund/LBNL Nuclear Data Search. Decay Properties of $^{176}$Lu. http://nucleardata.nuclear.lu.se/toi/nuclide.asp?iZA=710176, 1999. [Online; accessed 11. 01. 2019].

[55] The Lund/LBNL Nuclear Data Search. Decay Properties of $^{22}$Na. http://nucleardata.nuclear.lu.se/toi/nuclide.asp?iZA=110022, 1999. [Online; accessed 04. 04. 2019].

[56] SensL. C-Series Low Noise, Blue-Sensitive Silicon Photomultipliers, Datasheet. https://www.mouser.de/datasheet/2/308/DS-MicroCseries-1489568.pdf, 2014. [Online; accessed 01. 04. 2019].

[57] M. Urban et al. The New APD Based Readout for the Crystal BarrelCalorimeter. *Journal of Physics: Conference Series*, Vol. 587, 012043, 2015.

[58] StemLab. DS18B20 Temperature Sensor. https://datasheets.maximintegrated.com/en/ds/DS18B20.pdf, 2018. [Online; accessed 04. 04. 2019].

[59] C . van der Leun and C . Alderliesten. The Deuteron Binding Energy. *Nuclear Physics A*, Vol. 390:261–269, 1982.

[60] Units The NIST Reference on Constants and Uncertainty. The Deuteron Mass Equivalent in MeV. https://physics.nist.gov/cgi-bin/cuu/Value?mdc2mev, 2014. [Online; accessed 25. 03. 2019].

[61] N.P.M. Brantjes et al. Correcting Systematic Errors in High-Sensitivity Deuteron Polarization Measurements. *Nuclear Instruments and Methods in Physics Research A*, 664:49–64, 2012.

[62] J. Pretz on behalf of the JEDI and CPEDM collaboration. Electric Dipole Moment Measurements at Storage Rings. In *Proceedings of the Discrete 2018 Conference, Journal of Physics: Conference Series*, 2019.

[63] K. A. Olive et al. Particle Physics Booklet, 2014. Sec. 38 Statistics, (Particle Data Group).

[64] F. Ajzenberg-Selove and T. Lauritsen. Energy Levels of Light Nuclei A = 12. http://www.tunl.duke.edu/nucldata/fas/12_1959.pdf, 2017. [Online; accessed 07. 05. 2019].

[65] S. Kato et al. Analyzing Power Measurements for $d -^{12} C$ Elastic Scattering Between 35–70 MeV. *Nuclear Instruments and Methods A*, Vol. 238:453–462, 1985.

[66] 2004 KVI Run With Plastic Scintillator and NaI Detectors. courtesy of E. J. Stephenson.

[67] 2005 KVI Run With BBS Spectrometer. courtesy of E. J. Stephenson.

[68] H. Okamura et al. Mechanism of the Forward-Angle (d,pn) Reaction at Intermediate Energies. *Physical Review C*, Vol. 58:2180, 1998.

[69] C. Bäumer et al. Deuteron Elastic and Inelastic Scattering from $^{12}C$, $^{24}Mg$, and $^{58}Ni$ at 170 MeV. *Physical Review C*, Vol. 63:037601, 2001.

[70] SensL. ArrayJ - High Fill-Factor Arrays of J-Series SiPM Sensors. http://sensl.com/downloads/ds/UM-ArrayTSV.pdf, 2019. [Online; accessed 31. 03. 2019].

[71] SensL. J-Series High PDE and Timing Resolution, TSV Package Datasheet. http://www.sensl.com/downloads/ds/DS-MicroJseries.pdf, 2017. [Online; accessed 31. 03. 2019].

[72] Ketek. Product Data Sheet SiPM – Silicon Photomultiplier PM3325-WB-D0. https://www.ketek.net/wp-content/uploads/2018/12/KETEK-PM3325-WB-D0-Datasheet.pdf, 2018. [Online; accessed 31. 03. 2019].

[73] Ketek. Product Data Sheet SiPM – Silicon Photomultiplier PA3325-WB-0808. https://www.ketek.net/wp-content/uploads/2016/12/KETEK-PA3325-WB-0808-Datasheet.pdf, 2018. [Online; accessed 31. 03. 2019].

[74] Ketek. Product Data Sheet SiPM – Silicon Photomultiplier PM3315-WB-D0. https://www.ketek.net/wp-content/uploads/2018/12/KETEK-PM3315-WB-B0-Datasheet.pdf, 2018. [Online; accessed 31. 03. 2019].

[75] Maxim Integrated. MAX4213, Miniature, 300MHz, Single-Supply, Rail-to-Rail Op Amps with Enable. https://datasheets.maximintegrated.com/en/ds/MAX4212-MAX4220.pdf, 2019. [Online; accessed 30. 03. 2019].

# Acknowledgments

First of all, I want to express my gratitude to my Ph.D. supervisor Prof. Dr. Jörg Pretz and the director of IKP-2 Prof. Dr. Hans Ströher for giving me the opportunity to write my thesis at the *Forschungszentrum Jülich* in collaboration with the *RWTH Aachen*. Second, I would like to thank Dr. Irakli Keshelashvili for the invitation to join his polarimeter development group and his caring attitude towards me, both in the workplace as well as during my settling-in period in *Jülich*. Further, I want to thank Dr. Maria Żurek for the introduction she gave me into the WASA data analysis and the huge effort she did in preparing the raw data into a form that I could use, and all the countless other contributions she made to the analysis of the *database experiment*. Without her, I would have failed miserably in the task of analyzing the WASA data. I want to thank Dr. Volker Hejny for sharing his huge experience with the WASA detector with me and for the organization of the *database experiment*. I also want to express my gratitude to Dr. Edward Stephenson who helped me with the fundamental understanding of the WASA data analysis and provided all the reference data sets needed to produce the final results. Whenever I was stuck at some point in the analysis, he would find a solution or provided me with a model that would allow me to continue my work. A big thank-you goes to Dr. Aleksandra Wrońska and Dr. Izabela Ciepał for their useful inputs during our many analysis meetings. A large shout-out goes to the group of Georgians consisting of Dr. David Mchedlishvili, Dito Shergelashvili, Otari Javakhishvili, Mikael Gagoshidze, Giorgi Kvantrishvili and David Kordzaia who included me in their ”gang” even though I would often not understand a single word. Even if our common work was some times a bit chaotic, I am very much pleased with the polarimeter setup that we have built together. A special thank goes to Dr. Andro Kacharava who looked after me from the first day on and organized the trips to Georgia which were fruitful both in a scientific as well as in a cultural way. I would like to thank all my co-workers and co-students here at the *Institut für Kernphysik* for all the inspiring conversations we had and the friendly and peaceful work environment you created. Finally, I want to thank my family who supported me all the time especially when I was in states of doubt or despair. Last but not least, I want to express my gratitude to my beloved, favorite human Mihal. It was her who made all of this possible by carrying me, feeding me, providing a home for me, comforting and cheering me up when I was down and accompany my journey into the strange. Without you, none of this would have worked out and I owe you everything!

# Eidesstattliche Erklärung

Ich, Fabian Müller

erkläre hiermit, dass diese Dissertation und die darin dargelegten Inhalte die eigenen sind und selbstständig, als Ergebnis der eigenen originären Forschung, generiert wurden.

Hiermit erkläre ich an Eides statt

1. Diese Arbeit wurde vollständig oder grösstenteils in der Phase als Doktorand dieser Fakultät und Universität angefertigt;
2. Sofern irgendein Bestandteil dieser Dissertation zuvor für einen akademischen Abschluss oder eine andere Qualifikation an dieser oder einer anderen Institution verwendet wurde, wurde dies klar angezeigt;
3. Wenn immer andere eigene- oder Veröffentlichungen Dritter herangezogen wurden, wurden diese klar benannt;
4. Wenn aus anderen eigenen- oder Veröffentlichungen Dritter zitiert wurde, wurde stets die Quelle hier für angegeben. Diese Dissertation ist vollständig meine eigene Arbeit, mit der Ausnahme solcher Zitate;
5. Alle wesentlichen Quellen von Unterstützung wurden benannt;
6. Wenn immer ein Teil dieser Dissertation auf der Zusammenarbeit mit anderen basiert, wurde von mir klar gekennzeichnet, was von anderen und was von mir selbst erarbeitet wurde;
7. Kein Teil dieser Arbeit wurde vor deren Einreichung veröffentlicht.

Jülich, den 3. Dezember 2019
Ort, Datum

Fabian Müller